

# Improved modeling of segmented earthquake rupture informed by enhanced signal analysis of seismic and geodetic observations

vorgelegt von  
**Andreas Steinberg**

Dissertation  
zur Erlangung des akademischen Grades  
eines Doktors der Naturwissenschaften (Dr. rer. nat.)  
der Mathematisch-Naturwissenschaftlichen Fakultät der  
Christian-Albrechts-Universität zu Kiel

Kiel, Januar 2020  
Institut für Geowissenschaften  
Abteilung Geophysik

Referent: Dr. Henriette Sudhaus  
Korreferent: Prof. Dr. Wolfgang Rabbel  
Tag der mündlichen Prüfung: 12. April 2021



## Abstract

Earthquake source modeling has emerged from the need to be able to describe and quantify the mechanism and physical properties of earthquakes. Investigations of earthquake rupture and fault geometry requires the testing of a large number of such potential sets of earthquake sources models. Earthquakes often rupture across more than one fault segment. If such rupture segmentation occurs on a significant scale, a simple model may not represent the rupture process well. This thesis focuses on the data-driven inclusion of earthquake rupture segmentation into earthquake source modeling. The developed tools and the modeling are based on the joint use of seismological waveform far-field and geodetic Interferometric Synthetic Aperture Radar near-field surface displacement maps to characterise earthquake sources robustly with rigorous consideration of data and modeling errors.

A strategy based on information theory is developed to determine the appropriate model complexity to represent the available observations in a data-driven way. This is done in consideration of the uncertainties in the determined source mechanisms by investigating the inferences of the full Bayesian model ensemble. Application on the datasets of four earthquakes indicated that the inferred source parameters are systematically biased by the choice of model complexity. This might have effects on follow-up analyses, e. g. regional stress field inversions and seismic hazard assessments.

Further, two methods were developed to provide data-driven model-independent constraints to inform a kinematic earthquake source optimization about earthquake source parameter prior estimates. The first method is a time-domain multi-array backprojection of teleseismic data with empirical traveltimes corrections to infer the spatio-temporal evolution of the rupture. This enables detection of potential rupture segmentation based on the occurrence of coherent high-frequency sources during the rupture process. The second developed method uses image analysis methods on satellite radar measured surface displacement maps to infer modeling constraints on rupture characteristics (e.g. strike and length) and the number of potential segments. These two methods provide model-independent constraints on fault location, dimension, orientation and rupture timing. The inferred source parameter constraints are used to constrain an inversion for the source mechanism of the 2016 Muji Mw 6.6 earthquake, a segmented and bilateral strike-slip earthquake.

As a case study to further investigate a depth-segmented fault system and occurrence of co-seismic rupture segmentation in such a system the 2008-2009 Qaidam sequence with co-seismic and post-seismic displacements is investigated. The Qaidam 2008-2009 earthquake sequence in northeast Tibet involved two reverse-thrust earthquakes and a postseismic signal of the 2008 earthquake. The 2008 Qaidam earthquake is modeled as a deep shallow dipping earthquake with no indication of rupture segmentation. The 2009 Qaidam earthquake is modeled on three distinct south-dipping high-angle thrusts, with a bilateral and segmented rupture process. A good agreement between co-seismic surface displacement measurements and coherent seismic energy emission in the backprojection results is determined.

Finally, a combined framework is proposed which applies all the developed methods and tools in an informed parallel modeling of several earthquake source model complexities. This framework allows for improved routine determination of earthquake source modeling under consideration of rupture segmentation. This thesis provides overall an improvement for earthquake source analyses and the development of modeling standards for robust determination of second-order earthquake source parameters.

## Zusammenfassung

Die Modellierung von Erdbebenquellen ist notwendig, um die Mechanismen und physikalischen Eigenschaften des Bruchvorganges eines Erdbebens zu beschreiben. Untersuchungen des Bruchvorganges bedürfen des sorgfältigen Prüfens vieler möglicher Geometrien der kausativen Störung. Erdbebenbrüche treten oft nicht nur auf einer Störungsfläche auf. Ist solch eine Segmentierung des Bruchvorganges signifikant genug, kann der Erdbebenbruch nicht mehr hinreichend mit einem einfachen Modell erklärt werden. Diese Arbeit fokussiert sich auf die datengetriebene Einbindung von Erdbebenbruchsegmentierung in die Modellierung des Bruchvorganges. Die entwickelten Methoden sowie die Modellierung basieren auf der Zusammenführung zweier unabhängiger Datensätze, seismologischen Wellenformen und geodätischen Radarsatelliten-Deformationsmessungen zur robusten Charakterisierung von Erdbebenquellen unter sorgfältiger Beachtung von Daten- und Modell-Fehlern.

Eine Strategie basierend auf der Informationstheorie wurde entwickelt, um eine den Daten angemessene und datengetriebene Modellierung der Erdbebenbruchkomplexität vorzunehmen. Dies erfolgte unter Beachtung der Unsicherheiten der möglichen Modelle aus Bayesianischer Inferenz. Es wird anhand der Resultate von Analysen vier unterschiedlicher Erdbeben gezeigt, dass abgeleitete Erdbebenquellparameter systematisch von der gewählten Komplexität des Modells abhängig sind. Die Komplexität des Modells hat daher Einfluss auf nachfolgende Studien, wie die Berechnung von Spannungskräften im Störungssystem, sowie die seismische Gefährdungsanalyse, und muss daher beachtet werden.

Desweiteren werden zwei Methoden zur datengetriebenen und modellunabhängigen Beschränkung des Parameterraumes entwickelt. Die erste Methode ist eine seismologische Rückstrahlmethode, welche verfügbare seismologische Stationen zu Arrays gruppiert und anschließend die räumliche und zeitliche Entwicklung des Bruchvorganges abbildet mittels Arraymethoden. So kann durch das Auftreten von hochfrequenten kohärenten Signalen bestimmt werden, ob eine Segmentierung des Bruchvorganges aufgetreten ist. Die Laufzeitberechnungen der seismologischen Rückstrahlmethode werden mit empirischen Korrekturen verbessert. Bei der zweiten Methode werden Bildbearbeitungsmethoden auf Oberflächenverschiebungen angewendet und durch satellitengestützte Interferometrie abgebildet, um Bruchcharakteristika, wie Bruchdimension und Ausprägungsrichtung sowie die Anzahl von Quellen abzuleiten. Beide Methoden wurden angewendet um eine Modellierung der Erdbebenquelle des Momenten-Magnitude 6.6 Muji Erdbebens von 2016 vorzunehmen. Die Ergebnisse zeigen einen segmentierten und bilateralen Bruchvorgang.

Die Mechanismen eines Störungssystems während einer Erdbebensequenz wurden mit den entwickelten Methoden und Modellierungsstandards untersucht. Die 2008-2009 Qaidam Erdbebensequenz besteht aus zwei Beben von 2008 und 2009 in einem tiefen getrennten Störungssystem sowie aus einer post-seismischen Bewegung nach dem Erdbeben von 2008. Das Beben von 2009 zeigt Hinweise darauf, dass in den Bruchvorgang drei unterschiedlich Störungssegmente involviert waren. Es wurde eine gute Übereinstimmung zwischen den geodätischen Deformationsmessungen und den mittels der seismologischen Rückstrahlmethode beobachteten kohärenten Abstrahlungen gefunden.

Abschließend wird eine zusammenfassende Rahmenstrategie vorgeschlagen, welche die entwickelten Methoden dieser Arbeit nutzt. Dies geschieht mit Blick auf eine routinemäßige Anwendung von Erdbebenbruchmodellierungen mit Rücksichtnahme auf mögliche Erdbebenbruchsegmentierung. Insgesamt präsentiert diese Arbeit eine Verbesserung von Methoden und Modellierungsstandards von Erdbebenquellen zur robusten Bestimmung von detaillierten Erdbebenbrucheigenschaften.

# Contents

<b>1</b>	<b>Introduction</b>	<b>1</b>
1.1	Earthquake source modeling . . . . .	1
1.2	Earthquake rupture segmentation and fault segmentation . . . . .	6
1.3	Thesis outline . . . . .	10
<b>2</b>	<b>Paper I - Sensitivity of InSAR and teleseismic observations to earthquake rupture segmentation</b>	<b>14</b>
2.1	Summary . . . . .	14
2.2	Introduction . . . . .	15
2.3	Data . . . . .	17
2.3.1	Static near-field data: surface displacements measured using InSAR . . . . .	17
2.3.2	Far-field data: teleseismic waveforms . . . . .	19
2.4	Earthquake source modelling and model selection criteria . . . . .	20
2.4.1	Nonlinear optimisation strategy . . . . .	20
2.4.1.1	Near-field model setup . . . . .	21
2.4.1.2	Model setup for the far-field data . . . . .	22
2.4.2	Model fitness evaluation by using informational criteria . . . . .	23
2.4.3	Source parameter recovery tests using the informational criterion . . . . .	24
2.5	Results . . . . .	26
2.5.1	Optimisation results . . . . .	26
2.5.1.1	The 2009 L'Aquila earthquake . . . . .	26
2.5.1.2	The 2016 Amatrice earthquake . . . . .	27
2.5.1.3	The 2005 Zhongba earthquake . . . . .	27
2.5.1.4	The 2008 Zhongba earthquake . . . . .	28
2.5.2	Informational theory results and result significance . . . . .	29
2.6	Discussion . . . . .	35
2.6.1	Impact of modelling setup . . . . .	35
2.6.2	Theoretical limitations on source complexity resolution . . . . .	35
2.6.3	Model inferences towards source complexity resolution . . . . .	36
2.7	Conclusions . . . . .	39
2.8	Acknowledgements . . . . .	42
2.9	Appendix . . . . .	43
2.9.1	Source parameter and tradeoff scatter plots . . . . .	48
<b>3</b>	<b>Paper II - Data-driven constraints on earthquake modeling and segmentation from teleseismic multi-array backprojection and InSAR</b>	<b>59</b>
3.1	Abstract . . . . .	59
3.2	Introduction . . . . .	60
3.3	Methods . . . . .	62
3.3.1	Time-domain backprojection using multiple virtual arrays . . . . .	62
3.3.1.1	Introduction to the backprojection method . . . . .	62
3.3.1.2	Multi-array BP method . . . . .	64
3.3.1.3	Backprojection settings . . . . .	66
3.3.1.4	Empirical travelttime corrections . . . . .	66

## Contents

3.3.1.5	Defining the model space based on backprojection results . . . . .	67
3.3.1.6	Synthetic tests with multi-array backprojection . . . . .	68
3.3.2	Pseudo-probability of source location from image segmentation on InSAR displacement maps . . . . .	71
3.3.2.1	Defining the model space based on displacement map segmentation results . . . . .	73
3.3.3	Earthquake source optimization implementing data-driven model parameter prior distribution pseudo-probabilities . . . . .	75
3.3.3.1	Guided optimization . . . . .	76
3.3.3.2	Settings for the modeling of the far-field waveform data . . . . .	76
3.3.3.3	Settings for the modeling of static near-field data . . . . .	77
3.4	Application to the 2016 Muji earthquake . . . . .	77
3.4.1	The 2016 Muji earthquake . . . . .	77
3.4.2	Waveform data processing and multiarray BP setup . . . . .	78
3.4.2.1	Empirical travelttime correction on the Muji earthquake waveform data . . . . .	80
3.4.3	Near-field data . . . . .	80
3.4.4	Results . . . . .	81
3.4.4.1	Spatio-temporal evolution of the 2016 Muji earthquake . . . . .	81
3.4.5	2016 Muji earthquake two-segment rupture optimization results . . . . .	82
3.4.5.1	Exploratory and guided optimizations of the 2016 Muji rupture using the same data . . . . .	82
3.4.5.2	Backprojection of synthetic waveforms from the 2016 Muji minimum-misfit kinematic source model . . . . .	89
3.5	Discussion . . . . .	90
3.5.1	Discussion of multi-array backprojection . . . . .	90
3.5.2	Surface displacement map segmentation method . . . . .	93
3.5.3	Guided optimization . . . . .	93
3.6	Conclusions . . . . .	94
<b>4</b>	<b>Paper III - Illuminating the spatio-temporal evolution of the 2008-2009 Qaidam earthquake sequence with the joint use of InSAR time series and teleseismic data</b>	<b>97</b>
4.1	Abstract . . . . .	97
4.2	Introduction . . . . .	98
4.3	Materials and Methods . . . . .	101
4.3.1	Seismic back-projection source imaging . . . . .	101
4.3.1.1	Data and Station Clustering . . . . .	101
4.3.1.2	Muti-array back-projection method . . . . .	101
4.3.2	Kinematic fault inversion . . . . .	102
4.3.2.1	Teleseismic data . . . . .	102
4.3.2.2	InSAR time series (TS) data . . . . .	102
4.3.2.3	Fault inference method . . . . .	105
4.3.2.4	Fault inference of the 2008 earthquake . . . . .	105
4.3.2.5	Fault inference of the 2009 earthquake . . . . .	106
4.4	Results . . . . .	106
4.4.1	Back-projection imaging of the 2008-2009 sequence . . . . .	106
4.4.2	2008 fault characteristics estimations . . . . .	108
4.4.3	2009 fault characteristics estimations . . . . .	108
4.5	Discussions . . . . .	112
4.5.1	Benefits of InSAR time series (TS) for fault inference . . . . .	112
4.5.2	Back-projection imaging for moderate-size earthquakes . . . . .	114

## Contents

4.5.3	The 2008-2009 Qaidam earthquake sequence . . . . .	114
4.6	Conclusion . . . . .	116
4.7	Contributions . . . . .	117
4.8	Funding . . . . .	117
4.9	Acknowledgements . . . . .	117
<b>5</b>	<b>Summary and Discussion</b>	<b>118</b>
5.1	Summary . . . . .	118
5.2	Further application of the developed methods and tools . . . . .	119
5.3	Earthquake rupture segmentation modeling impact and outlook . . . . .	121
5.4	Inferences on rupture segmentation characteristics from studied earthquakes . . . . .	122
5.5	Data-driven optimisation schemes to determine appropriate source model complexity	124
5.5.1	Transdimensional earthquake source modeling . . . . .	124
5.5.2	Simultaneous parallel modeling of multiple earthquake sources model geometries with different number of sources . . . . .	125
5.6	Outlook on improved operational earthquake source modeling under consideration of potential rupture segmentation . . . . .	127
<b>6</b>	<b>Bibliography</b>	<b>128</b>
<b>7</b>	<b>Acknowledgments and Declaration</b>	<b>146</b>

# 1 Introduction

## 1.1 Earthquake source modeling

Since ancient times the source and origin of earthquakes has been speculated upon, in rather unscientific fashion, with ideas ranging from air in cavities of the Earth causing underground thunderstorms in ancient Greece, a snake dripping venom on a god as punishment in Norse mythology to giant underground trapped catfish in feudal Japan. The need for an explanation for earthquakes as a globally occurring sudden phenomena is clear, as earthquakes have strong socioeconomic impacts and threaten the lives of many people. Earthquake source modeling has emerged from the scientific need to be able to describe and quantify the mechanism and physical properties of earthquakes based on available seismological data. The goal of such earthquake source modeling is the identification of earthquake source geometry and the description of the rupture. A range of different earthquake source models have been developed over the years to enhance, improve or to put emphasis on particular properties of the rupture process and are driven by the desire for better and more complete and encompassing descriptions of an earthquake source.

Earthquake sources are investigated primarily by observation and analysis of the seismic waveform signals they emit, recorded as a high temporal resolution dataset of displacements at seismometers around the world. Earthquake source modeling is an under-determined and non-linear inverse problem and especially modeling a complex and heterogeneous source process is an ill-posed inverse problem (Minson et al., 2013a). Simple point source approximations were therefore the first modeling effort (Aki, 1966) to abstract and describe an earthquake's magnitude and mechanism (thrust, strike-slip or normal faulting earthquakes). The point source approximation is valid for periods and wavelengths that are long compared to the extent of the source and the rupture duration. Moment tensors describe seismic sources based on generalized force couples (Dahm and Krüger, 2014). The inversion for both location, time and mechanism of an earthquake source is highly non-linear and non-unique and the subsurface structure must be assumed to model earthquake sources (Dziewonski et al., 1981), which further adds model errors. Uncertainties in the earth structure influence the accuracy of earthquakes source estimation strongly (Weston et al., 2012) and some earthquake properties can not be resolved independently from others (Funning, 2005; Weston et al., 2014b). An earthquake with pure planar shear-failure can be represented in the far-field by its time and location centroid and two perpendicular force dipoles with zero angular momentum, a double-couple (DC) point source model (Dahm and Krüger, 2014; Aki and Richards, 2002). Seismic full centroid moment tensors (Dziewonski et al., 1981; Dahlen and Tromp, 1998) have become the standard source model in most operational frameworks reporting earthquake source modeling results, like the GCMT project (Dziewonski et al., 1981; Ekström et al., 2012) and Geofon (Hanka and Kind, 1994a). This operational services report source mechanism and location for earthquakes worldwide at least larger than magnitude 5 are the basis of modern earthquake science and statistics. Full centroid moment tensors are also used to describe explosions, implosions, rock falls, landslides and meteorite terminal explosions (Dahm and Krüger, 2014). The moment tensor can be decomposed into isotropic and deviatoric components (Aki and Richards, 2002). The deviatoric components can be further decomposed (Jost and Herrmann, 1989). How well a source is represented by a

## 1 Introduction

centroid moment tensor (CMT) model is often assessed by the magnitude of the non-double-couple components of the full moment tensor (Frohlich et al., 1994). Large positive or negative non-double-couple tensor component can hint at an unmodelled potential source complexity (Sipkin, 1986). Several source complexity effects that cause non-double-couple components for shallow earthquakes have been implied, such as source segmentation (Barker and Langston, 1982) and rupture on non-planar faults (Sipkin, 1986). Unrepresented near-source structure can also contribute to non-double-couple components (Kawasaki, 1982). However if the earthquake source is shallow, compared to the seismic wavelengths used, the isotropic components cannot reliably be determined (Julian et al., 1998). Usage of the non-DC is therefore a non-unique indicator for earthquake source complexity and not helpful for the investigation of rupture segmentation of shallow crustal earthquakes. For a complex and extended source a single CMT is not a complete descriptor of the causal process and the mechanism. This has been tried to be compensated by the use of multipole sources (Backus and Mulcahy, 1976; Kagan and Knopoff, 1987; Jordan and Juarez, 2019) as well as using multiple individual CMTs (Duputel et al., 2012b; Zahradnik and Sokos, 2014).

A point source model, however, does not explain an earthquake's rupture propagation, fault dimensions and slip. Energy during an earthquake is spread over an area, with the 2004 Sumatra earthquake as the most notable example, which gave rise to the method of seismic backprojection to image the spatio-temporal evolution of the earthquake rupture process (Krüger and Ohrnberger, 2005; Ishii et al., 2005). A range of finite source dislocation models have been developed to explain observed complex waveforms, such as the circular crack model (Brune, 1970), where the rupture propagates from the center to the edges of a circular crack or (several) slip ellipses (Vallée and Bouchon, 2004), with the rupture speed and crack size as additional source parameters. Since the 1970s, after the San Fernando earthquakes 1971 and the 1979 Imperial Valley earthquake, inference of the higher order characteristics of earthquake kinematics has become a focus of earthquake source modeling efforts, based on linearized inversion with multiple-time-window approaches (Vallée and Bouchon, 2004; Hartzell and Heaton, 1983; Archuleta et al., 1982; Olson and Apsel, 1982). Finite-source inverse modeling of earthquakes is generally challenging because of the the non-linearity of the problem, the large model parameter space and some parameter trade-offs as well as uncertainties in the medium model used (Weston et al., 2012; Ragon et al., 2018a; Lohman and Simons, 2005a; Razafindrakoto et al., 2015). Lack of dense near-field observations hampered such finite source modeling, due to the non-linearity of the problem, and lead to the development of other second-order modeling approaches, such as finite moment tensors (Chen et al., 2005) and other refined multi-point source models (Shimizu et al., 2019; Jordan and Juarez, 2019) where some source parameters, such as the location are usually fixed a priori. Finite rectangular source modeling based on linearized inversions of near-field and far-field seismic data has been developed since the 1980s (Dahlen and Tromp, 1998; Beroza and Spudich, 1988; Kikuchi and Kanamori, 1982; Das and Kostrov, 1990), and results have been shown to better explain observed rupture durations, rise times and rupture velocities of larger earthquakes and reduce the non-linearity of the inversion problem (Hartzell and Langer, 1993; Mendoza, 1995). Further observations of phenomena such as nucleation phases (Ellsworth and Beroza, 1995) and that bilateral rupture propagation (Aochi et al., 2000) warranted further refinement of the finite source model. Determining the slip distribution and evolution on a pre-determined rectangular finite-fault has become a standard second step in earthquake source modeling (Liu and Archuleta, 2004; Mai et al., 2016; Minson et al., 2014; Razafindrakoto and Mai, 2014). Non-linear slip inversions based on near-field seismic and teleseismic data are now routinely produced for large earthquakes of interest by the United States Geological Survey (Ji et al., 2002) with some source parameters, such as the location, constrained.

The inferences of finite earthquake source model parameters are directly needed for further analysis, as finite faults are an abstracted model needed to calculate recurrence of moderate and

## 1 Introduction

large magnitude events in probabilistic seismic hazard assessment (Visini et al., 2020) and also allow to investigate the characteristics of stress evolution (Dieterich and Richards-Dinger, 2010; Stein and King, 1984). For an isolated, non-segmented fault, the seismic hazard evaluation is relatively simple (Scholz and Gupta, 2000). Fault systems however have long been identified to be complex and coupled systems (Stirling et al., 1996). For the case of a fault with two fault segments a simultaneous rupture of both segments will cause the expected slip and shaking intensity to be potentially double that, compared to the case of only one segment rupturing (Scholz and Gupta, 2000). The use of multiple sources to model earthquakes has become common in case studies and some codes to match these observations (Sokos and Zahradnik, 2008; Duputel et al., 2012a). This shows the need for more complex earthquake source models describing the earthquake source process and more data to constrain them, especially in the near-field of earthquake displacements.

Interferometric Synthetic Aperture Radar (InSAR) is based on repeated passes of radar satellites, which illuminate the Earth’s surface with controlled and coherent radar waves. If the distance between the ground and the satellite changes between passes, e.g. because of the static displacement caused by an earthquake, the phase measured at the satellite will change for affected pixels (Wright, 2002; Hanssen, 2001a). This enables radar interferometry to measure the near-field static surface displacements caused by earthquake deformation with high spatial resolution after correction of e.g. orbital errors, atmospheric noise and topographic phases (Hanssen, 2001a). The rise of available geodetic data and especially InSAR data for observation of static surface displacements from co-seismic and post-seismic processes has highlighted the need for finite earthquake source models (Hanssen, 2001a). The pattern of near-field static displacements measured by InSAR contains information on the co-seismic displacement caused by the dynamic rupture process over a time integral, determined by the time between the two measurements. Modeling static surface displacement is often done by a rectangular dislocation source in a homogeneous halfspace with uniform slip (Okada, 1985; Okada, 1992), which is computationally fast and does not require knowledge about sub-surface structure except for the Poisson’s ratio. Modeling parameters for such a finite static dislocation source are the length, width, location, slip and the mechanism. Earthquake source modeling from InSAR data has developed significantly over the years with rigorous inclusion of data uncertainties (Sudhaus, 2010). Also finite source models with distributed slip are now widely used (e.g., Wright et al., 2004b; Biggs et al., 2006; Weston et al., 2012; Weston et al., 2014a). Distributed slip on faults are often modelled in a two stage process, where first the geometry is determined and as a second step the geometry is fixed and the slip distributions is inverted for (Vasyura-Bathke et al., 2020). InSAR displacement measurements provide high-resolution images of the near-field displacements of earthquakes but are not capable of imaging the spatio-temporal evolution of the co-seismic process. InSAR time series can however image parts of or even the full long-term earthquake cycle (Wright, 2002) and observe long-term fault segmentation processes (Cakir et al., 2014; Elliott et al., 2011a; Daout et al., 2019). InSAR displacement measurements also capture the surface expression of rupture segmentation. Prominently the first co-seismic interferogram from radar satellite data (Massonnet et al., 1993a) displayed a complex deformation pattern and was modelled with multiple dislocation sources. The use of geodetic data to model complex earthquake surface displacements with multi-finite source models has become standard practice in many studies (e.g., Sudhaus and Jónsson, 2011; Massonnet et al., 1993a; Li et al., 2019a; Magen et al., 2020; Elliott et al., 2010; Elliott et al., 2011a).

InSAR data have become more frequently available with the European Union’s open-data Earth Observation Programme (Copernicus) and the Sentinel-1 missions by ESA, imaging the surface displacements of 20–30 earthquakes per year thanks to a systematic global acquisition scheme (Biggs and Wright, 2020) with return times of less than six days for most European areas. Other radar satellites provide usable data for radar interferometry as well, like the missions



TerraSAR-X, RADARSAT and COSMO-SkyMed and the partly open-data from the L-Band mission ALOS. ESA is committed to follow-up missions (Torres et al., 2017) and together with future missions like NISAR (Rosen et al., 2015), this ensures availability of radar data in the future. Deformation measurements of small and intermediate sized earthquakes from InSAR data are limited to displacements caused by shallow crustal earthquakes. InSAR data allow to investigate the link between co-seismic and post-seismic processes (e.g. Wright et al., 2004a; Ingleby et al., 2020; Daout et al., 2019; Biggs and Wright, 2020). The amount of available InSAR data has become a big data issue and requires automated processing and analysis (Biggs and Wright, 2020; Anantrasirichai et al., 2018; Morishita et al., 2020; Lazecky et al., 2020; Bekaert et al., 2019). The use of InSAR data has become routine in many observation and monitoring tasks (Biggs and Wright, 2020), from volcanoes (Anantrasirichai et al., 2018) to slow slip (Guo et al., 2020; Anantrasirichai et al., 2019). Routine processing of InSAR data has been developed (Bekaert et al., 2019; Lazecky et al., 2020) and correction of InSAR data from atmospheric noise has become standard operational practice (Biggs and Wright, 2020) with automatic correction from services like LiCSBAS (Morishita et al., 2020). Tropospheric correction of interferograms is still not trivial in difficult areas with high topography (Daout et al., 2016b; Daout et al., 2016a). Several projects make processed InSAR data openly accessible, like LiCSAR (Lazecky et al., 2020) and ARIA (Bekaert et al., 2019). All this available data provide the opportunity for potential routine incorporation of InSAR data into operational source modeling of shallow crustal earthquakes. However this requires the development of robust joint-data earthquake source modeling routines and frameworks that considers of data and model errors.

Combination of far-field teleseismic waveform and near-field InSAR observations for earthquake source modeling has many advantages as both the static and dynamic displacements originate from the same source and from the same processes, which allows to model the earthquake source from a different and independent dataset perspective (Weston et al., 2012). Combination of seismic and geodetic datasets is done routinely by many studies (e.g., Delouis et al., 2002; Xu et al., 2010; Cheloni et al., 2014; Funning, 2005). The high temporal resolution of the seismic data and the high spatial resolution and area covering static near-field displacement measurements from InSAR complement each other. Joint-data inferred source models have complementary source parameter trade-offs and therefore support each other in inversions (Weston et al., 2012; Weston et al., 2014b). The combined use of seismic and geodetic also helps to separate co-seismic, post-seismic and aseismic processes (Ingleby et al., 2020) allowing for investigations of the full earthquake cycle (Elliott et al., 2016b; Wright et al., 2004b). For joint earthquake source modeling of seismic and geodetic data some studies apply a multistage approach, where the source geometry and location is explored using only geodetic data first and the spatio-temporal slip evolution is explored in a second step (Hernandez et al., 1999; Custódio et al., 2009). In general the combination of the independent seismological and geodetic data is helpful and reduces biases and uncertainties in the determination of finite source geometry parameters of earthquakes (e.g. Funning, 2005; Weston et al., 2012; Frietsch et al., 2019a). A 'deep-rooted' combination of both datasets is however necessary to account for the data and modeling uncertainties of the individual and independent datasets. Rigorous uncertainty estimation of earthquake source modeling (Stähler and Sigloch, 2016; Duputel et al., 2012b) and Bayesian methods (Vasyura-Bathke et al., 2020; Minson et al., 2013b) allows to determine the set of all plausible source model parameters, while accounting for model and data errors (Minson et al., 2013a). Without reliable estimates of those uncertainties no earthquake source model inference has value for further use. Data error uncertainties are communicated regularly, while model error, such as the choice of the degree of model complexity, is not.

During this thesis I collaborated and participated in the development of a number of projects to facilitate the robust joint data modeling of earthquake sources. For the fast forward modeling of both the dynamic seismic waveforms and static surface displacements I helped to develop

## 1 Introduction

a *python* framework for pre-calculated Green’s function stores (Heimann et al., 2019b), based on layered viscoelastic half-space models. Several source types can be modeled, using these Green’s function databases, in the seismological software package Pyrocko (Heimann et al., 2017a). The finite source models in Pyrocko have the additional source parameters nucleation point location, which effectively describes the rupture directivity, and the rupture velocity. Combination of geodetic and seismological data in a joint-modeling might help to constrain the nucleation location and rupture velocity. Rupture directivity is a very important factor in hazard estimations (Tothong et al., 2007). I helped develop the *Kite* software package (Isken et al., 2017a) for pre-optimisation handling of the InSAR data. *Kite* can sub-sample the data and calculate the data covariances needed for error propagation by adding synthetic correlated noise generated from real-data noise power spectra (Sudhaus and Jónsson, 2009; Sudhaus, 2010). I participated in the development of two joint-data earthquake source optimisation open-source frameworks. Firstly the Bayesian bootstrap-based probabilistic joint inversion scheme *Grond* (Heimann et al., 2018b), which uses a high-score based exploration of the full model space and maps model parameter trade-offs. The second developed framework is the *BEAT* software package (Vasyura-Bathke et al., 2020), which uses a Bayesian Markov Chain Monte Carlo based extensive exploration of the high-dimensional model parameter space. *BEAT* is based on a multistage approach to first explore the source geometry based on joint data input and in separate steps also the slip distribution and spatio-temporal evolution of the slip and is also able to employ multi-fault source models. Earthquake source geometry inferred in *Grond* can also be communicated to *BEAT*, allowing for a second stage slip distribution inversion.

This thesis investigates the potential model error stemming from the choice of the source model complexity in earthquake source modeling. Many studies fix the fault geometry based on geological parameters (e.g. Hamling et al., 2017; Feng et al., 2013). Models with too many parameters, which cannot be properly constrained by the data will result in unrealistically high uncertainty estimates and should be avoided (Dettmer et al., 2014). Underparametrization however leaves structure unresolved and inferred information biased (Dettmer et al., 2014). Source complexity is dealt with in an iterative fashion in several earthquake source modeling studies by adding more and more sources successively until no more significant reduction of the misfit is achieved (Huang et al., 2016a; Wright et al., 1999). This iterative approach has however been shown to lead to biased source parameter results (Frietsch et al., 2019a). The typical step after determination of the earthquake source geometry is to determine the slip distribution and evolution. Slip distribution inversions and spatio-temporal slip evolution inversion are highly non-linear and ill-posed, leading to many workings groups producing vastly different results, even given the same input data in a blind test (Mai et al., 2007). This is because source parameter trade-offs and uncertainties are inherited (Ragon et al., 2018a), in particular for source analyses with complex segmented models that involve the estimation of a large number of model parameters (Weston et al., 2012; Ragon et al., 2018a; Lohman and Simons, 2005a; Razafindrakoto et al., 2015). The slip distribution uncertainties therefore are necessary to be evaluated thoroughly (Duputel et al., 2014; Sudhaus and Sigurjón, 2009). Fixed source parameters and assumed degree of source complexity, e.g. based on geological inferences, or strongly constrained fault geometry and source model complexity will also affect the inferred slip distribution strongly (Ragon et al., 2018b; Ragon et al., 2019; Frietsch et al., 2019a). Determination of the source geometry and inferences on possible source complexity therefore are carried out in this thesis using uniform fault slip source models. This thesis focuses on the modeling of the earthquake source geometry under consideration of the appropriate source model complexity given the data. The choice of source model complexity of first order should ideally be based on and represent a physically meaningful observable process, the rupture segmentation.

## 1.2 Earthquake rupture segmentation and fault segmentation

Two terms are used in the literature, seemingly interchangeable, between geological, paleoseismological and geophysical studies, to describe complex deformation processes, fault segmentation and rupture segmentation, without strict definitions to distinguish them (DePolo, 1989). Seismically active faults can be divided into several smaller straight or slightly bend fault segments. In general discontinuities of any kind like geometric, structural, behavioral, paleoseismic, geomorphic, geological, geophysical, and rheological heterogeneity's along a fault constitute the identification of individual fault segments (DePolo, 1989; Aki, 1989). This fault segmentation can be along a fault's length but also along width at depth. Therefore fault segments have distinct geometrical properties and/or can be separated by step-overs and fault bends (Klinger, 2010) manifesting in an aseismic gap between segments. The fact that a fault consists of several segments does not mean that an earthquake will rupture across several segments (see sketch in Fig. 1.1).

Hereafter the term rupture segmentation is used to describe the partitioning of released co-seismic energy and slip of a single earthquake rupture into smaller packages on distinct fault segments. Rupture segments and fault segments do not have to be same, only parts of a fault can rupture for example (see sketch in Fig. 1.1). All moment is released during a single earthquakes duration. If the involved subevents are of comparable moment and occur within a time difference of minutes to days (to each other) they are referred to as doublets (Donner et al., 2015). Rupture segmentation is not only an abstract model assumption but geological evidence has been confirmed in field observations (Wesnousky, 2006; Graymer et al., 2007; Duman et al., 2005) and predicted in theoretical rupture propagation modeling (Harris and Day, 1993; Duan and Oglesby, 2006).

The term fault segmentation is more general and will be used hereafter to describe partitioning of faulting or the differentiation of a single fault into distinct fault segments on any longer time scale, i.e. the study of seismic sequences and geological and paleo-seismological studies. Inherently in those later studies it is difficult to ascertain if partitioning of slip and energy occurred simultaneously or if the fault segmentation occurred over a longer time period. Fault segmentation can be driven by co-seismic rupture segmentation, post-seismic deformation, aseismic processes or by a combination of these processes. Considering the rupture segmentation from seismic and geodetic data is necessary to be able to distinguish between the three processes. It is interesting to note that the persistence of fault segments remains in question (Schwartz, 1989) as over very long time periods faults could also tend to simplify and smooth over fault segments. This theory is based on the zones between fault segments developing over time from being wide areas of distributed, disorganized, secondary fissuring and faulting (Manighetti et al., 2007a) to strongly connected, narrow zones. Other studies have globally found a long-term persistence in rupture barriers (Philibosian and Meltzner, 2020) shaping geomorphology (Victor et al., 2011). Also long-term fault segmentation is thought to govern the evolution of a fault system (Wesnousky, 1988). Along with fault roughness (Zielke et al., 2017) fault segmentation is recognized however as one of the most important characteristic parameters of faults and fault systems (Philibosian and Meltzner, 2020; Wesnousky, 2006; Klinger, 2010). Existing catalogs of known fault segmentation have been compiled mostly based on paleo-seismological and geological studies (Wesnousky and Biasi, 2011; Klinger, 2010; Manighetti et al., 2007a). Nevertheless the question arises if and how geologically and paleo-seismologically determined fault segmentation is concurrent or related with co-seismic rupture segmentation. Without robust observations of a statistically significant number of rupture segmentation behaviour and occurrences this can not be investigated and fault segmentation can only be interpreted based on geological assumptions. Especially intra-plate earthquakes occur sometimes on previously unmapped faults (Berberian, 1979; Geersen et al., 2015; Donner et al., 2015). Therefore co-seismic rupture segmentation modeling should be independent of fault knowledge but fault segmentation inferences should be

informed by co-seismic rupture segmentation observations.

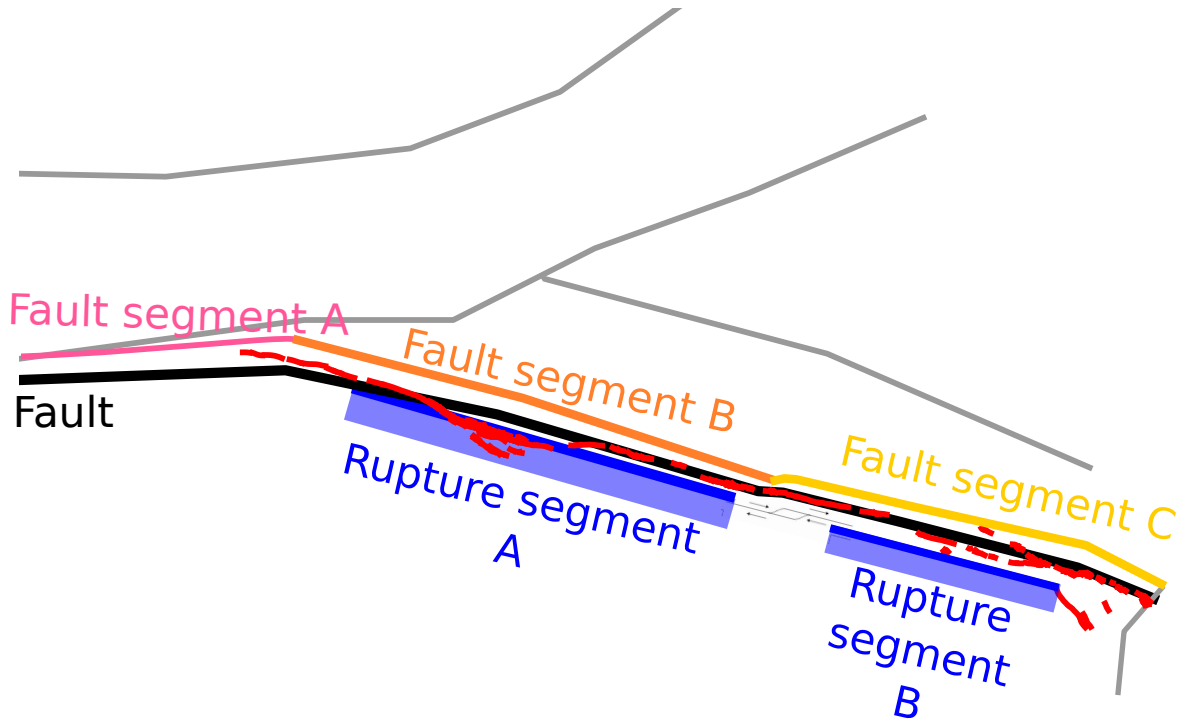


Figure 1.1: Sketch of a fault system on which a segmented earthquake occurred, to illustrate the differences between fault (solid black line), fault segments (pink, orange, yellow) and rupture segments (blue), based on the Muji area and the rupture of the  $M_w$  6.6 2016 Muji earthquake. The red lines indicate a typical surface trace of the fault reported by a geological survey (Li et al., 2019b). The rupture involves two rupture segments, blue A and B, on the fault segments B (orange) and C (yellow). Note how the rupture segment B does not break the entire fault segment C and that only a part of the fault participated (fault segment A). Rupture segment A and B are separated by an aseismic gap. The gray lines indicate other faults in the fault system, which are however not involved in the rupture.

The individual fault segments involved in an earthquake rupture can limit or increase the length of faulting in a single earthquake (Pizzi et al., 2017). Fault segments and zones between fault segments are observable. The zones bounding faults, called barriers (Philibosian and Meltzner, 2020), are structural discontinuities on a fault or at the end of a fault (DePolo, 1989) and have different elastic behaviour than the fault zones, as for example for the 2011 Tohoku-Oki earthquake (Nishikawa et al., 2019). Also the zones between fault segments are assumed to be of a different rheology and have different levels of damage (King, 1983; Sibson, 2003) than a fault segment, with fault damage also following fractal distributions (Savage and Brodsky, 2011). Rupture has been observed to both terminate and start at fault barriers (King and Nábělek, 1985; Aki, 1989). The size of this zone between fault segments is critical to arrest or allow further propagation of the rupture, as inferred from rupture propagation modeling (Harris and Day, 1993; Duan and Oglesby, 2006) and might change over time (Philibosian and Meltzner, 2020). The energy that is sufficient to start and rupture a certain segment might not be sufficient to rupture going across the inter-segment zone (Duan and Oglesby, 2006). The static and dynamic stress change caused by displacement on one fault segment might be enough to trigger co-seismic rupture on a completely different receiver fault (Mildon et al., 2019) or not even adjacent fault segment (Stein, 1999; King et al., 1994; Philibosian and Meltzner, 2020). This can lead to the rupture 'jumping' over the aseismic zone between fault segments. Observation of this rupture

## 1 Introduction

segmentation behaviour also has a direct impact on hazard estimations. Previous work based on limited available statics postulated a maximum jump of rupture between fault segments of 5 km (Biasi and Wesnousky, 2016; Biasi and Weldon, 2006), which was implemented in operational hazard calculations (Field et al., 2015). This maximum distance limitation had been included in hazard modeling (Field et al., 2014; Field et al., 2015). However recent observations of the 2016  $M_w$  7.8 Kaikōura (Hamling et al., 2017) earthquakes and also theoretical considerations (Bai and Ampuero, 2017) have shown that jumps between segments can be much larger than previously assumed, showing the need for more observations. Seismic sequences and so called assumed "super-cycles" of earthquake sequences also strongly depend on inter-fault segment interactions (Philibosian and Meltzner, 2020) and are also very relevant for moderate crustal earthquakes (Mildon et al., 2019).

Scaling relations, fault barriers and recurrence calculations depend on complete statistics of rupture segmentation occurrence. Consideration of fault and rupture segmentation is important for a variety of further down-stream analyses, statistics and inferences. Geometrical complexities of faults have been associated with the initiation and stopping of earthquake rupture (King and Nábělek, 1985; Aki, 1989). Efforts have been made to incorporate fault segmentation into fault length and slip relations but are hampered by incomplete statistics (Manighetti et al., 2007a). High performance computational dynamic rupture modeling (Heinecke et al., 2014; Wollherr et al., 2018) can reveal much about the physics of the rupture process and can calculate scenarios for rupture segmentation (Ulrich et al., 2019). They are limited however by pre-determined fault geometry and especially the assumption of the number of involved fault segments.

First order, i.e. single-source models, are known to not be able to work well in seismic cycle analysis as they do not capture the full range of fault behavior (Philibosian and Meltzner, 2020). The displacement on one fault causes changes of dynamic and static stress on the surrounding area (Stein, 1999; King et al., 1994). This stress change is relative as it strongly depends on the orientation of a receiver fault. If the receiver fault is optimally oriented it receives the maximum positive or negative stress change. It is possible that fault segments of neighboring fault systems are optimally orientated or better oriented than fault segments of the same fault system. A certain amount of stress change is possibly necessary to overcome the initial nucleation phase and develop a full rupture of a fault segment (Ohnaka, 2000). Co-seismic stress transfer between fault segments can lead to a cascading effect of earthquake rupture (Mildon et al., 2019; Philibosian and Meltzner, 2020), involving multiple fault systems, such as during the 2016  $M_w$  7.8 Kaikōura earthquake (Hamling et al., 2017). Theoretical simulated off-fault deformation interactions between faults in a system show that due to changing fault geometries and complex interactions the optimal orientations and off-fault deformation may vary through space and time (Preuss et al., 2020).

Other down-stream analyses are also affected by the modeling of rupture segmentation and inferred source parameters. The fault system geometry and complexity of the geometry highly impacts recurrence statistics (Dieterich and Richards-Dinger, 2010). The fault segmentation of the central Apennines fault system has been identified as a major factor in limiting the size of the individual earthquakes in the 2009-2016 Central Italian earthquake sequence (Pizzi et al., 2017). Fault and rupture segmentation is essential to define seismic cycle models (Klinger, 2010; Manighetti et al., 2007b; Schwartz and Coppersmith, 1984). Also the rupture dynamic is controlled by the fault geometry and the presence of fault segments (Bhat et al., 2007; Vallée et al., 2008). Resolving rupture segmentation and thereby defining the geometrical complexities of the rupture is crucial to better understand the role of geometric barriers at faults. Robustly resolving rupture segmentation and providing statistics is an important task in further earthquake source modeling and for dependent down-stream analysis.

Co-seismic rupture segmentation is well reported and known for earthquakes with large moment

## 1 Introduction

magnitudes above  $M_w > 7$  (Segall and Pollard, 1980; Barka and Kadinsky-Cade, 1988; Philibosian and Meltzner, 2020; Ji et al., 2003) and has been observed for a number of cases for normal and reverse type earthquakes (Walsh et al., 2003; Elliott et al., 2010) as well as strike-slip type earthquakes (Klinger, 2010; Wesnousky and Biasi, 2011). Some large earthquakes, such as the 1997  $M_w$  7.2 Zirkuh (Sudhaus and Jónsson, 2011), the 1999  $M_w$  7.1 Hector Mine (Hauksson et al., 2002) and 2016  $M_w$  7.8 Kaikōura (Hamling et al., 2017) earthquakes are known to have happened on over a dozen individual fault segments. Also earthquakes on rheologically relatively simple oceanic transform faults can exhibit complex rupture behaviour, for example the backpropagating super-shear rupture of the 2016  $M_w$  7.2 Romanche earthquake on an oceanic transform fault (Hicks et al., 2020b). However, multi-segment earthquake rupture can exhibit much more complex rupture and mechanical behaviour, for example involving orthogonal fault segments, such as the 2019  $M_w$  7.1 Ridgecrest earthquake (Ross et al., 2019) and the 2012  $M_w$  8.6 Sumatra earthquake (Meng et al., 2012a) or complex stress interactions as in the 2016  $M_w$  7.8 Kaikōura earthquake (Hamling et al., 2017).

Also some earthquakes of moderate size in the moment magnitude range between 5.5 and 7 are known to involve rupture segmentation, especially strike-slip and reverse-type earthquakes but also normal-fault earthquakes (Biasi and Wesnousky, 2016). There are few but a number of reported cases of moderate sized earthquakes with fault segments, such as e.g. the  $M_w$  6.6 Nura earthquake (Teshebaeva et al., 2014), the  $M_w$  6.2 2016 Amatrice earthquake (Huang et al., 2017), the  $M_w$  6.7 2008 Zhongba earthquake (Elliott et al., 2010), the  $M_w$  6.5 2016 Norcia earthquake (Bonini et al., 2019), the  $M_w$  6.6 2016 Muji earthquake (Bie et al., 2018) and the  $M_w$  6.4 2018 Hualien earthquake (Lo et al., 2019). Biasi and Wesnousky, 2016 have analysed surface traces of ruptures and found that around 47% of the ruptures in their study in the magnitude range 6-7 are segmented with one or more steps and that the number of co-seismically involved fault segments apparently increases with magnitude and rupture length. Also from reported earthquake source models it appears that large earthquakes with magnitudes above 7 are more often segmented, while earthquakes with magnitudes below 6.5 most often are not. A hypothesis stemming from this observations could be that segmentation is less common for smaller earthquakes.

However smaller earthquakes with magnitudes, even between  $M_w$  6 and 7, are most often investigated by using automated procedures that assume unsegmented rupture, i.e. single point source or single dislocation plane (e.g. Dziewonski et al., 1981, Geofon and USGS). The apparent observation that ruptures of smaller earthquakes are not or less segmented than larger earthquakes should be questioned, as it violates the assumption and observation of self-similarity (Scholz and Aviles, 1986; Manighetti et al., 2009). If this apparent observation represents the nature of faulting or if it is rather an artifact of our abilities to well observe and infer segmentation studying earthquake sources can not be answered without an objective strategy to constrain the modelled rupture complexity. Along with steadily increasing density of globally available data sets the data resolution increases continuously. It allows for more detailed studies using more realistic models, e.g. complex finite rupture models, and for magnitude ranges much less than 7. Moderate shallow crustal earthquakes are very frequent and also produce a significant amount of shaking and very significant damage but are often neglected in terms of resilience in favor of anticipation of very large earthquakes (Minson et al., 2021). This thesis therefore focuses on this type of earthquakes in the magnitude range  $M_w$  6-7 as case studies, investigating if rupture segmentation can reliably be resolved and modelled for earthquakes in this magnitude range.

### 1.3 Thesis outline

**Chapter 2:** I first investigate the sensitivity of globally available open-access data towards the capability of resolving rupture segmentation in the moment magnitude range  $M_w$  6-7. I systematically study the effect of the consideration of rupture segmentation in kinematic source modeling on the improvement of data fit and on the source model parameter inferences estimated, separately for far-field and near-field observations. The main interest is to evaluate the different in source mechanism inferences from models with different source model complexities and if the mean mechanism from multiple models is significantly different from the mechanism inferred for a single-source model. Differences in the inferred mechanism on a second-order scalar are important for e.g stress calculations as mechanism changes with Kagan angles (Kagan, 1991) larger than  $20^\circ$  are considered to lead to significant errors in stress inversions (Martinez-Garzón et al., 2016) and fault stress interaction calculations (Stein, 1999).

Two earthquake pairs with similar source characteristics are selected as study cases with real teleseismic and InSAR data, as far-field and near-field data respectively. The two pairs are the  $M_w$  6.3 April 6, 2009 L'Aquila earthquake and the  $M_w$  6.2 August 24, 2016 Amatrice earthquake in Central Italy, and the  $M_w$  6.2 April 7, 2005 and  $M_w$  6.7 August 24, 2008 Zhongba earthquakes in the Xizang Region, Tibet. Normal-type earthquakes are chosen to reduce non-essential degrees of freedom. Furthermore, both, normal and reverse type earthquakes are underrepresented in fault segmentation statistics (Biasi and Wesnousky, 2016; Stirling et al., 1996) but represent a significant amount of moment release of continental earthquakes.

Rigorous consideration of the impact of data noise towards the source parameter inference is done by applying Bayesian bootstrapping for the far-field data and perturbing the data with noise for both the far-field (Funning, 2005) and near-field datasets (Sudhaus and Sigurjón, 2009). An optimisation algorithm designed to handle multi-modal distributions based on highscores to tackle the issue of the complex search space arising from the consideration of multiple sources is developed. The associated algorithms this paper helped to develop, have since been improved and are implemented in the open-source earthquake source optimisation package *Grond* (Heimann et al., 2018a).

A data-driven approach based on Information theory is used to determine if a single-source model or a two-sources model is appropriate given the observations. This is done by contrasting the likelihood of the inferred source model parameters with the number of necessary source parameters employing the Akaike Informational Criterion (Akaike, 1985; Akaike, 1998). In this way the source model parameter sensitivity is governing the decision on the preferable source model complexity. This assumes that a good resolution of the source parameters is desirable over simple model fitness as criterion, to avoid overfitting. A complex model is only chosen over a simpler one if the additionally necessary source parameters do not justify the gain in model fitness and source parameter resolution.

The paper establishes that there is a significant difference in the earthquake source model inferences if rupture segmentation is considered. The inferred mechanisms of single-source models significantly deviate from the mechanisms of two-sources models. This is the case for inferences from both teleseismic far-field observation and as well as from InSAR near-field observations and for both studied earthquake pairs. If an earthquake process did include rupture segmentation, a single-source model introduces a systematic bias in the source parameter inference estimates. Consideration of rupture segmentation therefore matters for a robust estimation of source mechanisms of the studied earthquakes.

**Chapter 3:** I propose a strategy and develop methods for a rupture segmentation-sensitive source modeling analysis with data-driven source parameter constraints and evaluation on the occurrence of rupture segmentation. To realize a pre-optimisation data analysis I developed two independent toolsets, one for teleseismic data and one for InSAR displacement maps. I also develop a guided optimisation framework using the output of the two pre-optimisation data analysis toolsets as prior constraints. All developed methods are geared towards applicability in an operational framework.

Firstly I develop a time-domain, multi-array backprojection of teleseismic data with estimations of location and time of seismic energy pulses along with robust uncertainty estimates that are based on bootstrapping of the travel-time models and array weights. Backprojection of teleseismic data takes advantage of source-receiver reciprocity and has first been used to investigate the 26.12.2004  $M_w$  9.1 Sumatra earthquake (Krüger and Ohrnberger, 2005; Ishii et al., 2005) and has been developed and been improved with traveltimes corrections (Meng et al., 2016). Backprojection is capable of imaging the spatio-temporal evolution of the rupture process by mapping coherent radiators in space and time by stacking seismological waveforms windows in time steps with respect to possible source locations (Kiser and Ishii, 2017). The growing availability of global teleseismic data allows for backprojections with lower uncertainties as before (Fan and Shearer, 2017). Using traditional time-domain backprojection, it is unclear whether slip velocity or slip acceleration is mapped (Fukahata et al., 2013). This ambiguity vanishes when using hybrid backprojection (Yagi et al., 2012), which convolves the observed signal with the Green's functions from each assumed grid point. Hybrid backprojection however requires a priori information on the source model, contrary to the desire of data-driven and model independent additional information on the rupture's process. The initiation and the termination of rupture has been shown to emit high-frequency energy radiation, representing start/stop phases (Ide, 2002; Madariaga, 1977; Okuwaki and Yagi, 2017; Meng et al., 2012a). Furthermore this high-frequency energy can originate from abrupt relative and spatially variable changes in the fault slip or abrupt changes in rupture velocity (Okuwaki et al., 2018; Yin and Denolle, 2019; Madariaga, 1977). The information gained by mapping the higher frequency coherent energy release can therefore potentially be used to estimate prior information on the ruptures nucleation position, rupture velocity and the number of sub-sources for a kinematic fault model optimisation. Because traditional seismological backprojection uses a single array and is known to produce "swimming" artifacts, I implemented an improved multi-array backprojection method, based on an earlier approach by Rössler et al., 2010 and for use of globally available teleseismic data. As only few seismic arrays are available, I use a clustering algorithm to create optimally located and distributed virtual arrays from individual seismological stations. This approach is more robust to artifacts which affect other teleseismic backprojection approaches (Kiser and Ishii, 2017). I use corrections for each array based on empirical traveltimes shifts, which is an established procedure relying normally on hand picked phase onsets (Palo et al., 2014; Ishii et al., 2007; Meng et al., 2016; Fan and Shearer, 2017). I formulate the search for the traveltimes corrections maximizing the semblance of a fore- or aftershock, for which the point source assumption holds, as a linear optimisation problem. This allows for unbiased determination of traveltimes shifts and potential automated use. Novel is also the combined backprojection of P- and S-phase body waves, increasing reliability of the obtained semblance maps. Rigorous uncertainty estimation of data and model error is done by Bayesian bootstrapping (Rubin, 1981) of array weights and perturbation of traveltimes, allowing for a probabilistic evaluation of the results and consideration of a distribution of prior source parameter estimates.

Secondly I implemented automatized image analysis tools to be applied on InSAR surface displacement maps that use displacement gradients, signal amplitudes and phase coherence to infer constraints on rupture characteristics. The spatial pattern of coseismic surface displacement is to some extent characteristic for the properties of the source. This is exploited in recent



advances applying machine learning algorithms to InSAR data (Anantrasirichai et al., 2018; Anantrasirichai et al., 2019) and even machine learning based modeling of synthetic co-seismic interferograms (Rongier et al., 2019). It is debated how well observed surface ruptures and surface deformation represent the slip and fault geometry at depth (Dolan and Haravitch, 2014; Soliva et al., 2008). A common practice to reduce the search space and inter-parameter dependencies is to fix source parameters based on surface fault expressions (e.g., Hartzell and Heaton, 1983; Beroza and Spudich, 1988; Mai et al., 2016) especially for location (e.g., Elliott et al., 2010; Elliott et al., 2011a). Algorithms developed for image analysis (Otsu, 1979; Shaus and Turkel, 2016) can be helpful to provide independent estimates on source information before any inverse modeling and without the need for fixing source parameters. Amplitudes of displacement are high near the fault surface, while the gradient of the displacement field is high near the rupture plane. This allows to locate the faulting and to estimate the location of the fault trace for surface rupturing earthquakes. This is done in an effort to infer prior pseudo-probabilities on the earthquakes position, strike, length, width and the number of ruptured segments for a non-linear optimisation. The derived product should be probabilistic in nature, allowing for spatial offsets of surface expression and the causative fault, due to a variety of reasons (e.g. apparent shift due to line-of-sight and slip heterogeneity). By using image analysis such as gradient vectors and edge detection, I aim for an objective and unsupervised extraction of characteristics of the earthquake rupture of medium sized complex events.

I use the results obtained from the two presented methods as prior information to define meaningful parameter ranges to be searched in an optimisation of uniform slip kinematic source models with multiple rectangular-shaped fault segments. A guided optimisation is informed about prior parameter estimates of fault location, dimension, orientation and rupture timing and can further be used to define a probable number of source models to be explored. The developed framework also supports further constraining of the parameter space, e.g. in the absence of available data, by information from the World Strain Map (Kreemer et al., 2014) and the source time functions from the SCARDEC catalog (Vallée and Douet, 2016).

To demonstrate the usefulness of the developed tools, I apply them to data from the 25.11.2016 Muji  $M_w$  6.6 earthquake, located in the Pamir in the Muji basin. Previous studies modelled the Muji earthquake as a segmented rupture from teleseismic data (Bie et al., 2018) and from InSAR data (Fang et al., 2007). Strike-slip earthquakes are well known for segmentation along strike directions (Biasi and Wesnousky, 2016; Klinger, 2010) with compressional or extensional step-overs compensating motion between faults (Klinger, 2010). Continental strike-slip earthquakes can jump very large step-overs (Bai and Ampuero, 2017), affecting hazard calculations, and are therefore of primary interest for investigation of rupture segmentation. I conclude for the Muji 2106 earthquake that a rupture segmentation into two different discernible segments occurred. The rupture started on the eastern segment, propagated bilaterally and jumped a 5 km aseismic gap to the western segment.

**Chapter 4:** The developed methods and tools are applied to case study of the Qaidam 2008-2009 earthquake sequence to investigate the occurrence of co-seismic rupture segmentation as well as the behaviour of a along-dip and along-strike segmented fault system during a seismic sequence with co-seismic and post-seismic displacements. To investigate the potential connection between co-seismic rupture segmentation and long-term fault segmentation data-driven statistics are needed on the geometry of sequences, earthquakes therein and fault system geometry (Philibosian and Meltzner, 2020). Inferring the fault system geometry is usually done by aftershock distribution analysis but is difficult without near-field data (Donner et al., 2013).

The Qaidam 2008-2009 earthquake sequence in northeast Tibet consisted of the  $M_w$  6.3 2008 and 2009 Qaidam earthquakes. Based on InSAR data modeling a depth segmentation between the faults involved in the 2008 and 2009 earthquakes has been found (Elliott et al., 2010). Depth

## 1 Introduction

segmentation of earthquakes is known to be difficult to detect and describe (Frietsch et al., 2019b) and can potentially lead to an apparent fast repeat of co-seismic events at virtually the same location (Elliott et al., 2010) and is therefore of great interest for hazard analysis.

Through InSAR time series data a significant post-seismic afterslip signal was discovered between the 2008 and 2009 Qaidam earthquakes (Daout et al., 2019). On average a fault segment only releases about 85% of its strain budget co-seismically in large earthquakes and the rest in foreshocks, aftershocks, post-seismic slip and off-fault deformation (Hayes, 2017). Strain budget analysis and fault system interaction studies therefore require the inclusion of other signals than co-seismic signals and as well investigation of potential rupture segmentation.

I conduct a multi-array back-projection analysis from broadband teleseismic data and my co-authors and I carry out joint-inversions of teleseismic and InSAR data with free parameters for the geometry of the co-seismic and post-seismic fault geometry. The 2008 earthquake is a deep and shallow dipping earthquake, occurring on a single fault plane, with no indication of rupture segmentation from the backprojection results. The post-seismic afterslip of the 2008 earthquake occurred likely on a fault-plane in down-dip direction, however it was only modelled using a single-source model. The post-seismic signal however could also be caused by post-seismic deformation on a segmented fault plane. For the 2009 earthquake the teleseismic backprojection results indicate that rupture segmentation occurred on three distinct fault segments. The source parameter inferences for the three segments of the 2009 earthquake show south-dipping high-angle thrusts located at shallower depths than the source of the 2008 earthquake. From the combined inference of teleseismic backprojection and kinematic source model estimates it is likely that the rupture of the 2009 earthquake propagated from around 9 km depth to the surface, spreading bilaterally and jumping from the fault segment in the middle, on which rupture initiated, to both other ruptured segments.

## Contributions

**Paper I** I wrote the original draft, developed the method, visualized all figures and processed the seismological and geodetic data, co-developed the inversion and data processing software.

**Paper II** I wrote the original draft, visualized all figures, processed the seismological and geodetic data, conceptualized the study and methods, conceptualized and developed the surface displacement map segmentation method, developed the employed multi-array method and developed the software.

**Paper III** I performed the seismological analysis, conceptualized and co-conducted the inversions and developed the software tool for the backprojection and co-developed all other software tools used. I visualized the seismological figures. I wrote the seismological sections and parts of method sections of the first draft and participated in writing and editing in all other parts and figures of the paper.

# 2 Paper I - Sensitivity of InSAR and teleseismic observations to earthquake rupture segmentation

Andreas Steinberg<sup>1</sup>, Henriette Sudhaus<sup>1</sup>, Sebastian Heimann<sup>2</sup>, Frank Krüger<sup>3</sup>

<sup>1</sup> Department of Geosciences, Kiel University

<sup>2</sup> GFZ German Research Centre for Geosciences

<sup>3</sup> Department of Geosciences, University of Potsdam

Published in *Geophysical Journal International*, Vol. 223, Issue 2, Pages 875-907

## 2.1 Summary

Earthquakes often rupture across more than one fault segment. If such rupture segmentation occurs on a significant scale, a simple point-source or one-fault model may not represent the rupture process well. As a consequence earthquake characteristics inferred, based on one-source assumptions, may become systematically wrong. This might have effects on follow up analyses, e. g. regional stress field inversions and seismic hazard assessments. While rupture segmentation is evident for most  $M_w > 7$  earthquakes, also smaller ones with  $5.5 < M_w < 7$  can be segmented. We investigate the sensitivity of globally available datasets to rupture segmentation and their resolution to reliably estimate the mechanisms in presence of segmentation. We focus on the sensitivity of InSAR (Interferometric Synthetic Aperture Radar) data in the static near-field and seismic waveforms in the far-field of the rupture and carry out non-linear and Bayesian optimisations of single-source and two-sources kinematic models (Double-Couple point sources and finite, rectangular sources) using InSAR and teleseismic waveforms separately. Our case studies comprises of four  $M_w$  6 to  $M_w$  7 earthquakes: the 2009 L'Aquila and 2016 Amatrice (Italy) and the 2005 and 2008 Zhongba (Tibet) earthquakes. We contrast the data misfits of different source complexity by employing the Akaike Informational criterion (AIC). We find that the AIC method is well suited for data-driven inferences on significant rupture segmentation for the given datasets. This is based on our observation that an AIC-stated significant improvement of data fit for two-segment models over one-segment models correlates with significantly different mechanisms of the two source segments and their average compared to the single-segment mechanism. We attribute these modelled differences to a sufficient sensitivity of the data to resolve rupture segmentation. Our results show that near-field data are generally more sensitive to rupture segmentation of shallow earthquakes than far-field data but that also teleseismic data can resolve rupture segmentation in the studied magnitude range. We further conclude that a significant difference in the modelled source mechanisms for different segmentations shows that an appropriate choice of model segmentation matters for a robust estimation of source mechanisms. It reduces systematic biases and trade-off and thereby improves the knowledge on the rupture. Our study presents a strategy and method to detect significant rupture segmentation such that an appropriate model complexity can be used in the source mechanism inference. A

similar, systematic investigation of earthquakes in the range of  $M_w$  5.5 to  $M_w$  7 could provide important hazard-relevant statistics on rupture segmentation. In these cases single-source models introduce a systematic bias. Consideration of rupture segmentation therefore matters for a robust estimation of source mechanisms of the studied earthquakes.

## 2.2 Introduction

Coseismic rupture segmentation is common and evident for earthquakes with large moment magnitudes above  $M_w > 7$  (e.g. (Segall and Pollard, 1980) and (Barka and Kadinsky-Cade, 1988)). Coseismic ruptures can be segmented, with segments separated by step-overs and fault bends (Klinger, 2010). Segments have distinct geometrical properties or a spatial separation. While fault segment sizes appear to have a fractal distribution (Scholz and Aviles, 1986), the number of fault segments that is discernible and can be represented in a model should depend on the significance in seismic moment contribution.

Also earthquakes in the moment magnitude range between 5.5 and 7 show segmentation, especially strike-slip and reverse-type earthquakes but also normal-fault earthquakes (Biasi and Wesnousky, 2016). (Biasi and Wesnousky, 2016) have analysed surface traces of ruptures and found that around 47% of the ruptures in their study in the magnitude range 6-7 are segmented with one or more steps and that the number of segmentations into distinct rupture segments apparently increase with magnitude and rupture length. A hypothesis could be that segmentation is less common for smaller earthquakes. Smaller earthquakes with magnitudes between 6 and 7 are more often investigated by using automated procedures that assume unsegmented rupture, i.e. single point source or single dislocation plane (e.g. (Dziewonski et al., 1981), Geofon and USGS (United States Geological Survey)). The common belief that earthquakes in the magnitude range 6 to 7 are less complex might therefore stem from an artificial bias, i.e. observational and modelling bias. We therefore choose earthquakes in this magnitude range as case studies, which also narrows down the range in the signal-to-noise ratios that may have an influence on the resolution of rupture segmentation. We choose normal-type earthquakes first of all to reduce non-essential degrees of freedom in this study. Furthermore, both normal and reverse type earthquakes are underrepresented in fault segmentation statistics (Biasi and Wesnousky, 2016) but represent a significant amount of moment release of continental earthquakes. If rupture segmentation occurs within the resolution of the data used, a simple one-source model like a single point source or a single rectangular source may not represent the rupture process well. This raises the question to which level geodetic satellite observations, i.e. InSAR, and teleseismic far-field observations can well resolve rupture segmentation or if these individual observations supplement each others inferences on rupture segmentation. A further questions is if larger earthquakes of  $M_w > 7$  are more complex than smaller ones or if there is an observational bias due the fact that larger earthquakes are being researched by a multitude of in-depth case studies.

Resolving rupture segmentation and thereby defining the geometrical complexities of the rupture is crucial to better understand the observed link between geometric barriers at faults and the locations of rupture initiation and termination (King and Nábělek, 1985). Also, near-field hazard differs strongly for more or less segmented faults (Field et al., 2014; Field et al., 2015). Long-term fault segmentation might govern the evolution of a fault system (Wesnousky, 1988). Therefore, robustly resolving rupture segmentation and providing statistics is an important task in earthquake source modelling. In this study we look at the possible additional information to be gained from the data-driven exploration of a complex earthquake model geometry. We test the hypothesis that the observed source mechanism can be reasonably subdivided (or not) into sub-events of comparable moment share that differ significantly in the timing of the moment release and/or significantly differ in the inferred geometry. This study investigates the resolution

power of static deformation data and teleseismic wavefield data towards rupture segmentation of medium-sized earthquakes. The goal is to better describe segmented ruptures of medium-sized earthquakes.

For static near-field surface displacement data the motivation to use multiple sources in models is apparent, as changes in the properties (e.g. the strike) of the static deformation field are easily detectable due to the high spatial resolution of the data. Already in the first paper that made use of the InSAR technique for measuring earthquake deformation, a multi-source model was used (Massonnet et al., 1993a).

For far-field data (abbreviated FF in the manuscript) it has been claimed that the availability of data limits the resolvability of second-order features, like the source segmentation, for earthquakes  $< M_w 7$  (Ide et al., 2005). The data availability has improved considerably in the last two decades. In its far-field and for long wavelengths, an earthquake with pure shear-failure can be represented well by a double-couple point source model in space and time. So, as an indicator of how well such an earthquake is represented by a point source model, the magnitude of the CLVD components of the full moment tensor is often used (Frohlich et al., 1994). In the 1980s it was found that the non-double-couple tensor components hold information about not only data errors but also from unmodelled, but significant model complexity (Sipkin, 1986). Failure to account for these complexities could lead to overly-simplistic or incorrect earthquake source models. Several source effects that cause non-double-couple (DC) components for shallow earthquakes have been implied, such as source segmentation (Barker and Langston, 1982) and rupture on non-planar faults (Sipkin, 1986). Unrepresented near-source structure can also contribute to non-double-couple components (Kawasaki, 1982). For cases of obvious rupture segmentation also FF based studies use more complex models than single-source models (Barker and Langston, 1982; Sokos and Zahradnik, 2008; Duputel et al., 2012a).

The appropriate number of sources in a model for an appropriate level of data fit to be reached is usually a subjective judgment based on the used observations and their quality. We additionally seek an objective way to judge on the minimum segmentation required to meaningfully represent ruptures based on the sensitivity of the observations to these source complexities. In the scope of this sensitivity study we allow for one or two segments in the source model, in the following abbreviated as "one-source model" and "two-sources model". We analyse how different the source model mechanisms are for these two cases, in order to quantify the possible model bias and to investigate the possible importance of the source model complexity choice. We base our study on source model ensembles from kinematic source optimisations of single-source and two-sources models for real earthquakes. We evaluate the model performance by applying the Akaike Informational Criterion (AIC, (Akaike, 1985)) and also check the source model parameter trade-offs/uncertainties. To assess the sensitivity (or resolving power) towards source segmentation with regard to the type of dataset, we run these analyses separately for near- and far-field. We investigate the resolvability of source segmentation in absence of local data (e.g. in remote or sparsely instrumented areas) and therefore make use of static space-borne InSAR data for the near-field of earthquakes and broadband recordings at seismological stations for the far-field of earthquakes, respectively.

We analyse in this study four earthquakes. These are two geographical pairs of normal-faulting earthquakes, and moment magnitudes between  $M_W 6$  and  $M_W 6.8$ . The magnitude range of the studied earthquakes is chosen to explore the resolvability of the possible lower-magnitude threshold of earthquakes, which produces signals strong enough for non-local stations to detect rupture segmentation. We selected two regional earthquake pairs as case studies. (1) A pair in Central Italy, the April 6, 2009 L'Aquila earthquake ( $M_W 6.3$ ) and the August 24, 2016 Amatrice earthquake ( $M_W 6.2$ ). (2) And a pair in the Xizang Region, Tibet consisting of the earthquake of April 7, 2005 ( $M_W 6.2$ ) and the August 25, 2008 Zhongba earthquake ( $M_W 6.7$ ). For each pair,

the earlier events, the 2009 L'Aquila earthquake and the 2005 Zhongba earthquake, have been attributed to unsegmented ruptures (Atzori et al., 2009; Elliott et al., 2010) and were modelled using a single fault patch. Solutions from GCMT (Global Centroid Moment Tensor), USGS, Geofon and local agencies, where available, are plotted in Appendix Fig. 2.23. For tabulated locations, time and DC components for all four earthquakes see Tab. 2.1. All four studied earthquakes are of shallow depth ( $< 15\text{ km}$ ). The USGS determined DC component percentage vary strongly for each earthquake, depending on the method. They show no clear trend of non-DC components for this group of earthquakes. If the earthquake source is shallow, compared to the seismic wavelengths used, the isotropic components cannot reliably be determined (Julian et al., 1998). We therefore refrain from using the non-double-couple percentage as an indicator of earthquake source complexity. The later events in each pair of our study, the 2016 Amatrice earthquake and the 2008 Zhongba earthquake, were modelled in some previous studies with two fault patches (Huang et al., 2017; Elliott et al., 2010; Ryder et al., 2012).

We select two earthquake pairs in the two separate regions of Italy and Tibet with different observational circumstances to investigate whether or not our findings are similar in repeated inferences and if the results are transferable from one region to another. Observational differences for the seismological data are, e. g. the different seismic station distribution and different effects of 3D-Earth structure in our 1D-layered Earth model approximations. For the InSAR observations they generally include different data acquisition frequencies and different surface properties influencing the quality of InSAR measurements. For Tibet in particular, we expect lower InSAR data quality. Mostly because of temporal decorrelation due to the long time spans of the interferograms, due to strong seasonal influences with ice and snow cover, resulting in abundant data gaps (Elliott et al., 2011a) and additionally DEM errors in the data (Daout et al., 2018), due to strong relief. Differences in phase coherence, atmospheric noise etc. allow us to study their influence on the detectability of rupture segmentation. The similar source mechanisms of our selected earthquakes and fault strike realize a similar radiation pattern for the intra-pair analyses as well as for the inter-pair analyses. The similar source mechanisms also help to potentially avoid a bias for InSAR, as there is a higher sensitivity to the vertical surface deformation and a weakness in sensing northward displacement that generally leads to a preference of fault dip-slip to strike-slip motions in static source optimisations (Weston et al., 2012). The close proximity of the earthquake origins in each pair allows us to exclude influences of global path effects from 3D Earth-structure. Any corresponding bias would be very similar for both earthquakes of the pair. Using real data, results may also be influenced by noise. Data errors are correlated in space (static displacements) and time (waveforms). We propagate the data errors in the optimisation to derive source model parameter uncertainties and trade-offs.

## 2.3 Data

### 2.3.1 Static near-field data: surface displacements measured using InSAR

Static near-field data in this study are surface displacements derived from InSAR data. Interferometric processing of the SAR data is done using the Gamma Software (Werner et al., 2000). For each earthquake we use ascending and descending C-band ( $\lambda=5.6\text{ cm}$ ) SAR observations that span the earthquakes with the shortest possible re-visit intervals. For the earthquakes before 2012, we use Envisat SAR data, for the 2016 Amatrice earthquake Sentinel-1 data is employed. For topography phase correction we use the SRTM 4 Digital Elevation Models (Jarvis et al., 2008). We increase the phase coherence in the differential interferograms through multi-looking (Hanssen, 2001a) with factors between four and eight. To further enhance the signal-to-noise ratio (SNR) of the interferometric phase, we applied

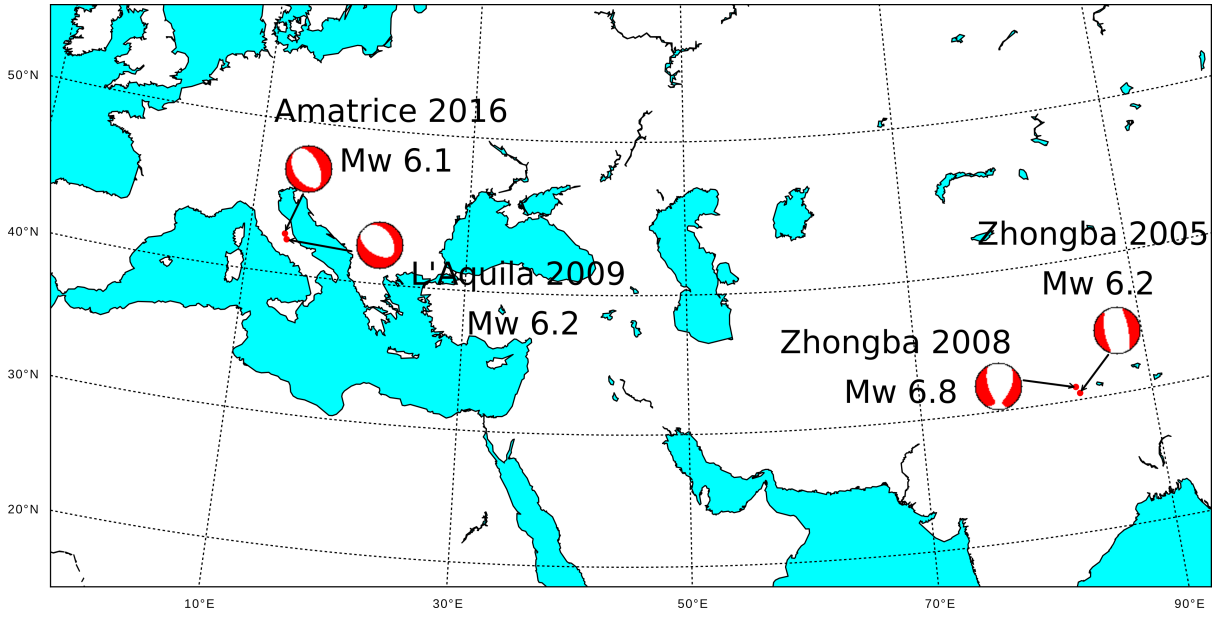


Figure 2.1: Locations and moment tensor solutions reported by the Global CMT project (Dziewonski et al., 1981) of the four studied earthquakes. Moment tensor solutions are shown in lower-hemisphere stereo-projections.

Table 2.1: Table of time, location and magnitude of events as reported by the USGS. Also given is the DC component from body wave and the W-phase inversions for the different earthquakes, as given by the USGS, except for the 2005 Zhongba (indicated by the star) where the DC component from the GCMT solution is given. The last column indicates the number of segments used in the literature in previous finite source modelling, with the models from (Atzori et al., 2009) for the 2009 L'Aquila earthquake, (Huang et al., 2017) for the 2016 Amatrice earthquake and (Elliott et al., 2010) for the two Zhongba earthquakes.

Earthquake	Date	Time (UTC)	Location		Magni- tude	DC body	DC w-phase	#segm. in lit.
			Latitude	Longitude				
2009 L'Aquila	2009-04-06	01:32:39	42.334°N	13.334°E	6.3	31%	64%	1
2016 Amatrice	2016-08-24	01:36:32	42.723°N	13.188°E	6.2	98%	86%	2
2005 Zhongba	2005-04-07	20:04:41	30.491°N	83.662°E	6.3	94%	59%*	1
2008 Zhongba	2008-08-25	13:21:58	30.901°N	83.520°E	6.7	31%	98%	2

adaptive filtering on the interferograms (Goldstein and Werner, 1998). We then unwrap the filtered interferograms using the tree-branch-cut algorithm (Goldstein et al., 1988). We subsample the unwrapped interferograms using a quadtree algorithm (Jónsson et al., 2002). With the quadtree subsampling we obtain a reasonable number of data points for the source optimisations and keep a good spatial representation of the LOS (line-of-sight) displacement pattern.

For our analyses we desire a comparable coverage of pixels above a correlation threshold of 0.4 covering about 60-70% of the deformed area in the near field for all earthquake studies. For the 2008 Zhongba earthquake, however, we retrieve at most half of the apparent deformed area with a single descending interferogram, which is much less than for the other static near-field datasets. We can increase the data coverage from the descending look direction sufficiently by adding displacement data of a second descending interferogram. However, overlapping data points from the same look angle cause an over-representation of the corresponding areas in the source analyses, potentially leading to a biased estimation of source geometry. Therefore, based on the linear dependence of overlapping data, we apply a compensating data weighting (Sudhaus and Jónsson, 2009).

In the source analyses we consider spatially correlated data noise. We obtain representative noise in areas of the interferogram with no apparent surface displacement signal, assuming that the data noise is stationary. Following (Hanssen, 2001a) we approximate the data noise character by a Gaussian random field, characterized by its variance and covariance functions. We use these functions to build variance-covariance matrices for the subsampled data of each interferogram. They are used to generate the noise perturbations for the randomize-then-optimize procedure described in Section 3.1.2.

### 2.3.2 Far-field data: teleseismic waveforms

As far-field data (FF) we use the seismogram components BHZ, BHN and BHE with sampling rates between 20 Hz and 50 Hz obtained from the International Federation of Digital Seismographic Networks (FDSN) via the IRIS web service (<https://service.iris.edu>). We select stations at epicentral distances with respect to the source between 24ř and 93ř, as these distances are large enough such that InSAR data wave terms have attenuated and also triplications do not occur. We use the Pyrocko software (Heimann et al., 2017b; Heimann, 2011) for seismological waveform data retrieval and processing. We select 70 to 90 stations with a good azimuthal coverage and manually check the data quality (see fig. 2.11).

We resample the seismograms after download to 0.5 Hz to match the Green’s functions sampling rate and the horizontal components are rotated into longitudinal and transverse components, based on theoretical azimuth of the phase. Only P and SH phases are used in the optimisation procedure. For the P phase fits we use only the vertical seismogram component. We extract a P-phase data window of 25 s duration. For the S phases we cut a data window of 40 s duration. The usable frequencies are limited due to high-frequency noise and by the need to satisfy the point source approximation, i.e. that source dimensions are much smaller than the considered wavelengths (tens of kilometers in this case) and the distance from the source. As we are interested in the first order source complexity we want to exploit frequencies up to the expected corner frequencies. In our cases, of  $M_w$  6.2 to  $M_w$  6.7 earthquakes with rupture dimensions of the tens of kilometres, we expect roughly 0.1 Hz. We filter the data with an acausal zero-phase filter in the frequency domain with corner frequencies of 0.025 Hz to 0.065 Hz for P phases and 0.025 Hz to 0.085 Hz for SH-waves.

Also for higher frequencies the considered wavelengths reach a scale at which they are affected



more strongly by local/regional velocity perturbations as can be modelled by averaged 1D velocity models. For these reasons it is better for FF source optimisations to use lower frequencies to achieve stable results.

To estimate and later propagate the data noise, real noise recorded at each station is extracted for a duration of at least half an hour, from 5 minutes and up to 2 hours before the earthquake. We require that no significant seismic activity is recorded in this time window, based on catalog information. The noise waveforms are processed in the same way as the earthquake data waveforms.

## 2.4 Earthquake source modelling and model selection criteria

### 2.4.1 Nonlinear optimisation strategy

In the source parameter optimisation for both InSAR data and FF we are seeking the minimum of the L2-norm between the observed data  $\mathbf{d}_{\text{obs}}$  and the predicted model  $\mathbf{d}_{\text{pred}}$ . The general form of this objective or *misfit* function is:

$$\|e\| = \sqrt{\sum (\mathbf{d}_{\text{obs}} - \mathbf{d}_{\text{pred}})^2}. \quad (2.1)$$

For the data predictions of both, the InSAR data and that of the FF, for each of the four earthquakes we use one setup with a single-source model and a two-source model for later comparison. These two models are optimized separately using either only static InSAR data or only FF, without combination of the datasets. The exact misfit definition and the model spaces are different for the InSAR data and FF modeling setup and are addressed below in Sections 3.1.1 and 3.1.2.

Our optimisation strategy is common for all the InSAR data and FF optimisations, as well as for each one-source and two-source earthquake source optimisations. Dealing with several sources can be difficult during an optimisation as the highly non-linear and multi-modal nature of the problem are not easy to handle. We therefore make use of an optimisation scheme which is able to keep several minima in the model space alive during the optimisation and investigate them without changing the objective function or model space in between steps.

The model space is sampled in three subsequent stages. The first sampling stage is an exploratory stage with uniform sampling of the entire model space. We draw 10.000 models in this first stage and keep the models with the lowest misfits in a sorted *high-score* list. The number of models the high score list can hold is defined dependent on the number of model parameters  $n_{\text{par}}$ . We choose a capacity of  $8 * n_{\text{par}} + 1$  models. The number of model parameters are 9 and 18 for the InSAR data one-source and two-sources rectangular dislocation models and 8 and 16 for the FF one and two-point-sources models, respectively. Using the high score list approach the sampler has the capability to retain multiple minima, which is especially important for optimizing the two-sources models. The high-score list of models guides the optimisation and carries a memory of low-misfit regions of the model space in the subsequent optimisation stages.

In the second sampling stage, the sampled model space is defined relative to the models currently participating in the high-score list. Here we subsequently draw model vectors from a multivariate normal distribution, based on the variance-covariance matrix of the high score model parameters  $\mathbf{R}$ , scaled by a factor  $a$ . The scale factor is logarithmically decreased from  $a_{\text{start}} = 2$  to  $a_{\text{end}} = 1$  during the second stage. This way the optimisation starts off a bit more explorative and densely

samples the low-misfit areas in model space at the end. A shrinking ellipsoid shaped search space is the result of this procedure. Any newly generated model with a low misfit may directly enter the high-score list, change the statistics of this model group and thereby affect the sampling radius. The second stage runs for 20.000 models. In the third sampling stage, the same procedure is continued but the factor scaling the variance-covariance matrix is fixed to a value of  $a = 1$ . Another 10.000 models are sampled in this final stage.

The implementation of this code is done using Pyrocko software tools (Heimann et al., 2017b) and is available online in a more developed form as the software package "Grond" (Heimann et al., 2018b).

We propagate data uncertainties in to source model parameter uncertainties by adding representative real noise to the observed data anew for each individual source optimisation as a form of Randomize-then-Optimize (Bardsley et al., 2014), which is similar to residual bootstrap. For each earthquake study and for NF and FF we perturb our datasets 500 times with noise generated as described in the respective method sections. This results in 500 different datasets. The resulting distribution has been shown to match the model parameter distributions obtained from Markov Chain Monte Carlo sampling of the model spaces by (Jonsson et al., 2014). These 500 different datasets are used in the optimisations for both one-source and two-sources model setups. This means that same noise perturbed datasets are used in both the one-source and two-sources optimisations, allowing to evaluate the significance of the inferred results between individual datasets.

#### 2.4.1.1 Near-field model setup

In the InSAR data optimisation we combine ascending and descending scenes into one data vector  $\mathbf{d}_{\text{obs}}$ . To consider the data error variances and covariances, the general misfit function (eq. 2.1) needs to be complemented by a weighting matrix  $\mathbf{R}$  that derives from the data error variance-covariance matrix  $\Sigma$ :

$$\|e\| = \sqrt{[\mathbf{R}(\mathbf{d}_{\text{obs}} - \mathbf{d}_{\text{pred}})]^T \mathbf{R}(\mathbf{d}_{\text{obs}} - \mathbf{d}_{\text{pred}})}, \quad (2.2)$$

with  $\mathbf{R} = \sqrt{\Sigma^{-1}}$ .

The synthetic noise  $\epsilon_{\text{syn},i}$  added to the data is generated by using the estimated covariance functions (Sudhaus and Jónsson, 2009). This modifies the objective function to:

$$\|e\| = \left\{ [\mathbf{R}(\mathbf{d}_{\text{obs}} + \epsilon_{\text{syn},i} \mathbf{d}_{\text{pred}})]^T \mathbf{R}(\mathbf{d}_{\text{obs}} + \epsilon_{\text{syn},i} \mathbf{d}_{\text{pred}}) \right\}^{1/2}, \quad (2.3)$$

with  $\mathbf{R} = \sqrt{\Sigma^{-1}}$ .

The forward model is either one rectangular dislocation in a homogeneous elastic halfspace (Poisson's ratio 0.25) (Okada, 1985) or two of such rectangular dislocations, with the condition of no overlapping. This dislocation problem has a computationally low-cost analytical forward solution. The dislocations are restricted to shear dislocation parallel to the fault plane. The optimized source model parameters are the location (north, east, depth), the fault dimension (length and width), the fault orientation (strike, dip) and the slip (dip-slip, strike-slip). We define the fault depth as the top center edge of the rectangular source (see model sketch in Appendix fig. 2.15). The seismic moment is calculated using  $M_0 = \mu AD$ , with shear modulus  $\mu$ , fault area  $A$  and the fault slip  $D$ . We use  $\mu$  based on the IASP91 1-D velocity model (Kennett and Engdahl, 1991a). This is comparable with the FF modelling setup. Additionally to

earthquake source model parameters, three additional data ambiguity model parameters are used for each InSAR data set to remove any residual average data offset and a linear orbital phase ramp in east and north direction (Ozawa et al., 1997; Simons et al., 2002)).

The model space boundaries for the optimisation are set above and below of optimum solutions reported in earlier studies, in (Atzori et al., 2009) for the 2009 L’Aquila earthquake, in (Elliott et al., 2010) for the 2005 and 2008 Tibetan earthquakes. For the 2016 Amatrice earthquake, we choose the model parameter bounds based on our own initial optimisations. However, for all cases, we choose them to be broad around these optimal solution values. The north and east position of the fault plane is allowed to change  $\pm 20$  km for each source or segment. The fault strike is allowed to vary either  $\pm 50^\circ$ , if initial tests could find a clear preference for one nodal plane, or it is not constrained. The fault dip is allowed to change  $\pm 25^\circ$ . The dip-slip on the fault is allowed to change  $\pm 0.4$  m and the strike-slip  $\pm 0.3$  m. We do allow for the top edge of the fault to be within the depth range of 0.1 to 12 km.

### 2.4.1.2 Model setup for the far-field data

In the FF setup we optimize with down-sampled (0.5 Hz sampling rate) and filtered waveforms. We use pre-calculated 0.5 Hz Green’s functions with spatial sampling of 4 by 4 km and use multilinear interpolation in space to account for source positions between the grid points. As sources we use pure double couples (DC). The Green’s functions were calculated using the QSSP code by (Wang, 1999) and based on the IASP91 1-D velocity model (Kennett and Engdahl, 1991a), which are set-up in database structure and handled by the *Pyrocko* software toolbox (Heimann et al., 2017b). The theoretical resolution limit of the FF for simultaneous but spatially separated point sources depends mostly on the upper corner frequency of the used filter, limiting us in our cases to resolutions of tens of kilometers. For the magnitudes of our case studies we can assume the rupture lengths (and also the longest radiated wavelengths) to be on the order of 10 - 20 km (**Blaser**). If several point sources can not be reliably resolved it is also possible that the moment share between the two sources is not significant enough to warrant the use of a multi-source model at the given frequencies and with the data used. For non-bilateral rupture we expect that segmentation will occur additionally separated in time, increasing the potential resolution.

We calculate the misfit according to equation 2.1 for each station individually. We allow each individual station recording to shift independently maximally  $\pm 4$  s (two samples in each direction) to account for possible difference in path ways for the different stations, using the shift with the lowest misfit. The data misfit at each station is calculated according to Eq. 2.1 for all time samples from P- and S-phase fitting windows.

We balance the contributions of stations to the misfit with *balancing* weights in the optimisation, to correct for geometrical spreading, amplitude differences between P and S phases, and different length of the cut-out windows. The balancing weights are determined prior to the optimisation, based on statistical assumptions on the expected signals and misfits. We follow the strategy of (Heimann, 2011) to derive these balancing weights. First, we sample 1.000 ( $k, \dots, K$ ) uniformly random models within the set model bounds and filter and taper as for the observed data optimisation. Generally, traces with large amplitudes result in large station misfits. At each station ( $i, \dots, N$ ) and each component (phase) ( $j, \dots, M$ ) we determine the balancing weights

$\mathbf{r}_{\text{balance},ij}$  as

$$\mathbf{r}_{\text{balance},ij} = \frac{1}{\frac{1}{K} \sum_k |\mathbf{d}_{\text{pred},ijk}|}. \quad (2.4)$$

We utilize for the FF the "Randomize-then-Optimize" procedure (Bardsley et al., 2014). We perturb the FF observations with real data noise. Noise is selected in pre-event windows as described above (Section 2.3.2). The noise trace added to the observed data is a compound of many real-noise traces created as follows. From the entire pre-event noise we extract 300 randomly positioned time windows of random duration between 10s and 50s for each traces and add them to the trace again at random positions at times between 1 min before and 1 min after the respective P- and S-wave theoretical phase arrivals. The noise traces are generated anew (using a different seed for the random numbers) for each of the 500 individual optimisations.

The final normalized objective function that needs to be minimized is defined with eq. 2.1 and eq. 2.4 as:

$$\|e\| = \frac{\sqrt{(\sum |\mathbf{r}_{\text{balance}} \cdot (\mathbf{d}_{\text{obs}\epsilon} - \mathbf{d}_{\text{pred}})|)^2}}{\sqrt{\sum |\mathbf{r}_{\text{balance}} \cdot \mathbf{d}_{\text{obs}\epsilon}|^2}} \quad (2.5)$$

with  $\mathbf{d}_{\text{obs}\epsilon}$  being the noise perturbed observed data.

For an initial source location and for the determination of model parameter bounds in the optimisation we use the GCMT (Global Centroid Moment Tensor, (Dziewonski et al., 1981)) solutions. The model space for a single DC is defined by eight source parameters: time, relative north and east shift with respect to the GCMT location, source depth, moment magnitude, strike, dip and rake. The source parameter bounds for the optimisation are centered in general on the GCMT values. The source times are defined relative to centroid time estimate by GCMT and are allowed to shift  $\pm 10$ s. The north and east shifts are allowed to vary  $\pm 30$  km. Strike range is set to be  $\pm 50^\circ$ , if initial tests could find a clear preference for one nodal plane, else it is left unconstrained, to allow for the flip of vergence. Dip is allowed to vary  $\pm 25^\circ$  and rake  $\pm 50^\circ$ . The moment magnitude is allowed to vary  $\pm 0.5$  relative the GCMT value. We constrain the depth to be between 1 km and 15 km for all cases.

The two-source point sources are optimized individually for strike, dip and rake and a set of relative source parameters, as we can expect a strong dependence. To separate the two point sources in the optimisation naturally in space and time, we define the time and position shifts of both sources relative to their common moment centroid (see model sketch in Appendix fig. 2.15). Both these relative time and location shifts are not allowed to be zero. The total number of source parameters to be optimised is 16 (strike, dip, rake for each point source and relative north, east, time and moment and also the total moment). For illustration and statistics however we afterwards derive the full set of source parameters for each sub-source. We also report the total moment tensor. It is simply the sum of the moment tensors of the two sub-sources. We disregard any potential isotropic components, which are not needed in our method and we do not calculate the non-double couple percentages as a measure.

We use the same frequency band for the one- and two-sources FF optimisations to investigate first order source complexity. At very low frequencies the point source approximation could be expected to hold, even for more complex ruptures, without introducing strong biases. This however might also not be the case if subevents are strongly separated in space and or time.

#### 2.4.2 Model fitness evaluation by using informational criteria

We use informational criteria to compare and evaluate our resulting models. An informational criterium is a measure of the goodness of fit of an estimated statistical model that, apart from the misfit alone, takes into account the model complexity or other criteria. The data misfit improves with an increasing number of free model parameters, however overfitting as well as

underfitting is to be avoided. This is crucial as inference of models with too few parameters can be biased, while too many parameters (more than can be supported by the data) lead to lower accuracy or identification of spurious effects (Burnham and Anderson, 2004).

Akaike information criterion AIC (Akaike, 1998) is a standard method of model selection and also works in cases where one of the two distributions to be tested is not a subset of the larger distribution (nested and non-nested models) (Akaike, 1985). Another method of model selection is the F-test, which has been used for model selection of earthquake sources before (Shi et al., 2018) but only works reliably with nested models and only compares one single F-test model against another (Kletting and Glatting, 2009). Another advantage of the AIC over the F-test is that for the AIC no arbitrary level of significance or selection procedure has to be chosen. Therefore the use of AIC over F-tests have been advocated in other fields of research (Kletting and Glatting, 2009).

Higher model complexity (here an additional source in the modelling) normally is expected to decrease the misfit at the cost of more parameters. As a consequence the information gain from a more complex model has to be weighted against the number of additional parameters introduced, to evaluate if the information gain of the higher complexity model is significant enough.

We derive the log-likelihood value  $\ln(\mathbf{l})$  for the model  $\mathbf{x}$  by evaluating the probability density function of a multivariate normal distribution given a vector of the mean model parameters  $\mu$ , the covariance  $\Sigma$  of the model parameter and the number of model parameters  $N_{\text{par}}$  for each model ensemble separately:

$$\ln(\mathbf{x}) = \frac{1}{N_{\text{par}}} \frac{1}{\sqrt{(2\pi)^{N_{\text{par}}} \det \Sigma}} \exp\left(-\frac{1}{2}(x - \mu)^{\text{T}} \Sigma^{-1} (\mathbf{x} - \mu)\right) \quad (2.6)$$

This approach to derive the likelihood of each model considers the resolution of the model parameter and also the tradeoffs between them by using the assumption of a multivariate normal distribution, which we also assumed in our sampling.

We use the maximum log-likelihood value from each model ensemble to calculate the AIC.

In contrast to the pure log-likelihood value  $\ln(\mathbf{l})$  the AIC penalizes additional model parameters in more complex models:

$$\text{AIC} = 2\ln(\mathbf{l}) + 2N_{\text{par}}. \quad (2.7)$$

The AIC value increases when the gain in data fit for a more complex model is not large enough to compensate the increase of the penalty added due to more model parameters. The individual AIC values derived from modelling results of different datasets have little meaning, because they contain arbitrary constants and depend on the number of observations (Burnham and Anderson, 2004). Hence, a comparison between modelling results from optimisations using different datasets and therefore having different likelihood functions, using AIC is not meaningful.

### 2.4.3 Source parameter recovery tests using the informational criterion

We assess the sensitivity of the AIC in the analysis of synthetic InSAR data and synthetic far-field datasets to recover one-source, two-sources and three-sources models. We test on the minimum distance required between two sources to resolve the correct source complexity using AIC. This allows us to gain insight into what the AIC can reliably recover when the sources are clearly separated. We test the recovery of the correct number of sources, but not if the individual source parameters are estimated accurately.

We first carry out three groups of synthetic tests on resolving one, two or three sources depending on spatial and temporal separation. We use a rectangular dislocation source for the static near-field data and a double-couple source for modelling waveform data. The modelled sources are of the same mechanism. For the input models with two or three sources we increase the horizontal distance from 1 km to 10 km. The distance between the rectangular dislocation planes is the along strike distance between the nearest edges of the sources segments. For the far-field we additionally separate the moment release in time by a 2 s and 4 s delay between the origin times of the two- and three- sources input models. This setup results in ten synthetic InSAR and 20 synthetic far-field datasets. To the synthetic InSAR data synthetic noise is added, based on the estimated variance-covariance matrix in the real datasets of the 2009 L'Aquila earthquake and quadtree subsampling applied. This optimisation setup is identical to the above described methods for the real data study on the 2009 L'Aquila earthquake.

The input source model parameters are based on the 2009 L'Aquila earthquake and are taken from the estimate by (Atzori et al., 2009) for the InSAR data analysis and GCMT (Dziewonski et al., 1981) for the far-field analyses. For the representation of the earthquake with two or three sources, we split the given fault plane of 12.2 km (Atzori et al., 2009) in two and three equal-length planes for the InSAR data analyses. For the far-field analyses we split the total moment equally between the two sources. We carry out separate source optimisations for InSAR data and far-field assuming one, two (Fig. 2.2) and three sources (Appendix Fig. 2.16). For the synthetic far-field optimisations we use real data noise as in the real-data analyses. We used for the far-field modelling also the same 2 Hz Green's function store with a spatial sampling of 4 km. We want to quantify a minimum separation distance between sources at which the AIC can reliably recover the true source complexity given our model setup.

The result of the test where the two-sourced model is the true one can be seen in fig. 2.2. The lowest AIC value should always be the two sources solution. For InSAR data with a two-sources input model, the AIC values of the two-sources optimisation drop from 2 km source separation on below the AIC values of the one-source optimisations (Fig. 2.2). In this case the three-sources optimisation keeps high AIC values for all source separations. In contrast, for the optimisations of data with a three-sources input model, the AIC values of three-sources optimisations drop below the one- and two-sources optimisations for source separations above 3 km (Appendix Fig. 2.16). For source separations of less than 2 km the improvement of the data fit is not significant enough to robustly constrain the increased number of parameters. Here, the one-source model always results in the lowest AIC values independent of the number of input source segments. Also, for a one-source input model the lowest AIC values results from the one-source optimisation.

The AIC's capability to recover the correct number of sources from the synthetic far-field optimisations depends not only on the distance between sources but also strongly on the time separation of the sources. If the rupture time difference of the segments was chosen to be below 2 s the correct number of sources could not be recovered for distances of less than 7 km, while a time delay of 4 s already leads to recovery of the correct source complexity at distances greater than 3 km. The smaller the delay between the sources the larger the separation distance needs to be, to reliably recover the complexity. Similar results are found for the three sources test case (Appendix fig. 2.16).

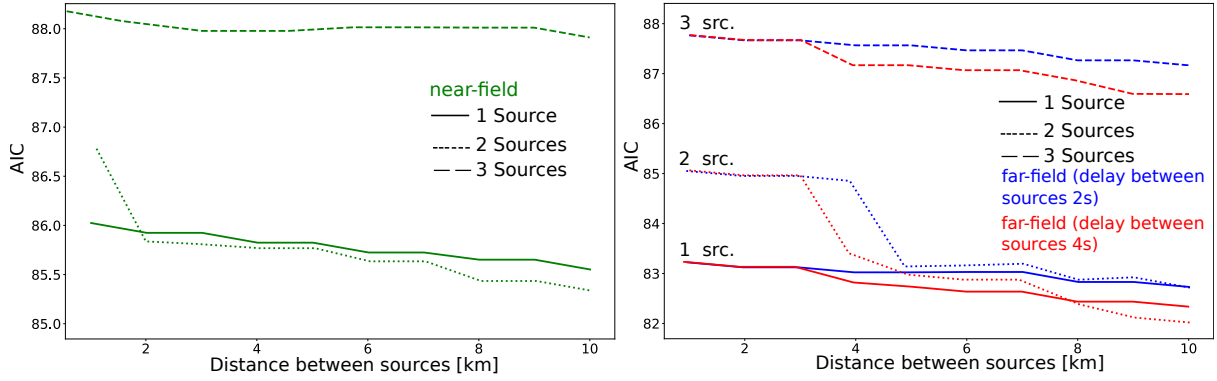


Figure 2.2: Results of the synthetic test for retrieval of complexity from noise perturbed inversions for one, two and three sources. The forward input model was two sources. The forward modelling was repeated for distances between the sources of 0-10 km and AIC value for A) static near-field and B) in blue for the far-field with a 2s delay between sources, and in red for a delay of 4s. The solid line is one source, dashed line for two and double dashed line for three sources.

## 2.5 Results

### 2.5.1 Optimisation results

The optimisation results of both, InSAR data and FF, for all the investigated earthquakes show a satisfying fit to the data (Figs. 2.9, 2.10 and 2.11). The InSAR data optimisations additionally consider linear orbital ramp parameters. They do not show any strong trade-off among each other or with the other source parameters. The source model parameters are in good agreement with the estimates reported in the literature for the investigated earthquakes (see Appendix Tabs. 2.3 & 2.4). These are, e.g. the results by (Atzori et al., 2009) for the 2009 L’Aquila earthquake, by (Lavecchia et al., 2016) for the 2016 Amatrice earthquake and by (Elliott et al., 2010) for the 2005 and 2008 Zhongba earthquakes, and generally the Centroid moment tensors published by the GCMT project (Dziewonski et al., 1981). We direct the reader to the appendix for the full record of the source parameter distributions and trade-offs (Figs. 2.18 to 2.20) and also for the tabulated median values and confidence intervals for each earthquake and each dataset (Tabs. 2.3 & 2.4).

#### 2.5.1.1 The 2009 L’Aquila earthquake

The one-source model parameters from InSAR data and FF optimisations are in good agreement with each other. Their model ensembles overlap to a large degree (Fig. 2.3). The model parameter resolution of InSAR data optimisations is higher compared to the FF optimisations, expressed by slightly lower uncertainties.

The uncertainties of the one-source and two-sources model parameter estimates from InSAR data optimisation are similar. The predominantly normal faulting mechanism of two-source models show about  $10^\circ$  left-lateral oblique mechanisms, while the one-source models have about  $10^\circ$  right-lateral oblique mechanisms (Fig. 2.3). This can be explained from a trade-off with depth (Fig. 2.18). Also, the two-sources model ensembles show a slightly steeper dip. These differences are persistent in the total mechanism of the two sources (Fig. 2.3). The two-sources model parameter estimates of the FF optimisations show no significant differences to the one-source model ensembles, except that the parameter uncertainties show an increase (Fig. 2.3).

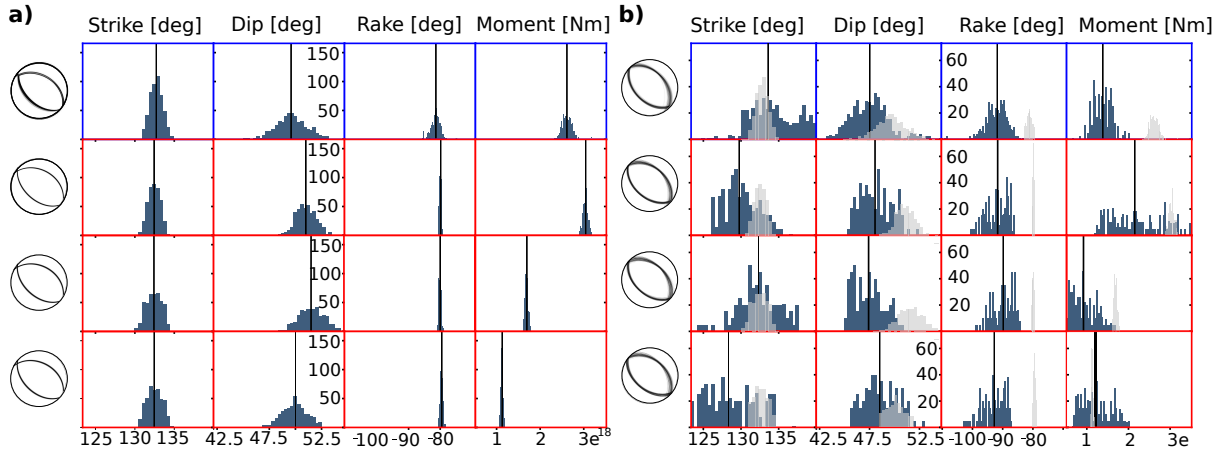


Figure 2.3: 2009 L'Aquila earthquake source results. Histograms of source mechanisms and moments and lower-hemisphere Lambert projection of the corresponding mechanisms ("beachballs") from the 500 noise perturbed static near-field data optimisations (a) and far-field data (FF) optimisations (b), with the y-axis being the model count. Top row: from top to bottom the solution of the one-source model in the second row, the average mechanism the two-sources, from adding the components of the moment tensor components and third and fourth row: the respective two-sources sub-sources mechanisms, respectively. The gray-shaded histograms on the right repeat the near-field histograms shown on the left for a better comparison of near-field and far-field data results.

### 2.5.1.2 The 2016 Amatrice earthquake

The one-source model ensembles of static InSAR data and FF optimisations show a good agreement for the majority of model parameters (Fig. 2.4), only dip and rake show differences of  $8^\circ$  and  $14^\circ$ , respectively. This also might be due to a trade-off between dip and depth (Fig. 2.19). Similar to the estimations for the 2009 L'Aquila earthquake we find that the parameter uncertainties are much smaller when using InSAR data compared to using FF.

Allowing for two sub-sources in the optimisation for both InSAR data and FF results in clearly separated source parameter ensembles for each of the sub-sources (Figs. 2.4 & 2.19). Significantly different mechanisms for the two sub-sources are retrieved. Their strike, dip and rake angles differ by several degrees (Tab. 2.3 & Fig. 2.4)). A larger moment is retrieved for the southern sub-source, consistently for both datasets.

### 2.5.1.3 The 2005 Zhongba earthquake

The one-source model parameter estimates agree well between InSAR data and FF optimisations for the majority of model parameter values (Figs. 2.5 and 2.20, Tab. 2.4). Also, the model parameter resolutions are similar between InSAR data and FF optimisations in this case. A significant difference is shown for the source parameters easting, rake and moment (Fig. 2.20). Notably, using InSAR data, we find a more oblique mechanism with a rake of  $-78^\circ$  compared to the almost pure normal faulting revealed by the FF optimisation (Tab. 2.4).

The individual sub-sources obtained using InSAR data (Fig. 2.5) show slightly different mechanisms compared to the one-source models, while the two sub-sources are very similar to each other. The strike of the southern sub-source is different by a few degrees and it has slightly more oblique mechanism. Using FF waveforms here results in large parameter uncertainties for



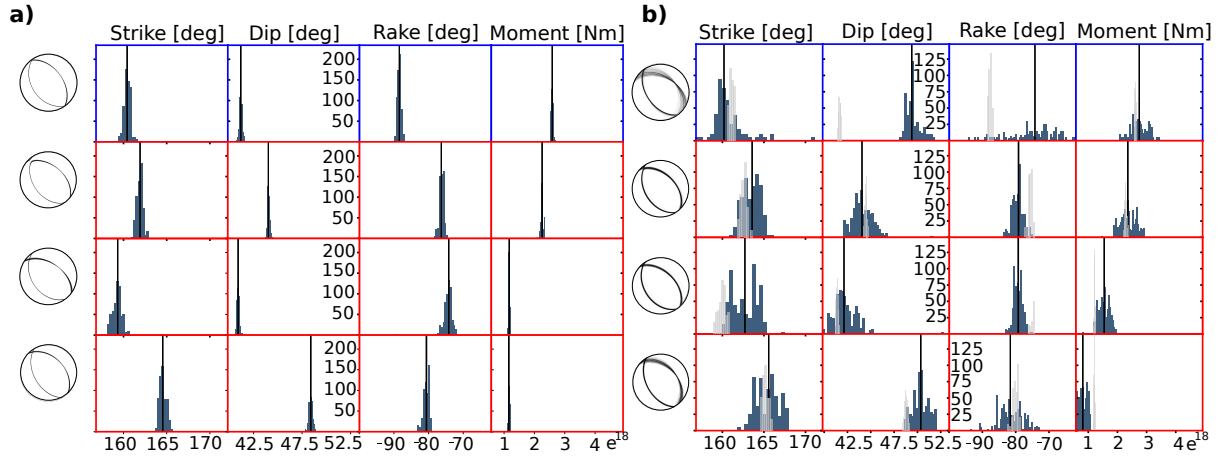


Figure 2.4: 2016 Amatrice earthquake. Uncertainty and distribution of source mechanisms from the InSAR data and FF (left and right panels respectively) optimisation runs. Other figure details as in Figure 2.3.

the two-sources models. Parameter distributions of the individual sub-sources overlap, except for the source position and depth (Tab. 2.4). The total mechanism of the two sub-sources show a significant difference to the one-source model mechanism (Fig. 2.5). Particularly, the dip is more steep and the rake is more oblique by  $10^\circ$  from pure normal for both sub-sources.

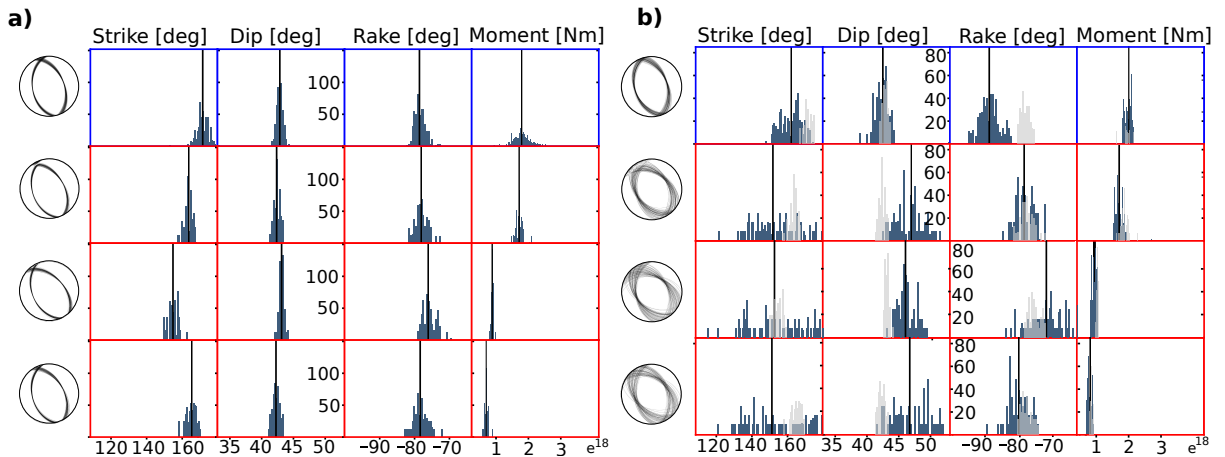


Figure 2.5: 2005 Zhongba earthquake. Uncertainty and distribution of source mechanisms from the InSAR data and FF (left and right panels respectively) optimisation. Other figure details as in Figure 2.3.

#### 2.5.1.4 The 2008 Zhongba earthquake

The one-source parameter estimates based on InSAR data and FF give significantly different mechanisms with several degree differences in strike and dip. The model parameter distributions are of comparable width showing little contrast of model resolution between the InSAR data and FF.

The individual sub-sources of the two-sources model parameter estimates differ significantly from the one-source models and from each other using either dataset (Fig. 2.6, Tab. 2.4 & Fig. 2.21). Interestingly though, the sub-source mechanisms estimates, using InSAR data and FF, agree very well (Fig. 2.6). A comparison of the total mechanisms reveals a rake change of around

Table 2.2: Table of misfits and AIC values for all considered models of all four earthquakes in this study.

Earthquake	2009 L'Aquila		2016 Amatrice		2005 Zhongba		2008 Zhongba	
	best misfit	AIC	best misfit	AIC	best misfit	AIC	best misfit	AIC
static near-field, one source	0.33	81.8	0.295	81.5	0.39	83.3	0.56	84.64
static near-field, two sources	0.32	82.2	0.25	81.17	0.37	83.64	0.4	84.08
far-field, one source	0.43	83.72	0.425	85.00	0.51	84.2	0.49	86.4
far-field, two sources	0.42	86.08	0.405	84.4	0.48	84.6	0.46	85.7

$5^\circ$  for the two-sources models compared to the one-source models and a significantly smaller combined moment. The results of the 2008 Zhongba FF optimisation for both the one-source and two-sources models have high uncertainty of the sources time (several seconds) and position in comparison to the other earthquake cases (Tab. 2.4).

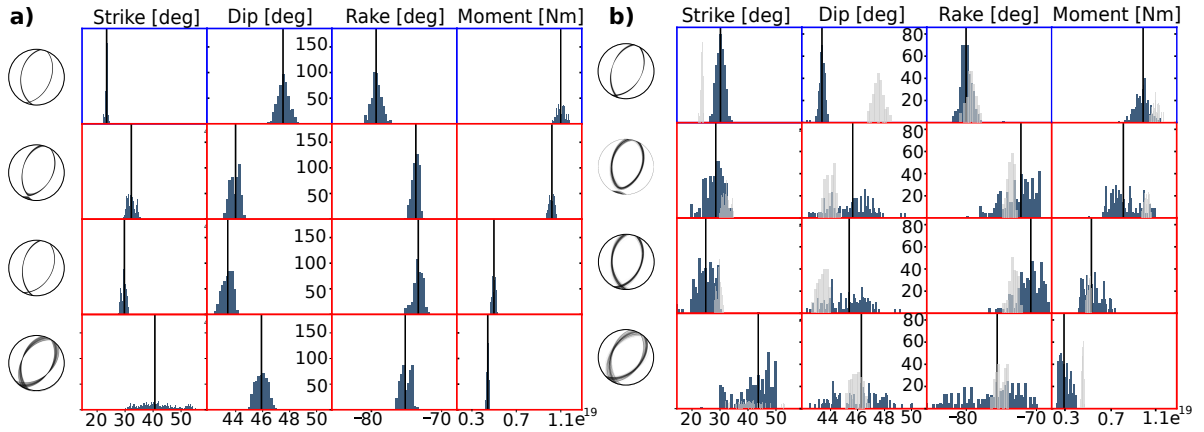


Figure 2.6: 2008 Zhongba earthquake. Uncertainty and distribution of source mechanisms from the InSAR data and FF (left and right panels respectively) optimisation runs. Other figure details as in Figure 2.3.

## 2.5.2 Informational theory results and result significance

From all resulting source models we calculate AIC values with Eq. 2.7, the P-T axis (Fig. 2.22), as well as the slip azimuth (trend of the slip vector) to evaluate the significance of the results (Fig. 2.17, Tab. 2.5) for all one-source models and the total mechanism (moment-weighted average) of the two-sources models.

The calculated AIC values in Tab. 2.2 show that for all four studied earthquakes the InSAR data and FF agree on a preferred degree of model complexity. For the 2009 L'Aquila and the 2005 Zhongba earthquakes a single source model is preferred by the AIC values and for the 2016 Amatrice and the 2008 Zhongba earthquakes a two-sources model.

The P-T axis plots and histograms (Fig 2.22, Fig 2.7, Fig 2.8) show the statistics of the T-axis points of the one-source models with T-axis points of the mean two-sources models and the first and second sub-source of the two-sources models. The impact of modelling with a one- or two-source model can be visually ascertained by the significance of the difference between the T-axis points of two-sources sub-sources (and its mean) to the T-axis points of the one-source model. The most significant difference in T-axis points position is visible for the 2016 Amatrice and 2008 Zhongba earthquakes, especially in the InSAR data.

Yet another characteristic derived from source mechanisms, which relates to the regional tectonics, is the slip vector azimuth (Aki and Richards, 2002, Fig. 4.20), also sometimes called slip vector trend. We provide illustrations for the slip vector azimuth in Figure 2.17. The slip vector azimuth Fig. 2.17 shows comparatively little difference for the 2009 L'Aquila and 2005 Zhongba earthquakes, while for the 2016 Amatrice and the 2008 Zhongba earthquakes a larger difference in the slip vector azimuth is shown between one-source models and the total mechanisms of the two-sources models.

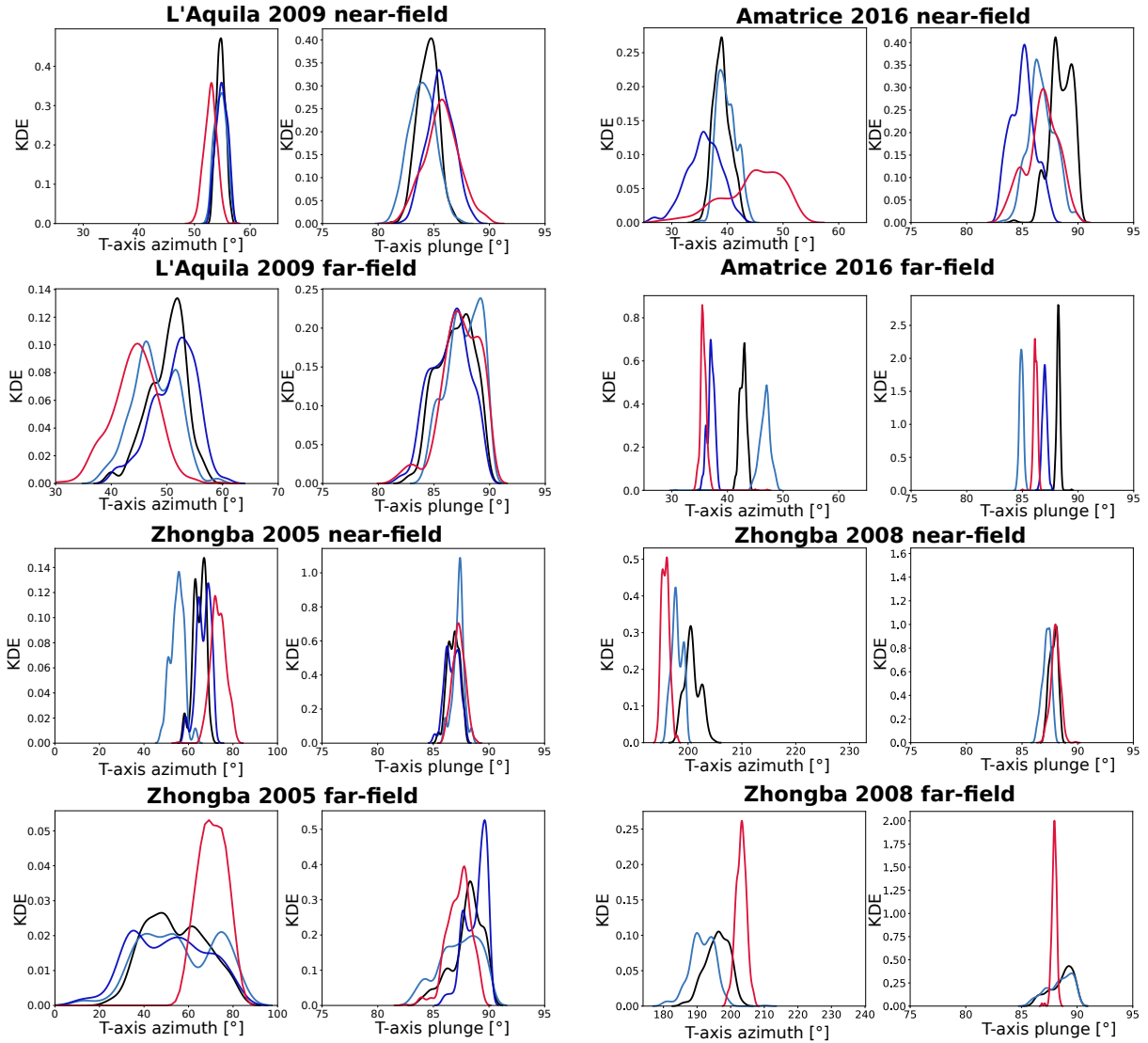


Figure 2.7: Histograms with Gaussian kernel density estimates (kde) of T-axis azimuth and T-axis plunge for InSAR data and FF datasets. The red curves are the kde for the one-source model and the black one the kde for the moment weighted mean of the two-sources. The light blue and dark blue are the kde for each of the two-sources sub-sources.

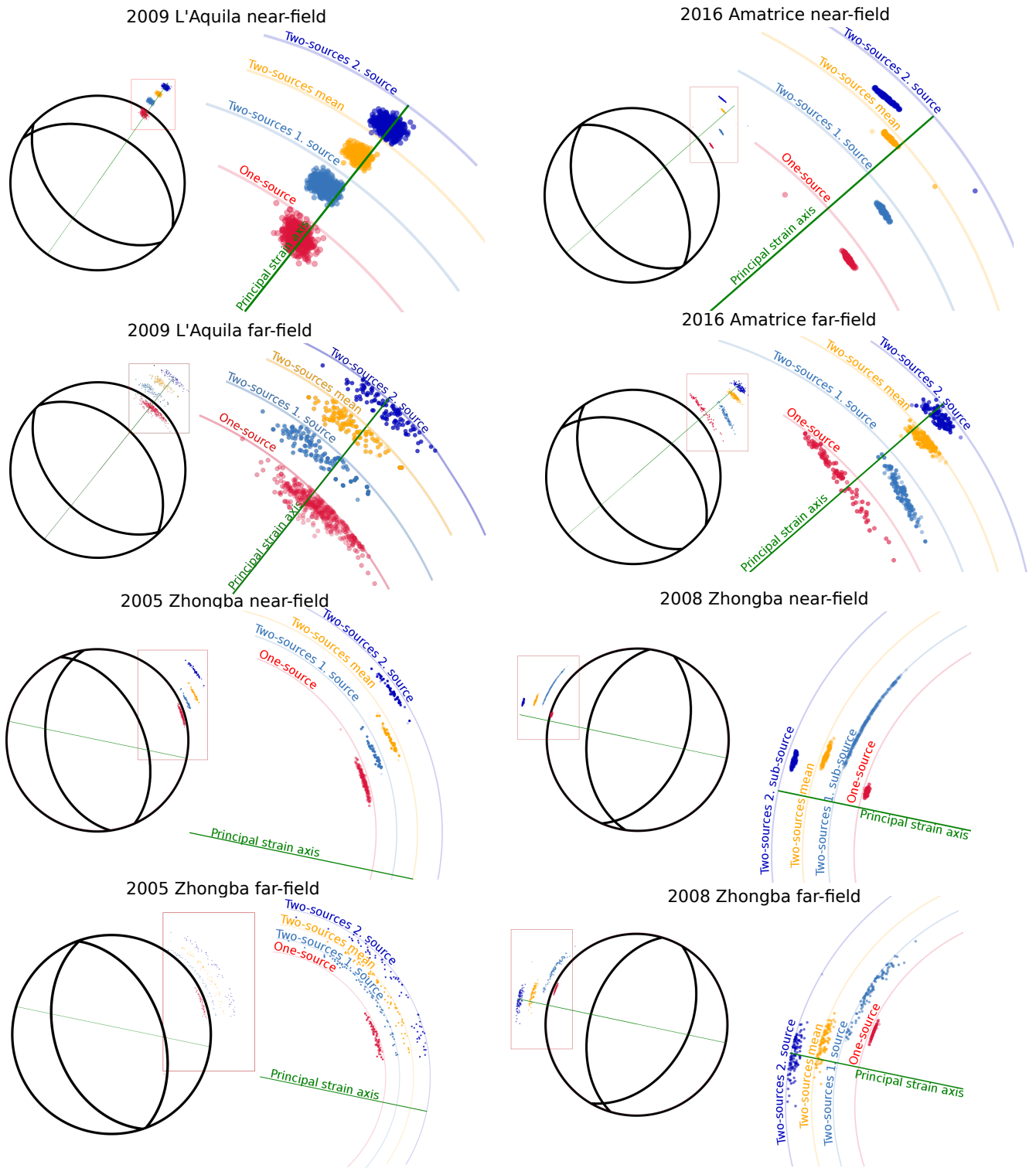


Figure 2.8: Focal sphere diagrams with T-axis piercing points of the models in the result ensemble for each studied earthquake case, together with a zoom in as indicated by the red box. The T-axis piercing points are plotted for one-source models (red), two-sources 1. and 2. source (light and dark blue) and the mean of the two-sources model (yellow), each with a different offset to ease visibility (matching color radii indicate the respective outer circle).

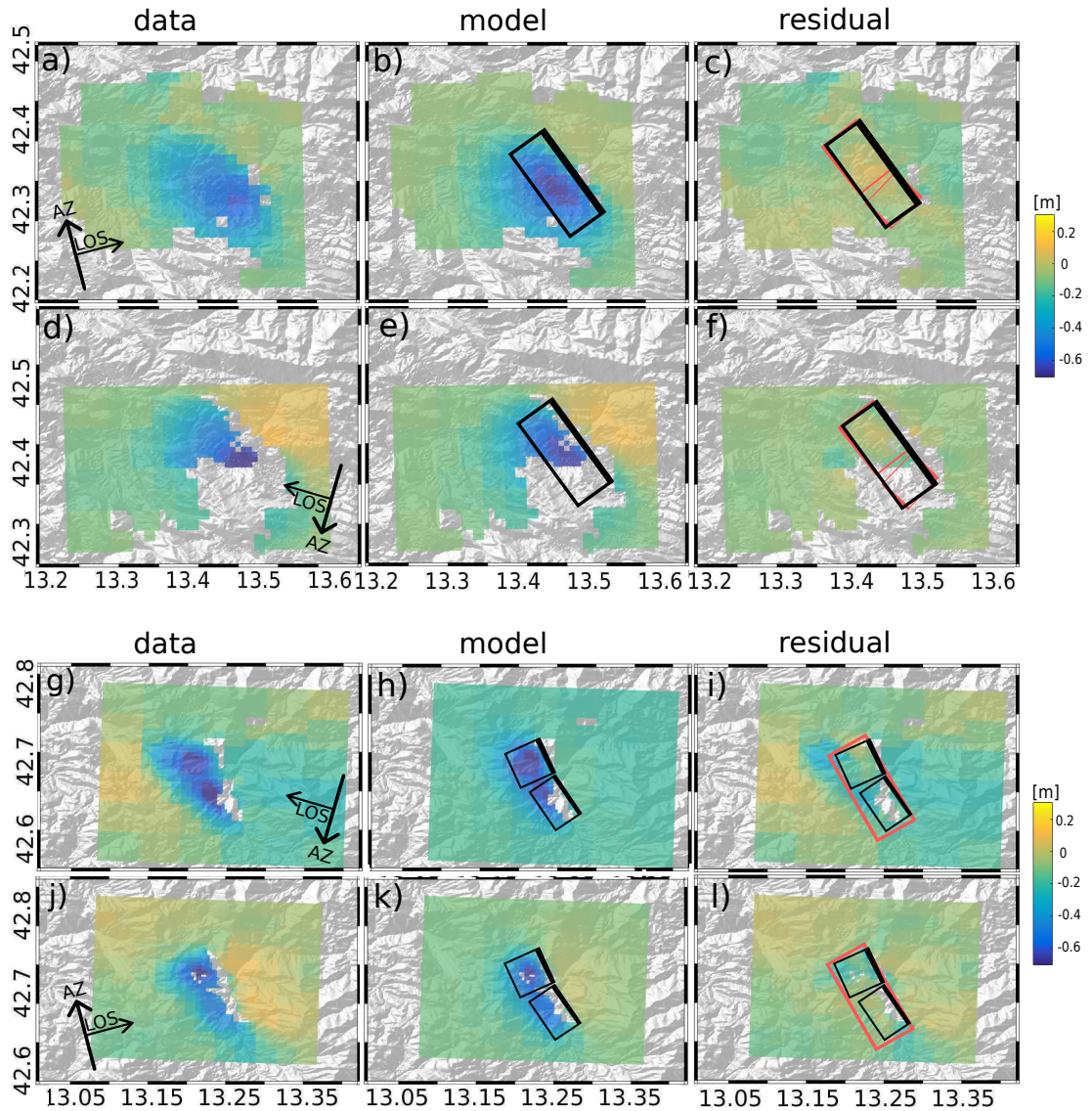


Figure 2.9: InSAR data, model predictions and model residuals for the 2009 L'Aquila earthquake from (a-c) ascending and (d-f) descending tracks, and the 2016 Amatrice earthquake from (g-i) descending and (j-l) ascending tracks. Data and predictions are filtered, unwrapped and quadtree-resampled with orbital ramps removed. Background in all figures is the grey-shaded topography from SRTM. The model predictions and corresponding model residual are the best fitting model with the AIC-preferred model complexity. Color shows the line-of-sight surface displacement. Black rectangles show the surface projection of the source model with thick black line marking the top edge. Red rectangles represent the best fitting source geometry from the not favored source complexity.



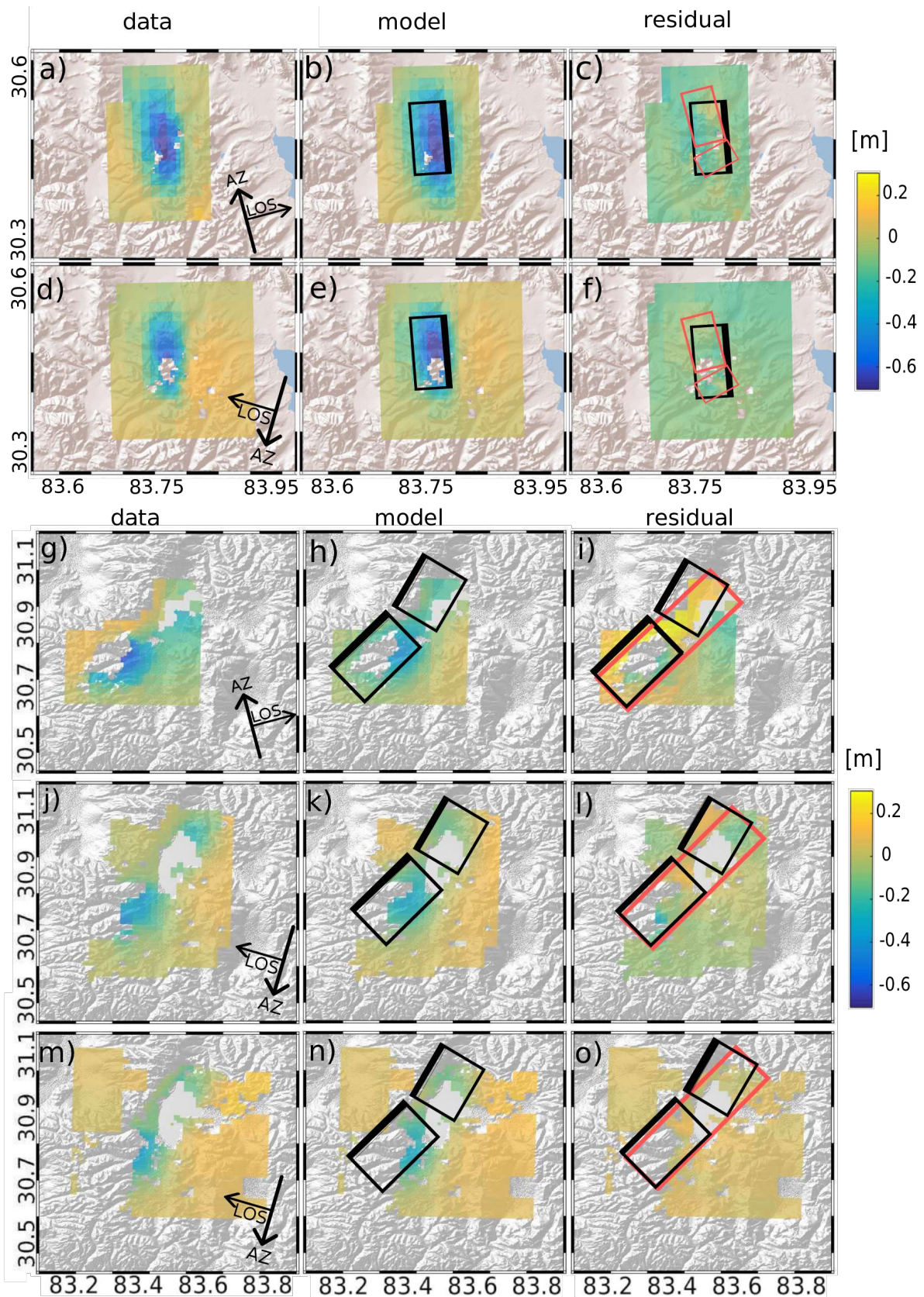


Figure 2.10: InSAR data, model predictions and model residuals for the 2005 Zhongba earthquake from (a-c) ascending and (d-f) descending tracks, and the 2008 Zhongba earthquake from (g-i) ascending and (j-l) and (m-o) two descending tracks. Other notations as in 2.9.

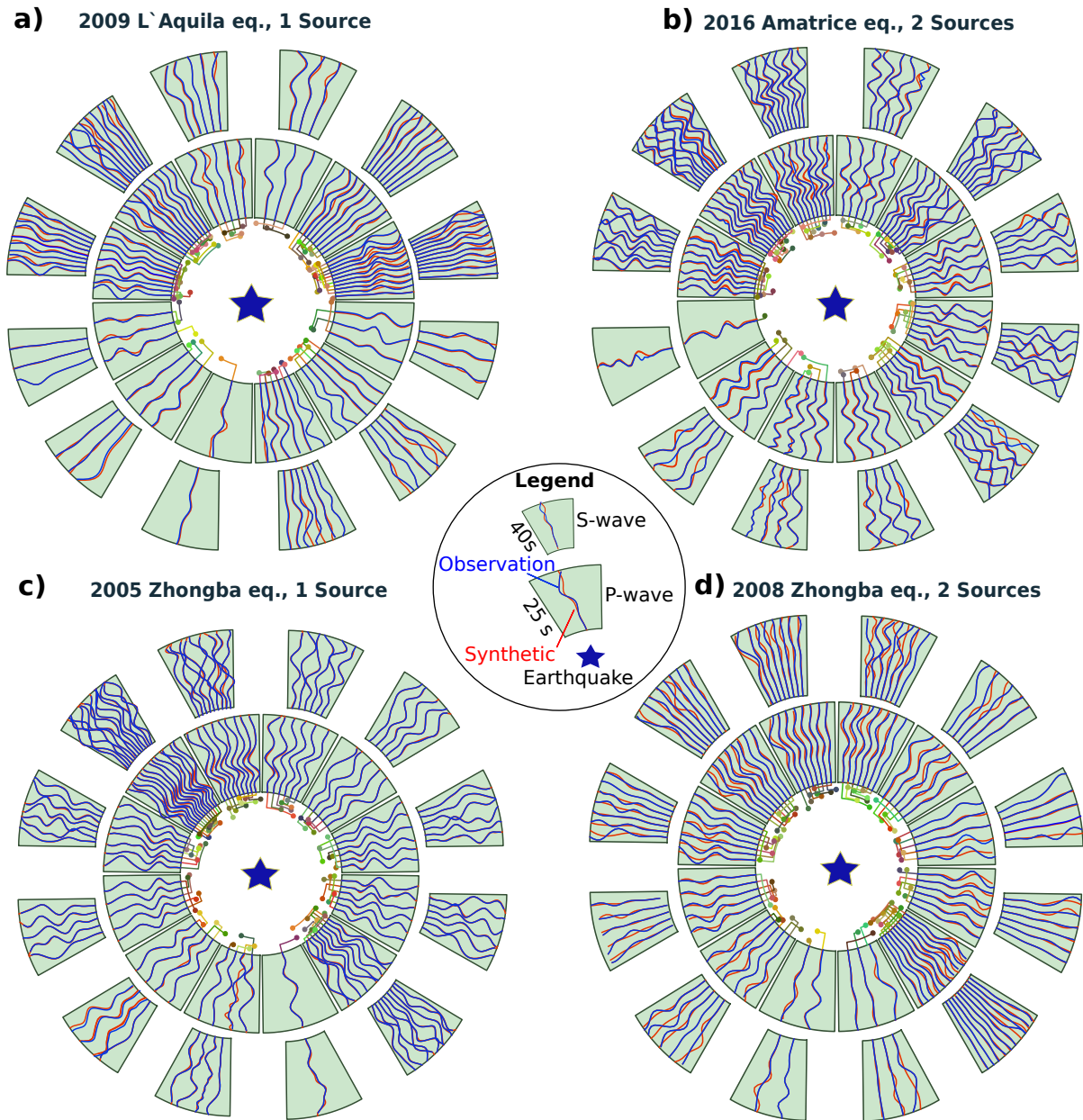


Figure 2.11: Seismological waveform data and modelling results for a) 2009 L'Aquila, b) 2016 Amatrice, c) 2005 Zhongba, and d) 2008 Zhongba earthquakes. The center star marks the earthquake location and the surrounding colored points show the azimuthal position and relative distance of the seismological stations. Each station dot connects to one trace pair (blue: tapered, filtered observed waveforms, red: tapered, filtered synthetic waveforms), which are ordered in 12 30-degree azimuth blocks. The traces in each azimuth block are sorted by earthquake-to-station distance (clock-wise descending). The inner trace blocks show the P phases and the outer trace blocks the S phases.



## 2.6 Discussion

### 2.6.1 Impact of modelling setup

The setup of the earthquake source modelling influences the source model parameter results and associated uncertainty estimates (Weston et al., 2012; Duputel et al., 2012c; Beresnev, 2003; Ragon et al., 2018a). We discuss here the potential influences of the medium model choices in this study with assumptions like neglecting topography and 3D Earth structure, the particular noise selection, the data weighting scheme, the kinematic source and the limits of realized complexity.

For the forward modelling of the InSAR data, a model bias can have been introduced by the use of an homogeneous elastic half-space, chosen because it kept the computational costs reasonable compared to using a layered medium. Such a simplified medium model leads to a systematic underestimation of source depth (Weston et al., 2012), because a more realistic layered model is at shallower depth weaker and at larger depth stronger than the halfspace of averaged elastic properties. Therefore, a deformation source of a given moment, embedded in an elastic halfspace, has to be shallower compared to a source in a layered model to produce the same amount of deformation at the surface. We expect this effect to be small in our study and, more importantly, to be of little influence on the complexity analysis.

Neglecting effects of topography and 3D Earth structure may add to potential mismodelling. For the FF optimisations, mislocation and other mismodelling caused by neglecting 3D Earth structure (Hartzell et al., 2007; Gallovič et al., 2015) is not considered, unlike proposed by (Duputel et al., 2012c). However the mislocation error in our study is within 21 km (maximum value), demonstrated with InSAR data (Tab. 2.3 and Tab. 2.4. Unmodelled 3D Earth structure can result in biases in the inferred source mechanism (Ferreira et al., 2011). We allow for individual shifting of the predicted waveforms in time, which compensates for the errors in modelled traveltimes that stem from the use of a 1D medium model. For the two-source models we enforce a minimum separation of the sub-sources in space and time (see respective method sections), which leads to an enforced separation of the corresponding northing, easting and time parameters.

For the data error propagation in the FF optimisations we use real station noise (Section 2.3.2), with noise samples taken from before the P-phase onset. While this approach should provide a valid estimate of the noise affecting the P phase measurements, it likely underestimates the noise affecting the S-phase. In scattering media the P-wave produces a coda that is neglected (Stähler and Sigloch, 2016).

### 2.6.2 Theoretical limitations on source complexity resolution

For static InSAR data modelling (Atzori and Antonioli, 2011) have shown that the spatial resolution to small-scale slip features depends mostly on the distance of the observations to the source and the signal strength compared to the data error variance and covariance and can therefore vary for different parts of the model. With surface displacement data, shallow and horizontally separated sources can be identified with relatively high resolution. Down-dip segmentation and segmentation of relatively deep sources are harder to resolve because the signal strength of the observed displacement decreases inversely to the squared distance between source and observation.

In FF optimisations, limits in resolving the source location strongly influences the limits in resolving rupture segmentation. Here, the uncertainties in the location of earthquakes are



typically tens of kilometers (Sweeney, 1998; Bondár et al., 2004) and they arise from errors in the velocity model and very often imperfect station distribution. Such uncertainties are considerable when we endeavor to resolve segmentation for rupture dimensions, which are of similar spatial scale. On the other hand, intra-source relative location uncertainty may be lower than typically reported absolute location uncertainties.

Also the sampling rate and filter settings put some theoretical limits on the resolution of sub-sources in space and time for the FF (see Section 2.3.2). A bias might be introduced by the assumption of the corner frequency to be at roughly 0.1 Hz in the studied cases to design the filter. The corner frequency is not known a priori. The resolution limit for several sources of roughly equal moment share will depend on the mixture of spatial separation and centroid time differences.

To test our sensitivity in distinguishing the number of sub-sources given different spatial and temporal separations of sources with equal moment share, we carried out AIC recovery tests (Fig. 2.2). For the FF dataset the tests show that a larger time difference between the two sub-sources allows for better recovery of the correct source model complexity, even for closely spaced sources. We also found for the FF dataset that the distances between sources should be at least more than one and half P-wave wavelengths and additionally also separated in time, to reliably recover the sources as distinct features.

### 2.6.3 Model inferences towards source complexity resolution

To evaluate our model solutions with respect to source complexity of first-order unsegmented or segmented ruptures, we use the strictly quantitative AIC and additionally consider more physical aspects of the segmented rupture mechanisms. These physical aspects include similarities and differences of estimated segment mechanisms and model parameter stability comparing unsegmented and segmented models. The use of earthquake pairs is not required by the introduced method to study earthquake complexity but allows us to evaluate the inferred results within a comparable tectonic regime and a comparable data framework for this sensitivity study. Under these conditions systematic errors in the pair results are similar and become negligible in comparisons between the events of the pair.

We find that in all our study cases the AIC values are in agreement between InSAR data and FF (in the used frequency band). Based on the AIC values, the 2009 L'Aquila and 2005 Zhongba earthquakes appear to be sufficiently described with a single-segment source, while the 2016 Amatrice and 2008 Zhongba earthquakes appear to be significantly better represented with two rupture segments. The percentage of the DC component and in turn the non-DC component indicated by the solutions of the USGS (Tab 2.1) do not agree with the rupture segmentation inferred in our study. For example the 2016 Amatrice earthquake is given rather high DC component percentage (98% from body waves and 86% from W-phase) but our results strongly suggest rupture segmentation. For the 2009 L'Aquila earthquake the reported DC component percentage heavily depends on the considered solution (31% from body-waves and 64% from W-phase) but our results do not support rupture segmentation. We are therefore, at least for our studied cases, critical of the non-DC component percentage as indicator of rupture segmentation as it also describes structural complexities. This might need further studies with well constrained non DC results to compare to other cases.

Our result of a single-segment rupture during the 2009 L'Aquila earthquake is consistent with previous findings reported in the literature (e. g. (Walters et al., 2009) and (Atzori et al., 2009)). It is also consistent with heterogeneous slip models reported by (Pino and Di Luccio, 2009) and (Cirella et al., 2012) from inferences by using strong motion data that show secondary slip patches on the order of 2 km to 3 km in length and width on a single fault plane. From InSAR

data inversion results alone, (Cirella et al., 2012) use a single-segment rupture model as well. Apart from the AIC values, we find for the 2009 L’Aquila earthquake that the resulting source mechanisms are basically the same for a single segment and two segments, for both the InSAR data and FF optimisations. This means that also enforcing two segments results in consistent estimates of the mechanism. Additionally the model parameter uncertainties do not increase strongly for a doubled degree of freedom. This suggests that with the data used a first-order source segmentation would have been resolved.

The results for the 2016 Amatrice earthquake support resolution on first-order rupture segmentation as we suggest for 2009 L’Aquila earthquake. For the 2016 Amatrice earthquake not only the AIC values clearly support a rupture segmentation, also the mechanisms between two segments differ from a single-segment model. The increased degree of freedom helps to significantly better explain the observations. The stable and partly improved parameter estimates (lower uncertainties, Fig. 2.19) show that the better data-model misfits are not related to less stable parameter estimates. Especially the rake estimate improved. Also previous investigations suggest complex faulting for this earthquake. (Lavecchia et al., 2016) found very similar differences in the mechanisms between unsegmented and segmented rupture models with their InSAR data optimisations. By using strong-motion, near-field seismic waveforms (Tinti et al., 2016) inferred two high-slip patches on the Amatrice fault with around 7 and 10 km length, and their centroids being about 6 km apart. Their results are in good agreement with our findings for the two sub-sources with lengths of 10 and 6 km, being 6 km apart.

However, the resulting mean mechanism of assumed unsegmented rupture differs from the mechanisms of two rupture segments for both InSAR data and FF optimisations, and in a consistent way (Fig. 2.6). Both show similar strike and rake values for the segmented model, even though the parameter uncertainties increase with respect to the unsegmented models (Fig. 2.6). We find that using FF in the frequency band applied the timing uncertainties are quite large for this earthquake, while we reach small uncertainties for the segment location. The segmented rupture on the other hand shows better convergence for the rupture timing and decreased resolution on the location of each segment (Tab. 2.4).

The segmented rupture models improve fit and resolution for the 2016 Amatrice and the 2008 Zhongba earthquakes. For both, we find different mechanisms compared to their unsegmented rupture models. This is the case for the individual segments as well as their overall mechanism. So if the data sensitivity is sufficient to resolve rupture segmentation, an unsegmented model loses its ability to well represent the process and neglecting complexity biases the model estimates. For our study we visualize the differences in mechanisms with plots of the T-axis piercing points for all tested source models (Fig 2.22).

To assess if consideration of a two-sources model adds new and robust information over using a simple one-source model, we calculate the angle of rotation distance  $\omega$  in Fig. 2.12, which is a measure of difference between two moment tensor radiation patterns (Tape and Tape, 2012). We use the cosine-based formalism proposed in (Tape and Tape, 2012) resulting in distance range values between 0 and 1, which correspond to no difference and an opposite polarity. We calculate this so-called  $\omega$  angle for the models within an optimisation ensemble, to reflect the uncertainty in the modelled mechanisms for all our case studies. We then compare them to the  $\omega$  angles between one-source models and the two-subsources of two-source models. We find that for both the 2016 Amatrice and the 2008 Zhongba earthquakes the rotation distances between one-source models and the subsources are significantly larger than the rotation distances in the model ensembles uncertainties. This means that we resolve the differences in the corresponding radiation patterns of two subsources. Another common measure of the geometrical difference of source mechanisms is the Kagan angle (Kagan, 1991). It is the three-dimensional angular difference in mechanism rotation and useful in the geological interpretation of the difference of

two source mechanisms.

We calculate the Kagan angles for the models within optimisation ensembles and between model ensembles with different model complexity (Fig. 2.13). We find the Kagan angles show the same pattern than  $\omega$  angles. The Kagan angles between unsegmented and segmented model mechanisms are large and significant for the 2016 Amatrice and the 2008 Zhongba earthquakes ( $\geq 10^\circ$ ). Also the 2005 Zhongba earthquake shows large Kagan angle values. However the increased model complexity for this event does not result in significantly improved data fit and the model resolution decreases for increasing source complexity. This is reflected, for example, in a higher uncertainty of the Kagan angle measures (Fig. 2.12). For the 2009 L'Aquila earthquake the mechanisms do not show significant rotation distances between for the tested models. According to (Martinez-Garzón et al., 2016) mechanism changes with Kagan angles larger than  $20^\circ$  are considered to lead to significant errors in stress inversions. They also state that uncertainties in the focal mechanism will propagate down to the uncertainty of the inverted stress field.

It follows that accounting for rupture segmentation, whenever possible, improves all calculations and interpretations based on source mechanisms. This is supported by findings and recent method developments of multiple fault segment inversion methods of (Shimizu et al., 2019) and (Frietsch et al., 2019a). We propose that, additionally to taking into account the geometrical uncertainty of a single source plane (as done in (Ragon et al., 2018a)), also source model complexity should be considered in rigorous uncertainty estimations in kinematic source inversions, even for smaller earthquakes. The significance of using multiple point sources for smaller earthquakes was also demonstrated for the  $M_w$ 6.2 Kumamoto earthquake by (Shi et al., 2018). Here, for strong-motion data inversions, the inferred mechanisms of several point sources could significantly better outline the rupture geometry compared to a single source. (Frietsch et al., 2019a), found in the synthetic test of their developed multiple fault segment inversion method also that local strong-motion data was important in recovering the correct geometry.

In the analyses of our case studies, both InSAR data and FF have been sensitive to rupture segmentation. In joint source optimisations using these data sets we expect that the sensitivity for rupture segmentation further increases, because generally for the combined use of independent data sets, the constraints for the source model parameters improves (Funning et al., 2014; Frietsch et al., 2019a). In our case studies in particular, a such increased sensitivity for rupture segmentation could help to improve the estimated segmentation for the 2005 Zhongba earthquake. Further, we expect that the number of source segments that can be well constrained generally increases in joint optimisations.

We draw some conclusions based on the AIC and synthetic tests we have conducted. These conclusions are limited to the framework of the study, which mainly means to tectonic regimes with normal faulting earthquakes and horizontal segmentation. Segmentation is insignificant for the data we tested, when for similar mechanisms and geometries the horizontal separation is less than 2 km. If segments have different mechanisms, geometries, and/or depths, the sensitivity for segmentation may increase and also smaller separations than 2 km may suffice. For the far-field data the time and spatial distance between sources is important for the resolution of rupture segmentation. Our synthetic tests, using the AIC, suggest that a minimum separation distance of 3 km between point sources with a 4 s time delay are separated significantly to warrant a robust modelling with two point sources. With a time separation of only 2 s the minimum spatial distance for robust modelling increases to more than 7 km between sources. This is supported by our real data cases. For the 2009 L'Aquila earthquake by using InSAR data we may resolve smaller features than a single uniform slip rupture plane. However, already the use of a second model adds more parameters (and therefore also tradeoffs) than is justified given the decrease in data misfit. The estimated separation of the two rupture plane edges is less than 500 m and they have very similar estimated mechanisms. This means the two-sources model is

essentially identical to the single source. Similarly, based on far-field data, the optimisations do not resolve a meaningful second source for the 2009 L'Aquila earthquake with both estimated point sources being very close together in space and time with only 4 km and 1-3 s separations. For the 2016 Amatrice earthquake the estimated two point sources are separated by 8 km and 3 s, with significantly lowered AIC values. So possibly, the results of these two earthquakes enclose the lower bound for time and space separation for the far-field data to resolve rupture segmentation. However in this study we do not cover the resolution of rupture segmentation with other earthquake mechanisms, which we expect to be different. From the limited number of cases in our study it is not possible to draw a minimum temporal and spatial distance function for rupture segments to be resolved. Finding such a relationship requires a far more general approach with many different scenarios for source and data coverage. Our results imply that the appropriate degree of the modelled source complexity should be considered as an additional part of the individual source modelling problem. We demonstrate that the combination of source inferences based on static InSAR data and FF using the AIC and mechanism rotational distances delivers robust information to decide on which degree of model complexity a source optimisation is meaningful. If no additional information on the source mechanism beyond the inherent uncertainties can be obtained, we argue that a simpler model should be used.

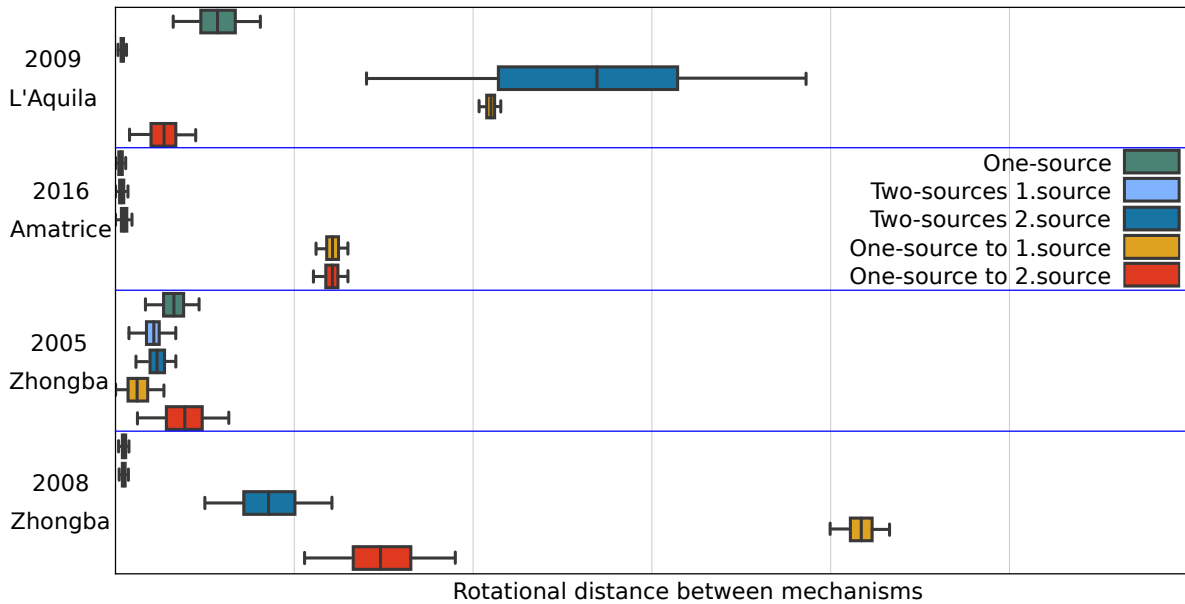
## 2.7 Conclusions

We conclude that a data-driven decision of the adequate model complexity to describe the source process is enabled by today's globally available ground displacement observations in form of near-field (InSAR) and to a lesser degree far-field (teleseismic waveforms) for the studied medium-magnitude earthquakes (Mw 6-7). For three of the four considered case studies, the L'Aquila 2009, the Amatrice 2016 and the Zhongba 2008 earthquakes, we found that the static near-field data outperformed the far-field data in resolving whether a one-source or a two-source model is the appropriate description of the the earthquake source with high confidence. The inferred source model complexities from near-field and far-field data in the used frequency band are consistent. For three of the four considered case studies, the L'Aquila 2009, the Amatrice 2016 and the Zhongba 2008 earthquakes, we found that the near-field data outperformed the far-field data in resolving earthquake source segmentation with high confidence. Reduced near-field data coverage e. g. due to strong correlation, can affect the resolution strongly, as we demonstrate for the Zhongba 2005 earthquake. In this case the far-field data analysis provided better constraints. Such effects can also be expected for deeper sources than the ones studied here.

We find that consideration and combination of near- and far-field data can be helpful in assessing rupture segmentation as the resolving power for both datasets can vary depending on the data quality in some settings. Consideration of both datasets also gives additional justification to the modelling of an earthquake with several sources to actually represent a physically meaningful state of rupture segmentation. This strongly suggests the resolution of rupture segmentation benefits from joint data modelling approaches that combine the spatial and temporal constraints given by the near-field and far-field datasets, respectively. The static-near field surface deformation data are potentially capable of resolving higher degrees of source complexities than studied here. We note that this is complicated by the question of how well shallow expressions of geometrical complexity track down to depth and can not be answered in the scope of this study.

From our results we conclude that AIC in combination with an analysis of source model parameter uncertainties and significance is a data-driven and objective way to estimate the degree of source model complexity. It is useful for finding a minimum bias source model parametrization for far- and near-field observations. A practical approach to consider source complexity in source modelling is the following. At least two non-linear, Bayesian optimisations need to be conducted

**A) near-field data**



**B) Far-field data**

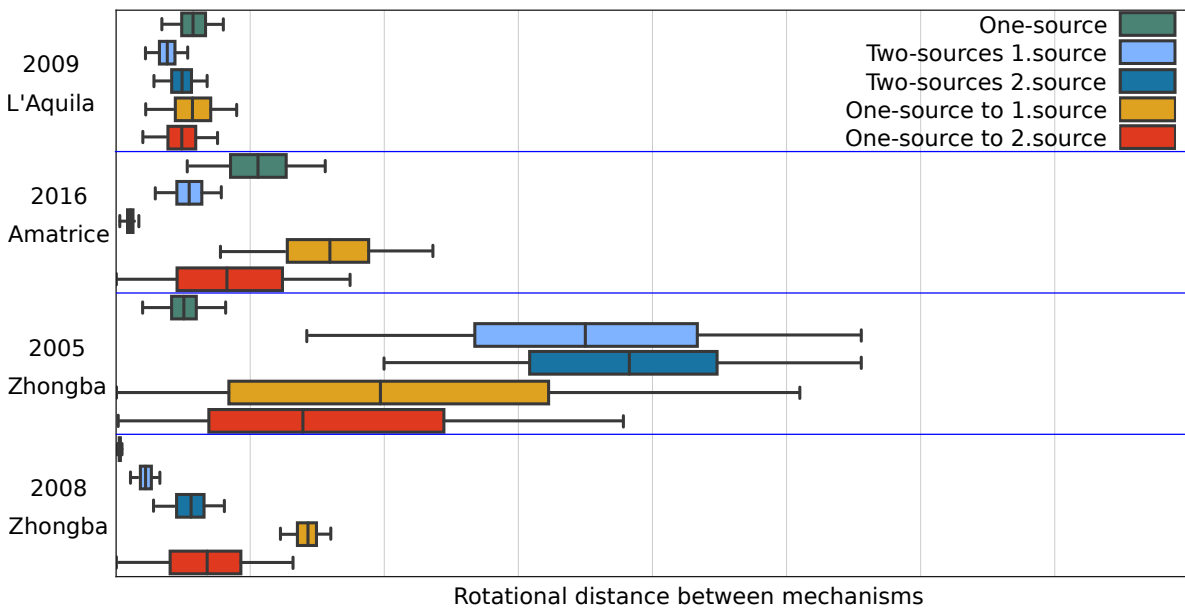
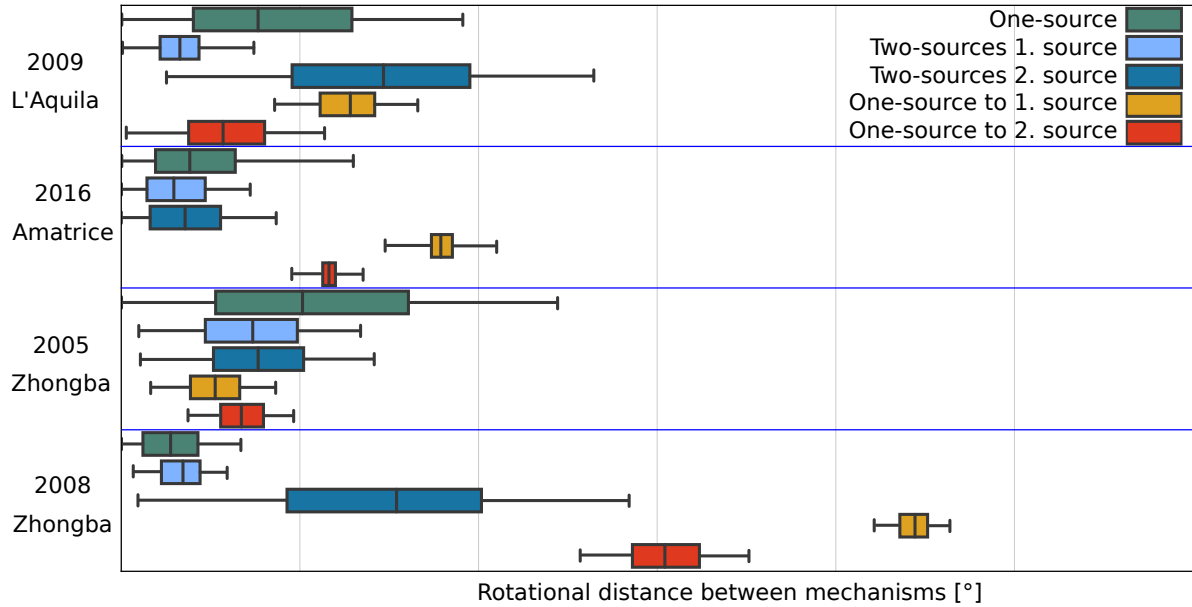


Figure 2.12:  $\omega$  angle distances (Tape and Tape, 2012) for each studied earthquake model ensembles for each considered source model (green one-source, yellow two-sources 1. source, blue two-sources 2. source) and for between one-sources models and the two-sources subsources models (orange and red). Top figure a) for the far-field data and bottom figure b) for the near-field data. For the calculation we use the cosine based formalism proposed in (Tape and Tape, 2012) resulting in distance range values between 0 (no difference) and 1 (maximum difference, which is the case for the same but polarity switched radiation pattern).

**A) near-field data**



**B) Far-field data**

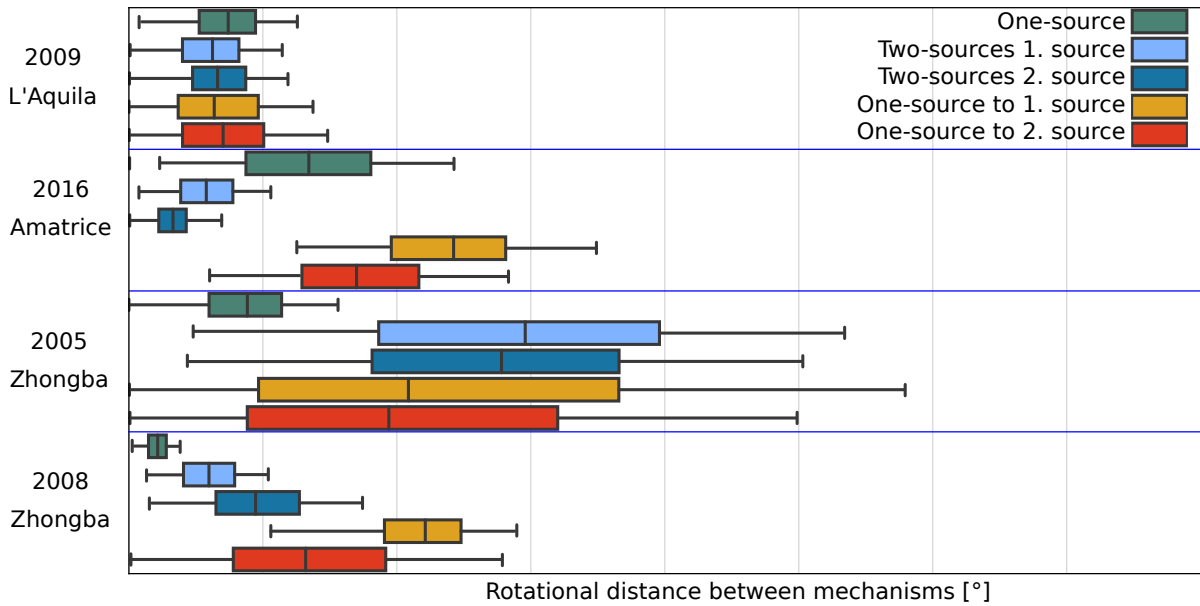


Figure 2.13: Kagan angle distances (Kagan, 1991) for each studied earthquake model ensembles for each considered source model (green one-source, yellow two-sources 1. source, blue two-sources 2. source) and for between one-sources models and the two-sources subsources models (orange and red). Top figure a) for the far-field data and bottom figure b) for the near-field data. Values range from 0° (no distance) to 90° (maximum distance).

with two different source segmentations, e. g. as demonstrated here with a single source and a two-sources model. Of course, depending on the individual case, a larger number,  $n > 1$ , of subsources can be tested against a model with  $n+1$  subsources. Then, first, the data fit is evaluated with the AIC. The model complexity corresponding to the clearly lower AIC points out the more appropriate model complexity of the two. If the AIC difference is not conclusive, the two model ensembles are evaluated regarding their significance by testing the modelled source differences, differences in mechanisms by using rotation angles and/or subsources distances in space and/or time. The more significant result is chosen or if there is no significant difference the less complex model. If results based on the more complex source model show a very clear improvement, with clearly lower AIC values and significant model differences, testing the next level of complexity with yet another subsurface added can be considered. Such a strategy can be useful and may become important to include source complexity in an operational environment. Furthermore with this strategy source model complexity can be considered as part of the model uncertainties in future inferences.

In our studied cases the inferred overall source mechanism of the sources changes significantly, depending on the chosen model complexity. This implies that under- but also over-estimation of the sources geometrical complexity can produce a bias on the inferred source mechanisms. Our results also show that the difference between the two sub-source mechanisms geometry of the two-sources models is significant, especially for the Amatrice 2016 and Zhongba 2008 earthquakes. This localized difference of source mechanisms is potentially of interest for seismic hazard assessments. Also local stress studies might be impacted when considering, or not considering, source complexity of first order, as the inferred stress fields for the source segments will be different. Taking into account the potential first order source complexity of medium magnitude earthquakes can significantly change the inferred source mechanisms. The potential for better resolved source mechanism analysis for earthquakes of this magnitude range exist today by combining near- and far-field data and should be exploited in further studies.

## 2.8 Acknowledgements

A.S. and H.S. acknowledge funding by the German Research Foundation DFG through an Emmy-Noether Young-Researcher-Grant.

We thank the reviewers Théa Ragon and Gareth Funning and as well the editor Carl Tape for thoughtful comments which helped greatly to improve the quality of this manuscript. This study contains modified Copernicus Sentinel data (2016) for Sentinel data. The Envisat SAR data for this study have been kindly provided by ESA through the SOAR-EU2 program, project 16736. The facilities of IRIS Data Services, and specifically the IRIS Data Management Center, were used for access to waveforms, related metadata, and/or derived products used in this study. IRIS Data Services are funded through the Seismological Facilities for the Advancement of Geoscience and EarthScope (SAGE) Proposal of the National Science Foundation under Cooperative Agreement EAR-1261681.

## 2.9 Appendix

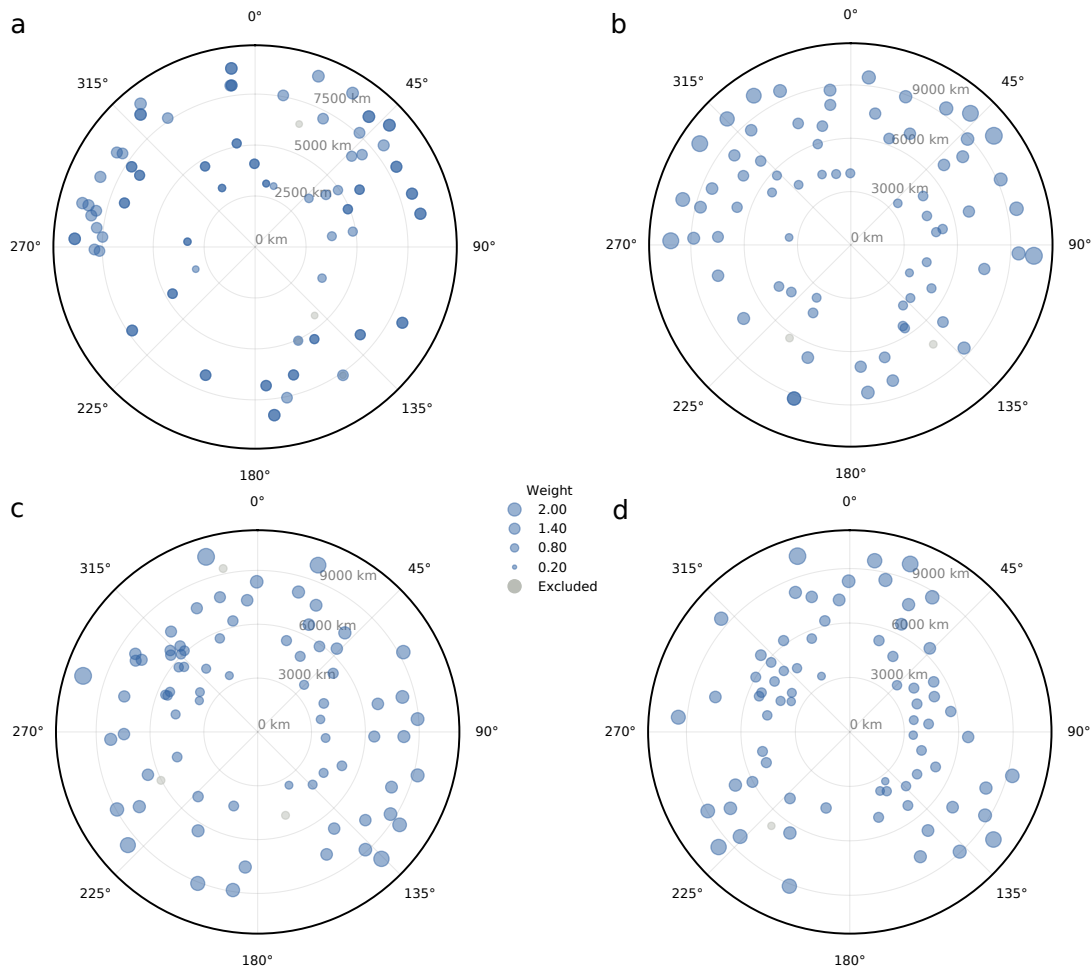


Figure 2.14: Balancing weights of the far-field stations as calculated in eq. 2.4 for a) the L'Aquila earthquake, b) the Amatrice earthquake, c) the Zhongba 2005 earthquake and in d) the Zhongba 2008 earthquake. Markers are scaled according to the weighting factor of the corresponding station's contribution in the misfit function with the center of the circle being the origin of the earthquake.



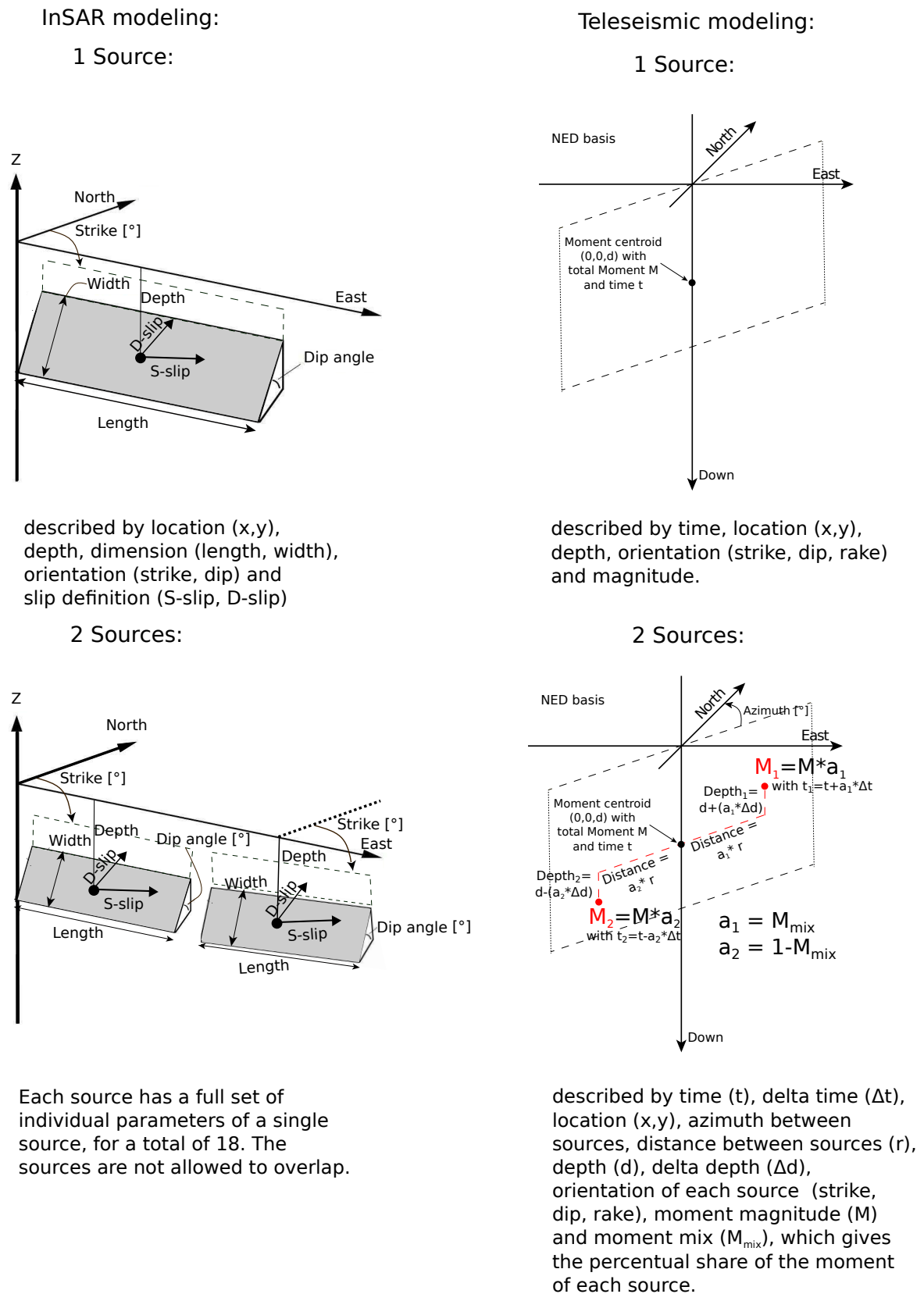


Figure 2.15: Sketch of the setup of the different forward models for InSAR (near-field) and teleseismic (far-field) modelling.

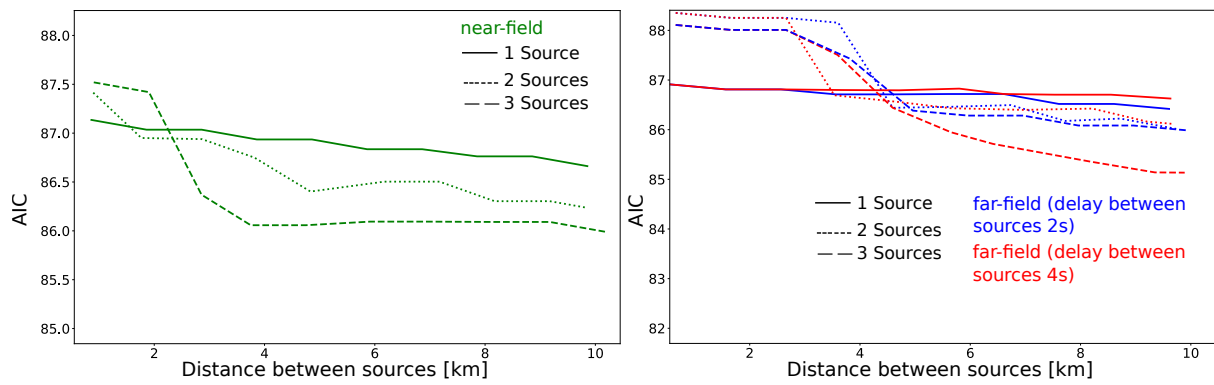


Figure 2.16: Results of the synthetic test for retrieval of complexity from noise perturbed inversions for one, two and three sources. The true forward input model was three sources. The forward modelling was repeated for distances between the sources of 0-10 km and AIC value for A) static near-field and B) in blue for the far-field with a 2s delay between sources, and in red for a delay of 4s. The solid line is one source, dashed line for two and double dashed line for three sources.



Table 2.4: The estimated source model parameters of the Tibetan earthquakes with median values and  $2\sigma$  uncertainty. Derived parameters are marked italic and fixed parameters are shown in bold. Listed for comparison are the preferred model parameters for the static near-field by Elliott et al., 2010 and for the far-field from GCMT. For each earthquake the static near-field (dislocation for a rectangular dislocation source) and far-field (DC for Double-Couple) source parameter estimates are given for one and two sources.

Event	North (km)	East (km)	Depth (km)	Strike (deg)	Dip (deg)	Rake (deg)	Timeshift (s)	$\delta$ time (s)	Length (km)	Width (km)	S-Slip (m)	D-Slip (m)	$M_0$ (N)	
<b>2005 Zhongba</b>	single DC	median	770.4	162.15	42.5	-88.7	0.6						1.9E+018	
		$2\sigma$	3.0	1.4	11.4	2.3	5.7	0.01						5.6E+017
	two DCs	median 1st	3376.2	773.2	6.8	152.2	45.9	0.3	4.1					1.03E+018
		median 2nd	2.59	2.7	3.0	33.0	5.6	0.9	8.1					3.1E+017
	single dislocation	median	3373.4	773.1	7.9	151.4	46.7	4.3	4.1					7.14E+017
		$2\sigma$	2.37	11.5	3.1	32.1	2.8	0.9	8.1					3.4E+017
two dislocations	single dislocation	median	3376.4	773.3	5.6	171.5	42.8	0.9	15.6	5	0.14	0.6	1.73E+018	
		$2\sigma$	1.7	1.3	0.9	6.3	0.9	3.1	2.1	1.3	0.01	0.16	1.16E+018	
	two dislocations	median 1st	3377.6	770.7	5.3	154.8	43.1	-76.0	10.1	4.6	0.13	0.53	9.2E+017	
		median 2nd	0.9	1.1	0.7	5.4	0.7	3.8	0.9	1.5	0.02	0.13	1.9E+017	
	GCMT	median	3373.1	775.6	5.2	165.3	42.2	-78.3	6.3	6.6	0.1	0.51	7.6E+017	
		$2\sigma$	0.86	2.1	0.6	5.5	1.2	4.2	0.9	1.6	0.02	0.1	3.7E+017	
Elliott et al., 2010	3347.4	761.7	12	171	43	-89						3.00E+18		
Elliott et al., 2010	3375.3	769.76	5	174	40	-68		15	5		total slip: 0.7	2.8E+18		
<b>2008 Zhongba</b>	single DC	median	3421.5	744.4	12.7	30.2	43.4	-80.0					9.95E+018	
		$2\sigma$	1.85	1.6	1.8	2.9	0.4	1.5	4.5				1.21E+018	
	two DCs	median 1st	3443.7	744.9	10.6	24.8	45.4	-70.8	5.7				5.31E+018	
		median 2nd	3426.1	738.0	8.0	43.7	46.2	-75.6	1.9				1.6E+018	
	single dislocation	median	3427.7	743.1	7.8	23.4	47.5	-79.3	5.7				2.9E+018	
		$2\sigma$	2.3	0.4	3.3	1.0	0.8	1.5	1.9	35.5	11.4	0.14	0.78	8.9E+017
two dislocations	median 1st	3439.3	747.1	9.9	29.5	43.7	-73.3	18.8	0.6	0.01	0.07	7.0E+017		
	median 2nd	2.5	1.1	0.6	2.2	0.7	1.3	0.7	11.6	0.09	0.63	4.7E+018		
GCMT	median	3419.1	740.2	10.4	41.1	45.9	-75.1	17.4	11.8	0.18	0.55	4.5E+018		
	$2\sigma$	1.0	0.9	0.5	8.3*	0.8	1.4	0.4	0.7	0.02	0.06	1.57E+017		
Elliott et al., 2010 - 1. S.	3412.1	725.6	17.3	30	48	-48						1.39E+19		
Elliott et al., 2010 - 2. S.	<b>3429</b>	<b>741.64</b>	8.9	<b>20</b>	43	-51		<b>20</b>	7.5		total slip: 0.6	4.50E+18		
Elliott et al., 2010 - 2. S.	<b>3412.1</b>	<b>750.5</b>	8.4	<b>40</b>	42	-53		15.6	10		total slip: 0.9	6.90E+18		

Table 2.5: Table of the azimuth of the slip vector (slip vector trend) from each studied earthquake for the median of the one-source models and for the median two-sources models source mechanism between the two sub-sources (mean moment weighted) and also for each sub-source individually. Additionally given is the principal axis of strain from the nearest grid point of the world strain map (Kreemer et al., 2003). The last row gives the absolute difference between the azimuth of the one-source and that of the median of the two-sources.

InSAR	median two-sources	1.sub-src	2.sub-src	one-source	principal strain axis	$\Delta$
2009 L'Aquila	228.1	228.58	227.98	226.63	46.48	4.1
2016 Amatrice	237.66	240.49	228.55	222.38	41.1	13.1
2005 Zhongba	239	238.7	239.8	233.85	98.3	4.1
2008 Zhongba	280.1	276.7	290.2	271.87	98.3	8.6
far-field	median two-sources	1.sub-src	2.sub-src	one-source	principal strain axis	$\Delta$
2009 L'Aquila	222.38	222.24	222	226.48	46.48	1.5
2016 Amatrice	240.316	238.5	241.8	227.24	41.1	15.3
2005 Zhongba	267.48	267.2	267.79	271.58	98.3	5.2
2008 Zhongba	273.8	268.4	293.3	265.22	98.3	8.4

### 2.9.1 Source parameter and tradeoff scatter plots

#### The 2009 L'Aquila earthquake

For the 2009 L'Aquila earthquake the one-source models, the trade-offs between model parameters in the InSAR data optimisations are apparent for moment and rake, moment and dip, moment and location (easting and northing) as well as rake and dip. Similarly, model parameter trade-offs in the FF optimisations show up for rake and dip, rake and depth, moment and rake as well as moment and location, while here very pronounced parameter trade-offs show for moment and dip, moment and depth as well as dip and depth. Interestingly, the parameter trade-offs between dip, rake and moment show an anti-correlation for InSAR data optimisations and a positive correlation for the FF optimisations.

The horizontal source position parameters of the static InSAR data optimisations have a high spatial resolution with typical parameter uncertainties of less than a kilometer in both directions (Appendix Fig. 2.18). The spatial resolution of the FF optimisation results are lower by a factor of two in comparison with the static InSAR data estimates for the L'Aquila earthquake (Appendix Fig. 2.18).

For the two-sources models of the FF optimisations the trade-offs appear to generally decrease as well. Exceptions to this are strong correlations between moment and rake and dip and depth. Trade-offs between the two-sources model parameters of the InSAR data optimisations are not as apparent as for the one-source model.

#### The 2016 Amatrice earthquake

For the 2016 Amatrice earthquake the static InSAR data optimisations provide smaller source model parameter uncertainties compared to the FF optimisations. For example for the static

## 2 Sensitivity of InSAR and teleseismic observations to earthquake rupture segmentation

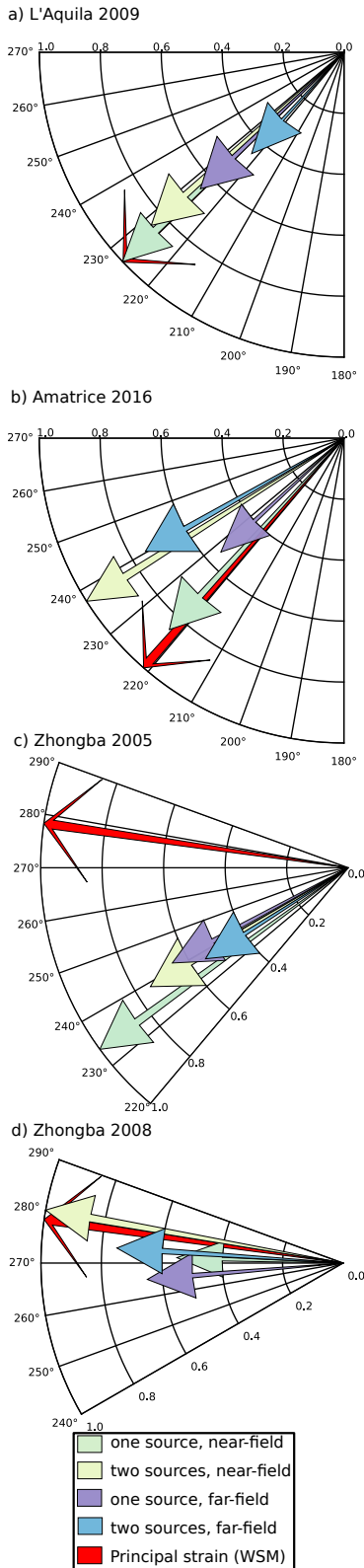


Figure 2.17: The mean azimuth of the slip vectors (slip vector trend) from the solution ensemble (projection of the slip vector to the horizontal) in a polar plot. The length of the vector indicates the inverse AIC value of the model, normalized from 0.0 to 1.0, with 1 being the lowest AIC value for this model set. A longer arrow therefore indicates a higher probability for the respective model over model AIC's represented by shorter arrows. The red arrow indicates the principal strain axis from the nearest grid point of the World strain map project (Kreemer et al., 2003), with a fixed vector length of 1. The subfigure a) gives the slip vector azimuth for the 2009 L'Aquila, b) for the 2016 Amatrice and c) for the 2005 Zhongba, d) for the 2008 Zhongba earthquakes.

Table 2.6: Kagan angles (Kagan, 1991) and  $\omega$  angle distance (Tape and Tape, 2012) for all studied earthquakes giving the angular differences between unsegmented and segmented models. The Kagan angles denote the three-dimensional rotation needed to turn one DC into another DC. The  $\omega$  angle distance in the cosine formalism gives the difference of the radiation pattern between two moment tensors from 0 to 1. For each earthquake they are given between the one-source median model and the moment-weighted median of the two-sources models with their standard deviations  $\sigma$ .

Earthquake	kagan angle InSAR [deg]	kagan angle far-field [deg]	$\omega$ InSAR	$\omega$ far-field
2009 L'Aquila	4 $\pm$ 1.5	6 $\pm$ 4	0.002	0.001
2016 Amatrice	11 $\pm$ 1	24 $\pm$ 4	0.01	0.04
2005 Zhongba	8 $\pm$ 11	19 $\pm$ 9	0.005	0.03
2008 Zhongba	13 $\pm$ 1	10 $\pm$ 3	0.02	0.01

InSAR data optimisations of the one-source models the source parameter uncertainties of the horizontal source location is only 2.1 km in northing and 0.9 km in easting, compared to the much larger values for FF optimisations with 21.1 km in northing and 8.6 km in easting direction (Appendix Fig. 2.19). Comparing the one-source parameters with the two-sources parameters of the static InSAR data optimisations, no significant change can be noted. In the FF optimisation the  $2\sigma$  uncertainty of the source horizontal position decreases from 21 km in northing and around 9 km in easting for one-source to 5.6 km and 4.2 km for the first source of the two-sources and to 1.9 km and 0.8 km for the second source of the two-sources, for northing and easting respectively (Appendix Tab. 2.3).

For the FF optimisations the model parameter distributions northing, depth, fault strike and fault rake distributions from the two sources overlap. The estimated depth from the FF optimisation's shows also a slightly deeper northern source (Appendix Fig. 2.19). The one-source model parameter tradeoffs are apparent for InSAR data optimisations between dip and northing as well as dip and depth. Also dip and depth show a model parameter trade-off in the FF optimisations, additionally to a further crescent-shaped trade-off between rake and northing. The depth parameters are clearly separated in the InSAR data optimisations and show an at least 0,5 km deeper northern source. This is different for the FF optimisations, where only the strike parameters have overlapping parameter distributions between the two sources and the depth parameters show no clear separation of the distributions. There is an observable strong trade-off for the InSAR data optimisation between source parameters dip and depth. The far-field source parameters show source parameter trade-offs between dip/rake and dip/moment, with the northern source models having stronger dip/rake source parameter tradeoffs. Notable is also that there is a difference in the source parameter tradeoff between rake and moment for the northern and southern segments for the FF optimisation source parameters.

In conclusion, for the 2016 Amatrice earthquake the static InSAR data optimisation estimated source mechanisms show less uncertainty than the far-field ones. Also the moment weighted mean source mechanism of the two-sources model varies more from the one-source models source mechanism for the static InSAR data optimisation as for the far-field.

### Comparison of 2009 L'Aquila and the 2016 Amatrice earthquakes optimisation results

Comparing the results of one-source and two-sources models from optimisations for the 2009 L'Aquila and the 2016 Amatrice earthquakes, we make out several differences. For the 2009 L'Aquila earthquake the mean values of two-sources model parameters strike, dip and rake are very similar and the parameter distributions overlap to a large extent. For the

2016 Amatrice earthquake many parameters of the two-sources models show well-defined separations in mean values and parameter distributions. For 2009 L'Aquila earthquake the estimated model parameter uncertainties mostly increase when a two-sources model is used instead of a one-source model (Appendix Tab. 2.3). In contrast to that, for the 2016 Amatrice earthquakes they decrease for most of the model parameters when modelling two sources, except for the location and timing parameters (Appendix Tab. 2.3). In conclusion, based on the model parameter ensembles, the 2009 L'Aquila earthquake source estimation does not seem to profit from additional degrees of freedom. The two-sources models, which are forced to be separated in space and time, align for several of the 500 solutions to be on the same plane, resembling a sub-divided one-source model. In this case the evidence for an increased model complexity is weak. In contrast to that, the 2016 Amatrice earthquake source estimation seems to diverge from a one-source solution into two well-defined sources. Also the estimated source parameters strike, dip, rake and depth for the one-source model from static InSAR data for the Amatrice earthquake are approximately intermediates of the two-sources model estimated source parameters. This is not the case for the L'Aquila earthquake.

### **The 2005 Zhongba earthquake**

For the 2005 Zhongba earthquake depth and dip display the strongest source parameter trade-offs, which are similar for both InSAR data and FF optimisations. Rake and depth source parameter estimates are slightly anti-correlated for the InSAR data optimisations. Rake and moment are slightly and clearly anti-correlated for the InSAR data and FF optimisations, respectively. For the 2005 Zhongba earthquake the source location estimates of the static InSAR data optimisations are systematically shifted 3km eastwards compared to the FF optimisations (Appendix Tab. 2.4). This coincides roughly with the dip direction. The far-field estimated source parameters for the position of the 2005 Zhongba earthquake have larger uncertainties than the one-source models (Appendix Tab. 2.4).

### **The 2008 Zhongba earthquake**

The Zhongba 2008 one-source models parameter estimates display tradeoffs between the source parameters dip and moment for the InSAR data optimisations are observable. Also source parameters strike and depth have strong parameter tradeoffs for the FF optimisations. The source parameters dip/rake and dip/moment are strongly correlated in both cases. The dip of the InSAR data optimisations the dip is clearly separated for the two sources (Fig. 2.6), while in the far-field the distributions merge and the dip is correlated with depth (Appendix Fig. 2.21). Tradeoffs between source parameters dip and moment can be observed for the InSAR data optimisations, while the source parameters dip and rake tradeoffs for the northern segment for the FF optimisations. The sources parameter east and northing are lesser correlated in the InSAR data than in the FF.

Rake is estimated in good agreement from both near- and FF for the two-sources models. The uncertainties increase from the one-source to the two-sources model for both the near- and the far-field. For example the strike of the one-source model has a  $2\sigma$  of  $1.0^\circ$  and  $2.9^\circ$  for the near- and far-field, while the two-sources uncertainties show  $2\sigma$  values of  $2.2^\circ/8.3^\circ$  and  $12.1^\circ/6.8^\circ$ , for the two sources in the near- and far-field, respectively (Appendix Tab. 2.4).



### **Inter-pair comparison**

Several observations can be made when comparing the estimated source parameter distributions across all four cases. In comparison with the L'Aquila earthquake the 2005 Zhongba earthquake has greater uncertainty for all source parameter estimates. This is also true for the static InSAR data optimisation estimates. In general depth and time are the least well resolved parameter estimates for the FF optimisations. For the L'Aquila and 2005 Zhongba earthquakes the far-field optimisation inferred source position is biased towards a position in dip direction of the static InSAR data solution, whereas for Amatrice and 2008 Zhongba the far-field position of the one-source appears to be more randomly scattered around the considered search areas. The uncertainties associated to the far-field one-source parameter estimates for the Amatrice earthquake are in general considerably larger than the ones for the 2008 Zhongba earthquake, e.g. strike with a  $2\sigma$  of 7.9 and 2.9, respectively. More tradeoffs are well developed and observable for the one-source models distributions for L'Aquila and 2005 Zhongba earthquakes than for two-sources models distributions. This is the opposite case for the Amatrice and 2008 Zhongba earthquakes, where the source parameter distributions of the two-sources models display more parameter tradeoffs than the one-source models.

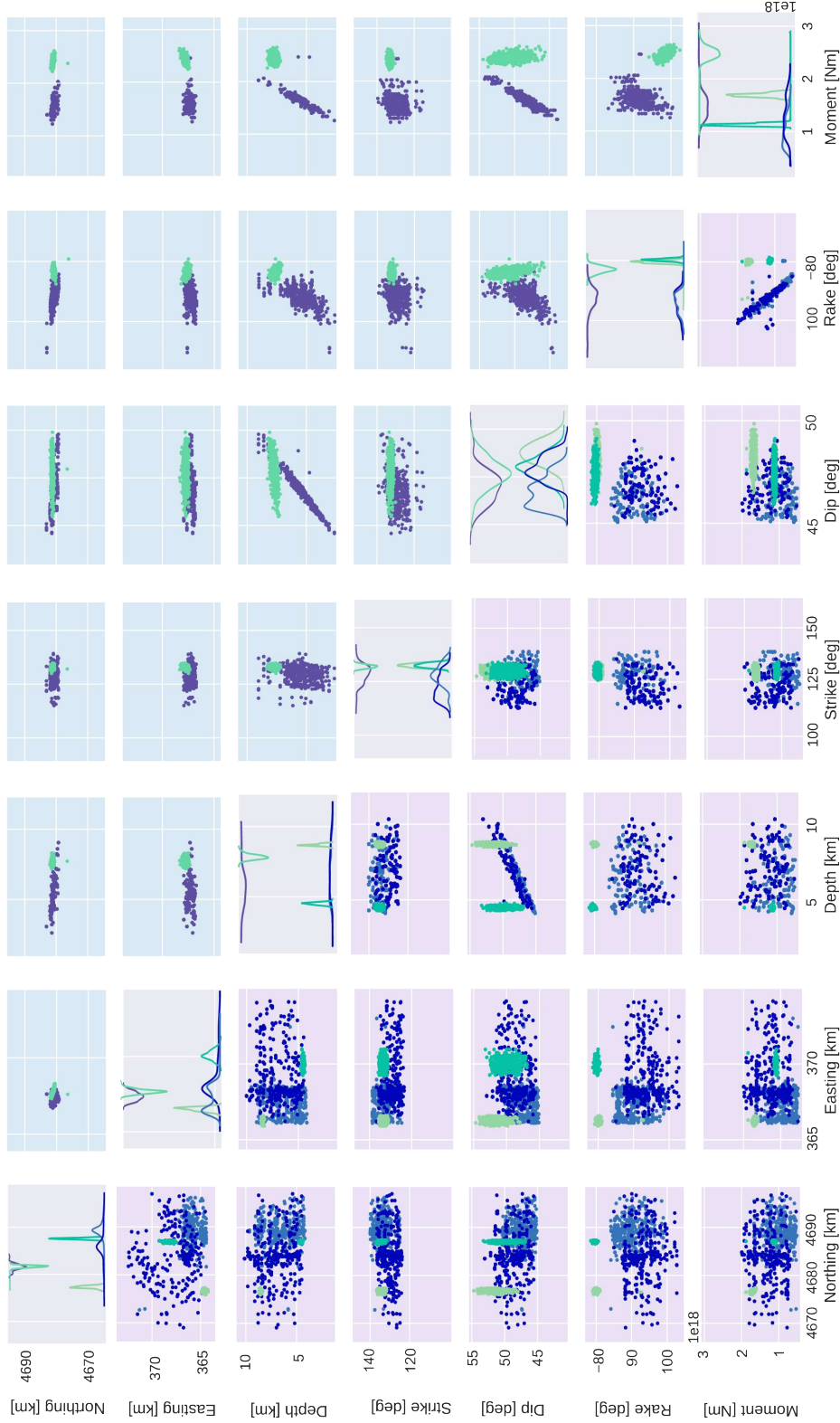


Figure 2.18: The 2009 L'Aquila earthquake source parameter distributions. Each element shows the dependences of the source parameter of the row to the one in the column. On the lower triangle are plotted the tradeoff scatter plots for two sources for both near- (green colours) and far-field (blue colors) and on the upper triangle the scatter plots for the ones using a single source. On the diagonal are plotted the histograms for the separate source parameters. In the lower triangle the two different source parameters for each different source are highlighted in a darker colour and lighter colour for the northern source and southern source to the dataset. Only source parameters common to all models are shown.

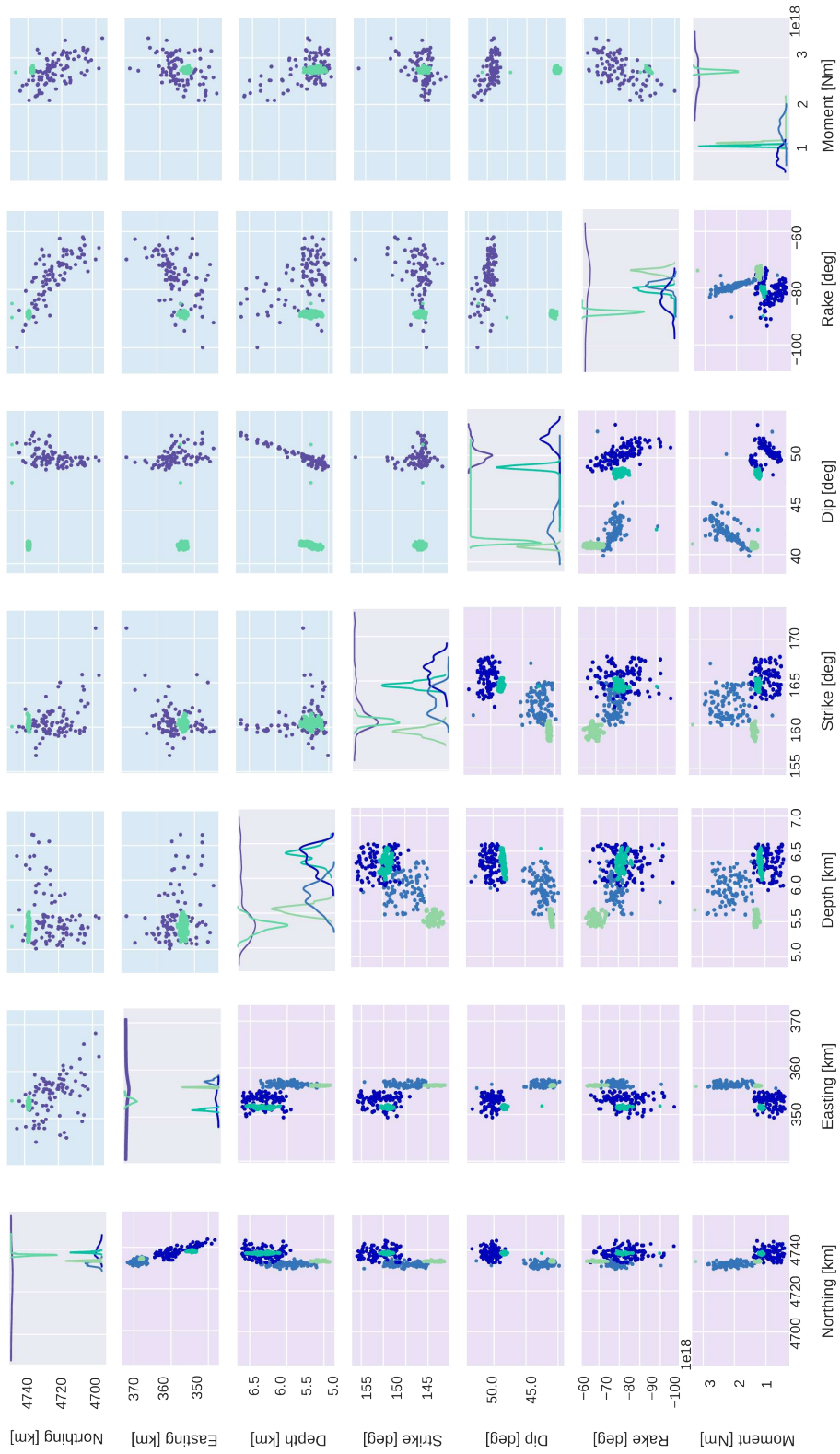


Figure 2.19: Amatrice earthquake source parameter distributions. Details as in figure 2.18.

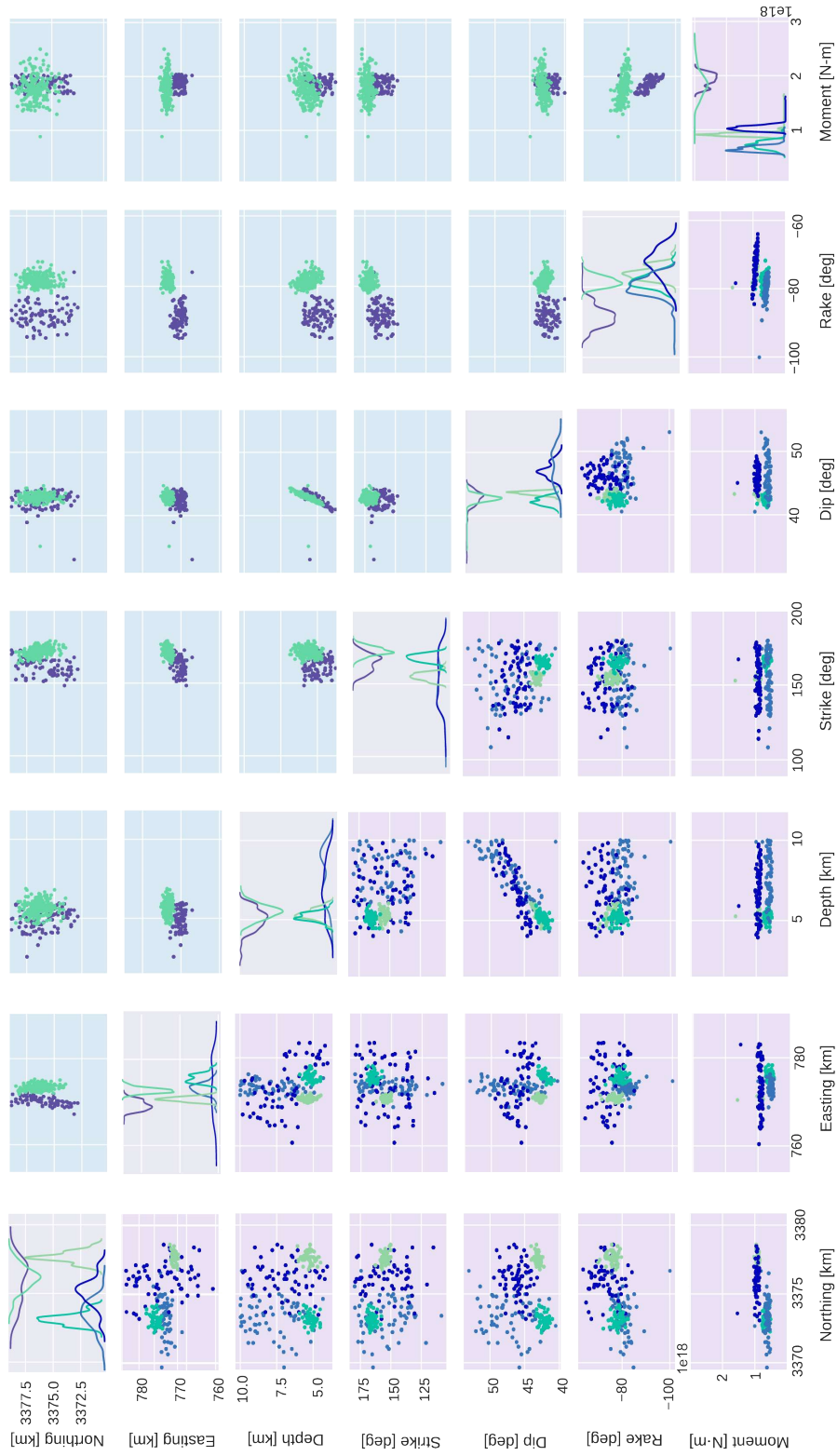


Figure 2.20: Zhongba 2005 earthquake source parameter distributions. Details as in figure 2.18.

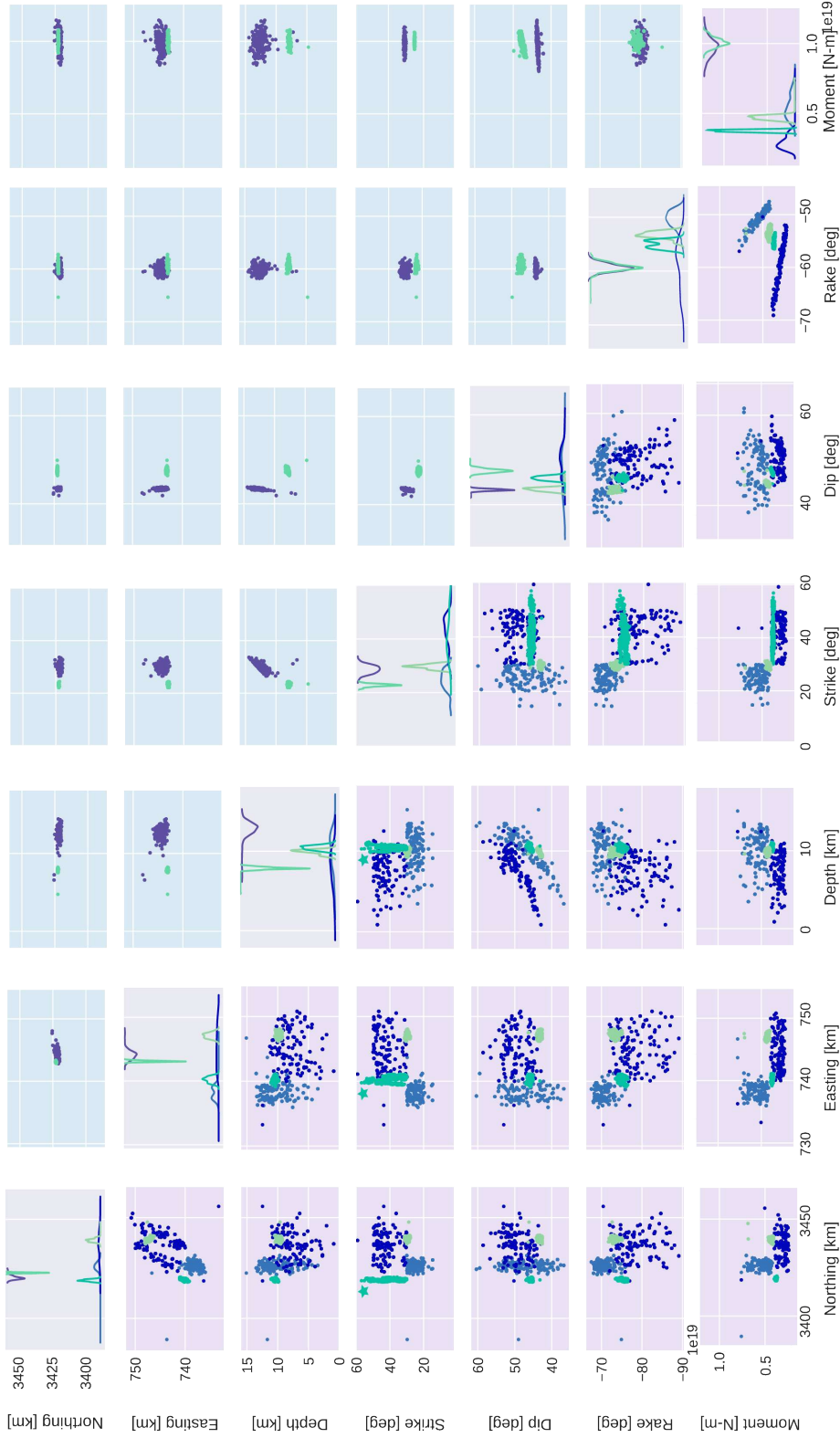


Figure 2.21: 2008 Zhongba earthquake source parameter distributions. Details as in figure 2.18. The star for the source parameter strike indicates that there is a set of 67 models that have a strike of about  $220^\circ$ , which are not shown here, indicating that the dip vergence of the fault is not fully explained by the available data.

## 2 Sensitivity of InSAR and teleseismic observations to earthquake rupture segmentation

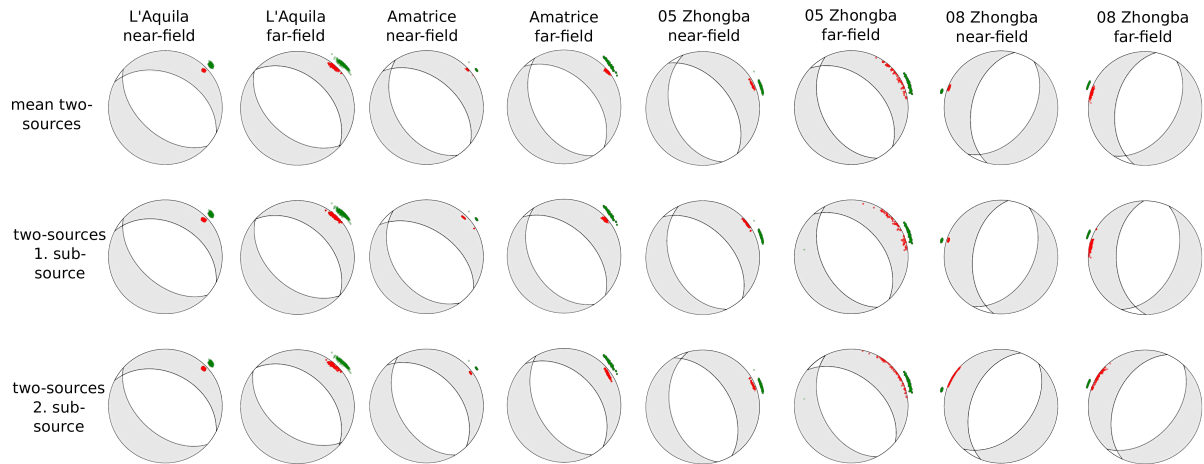


Figure 2.22: T-axes comparisons of the earthquake model ensembles. One-source models T-axis (green dots, outside the stereo plots) T-axis are compared to T-axis points of ensembles of the mean two-sources model (red dots, top row), the first sub-source (red dots, middle row) and the second sub-sources (red dots, bottom row). The one-source model T-axis (green dots) give a reference in each column. The stereo plot in each column corresponds to the mean two-sources model.



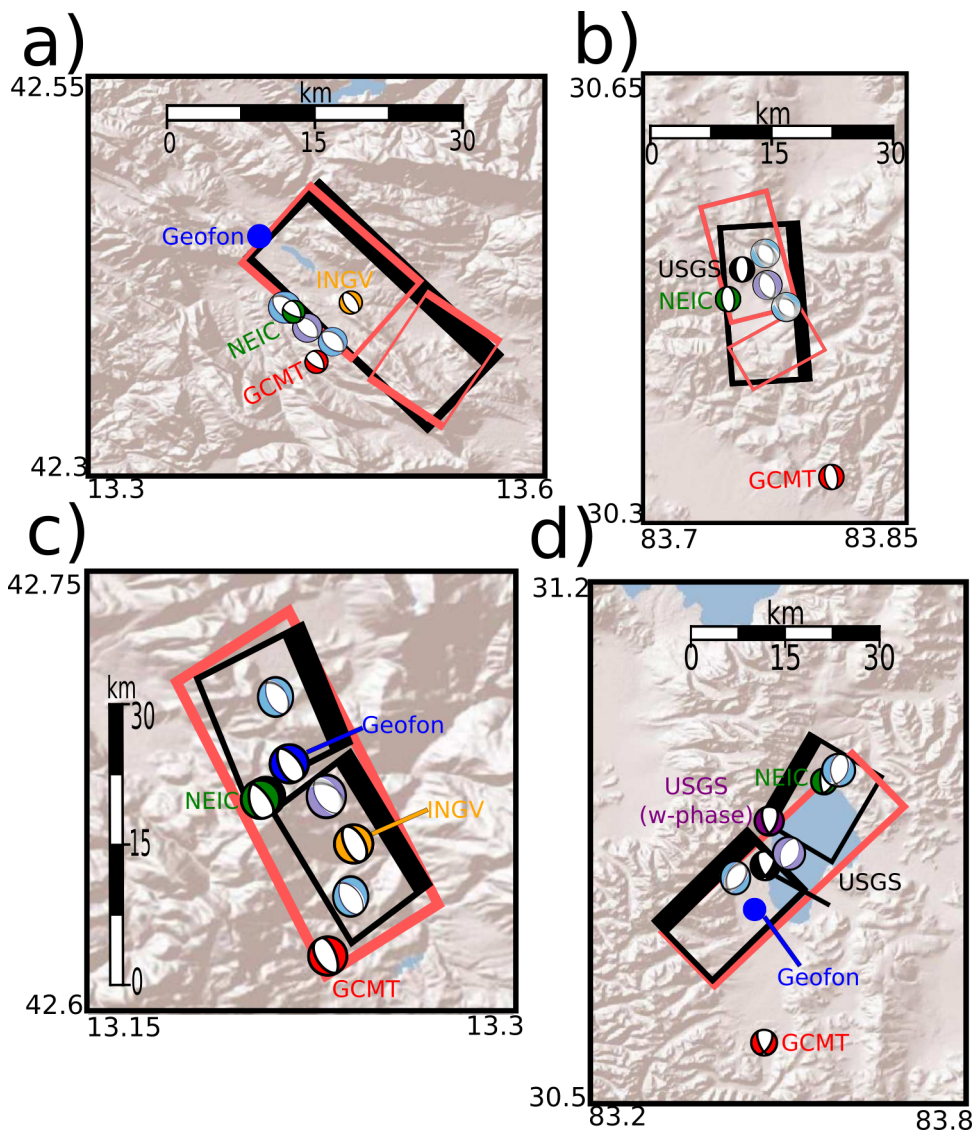


Figure 2.23: Map for each earthquake with the best fit location of the one- and two-sources model from both InSAR data and FF optimisations results plotted on a DEM. Figures are given for a) L'Aquila, b) 2005 Zhongba, c) Amatrice and d) 2008 Zhongba earthquakes. The best fitting InSAR data model is shown as a rectangular outline of the source, with the solid line indicating the upper edge. The AIC favoured model outline is shown with a black rectangle, while the best fitting non favoured model is shown with a red rectangle. The FF focal mechanisms are plotted for one-source model results in light purple and in blue for the two-sources model results. The beach balls are plotted as fuzzy beachballs, drawn from the entirety of the solution ensemble of the respective 500 optimisations. The size of the beachballs is given by their respective moments. Reference solutions are also plotted where available as beachballs for focal mechanism from GCMT (red), USGS (black), NEIC/ISC (green) and Geofon (blue, solid blue indicates that only origin is available). For the Italian earthquakes (A and C) also the focal mechanism from the INGV is plotted and for the 2008 Zhongba in deep purple the w-phase determined focal mechanism from USGS (Duputel) is plotted.

# 3 Paper II - Data-driven constraints on earthquake modeling and segmentation from teleseismic multi-array backprojection and InSAR

Andreas Steinberg<sup>1, 2</sup>, Henriette Sudhaus<sup>2</sup>, Frank Krüger<sup>3</sup>

<sup>1</sup> Department of Geosciences, Kiel University

<sup>2</sup> Federal Institute for Geosciences and Natural Resources (BGR)

<sup>2</sup> Department of Geosciences, University of Potsdam

Submitted to *Journal of Geophysical Research: Solid Earth*

## 3.1 Abstract

Earthquakes have been observed to rupture in segments. A good understanding of rupture segmentation is important to characterize fault geometries at depth for follow-up tectonic, stress-field or other analyses. Earthquakes with magnitudes  $M_w < 7$  are however often modeled with simple source models. We propose a data-driven strategy and develop pre-optimization methods for a segmentation-sensitive source modeling analysis. The first method we develop is a time-domain, multi-array backprojection of teleseismic data to infer the spatio-temporal evolution of the rupture, including a potential occurrence of rupture segmentation. We calibrate the backprojection using empirical traveltime corrections and we provide robust precision estimates based on bootstrapping of the travel-time models and array weights. Secondly we apply image analysis methods on InSAR surface displacement maps to infer modeling constraints on rupture characteristics (e.g. strike and length) and the number of potential segments. Both methods can provide model-independent constraints on fault location, dimension, orientation and rupture timing, applicable to form prior pseudo-probabilities of model parameters before modeling. We use the model-independent constraints delivered by these two newly developed methods to inform a kinematic earthquake source optimization about parameter prior pseudo-probability estimates. We demonstrate and test our methods based on synthetic tests and an application to the 25.11.2016 Muji  $M_w 6.6$  earthquake. Our results indicate segmentation and bilateral rupturing for the 2016 Muji earthquake. The results of the backprojection using high-frequency filtered teleseismic wavforms in particular shows the capability to illuminate the rupture history with the potential to resolve the start and stop phases of individual fault segments.



## 3.2 Introduction

The accuracy in estimating earthquake source characteristics is limited by many factors. Among them are a limited data resolution, non-linear dependencies between observations and some of the sought source parameters as well as simplifications applied to a model representation compared to the real rupture process (Steinberg et al., 2020a). Also, based on surface observations alone, uncertainties in the earth structure influence the accuracy of earthquakes source estimation strongly (Weston et al., 2012) and some earthquake properties can not be resolved independently from others. Continuous progress is made regarding the data resolution, because the density of global sensors is increasing steadily. This enables more detailed studies of shallow crustal earthquakes of moderate magnitude and allows applying more realistic earthquake models that represent better potentially common source complexities such as segmentation into sub-sources and slip heterogeneities. The challenges of solving the non-linear problem and dealing with parameter dependencies remain, in particular for source analyses with complex segmented models that involve the estimation of a large number of model parameters (Weston et al., 2012; Ragon et al., 2018a; Lohman and Simons, 2005a; Razafindrakoto et al., 2015).

Most current operational earthquake analysis frameworks (Dziewonski et al., 1981; Hanka and Kind, 1994a) providing earthquake catalogues, only consider point-source models to represent any given earthquake (e.g. a single Double-Couple or moment tensor). It has been shown that in presence of significant source complexity also the apparent earthquake characteristics based on point-source or single-source kinematic models can be significantly biased (Steinberg et al., 2020a). As these earthquake catalogues form the basis for many statistical studies on earthquake characteristics (i.e. (Heidbach et al., 2018; Woessner et al., 2015) and inferred dependent properties like spatio-temporal aftershock patterns (McCloskey and Nalbant, 2009), the observational bias from single earthquakes could introduce a bias in the currently possibly incomplete earthquake statistics. Inferred source behaviour used in dynamic modeling and empirical analysis is often based on statistics derived from kinematic modeling. As mentioned above, these statistics however might be influenced by observational bias. Rupture segmentation is an important source characteristic which is often based on expert judgement in case studies of larger earthquakes.

An objective and data-driven study of the segmentation of shallow crustal moderate magnitude earthquakes is difficult but necessary to increase these statistics on source complexity. Such a study approach should be data driven and minimize expert bias (e.g. the choice of the model and complexity). This undertaking is challenged by a strongly enlarged model space to be sampled and by increased parameter trade-offs compared to point-source or single-source kinematic inversion. Very slow converging or even non-convergent optimizations can be the consequence.

In this study we demonstrate how model-independent and data-based methods can be employed to inform kinematic modeling of earthquake sources objectively. We put a special focus on the minimum modelled segmentation required to meaningfully represent earthquake ruptures. Our here presented methods are designed to enable the investigation of rupture segmentation with globally available datasets, e.g. space-borne InSAR data of co-seismic static near-field displacements and broadband recordings at distant seismological stations. The suggested methods extract information on the earthquake source in a pseudo-probabilistic way. This information can be used to judge on the occurrence of fault segmentation independent from inverse modeling and to enable enriched statistical analyses of medium-sized earthquakes in an effort to reduce potential observational bias. We use this source information further on to set up the model parametrization of earthquake source optimizations, which includes the number of relevant model parameters and their prior pseudo-probabilities.

We present a multi-array backprojection (BP) approach based on teleseismic waveform data

to image the location and dynamics of a rupture. From the evolution of the rupture dynamics we aim to detect the number of significant sub-sources. Seismological backprojection takes advantage of source-receiver reciprocity and has proven to be a reliable tool to image the dynamic rupture process by mapping coherent seismic radiators in space and time (Kiser and Ishii, 2017). The principal idea of the seismic backprojection method here used is the alignment and then stacking of the seismic waveforms to the predicted P-wave and SH-wave onsets of potential point sources located on a 2D or 3D grid in sliding time windows. If energy is coherently emitted in a certain time window from a certain grid point, the time-shifted waveforms should stack constructively. The grid point is therefore a potential source of the signal at that time. The waveforms should stack destructively if the grid point is not a source of seismic energy during the given time window. Backprojection of teleseismic data has first been used to investigate the 26.12.2004 Mw 9.1 Sumatra earthquake (Krüger and Ohrnberger, 2005; Ishii et al., 2005) and is usually carried out for larger earthquakes ( $M_w > 7$ ) (Bao et al., 2019; Meng et al., 2016; Kiser and Ishii, 2017; Hicks et al., 2020b).

Seismological backprojection is applied in different frequency bands of the seismic waves. From frequencies below the corner frequency we gain prior information on the fault location and potentially also the number of sub-sources. High-frequency energy radiation is concentrated near the hypocenter and the asperities rupture initiation points, representing start/stop phases (Ide, 2002; Madariaga, 1977; Okuwaki and Yagi, 2017). The mapping of higher frequency coherent energy release can therefore potentially be used as prior information on the ruptures nucleation position, rupture velocity and the number of sub-sources for a kinematic fault model optimization. Seismological backprojection is an ideal tool to inform our modeling about rupture segmentation and validate that modelled rupture segmentation is not only a requirement to fit our models better but really representative of an actual physical process. Because traditional seismological backprojection uses a single array and is known to produce "swimming" artifacts, we implemented a new multi-array backprojection method resistant to this effect (Kiser and Ishii, 2017) based on an earlier approach (Rössler et al., 2010).

Static surface displacement as measured through the InSAR technique can reveal an earthquake source location by apparent significant displacement. To the eye of an expert the pattern of the displacement potentially reveals more characteristics directly, such as the approximate rupture dimension, the fault orientation and the mechanism. We mimic, formalize and automate a similar extraction of information prior to modeling by employing image analysis methods like edge detection on the gradient of the displacement. Using the presented method we estimate the source location, size and the number of sources from the gradient of displacement maps among other source features.

We first present the two data-driven analysis methods developed for far-field and near-field data. The methods are implemented in python-based open-source software codes. We test the methods with synthetic data first. We then present a framework with a focus on moderate and larger sized shallow crustal earthquakes in mind in which we use the extracted information for estimating model parameter prior pseudo-probabilities to guide a finite fault optimization and constrain the modeling of segmented ruptures. We finally apply the presented methods in an investigation of the 25.11.2016 Muji Mw 6.6 earthquake to better inform a joint optimization of teleseismic and static near-field data.

### 3.3 Methods

#### 3.3.1 Time-domain backprojection using multiple virtual arrays

The reported applications of teleseismic backprojection (BP) enclose only a few studies dealing with shallow crustal intermediate-sized earthquakes of magnitudes between  $M_W6$  and  $M_W7$  (Kiser and Ishii, 2013; Fan and Shearer, 2017; Yin and Denolle, 2019). A likely reason is that the spatial precision of traditional time-domain teleseismic BP by using large arrays are similar to the size of the rupture area of  $M_w < 7$  earthquakes (Fan and Shearer, 2017).

##### 3.3.1.1 Introduction to the backprojection method

Traditional time-domain BP involves an alignment of seismic recordings within an array and a subsequent stacking (Krüger and Ohrnberger, 2005; Ishii et al., 2005). Phase arrivals of earthquakes stack constructively to high amplitudes if the trace alignments correspond well to the actual source-receiver configuration. Different phase arrivals are separated by moving time windows along the waveform on which the BP is applied. Then, mapping the source locations that lead to high-amplitude stacks for the corresponding time window provides images of the seismic energy release of a rupture. This energy originates from abrupt relative and spatially variable changes in the fault slip or abrupt changes in rupture velocity (Okuwaki et al., 2018; Yin and Denolle, 2019; Madariaga, 1977).

The main assumption of time-domain BP is that wave traveltimes from the source to global receivers correspond well to those of commonly used 1-D velocity Earth models. Unwanted effects of this strong assumption for real data applications can be weakened by applying empirical traveltimes corrections (Section 3.3.1.4). Other common assumptions are that the waveforms of phases are coherent within an array, e. g. no occurrences of polarity changes as across a nodal plane of the focal mechanism, and furthermore that noise is uncorrelated. Constructive stacking of coherent coda waves can create secondary sources and introduce a bias in the time-domain BP imaging.

We implemented the time-domain BP in the following way. We stack P- and SH-phases separately, using their respective slowness values. Other phases with different slowness values inherently stack destructively. The depth phases of P and SH-phases, pP, pPP and sS, however, have similar slowness values as the corresponding direct phase for shallow events and will therefore also stack constructively. Depth phases can have relatively large amplitudes compared to the direct phase and, for shallow earthquakes, follow them very close in time. Therefore they generally significantly influence the stack of the direct phase. With higher frequencies the importance of depth phases decreases, because these are more strongly influenced by topography and shallow structure at the surface reflection point, which results in less coherent high-frequency waveforms with reduced constructive stacking.

We use the phase-weighted stacking method (Schimmel and Paulssen, 1997) to increase the signal-to-noise ratio of the stacks, which basically realizes a trace weighting based on the phase coherence within the array. Specifically, the phase-weighted stacking is a non-linear stacking method, where each sample in a linear stack is weighted by an amplitude-unbiased coherence measure. In this way, phase-weighted stacking sharpens up signals, reduces signal artifacts and suppresses noise. Phase-weighted stacking comes at the cost of loss of absolute amplitude information (Fan and Shearer, 2017; Schimmel and Gallart, 2007) and of a strong relative enhancement of the dominant period. However, the advantages outweigh the disadvantages of the method.

We first calculate the coherence based on complex traces in a phase stack and then multiply this coherence with the linear stack, sample by sample. Therefore we first calculate the phase stack  $c(t)$  for all  $N$  waveforms:

$$c(t) = \left\| \frac{1}{N} \sum_{j=1}^N e^{i\Phi_j(t)} \right\|. \quad (3.1)$$

$c(t)$  is based on the similarity of the phases  $\Phi_j(t)$  of the complex signals of the  $N$  traces  $u_j(t)$  at time  $t$  (Bracewell and Bracewell, 1986). The amplitudes of the phase stack are coherence measures and range between 0 for non-coherent and 1 for coherent signals.

We carry out the BP for point locations that form a horizontal grid of source points. We stack the waveforms for each of these grid points according to Eq. 3.2, with the specific expected arrival time from a grid point source to each station. Each waveform  $u(t_r)$  of the linear stack is multiplied with the phase coherence (Schimmel and Paulssen, 1997) to calculate for each grid point the phase-weighted stack  $\hat{S}_k(t_r)$  of an array:

$$\hat{S}_k(t_r) = \frac{1}{N} \sum_{j=1}^N u_j(t_r + t_{kj}) \left\| \frac{1}{N} \sum_{j=1}^N e^{i\Phi_j(t_r + t_{kj})} \right\|^\nu, \quad (3.2)$$

with  $t_r$  being the rupture onset time and  $t_{kj}$  the source-receiver traveltimes. The coherence weighting here is tuned with the parameter  $\nu$  for an adaptable transition between coherent and less coherent signal summation.  $\nu=0$  realizes a linear stack, while we use  $\nu=2$  to increase the signal-to-noise ratio.  $t_{kj}$  is the traveltimes for the respective grid point  $k$  of the waveform record  $j$ .

Waveforms that get stacked in this way form the semblance  $S_k$  of the array for the respective source grid point  $k$  by normalization:

$$S_k(t_r) = \frac{\hat{S}_k(t_r)}{\sum_{k=1}^K \hat{S}_k(t_r)}. \quad (3.3)$$

The semblance  $S_k(t_r)$  can be seen as in terms of a pseudo-probability of coherent radiation of seismic energy from a given source point  $k$  at a time  $t_r$  (Rössler et al., 2010; Douze and Laster, 1979). We can form maps of spatial semblance for single time steps or of the cumulative semblance, to which we refer to as incremental or cumulative semblance maps. The semblance spatial resolution is described by the frequency- and azimuth-dependent beam pattern and is an analogue to the *array response* or *array transfer function* (Rost and Thomas, 2002), defined by stacking with respect to slowness (Johnson and Dudgeon, 1993). The spatial resolution of a seismic array increases with array aperture as well as with frequency and aliasing is decreased with increasing station coverage (Rost and Thomas, 2009). Therefore, large and dense arrays are desirable to image rupture evolution, but there are limits. The use of very large arrays has been found to result in relatively low resolution of the semblance (Xu et al., 2009). The reason is that the waveform recordings from a very large range of source distances and source azimuths resemble each other less and less and lose their coherence. This coherence loss is stronger for high frequencies and leads to a decrease of the upper frequency that remains coherent (Rost and Thomas, 2009). Less high frequency content in the semblance decreases the spatio-temporal resolution as mentioned above.

Additionally, we calculate the beampower  $E(t_r)$ , which is an absolute measure of the amplitudes at the  $i$ th array and a time window centered around  $t$  for waveforms  $\mathbf{u}$  recorded at  $N$  stations of

an array. Beampower is the sum of the energy at all arrays:

$$E(t_r) = \sum_{k=1}^K \frac{1}{L+1} \sum_l^L \left| \frac{1}{N} \sum_{j=1}^N u_j(t_r + l + t_{kj}) \right|^2, \quad (3.4)$$

where  $l$  is the sample index of the waveform in the time window with total number of samples  $L$ ,  $\Delta t$  is the duration of the time window. The beampower time trace in our case is closely related to the source-time-function (STF) as it is a stack of body waves. This should be similar to a STF but scaled by a factor depending on the radiation pattern, the source-receiver distance and the elastic medium properties (Vallée and Douet, 2016).

### 3.3.1.2 Multi-array BP method

The combination of several arrays subdues side lobes of the array response compared to a single-array BP. It also minimizes the effect of azimuth-dependent "smear" or "swimming" artifacts, which are systematic apparent drifts of the energy towards the array (Meng et al., 2016). The reasons are that the sidelobes of the single-array response functions are at different positions for each array, while the central lobe is always at the same position in the slowness plane. Migration artifacts "swim" in different directions with different apparent velocities. Additionally the combination of P- and SH-phases BPs suppresses sidelobes and migration artifacts, because of the different delays between the P-phase depth phases (pP, sP) and the SH-phase depth phases (sS) (Hong and Fujita, 1981). Multi-array BP results in more certain and better resolved spatio-temporal imaging.

In our multi-array BP we cluster all globally available stations at reasonable teleseismic distances to form a multitude of small virtual arrays using the k-means algorithm (Steinhaus, 1956). The combination of many small virtual arrays has the advantage of minimizing the effect of velocity differences between stations in the array as well as the effect of radiation patterns and source directivity across arrays (Rössler et al., 2010). Virtual arrays are formed assuming a lower limit for the number of array stations, distance between stations and a maximum aperture. Included stations are part of one array only. We multiply the single-array semblance maps instead of adding them which further suppresses sidelobes in the multi-array response function and is related to the interpretation of semblances as relative pseudo-probability (Rössler et al., 2010). The multiplication of the array responses also corresponds to a multiplication of the transfer functions of the arrays (Rössler et al., 2010).

We calculate the multi-array semblance from the product of the semblances from  $M$  arrays:

$$S_k(t_r) = \prod_{m=1}^M S_{km}(t_r). \quad (3.5)$$

The global distribution of virtual arrays may have gaps. To avoid an azimuthal bias in the multi-array response function we subdivide the azimuth into 12 sectors and, based on the azimuth of the earthquake epicenter to the array center, each array is assigned to a corresponding azimuth sector. The semblance from all virtual arrays in each azimuth sector is normalized to 1 for each time window, so that each azimuth sector has the same influence on the combined semblance. The azimuth weight  $w_{azi,m}$  for the  $m$ th virtual array is then:

$$w_{azi,m} = \frac{S_{mk}(t_r)}{\sum_{m=1}^M \max_{k..K, t..T} (S_m(t, k))}. \quad (3.6)$$

The weighted semblance becomes:

$$S_k(t_r) = \prod_{m=1}^M w_{azi,m} \cdot S_{km}(t_r). \quad (3.7)$$

Multi-array BP is associated with uncertainties, particularly for locating the source of energy, that we want to account for. Several studies have investigated these limitations. Yin and Denolle, 2019 found from theoretical considerations that the minimum resolvable feature in a semblance map should have a dimension of at least twice the P-wave wavelength. The resolution length of beamforming, which is the minimum distance between sources that can be distinguished, is estimated as the width at half-peak amplitude of the main lobe of the array response function (Meng et al., 2012b). The array’s spatial accuracy is the error in the estimation of the true source location (Meng et al., 2012b). (Fan and Shearer, 2017) found a median location error of around 25 km for traditional time-domain BP using large arrays. They also found, from the methods they considered, that the best sub-event resolution is achieved if a global phase-weighted stack is used (Fan and Shearer, 2017). To estimate the spatial precision and accuracy of a BP for individual cases, bootstrapping methods have been used (Yao et al., 2012; Shearer, 1997; Wang et al., 2016; Meng et al., 2012a).

We use Bayesian bootstrapping (Rubin, 1981) to quantify the spatial and temporal precision of the multi-array BP results. The bootstrapping is applied to the weights of the combined virtual arrays in the multi-array semblance at each timestep. For each timestep we create a set of 100 differently weighted BP stack. This bootstrapping of the weights is then further combined with traveltimes perturbations to assess the impact of the velocity model choice. The array weight controls how strongly each virtual array contributes to the multi-array semblance (see Eq. 3.10). We draw  $n_{\text{clusters}}$  random real numbers  $r \notin [0, n_{\text{clusters}}]$  from a uniform distribution. We then sort the obtained random values in an ascending order and ensure  $r_1 = 0$ . The  $i$ th bootstrap weight  $w_{\text{boot},i_{\text{boot}}}$  for a virtual array is then defined as:

$$w_{\text{boot},i_{\text{boot}}} = r_{i_{\text{boot}}+1} - r_{i_{\text{boot}}}. \quad (3.8)$$

The traveltimes perturbation simulates the effect of model errors in the semblance that are introduced by assuming a 1-D velocity model in the phase alignment before stacking. We assume these traveltimes errors to be random and normally distributed, with a standard-deviation of 2 s for the P-phase arrivals and with 4 s twice as large for SH-phase arrivals. So in each bootstrap set, we apply these traveltimes shifts to the waveforms before stacking. The semblance of each array is therefore affected by the bootstrapping of the traveltimes and we arrive at 100 sets of semblances for each virtual array. From the chosen 100 bootstrapping realizations we get from each bootstrap the weight  $w_{\text{boot},m}$  and also take into account the azimuthal balance weights  $w_{azi,m}$  to calculate the combined weighted semblance:

$$S(t_r) = \prod_{m=1}^M \frac{1}{100} \sum_{i=1}^{100} w_{\text{boot},mi} \cdot w_{azi,mi} \cdot S_{mi}(t_r). \quad (3.9)$$

We combine the results for each timestep from the individual P- and SH-phase BP to phase-combined BP. The phase-combined multi-array semblance  $S_{\text{comb}}(t_r)$  from P- and SH-phases BP is derived by the multiplication of the semblances at each timestep  $t_r$  (after Eq. 3.9):

$$S_{\text{comb}}(t_r) = S_P(t_r) \cdot S_S(t_r). \quad (3.10)$$

The final result of the multi-array BP obtained is a phase-combined multi-array semblance map for each timestep of the BP, which we call time-incremental semblance maps. The earliest mapped occurrence of coherent energy release is likely located close to the nucleation point, indicating the start phase. The latest semblance peak is likely to represent the stop phase. We also combine the semblance from all timesteps in a single cumulative semblance map.

### 3.3.1.3 Backprojection settings

We consider waveforms from broadband stations between 28 degree and 93 degree distance from the source, to avoid phase triplications and having P- and SH-wave arrivals clearly separated from later arriving bodywaves with significant amplitudes. After removing the instrument response from velocity seismograms through restitution, the waveforms are rotated from an ENZ (east, north, vertical) into the RTZ (radial, transversal, vertical) coordinate system, and they get downsampled to 10 Hz. We select the Z-component of the records for the P-wave BP and the T-component for the SH-wave BP. The virtual arrays have a maximum aperture of  $5^\circ$  and a minimum number of 5 stations. If in any of the 12 azimuth sectors no virtual array can be formed, to increase the azimuthal coverage, we allow for successively larger array apertures up to  $10^\circ$  and a smaller number of stations down to 3. Generally, we perform separate low-frequency BPs (LF BP) and high-frequency BPs (HF BP), within a total frequency range of 0.003 Hz up to about 1.5 Hz. The LF BP and HF BP frequency bands are separated by the expected corner frequency  $f_c$  of the earthquake studied. We estimate the corner frequency  $f_c$  of the seismic radiation based on the rupture duration  $T_r$ , which we take from the GCMT catalog, with  $f_c = 2/T_r$  (Aki and Richards, 2002). In other words,  $f_c$  is the upper frequency limit of the LF BP records and the lower frequency limit of the HF BP records. We filter with a butterworth bandpass filter of fourth order.

The BP is carried out with fixed-length time windows over the recorded waveforms, which are moved with small timesteps of a few seconds. The window length depends on the longest period at which the data is filtered. This results in longer time windows for the LF BP of 20 s to 30 s and shorter time windows for the HF BP of around 10 s. At this stage we discard seemingly poor quality records. As a measure we calculate the cross-correlation between the P- and SH-wave records of an array station with the corresponding records of the center-most station within the array. We only include waveforms with a cross-correlation coefficient of at least 0.6. By chance, this center-most station can have serious quality problems itself, which would lead to low cross-correlations for all stations and in effect to an exclusion of all waveforms of the array. In such a case the center-most station is excluded and the cross-correlation coefficients are recalculated for a randomly chosen new reference station. Before the stacking of the time windows (Eq. 3.2), the waveforms in each array are aligned based on pre-calculated traveltimes tables using the AK-135 1-D velocity model.

We multiply the responses of all virtual arrays at each timestep, which gives the response of the global array (Eq. 3.10). We account for the effect of unmodelled site effects close to the stations by including traveltimes perturbations per station (traveltimes shift bootstrapping). The effect of systematic traveltimes shifts due to unmodelled large-scale 3-D path effects can be reduced with empirical traveltimes corrections.

### 3.3.1.4 Empirical traveltimes corrections

Large-scale 3-D velocity structures affect the waveform paths and the traveltimes in systematic ways for stations within an array and across neighboring arrays. By using traveltimes predictions based on 1-D velocity models only, residual systematic traveltimes shifts persist. If these time

shifts remain unaccounted for, they may produce spatially and temporally, significantly shifted and defocused BP results. We can reduce this bias by automatically calibrating the traveltimes for each station based on empirical traveltime shifts (Palo et al., 2014; Ishii et al., 2007; Meng et al., 2016; Fan and Shearer, 2017).

We estimate arrival time shifts empirically by selecting a cataloged reference event from single fore- or aftershocks, which occurred close to the investigated earthquake. For this reference event we assume that catalog location and time are accurate and fix them to a single grid point and a single time window. Unknown is a set of traveltime shifts, maximizing the semblance for this setup. Per array and for each station individually we vary the traveltime shifts of P- and SH-waves such that the single-array semblance at the reference location is maximized. For this optimization problem we use the differential evolution algorithm (Storn and Price, 1997). We allow the traveltime to vary by  $\pm 2$  s for the P-wave and  $\pm 4$  s for the SH-wave, with respect to the theoretical onset, assuming the same 1-D velocity model as for the main event BP.

For a successful traveltime correction, the reference event has to be near the studied earthquake, small enough such that the point-source approximation holds well, but also large enough that its phase arrivals have a high signal-to-noise ratio globally. Preferably, the location of the reference event is very well known from local or regional station data analysis. Ideally, the reference event has a similar focal mechanism compared to the main event. An error in the location of the reference event will cause a wrongly estimated global time shift for the phases of the main studied earthquake. Typical mislocation errors that have to be expected for smaller earthquakes in remote areas are of the order of tens of kilometers (Fan and Shearer, 2017; Palo et al., 2014). An important gain of the empirical traveltime correction is an increased phase coherence, because unmodelled path effects are generally well compensated (Palo et al., 2014).

The rupture dimensions of intermediate-sized earthquakes, which we primarily want to investigate, are of the order of several tens of kilometers. When applying timing corrections for larger earthquakes however the validity of the timing corrections is spatially limited to a spatial extent of several tens of kilometers (Fan and Shearer, 2017). For earthquakes that rupture larger areas therefore traveltime corrections from multiple fore- or aftershocks along the potential rupture area should be considered (Palo et al., 2014).

#### 3.3.1.5 Defining the model space based on backprojection results

We propagate the information on the source obtained using multi-array BP to define the model space for a direct search optimization. These BP results are the low-frequency (LF) and high-frequency (HF) time-incremental semblance maps, which include 100 bootstrap realisations of the semblance for each time step. From these semblance maps we extract information on the location of the rupture, rupture size and orientation as well as the rupture evolution in time.

The centroid location and dimension of the rupture are outlined by significant cumulative LF semblance, which maps the area of significant seismic energy release. The semblance values can be related to relative pseudo-probability (Rössler et al., 2010). So based on the LF semblance grid, we construct discrete probability functions for the longitude and latitude parameters of the source centroid location.

For the strike and length source parameters we estimate the prior distributions using different approaches on LF and HF semblances, and finally combine their results afterwards. Based on the LF cumulative semblance map, we fit arbitrarily one or more oriented minimum bounding boxes and minimum bounding ellipses to neighboring grid point values with semblance values that exceed 1% of the maximum semblance. The bounding box orientations and lengths of the major axis enter as single values in the estimation of the strike and length prior distributions,



respectively. We calculate azimuth and distance from consecutive HF increments between their semblance maxima, for all bootstrap realisations. This produces an ensemble of azimuth and distance values, which translate directly into probable strike and length values. We simply merge the single estimates for strike and length from the cumulative LF semblance and the ensemble of estimates from the incremental HF semblances to construct Gaussian prior distributions for these values.

Rupture velocity can be inferred from the calculated distance and time separation of subsequent time-incremental maxima in the HF semblance maps (Ishii et al., 2005; Meng et al., 2012b). We assume here that between semblance maxima the rupture velocity does not change. We estimate the rupture velocity by dividing the collected apparent distances through the difference of the occurring times. Similar to (Rössler et al., 2010) we select the start, stop and duration of the rupture using a STA/LTA trigger algorithm on the obtained combined HF semblance map but also on the individual bootstrap semblance maps before combining as in Eq. 3.9. We divide the largest distance between two semblance maxima by their time separation and obtain another set of average rupture velocity estimates. From this procedure one could pick up the ensemble of apparent source durations as well.

The location of the earthquake hypocenter, or nucleation point, and the relative onset time of the rupture are also parameters we want to estimate in an optimization. To retrieve prior pseudo-probability distributions of the horizontal nucleus position we use incremental HF semblance maps normalized to a two-dimensional, discrete probability function. We extract the horizontal location of the first excitation of coherent energy. With there being only horizontal information in the HF semblance maps, we can not retrieve information on the depth of the nucleation point. To infer the source parameter of time we assign for each grid point the first time when significant semblance is mapped in this grid point. This time is given in relative seconds after the first semblance peak. Potentially, the time of the first semblance mapping onto a grid point is different in each bootstrap realisation of the multi-array BP. The result is an ensemble of potentially different semblance values for potentially different time steps for each grid point from each bootstrap. We choose one of the times associated to the drawn nucleation point at random as the source parameter time.

Potentially also the number of significant sub-sources, or segments, involved in the rupture can be estimated from the BP results, e.g. to define the initial number of segments in modeling or the range of possible significant segments in an multi-dimensional modeling framework. In LF semblance maps individual regions of high semblance can mark segments and these regions could be analysed individually. In HF semblance maps we can estimate the number of segments based on the number of significant high-frequency semblance peaks. For the simplest case, assuming smooth unilateral rupture along a single segment, two high-frequency energy emissions, one from a start phase and one from a stopping phase, should occur for each segment. In case of significant segmentation, HF semblance can be used to also estimate sub-source nucleation point positions and sub-source onset times. In our current application we do that, only at a later stage of the analysis. We make these sub-source nucleation point estimations dependent on other geometrical source parameters that defined the source's outline based on position, length, width and strike. These parameters are estimated not only from the BP results as outlined, but also from results of the surface displacement map segmentation introduced below (Section 3.3.2).

#### 3.3.1.6 Synthetic tests with multi-array backprojection

We evaluate the introduced multi-array BP method carrying out several synthetic tests. With these tests we assess the spatial and temporal resolution of the method and the capabilities to recover input models of earthquake sources. The station distribution that we use in these

synthetic tests is identical to the one that was available for an investigation of the intermediate-sized  $M_w$  6.6 Muji earthquake on 25 November of 2016, 14:24:30 (USGS) in the Pamir region (Fig. 3.1).

For the synthetic tests we use kinematic model parameters for a moment tensor point source or a finite rectangular source (see also section 3.3.3 and Fig. S1.1), equivalent to a Mw 6.6 earthquake. To model a segmented source with two sub-sources, we divide this seismic moment equally between the two sources. The medium model is based on the AK-135 global velocity model and we use 4 Hz Green’s functions based on the QSSP code by (Wang et al., 2017a) to calculate synthetic waveforms. The Green’s functions have been pre-calculated and stored (Heimann et al., 2019a). We carry out LF BP and HF BP with the frequency bands from 0.003 Hz to the corner frequency  $f_c$  of 0.25 Hz and from  $f_c = 0.25$  Hz to 1.5 Hz, respectively. The array weights have been bootstrapped 100 times and azimuthal array weights have been applied. To each synthetic waveform real pre-event noise from the corresponding real waveform record before the 2016 Muji earthquake is added.

In a first test Test 1 we estimate the ability of the multi-array BP method to recover the position of a single point source. The source is pure a double-couple with a triangular source-time function that has a duration of 3 s. The source is located at 8.7 km depth and the BP is calculated for a source point grid at that same depth.

The LF BP and HF BP results of Test 1 (Fig. 3.2) show that the source position can be well recovered within 2 km using LF BP and within 0.2 km using HF BP. Test 1 results with separate P- and SH-wave BPs can be found in the Supplement (Fig. S1.2). They give similar results as the combined P- and SH semblance results, but show systematically lower spatial precision compared to the phase-combined semblance results.

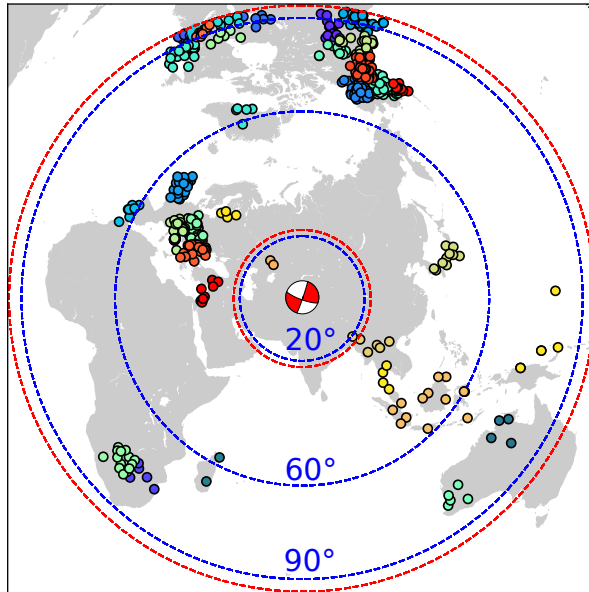


Figure 3.1: The stations used for the BP with the virtual clusters of the 2016 Muji earthquake plotted on a world map. The stations of the same virtual array have the same color.

In a second test Test 2 we keep all parameters as they are in Test 1, apart from the size of the virtual arrays, which may increase from an average aperture of 3.5 degrees in Test 1 to much larger apertures of up to 30 degrees in Test 2 (Fig. S1.3). The results of Test 2 (Fig. S1.4) show larger uncertainties in the precision for the position of the mapped semblance of about 50-60% in comparison to the smaller virtual arrays used in Test 1.

In Test 3 we further test the recovery of signals from a line source of 80 km length that ruptures

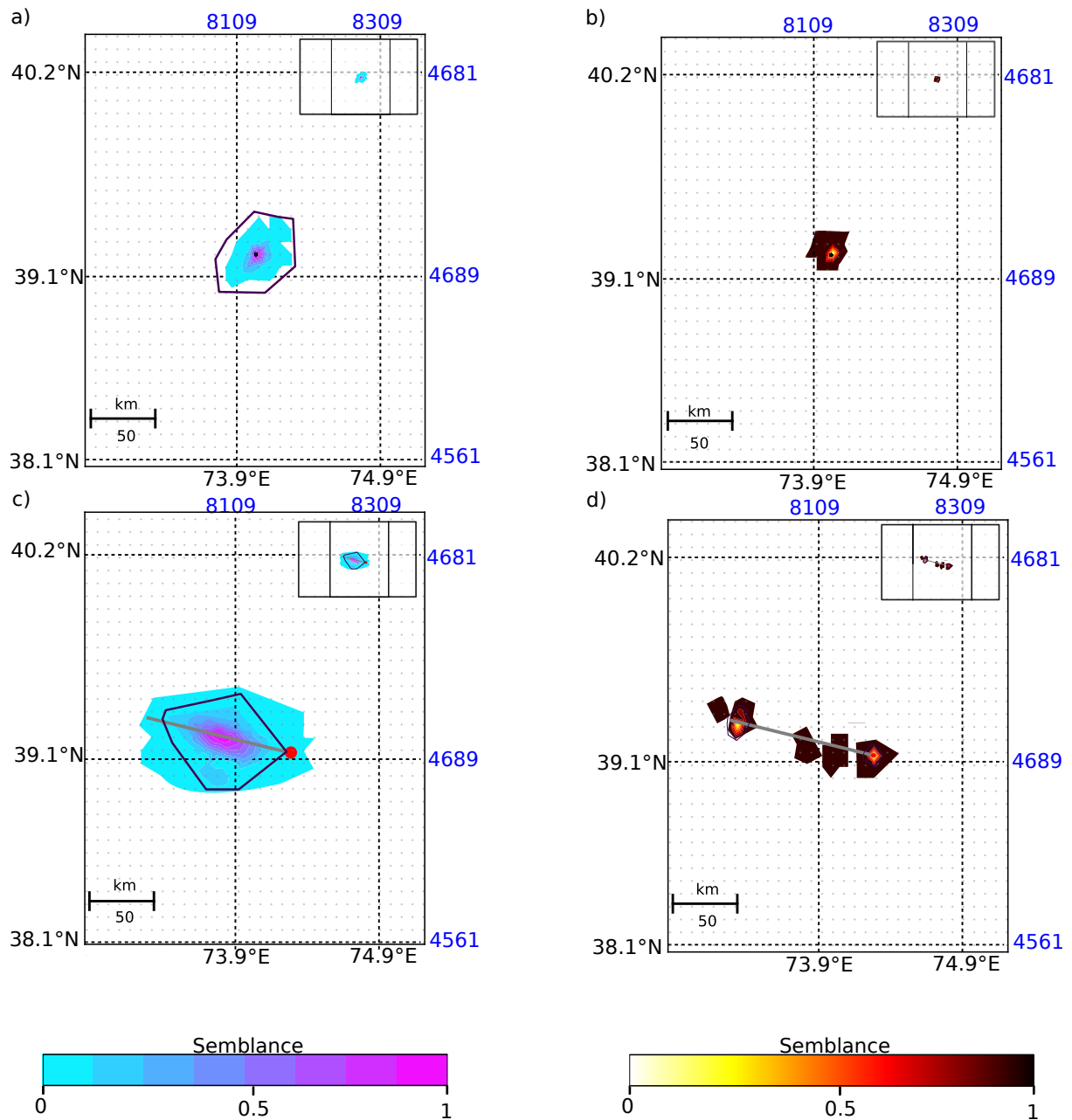


Figure 3.2: Cumulative LF and HF semblance for Test 1 (a,b) and Test 2 (c,d) as color-coded contours. a) LF and b) HF semblance of a double-couple source (Test 1). The black dot shows the model input position. c) LF and d) HF cumulative semblance of a line-source source (Test 2). Model outline and input nucleation point are indicated by a grey line and a red circle, respectively. In all subplots, the black outlines around high semblance values represent the 98 %spatial precision of the semblance maxima estimated from bootstrapping. Top-right insets in each subplot show the extent of the whole search grid. Gray background dots mask the BP source point grid. Coordinates are given in Latitude/Longitude (black labels) and UTM (blue labels).

unilaterally from the eastern edge with a rupture velocity of 4000 m/s. LF semblance shows a broader distribution (Fig. 3.2c) that well matches with the extent of the source. In HF semblance maps (Fig. 3.2d) two regions of high-energy release are recovered, which show well localized start and stop phases. The corresponding rupture velocity is derived from the distance between the first and last semblance maxima, which is here approximately 78 km and their time difference of 20 s. The resulting rupture velocity estimate is 3900 m/s (Fig. S1.6). The small difference of 100 m/s between input rupture velocity and recovered rupture velocity can be attributed to discretizations in the semblance calculation, both in space by the choice of the semblance calculation grid, and in time by the choice of time window sizes and time steps.

In a Test 4 we use two point sources with the same moment, duration and timing that are spatially separated by 50 km (Fig. S1.5). The individual locations of both sources are successfully recovered. The spatial precision for each source is about 20-30 km, estimated through bootstrapping and velocity model perturbations.

We also carry out all synthetic tests based on a different and more sparse station distribution that resembles the station situation at the time of the Mw 6.3 Ahar earthquake doublet on August 8, 2012. We use the real noise from before the Mw 6.3 Ahar earthquake to perturb the corresponding synthetic waveforms. The semblance resolutions in the results of these additional tests (see figures in Supplement 7), compared to the tests based on the Muji 2016 earthquake setup, suffer from the combined effect of mainly two factors. First, the Ahar earthquake has a smaller signal-to-noise ratio because of the smaller earthquake magnitude of Mw 6.3 compared to Mw 6.6 in the earlier tests. Secondly, the sparser station coverage at that time leads to a lower number of virtual arrays and therefore creates azimuth and distance gaps.

#### 3.3.2 Pseudo-probability of source location from image segmentation on InSAR displacement maps

The spatial pattern of coseismic surface displacement is to some extent characteristic for the properties of the source. It can therefore provide valuable source information before any inverse modeling. These apparent characteristics of the surface displacement pattern are that 1) the highest displacement gradients usually occur very close to the rupture, 2) loss of interferometric coherence, producing InSAR data gaps, can be caused by very high displacement gradients, surface rupture or near-fault landslides, 3) elongation of significant displacement is parallel to the strike direction of the causative fault and 4) sign changes of the displacement separate footwall and hanging wall of the faulting. Furthermore, complexity in these displacement characteristics hint at the occurrence of significant changes in source properties, e.g. distinctly separated regions of relatively high displacement gradients point to rupture segmentation. We formalize the extraction of displacement pattern characteristics by using image segmentation methods on the surface displacement maps. Based on the results we form a pseudo-probability map of the rupture location from which we then derive other first-order rupture properties in an automated framework as described in Section 3.3.2.1 below.

The here proposed image segmentation of InSAR surface displacement maps includes phase coherence evaluation, displacement gradient calculation, sign change tracing in the displacement amplitudes and combination of the resulting gradient maps. We describe and illustrate the steps in detail in the following and test them, based on synthetic displacement maps and a real-data example. The tests include the analysis of synthetic data of two vertical, two-segments strike-slip faults, one 6 km deep (top edge) EW-striking and one 1 km deep NS-striking faults, and real data of the 2009 L'Aquila earthquake in Italy, a shallow unsegmented normal-faulting earthquake. The first example resembles our application to the 2016 Muji earthquake (Pamir) presented below, and the second and third tests are set up to show a variety of mechanisms with

different imprints on InSAR displacement maps. Only the third, real-data example contains data gaps due to interferometric phase incoherence.

InSAR displacement maps show the three-dimensional surface displacement projected into the line-of-sight of the satellite. Different satellite look directions lead to different displacement projections, which cause apparent shifts of the surface displacement signals up to several kilometres between. We mitigate the projection effects by combining at least two different look directions, one from ascending and one from descending satellite tracks. For the synthetic tests the forward modeling was done using a layered 1-D velocity model (Xu et al., 2006; Li et al., 2018) and the PSGRN/PSCMP code (Wang et al., 2006a) to produce a Green’s functions database (Heimann et al., 2019a). We add synthetic correlated noise generated from real-data noise power spectra (Sudhaus and Jónsson, 2009).

The first step in our displacement gradient segmentation is treating incoherent areas that are either marked by no-data values or get marked, e.g. based on a coherence map and using a coherence threshold. Pre-processing of the displacement data should include deramping to minimise potential bias on results.

We assign a zero displacement value to incoherent pixels to enable numeric calculations and to contrast incoherent areas to areas showing large displacements. We then calculate the absolute displacement gradients for each pixel pair. For the displacement gradient map we apply a moving average across the pixels with Gaussian weighting using a window that spans about 500 m by 500 m in the examples (Fig. 3.3b and e). Next we trace sign changes of the displacement amplitudes. This is done based on a binary image that distinguishes positive and negative displacements, on which we apply the same gradient calculation with the same settings as described above. Non-zero gradients are normalized to 1 and effectively provide the sign change traces (Fig. 3.3c and f).

We determine the area of interest (AOI) as a minimum bounding box which comprises the 95% highest displacement values. For a pseudo-probability map of rupture location, we first combine the displacement gradient maps and the sign change traces for each data set individually by multiplying the two maps pixel-wise, with a relative weight in place based on the data set signal-to-noise ratios. Signal-to-noise ratio is evaluated between the signal in the area of interest and the noise from surrounding areas. The following processing steps include summing up the combined gradient maps of all available data sets, masking values of less than 1% of the maximum combined gradient, and applying a normalization (Fig. 3.3g). In other words, we keep the non-negligible gradient information only in places where there is displacement sign change in one of the data sets. In these remaining areas, the pseudo-probability of rupture location scales with sum of the displacement gradients from all data sets.

As a final processing step we aim to clean the simple pseudo-probability map of spurious pixels with non-zeros probabilities. A simple threshold for distinguishing signal and noise in the pseudo-probabilities seems inappropriate given the variety of displacement patterns. To best outline areas with significant pseudo-probability, we therefore apply the Otsu’s method (Otsu, 1979) thresholding to classify pixel-wise the pseudo-probabilities into signal and noise. The Otsu’s method is an iterative and exhaustive approach that seeks to minimize the differences of the pixel values in two distinct classes (Otsu, 1979; Shaus and Turkel, 2016).

In our first two tests with shallow and deep (top edge depth 0.5 km and 6 km, respectively), EW and NS striking strike-slip faults, the area of significant surface displacement and near-field of the rupture are highlighted well with relatively high gradients (Figs. 3.3 and S1.15, b and e). Together with sign change traces, the location of the causative fault is marked in the pseudo-probability map of rupture location. In the first test with a deeper source and a consequently lower signal-to-noise ratio the pseudo-probability is more scattered than in the second test. Still,

the highest pseudo-probabilities occur very close to the input fault in both cases (Figs. 3.3g and S1.15g).

For vertically dipping strike-slip faults, the displacement exactly above the fault is zero and coincides with high displacement gradients. For inclined and blind faults the so-called hinge line of largest displacement gradients will be offset in the direction of a projected surfacing of the fault, as is the displacement sign change.

A small signal-to-noise ratio of around 1 or less is in our experience challenging for the described simple gradient based sign-change tracing. In such cases, sign changes are abundant which results in very wiggly sign-change traces. Therefore, in these cases we substitute the gradient-based sign change tracing with less scattered contours of Chan-Vese image classes. The well established iterative Chan-Vese segmentation method (Chan and Vese, 2001; Getreuer, 2012) divides an image into two classes of minimum intra-class variance. These classes represent the topological changes of an image (Chan and Vese, 2001). The Chan-Vese image segmentation was applied in the real-data test to the 2009 L'Aquila earthquake displacements (Fig. S1.18).

In the displacement gradient maps the large window size used for averaging the gradients across pixels (500 m by 500 m) has the desired effect of a smeared-out gradient estimation. This estimation may therefore bridge over high gradient values surrounding incoherent areas. It also somewhat reflects the slightly ambiguous relationship between fault location and high displacement gradient location.

#### 3.3.2.1 Defining the model space based on displacement map segmentation results

The displacement pattern analysis using image segmentation methods (Section 3.3.2) provides a pseudo-probability map of rupture locations. Similarly to the methods we apply to the semblance maps, we use this pseudo-probability map to derive arbitrarily-oriented minimum bounding boxes and ellipses that enclose highly probable rupture locations, provide information on the probable number of rupture segments, and based on the ellipses individual segment dimensions and orientations.

On the pseudo-probability map of the rupture location we mark regions using the python scikit-image pack (Van der Walt et al., 2014) by evaluating the neighbourhood of each pixel to find connected pixels of any value, i.e. pixels share an edge or a corner. Connected pixels form regions, which potentially correspond to individual fault segments. A minimum size for a region can be given. A single connected region at this stage points to an unsegmented rupture. If, however, two or more of separated regions with extents larger than about 300 m in any direction occur, we apply minimum arbitrarily-oriented bounding boxes and ellipses to these regions to define the properties of those for potential sub-sources used in multi-segment or multi-dimensional fault modeling. We also apply a minimum arbitrarily-oriented bounding box and ellipse encompassing all regions.

Based on a single region or several, an arbitrarily-oriented minimum bounding box and an ellipse are defined each using the image processing algorithms provided by the scikit-image project (Van der Walt et al., 2014). The minimum bounding box length and width provide estimates of the fault length or segment length. The center of the best-fitting ellipse is defined by the focal point of the pixels within a region, with pixels of high pseudo-probability value having a large weight in this calculation. The major axis of the ellipse is likely a good indicator for the strike direction and is used as a prior. By slightly changing the threshold settings and minimum separation distance between patches to connect them to regions we retrieve a set of length and strike values for each region.

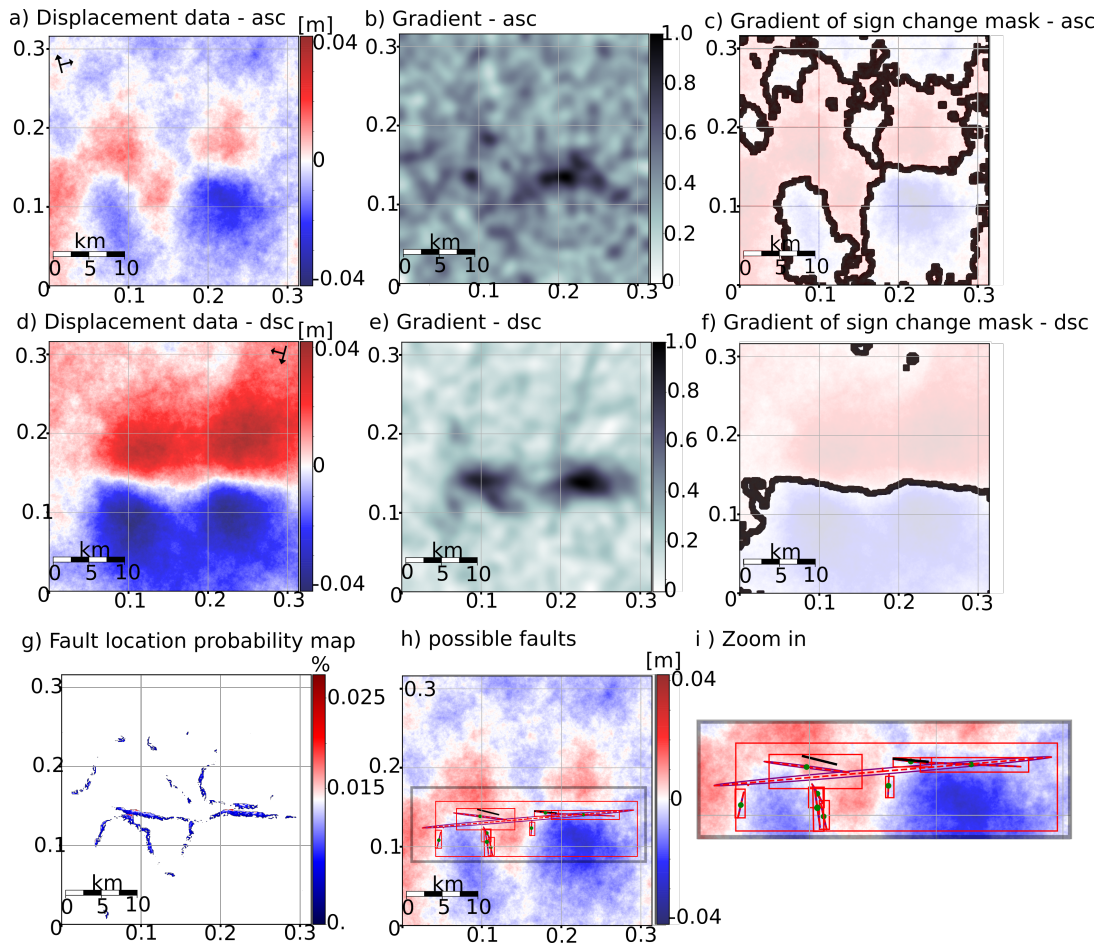


Figure 3.3: Image segmentation applied to synthetic displacement maps two-segments strike-slip source at 6 km depth (top edge). a) and d) show ascending and descending displacements, b) and e) the corresponding displacement gradients, c) and f) the corresponding sign-change trace (black) over the displacement. g) Pseudo-probability map of fault location. h) Bounding boxes and ellipses applied on g). The green box surrounds the area of interest, also enlarged in i). The red dashed lines indicate the major axes of the ellipses containing the highest pseudo-probability values in each region found as described above. The outline of the synthetic source(s) is indicated in the figures with black lines. The ellipse (purple outline) is centered at the centroid of each region.

We can now construct Gaussian distributed continuous pseudo-probabilities for the source parameters strike and length for each source from these estimates. The prior pseudo-probability functions are guiding the first stage of sampling the model space during the actual optimizations as described below.

### 3.3.3 Earthquake source optimization implementing data-driven model parameter prior distribution pseudo-probabilities

To characterize earthquakes we carry out a joint kinematic source modeling applying a non-linear, randomized direct-search optimization. We represent the co-seismic faulting with rectangular dislocations (see model sketch in Fig. S1.1b) embedded in a horizontally layered elastic medium. We optimize for each such dislocation the following model parameters: the fault location (north, east, depth), the fault dimension (length, width), the fault orientation (strike, dip), the slip, the rupture velocity, the relative position of rupture nucleation on the fault plane and rupture onset time. We define the fault location at the center of the top edge of the rectangular plane. An earthquake can be represented by more than one of these dislocations, e.g. if segmentation plays a significant role. For such segmented sources, the optimization setup enforces non-overlapping and non-intersecting dislocations.

The boundaries of the model parameter space in which the direct search optimization is applied and the model parameter prior pseudo-probability distributions, commonly called *priors*, have to be pre-defined. Here we set these based on the pseudo-probabilities of fault locations and the time evolution of the rupture estimated in displacement map segmentation and multi-array backprojection (Sections 3.3.2.1 & 3.3.1.5). We point out that the choice of the specific optimization method, with its objective function and model space sampling strategy, is independent from the presented approach. We use and extend the open-source optimization code Grond (Heimann et al., 2018b), which has the capabilities to estimate model uncertainties through the use of Bayesian bootstrapping.

Our optimization procedure works in adaptable sampling phases. The first sampling phase usually involves uniformly random sampling. It is followed by "directed" sampling phases that become more and more directed to good-fit models in the course of sampling. Each drawn model is evaluated against a set of different data weights, based on Bayesian random station weighting for the seismological data, and different noise perturbations for the static InSAR data. Source models are collected in a fixed-size highscore list for each of these sets of weights, forming a so called *bootstrap chain*. A detailed description of the method can be found in Section 7 and the online documentation (Heimann et al., 2018b). In the optimization we are seeking the minimum of the L2-norm between observed data  $\mathbf{d}_{\text{obs}}$  and predicted data  $\mathbf{d}_{\text{pred}}$ . The general form of this objective or *misfit* function is:

$$\|e\| = \sqrt{\sum (\mathbf{d}_{\text{obs}} - \mathbf{d}_{\text{pred}})^2}. \quad (3.11)$$

The prior information of source characteristics is taken into account from the start of the optimization by setting corresponding model parameter bounds and for some model parameters non-uniform prior probabilities. In this way we replace in our optimization a usually much more exploratory first phase of model space sampling, i.e. within wide bounds for the model parameters and with uniform random sampling therein, with a more focused and guided sampling. After a defined amount of sampling and based on a selection of low misfit models, the model space is reshaped and defined by the multi-dimensional distribution of low-misfit model parameters, the highscore list, which is constantly updated. In this way the start set of parameter bounds



and prior distributions is dropped such that the optimization is entirely driven by the objective function. Wide fall-back parameter bounds can be used to facilitate exploration.

### 3.3.3.1 Guided optimization

We call our first optimization phase that uses source parameter priors *guided* optimization phase to reflect the narrowed model space settings. We describe how we form model parameter prior distributions from either method, the multi-array BP (3.3.1.5) and the displacement map segmentation (3.3.2.1), individually. If both methods are used complementary, we first combine their pseudo-probability maps of rupture locations. We re-sample the grid of the BP location pseudo-probabilities to the grid spacing of the fault pseudo-probability map using a nearest-neighbor interpolation. We then combine these two prior distributions by multiplication. This procedure inherently gives weight to the better resolved prior parameter distribution of each method. From the defined joint discrete pseudo-probability functions the source models locations are sampled for a given number of models.

The horizontal location parameters in the optimization are relative east and north shifts in a metric coordinate system with the chosen reference location at the origin. If more than one source segment is considered, parameters of a single source segment are drawn first, which define the first segment’s outline. A second source is then drawn from the prior distributions and accepted if its outline is not intersecting the outline of the first source. A redrawing of models is necessary until this condition is fulfilled. This sampling scheme can be extended to an arbitrary number of sources.

For strike and length we also combine the Gaussian-distributed continuous pseudo-probabilities obtained from the multi-array BP and the displacement map segmentation methods by multiplication. In most cases this gives more weight to the displacement map segmentation methods result. The source parameters time and velocity are only drawn from prior distributions inferred from the multi-array BP.

### 3.3.3.2 Settings for the modeling of the far-field waveform data

For the forward modeling of seismic waveforms we make use of pre-calculated Green’s function stores (Heimann et al., 2019b) to speed up calculation. The Green’s functions stores (Heimann et al., 2017b) are calculated for up to 0.5 Hz using the QSSP code by (Wang, 1999) and are based on the AK-135 1-D velocity model (Kennett and Engdahl, 1991a). The Green’s functions are calculated with spatial sampling of 4 by 4 km and we enable continuous source-receiver distances by multilinear interpolation in space between the grid points.

Before the optimization we determine waveform balancing weights after Heimann, 2011 in an empirical way from 1.000 ( $k, \dots, K$ ) uniformly random models. This balancing corrects amplitude differences due to geometrical spreading, amplitude differences between P and S phases and different length of the cut-out windows. At each station ( $i, \dots, N$ ) and for each component (phase) ( $j, \dots, M$ ) we determine the balancing weights  $\mathbf{r}_{\text{balance},ij}$  as:

$$\mathbf{r}_{\text{balance},ij} = \frac{1}{\frac{1}{K} \sum_k |\mathbf{d}_{\text{pred}ijk}|}. \quad (3.12)$$

The objective function for waveforms that needs to be minimized is defined with Eq. 3.11 and

Eq. 3.12 as:

$$\|e\| = \frac{\sqrt{(\sum |\mathbf{r}_{\text{balance}} \cdot (\mathbf{d}_{\text{obs}} - \mathbf{d}_{\text{pred}})|)^2}}{\sqrt{\sum |\mathbf{r}_{\text{balance}} \cdot \mathbf{d}_{\text{obs}}|^2}}. \quad (3.13)$$

We calculate the misfit according to Eq. 3.11 for each waveform individually and thereby allow for an individual, fit-maximizing time shift from -4s to +4s. With those time shifts we account for traveltime deviations due to 3D velocity variation not represented in the AK-135 1-D velocity model.

### 3.3.3.3 Settings for the modeling of static near-field data

We use PSGRN/PSCMP (Wang et al., 2006a) to calculate static Green's function stores for the forward modeling (Heimann et al., 2019b).

We combine ascending and descending scenes into one data vector  $\mathbf{d}_{\text{obs}}$ . The data error is considered in Eq. 3.11 by a weighting matrix  $\mathbf{R}$  that derives from the data error variance-covariance matrix  $\Sigma$ :

$$\|e\| = \sqrt{[\mathbf{R}(\mathbf{d}_{\text{obs}}\mathbf{d}_{\text{pred}})]^T \mathbf{R}(\mathbf{d}_{\text{obs}}\mathbf{d}_{\text{pred}})}, \quad (3.14)$$

with  $\mathbf{R} = \sqrt{\Sigma^{-1}}$ .

Following the "Randomize-then-Optimize" (Bardsley et al., 2014) procedure we add synthetic noise, which modifies the objective function to:

$$\|e\| = \left\{ [\mathbf{R}(\mathbf{d}_{\text{obs}} + \epsilon_{\text{syn},i}\mathbf{d}_{\text{pred}})]^T \mathbf{R}(\mathbf{d}_{\text{obs}} + \epsilon_{\text{syn},i}\mathbf{d}_{\text{pred}}) \right\}^{1/2}, \quad (3.15)$$

with  $\mathbf{R} = \sqrt{\Sigma^{-1}}$ .

The seismic moment is calculated using  $M_0 = \mu AD$ , with shear modulus  $\mu$ , fault area  $A$  and the fault slip  $D$ . We use  $\mu$  based on the layered 1-d velocity for the region based on Xu et al., 2006 and Li et al., 2018. Additionally to earthquake source model parameters, three data ambiguity model parameters are used for each InSAR data set to remove any residual average data offset and a linear phase ramp in east and north direction.

## 3.4 Application to the 2016 Muji earthquake

### 3.4.1 The 2016 Muji earthquake

The Muji earthquake struck in north-eastern Pamir in the Chinese county Aketao on the 25 November of 2016 at 14:24:30 (UTC) and is sometimes also called Aketao earthquake in the literature after the region. It had a moment magnitude of  $M_w$  6.6. The rupture occurred along the Kongur Extensional System (Chevalier et al., 2011; Li et al., 2019b; Chevalier et al., 2015), located between the Tarim basin and the Muji-Tashkorgan basin. The 2016 Muji earthquake is the first instrumentally recorded earthquake of  $M_w > 6$  to have ruptured the transpressional Muji fault (Fig. 3.4). This fault bounds the south side of the Muji range and the northern margin of the Muji graben. In the east the Muji fault starts at the eastern side of the impact crater

lake Karakul (Gurov and Yamnichenko, 1995) and extends south-eastwards until connecting with the perpendicularly running Kongur Shan fault (Chevalier et al., 2011). Farther south the Kongur Shan fault ultimately connects with the major Karakoram fault.

The Muji fault accommodates EW extension due to the northward indentation of the Pamir salient (Chevalier et al., 2011). Fluvial terraces cover parts of the surface expression of the fault (Chevalier et al., 2011). Geological markers in the western part of Muji fault indicate right-lateral fault movement, while the eastern part of the fault displays mostly evidence of normal faulting that is associated with a small component of right-lateral movement (Chevalier et al., 2016; Chevalier et al., 2011). In field investigations Chen et al., 2016 found some surface breaks that appear to have formed co-seismically during the 2016 Muji earthquake.

The 2016 Muji earthquake has been studied by several authors who used InSAR, GNSS and/or seismic waveform data in earthquake source inversions (Li et al., 2019a; Feng et al., 2017; Bie et al., 2018; He et al., 2018; Ma et al., 2018), compiled in Table S1.2. They unanimously suggest a complex faulting mechanism that involves more than one fault segment. Feng et al., 2017 found the coseismic displacement signal to be consistent with two spatially separated segments.

He et al., 2018 first assumed for the 2016 Muji earthquake a listric geometry based on the aftershock distribution, but using geodetic data found a better fit to the data using a planar fault geometry. Bie et al., 2018 modelled the rupture using regional waveform data and estimated a sub-shear rupture velocity of 3.7 km/s as the most plausible scenario. Bie et al., 2018 also found a significant overlap of the modelled source-time functions (STFs) from the two sub-events, indicating a near simultaneous rupture of the two segments. In their study, the eastern sub-event displays a temporally more compact STF. However, they relate that the modeling of the STFs of the two sub-events proved difficult. Furthermore, Bie et al., 2018 state that they could not distinguish the rise and fall times for each sub-event. Bie et al., 2018 concluded that the 2016 Muji earthquake, being an intermediate-sized earthquake, has the smallest reported temporal gap between two sub-events upon publication date.

#### 3.4.2 Waveform data processing and multiarray BP setup

In our analyses of the 2016 Muji earthquake we use seismic waveforms from broadband stations with sampling rates of at least 10 Hz and with locations at teleseismic epicentral distances between 23° and 93°. The data are accessed via the FDSN services IRIS and Geofon, and additionally RESIF and ORFEUS for the multi-array BP. For the seismological waveform processing we use the Pyrocko software (Heimann et al., 2017b; Heimann, 2011; Cesca et al., 2010). We use a layered 1-d regional velocity model (Fig. S1.19) based on Xu et al., 2006 and Li et al., 2018.

For the teleseismic BP we can use the downloaded data without further manual data checks and/or selection. Through the stacking process for the BP noisy data and faulty response functions of singular stations have a comparatively small impact. The method strongly benefits from more stations and hence more virtual arrays. We resample the waveforms to a common 10 Hz, rotate the seismogram components into the source-centred RTZ coordinate system, and reconstitute the data to ground velocity by removing the instrument answer. While we use the frequency range from 0.003 Hz up to 1.5 Hz for the BP, we separate within that band a low-frequency and a high-frequency band at the estimated corner frequency, here 0.16 Hz, through bandpass-filtering as described in Section 3.3.1.3. We obtain two LF and HF waveform sets using the Z-components for P-wave BP and the T-components for the SH-wave BP. We show exemplary normalised waveform data and spectra of P-waves and SH-waves from an array with stations located between epicentral distances of 5633 km and 6243 km in Figures S1.21 and S1.22.

In our multi-array BP of the 2016 Muji earthquake we form 34 virtual arrays from 563 stations

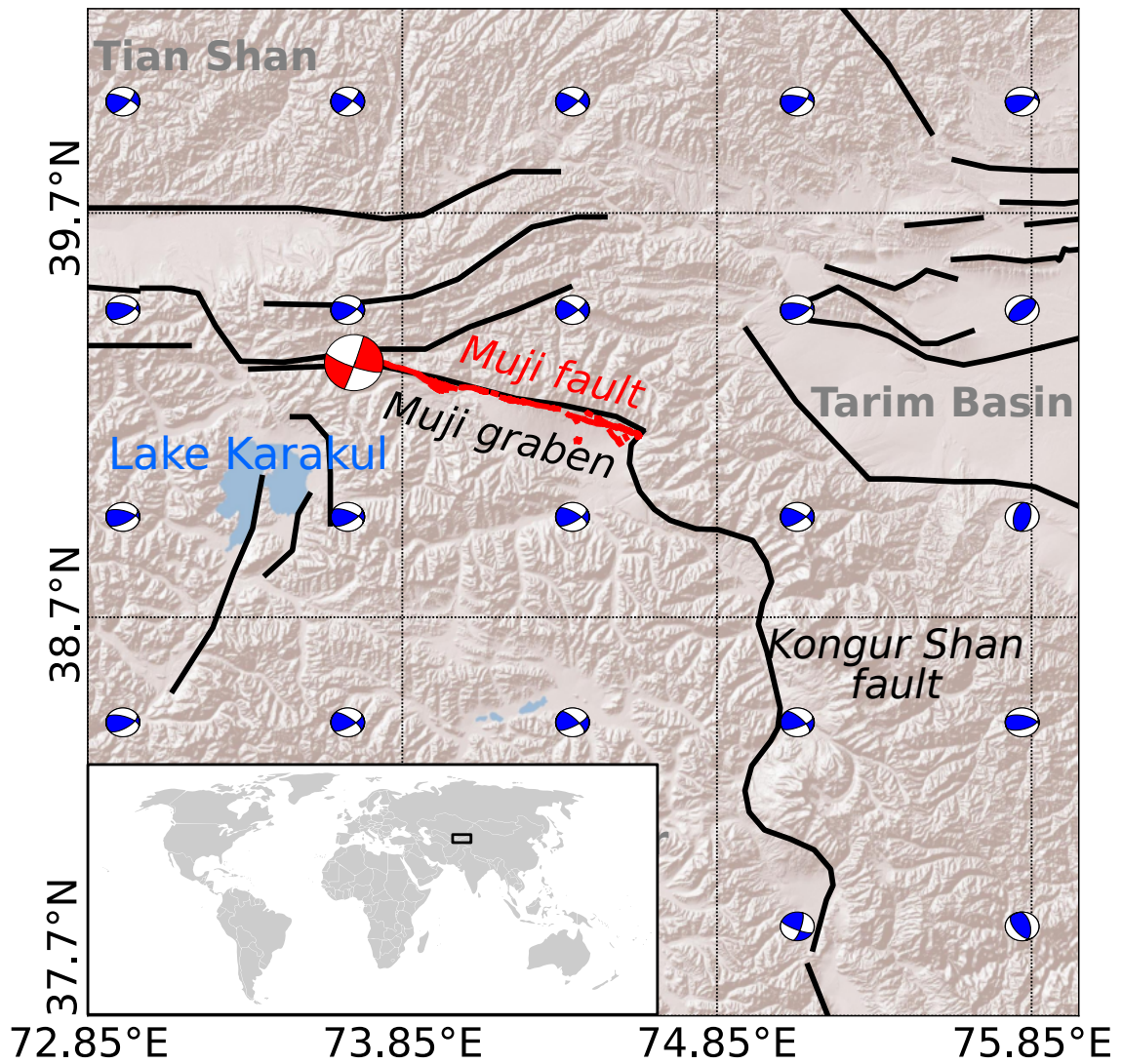


Figure 3.4: Setting of the Muji 2016 earthquake. Map of the region around the area of the 2016 Muji earthquake. Black lines indicate regional faults as mapped in the GEM fault database (Styron, 2019). Red lines are reported co-seismic surface ruptures (Li et al., 2019b; Chen et al., 2016). The red beachball indicates the USGS hypocenter and body-phase determined focal mechanism. Other beachballs are representing the potential focal mechanisms from the World Strain Map (Kreemer et al., 2014). Inset shows the location of the area on the world map.

in total (Fig. 3.1). The virtual arrays have a maximum aperture of  $5^\circ$  and at least 5 stations. To form an array in the Pacific we allowed for larger array apertures of up to  $10^\circ$  and decrease the number of required stations to 4, to increase coverage. The resulting average number of stations per array is 9. Most stations are located in North America and Europe. Only waveforms with a cross-correlation coefficient above 0.6 to the center-most station of each array are taken into account for further processing. The cross-correlation coefficient is calculated after shifting the waveforms with regard to the theoretical onset time given by the USGS hypocenter location and the velocity model. The horizontal grid of locations for which the BP is performed is at 9 km depth and extends 1.5 degrees around the USGS hypocenter. The grid spacing is about 0.018 degree or 2 km.

We apply phase-weighted stacking of the waveform sets in virtual arrays to calculate the multi-array semblance, as described in Section 3.3.1.1. For comparison, we show an example of single-array semblance formed with phase-weighted stacking together with the semblance formed with linear stacking in Fig. S1.20. To investigate the time evolution of the rupture we carry out BPs with moving times windows. In LF BP these time windows have a duration of 24 s and are moved by 8 s in each step. In the HF BP the time windows and step sizes are shorter with only 10 s and 2 s, respectively.

For the finite-rupture optimization we resample the waveforms to 0.5 Hz, apply a bandpass-filter from 0.01 Hz to 0.13 Hz and reconstitute the waveforms to ground displacement. For the P-wave we only use the Z-component of the waveforms and evaluate the full-waveform misfit in a time window from 15 s before to 25 s after the theoretical onset of the P-wave. For the SH-wave we use the T-component of the waveforms and evaluate the misfit in a time window from 25 s before to 35 s after the theoretical onset.

#### 3.4.2.1 Empirical traveltimes correction on the Muji earthquake waveform data

We apply empirical traveltimes corrections (see also Section 3.3.1.4) to the processed waveforms of the Muji earthquake. For the estimation of the corresponding traveltimes shifts we use as the reference event the Mw 5.2 November 25 earthquake in 2016, which occurred at 14:18:59, so 5:30 minutes before, and about 10 km south-east of the main shock. Its mechanism is similar to the main earthquake (USGS catalogue) but the source is about 10 km deeper. To estimate traveltimes shifts we use the exact same set up of stations, filters and array forming as for the main earthquake and maximise the semblance of the reference event for each waveform set independently (Fig. S1.23). For this operation we use a single time window of 32 s for the LF BP and 24 s for the HF BP, which begins 4 s and 6 s before the theoretical onset of the P- and SH-phases, respectively.

We find strong azimuthal correlations of traveltimes shifts between the stations (Fig. S1.23). In general, stations north of the event display negative time shifts and stations south of it positive shifts, for both P- and SH-waves. Also the differences between the empirically estimated time shifts found for the LF and HF BPs are generally small and in good agreement for P- and SH-phases. Only a few individual stations display significantly different time shifts to other stations of the same array and/or show a sign change in the time shifts between LF and HF BPs. For the P-waves time shifts are in the range of  $\pm 1.5$  s and increase for SH-waves to  $\pm 3.5$  s.

#### 3.4.3 Near-field data

For the estimation of the Muji fault location based on the gradient of the surface displacement data we employ an ascending and a descending SAR interferogram, based on Sentinel-1 interferometric wide-swath satellite data in VV polarization. The SAR data were downloaded from the

Copernicus Open Access Hub (<https://scihub.copernicus.eu/>). Primary and secondary image dates are 2016/10/20 and 2016/12/07 for the ascending data, and 2016/11/25 and 2016/12/19 for the descending data. The differential interferograms are processed using the ESA SNAP Sentinel-1 toolbox (s1tbx) and the SRTM elevation model (Farr and Kobrick, 2000). The interferograms have been filtered using an adaptive Goldstein filter with a window size of 16 and a filter factor of 0.8. Unwrapping was conducted using the tree-branch-cut algorithm (Goldstein et al., 1988), with a coherence threshold of 0.1. We account for the presence of correlated data errors in the displacement maps in the optimization. We empirically estimate the variance-covariance functions of the data error, assuming that they resemble Gaussian random field and stationarity (Hanssen, 2001a). This estimation takes place in areas of the displacement map that show no apparent surface movement. Before the kinematic source modeling using these data, their number is reduced through irregular data subsampling with the quadtree algorithm (Jónsson et al., 2002). Data error estimation, data subsampling and the implementation of the variance-covariance functions to build variance-covariance matrices for the subsampled data (Sudhaus and Jónsson, 2009) are done using the Kite software package (Isken et al., 2017b). For forward modeling the near-field displacement, we calculate Green’s function based on the layered 1-d regional velocity model by Xu et al., 2006 and Li et al., 2018.

### 3.4.4 Results

#### 3.4.4.1 Spatio-temporal evolution of the 2016 Muji earthquake

The LF (0.003-0.16 Hz) BP results of the 2016 Muji earthquake display two, in east-west direction spatially separated, high semblance regions (Fig. 3.5a). This pattern also appears in the individual BP results of P- and SH-phases (Figs. S1.27 and S1.28), with the P-phase BP providing somewhat better resolution. This semblance pattern points to a segmented rupture. The temporal evolution retrieved from LF BP in moving time windows suggests that the earliest coherent energy release took place in the western region before seismic energy excitation occurred in the eastern region (Fig. S1.24). The western region seems to remain activated throughout the duration of the rupture (Fig. S1.24). The LF BP results are used quantitatively to inform about the model space for the parameters onset time and rupture velocity (Fig. 3.8) in the optimization, and will be used as well to set model parameter priors for strike, length and position in combination with the results from the surface displacement image segmentation method results.

The HF BP results show spatially more localized areas of high semblance (Fig. 3.5b) compared to the LF BP results, while the location and orientation of LF and HF semblances agree very well. Also the time evolution revealed in HF BP is similar to the LF BP results, with some more detail (Fig. 3.6 and 1 s steps in Fig. S1.26). The first HF semblance peak occurs in the western corner of the Muji basin, close but slightly west of the Muji fault centre (Fig. 3.6b). All BP-derived semblance times are relative to this first occurrence of coherent energy mapping. This first semblance peak is associated with the strongest beampower of the sequence. The rupture then propagates simultaneously west- and eastward along the Muji fault (Fig. 3.6b-f). In the time from 6 s to 10 s seismic energy is continuously radiated in the onset area, in the area within 15 km east of it and also slightly west of it. At the latest stage of the rupture, between 12-14 s, the second strongest semblance peak within a somewhat widespread semblance high is found, located almost 30 km west of the onset peak. The location precision estimates based on bootstrapping (Section 3.3.1.1) range from 5 km to 15 km (Fig. 3.6). From the HF BP spatio-temporal semblance results of the 2016 Muji earthquake we estimate a rupture velocity, considering fault segmentation, and the length of segments. For each segment we take the distance and time between the first and last occurrence of HF semblance in the time-incremental

semblance maps as nucleation and stop phase, respectively. For the western segment these estimates deliver rupture velocities between 1.8 km/s and 2.1 km/s (Fig. S1.25) and for the eastern segment between 2.1 km/s and 2.6 km/s. Using straight-line distances between the semblance peaks and ignoring the first peak as potential nucleation point, because of the indications that the rupture is likely bilateral our method estimates for the western segment a length of 25 km to 30 km and for the eastern segment a length of 10 km to 15 km. The source parameter estimates for length, rupture velocity and the locations of the nucleation points for each fault are used as described as prior information (Fig. 3.8) for the guided optimization.

Based on InSAR data of the 2016 Muji earthquake we create a pseudo-probability fault location map applying image segmentation methods (Section 3.3.2). As detailed in the given section, we use the interferometric phase coherence, the displacement gradients and sign changes of the displacement to get information on the deformation source (Fig. 3.7). Based on the pseudo-probability fault location map (Fig. 3.7,g), we surround all areas that mark a high pseudo-probability of fault activation with a single minimum bounding box (Fig. 3.7,h) to estimate the dimension of the entire fault. Furthermore, we identify two distinct areas with high pseudo-probability of fault activation and enclose these with bounding boxes and ellipses, respectively (Fig. 3.7,h). We interpret these separated areas as markers for two distinguishable fault segments, which we represent with two kinematic sources in the optimization. For each segment we estimate independent parameter priors. The source parameter priors for length, strike and position obtained agree well with literature values (Fig. 3.8, Tab. S1.2).

#### 3.4.5 2016 Muji earthquake two-segment rupture optimization results

##### 3.4.5.1 Exploratory and guided optimizations of the 2016 Muji rupture using the same data

We carry out two independent non-linear kinematic source optimizations for a two-segment fault model, without and with including prior information from data analyses as described in the method section (3.3.3). From the Bayesian bootstrapping of the data we realize 100 sets of different combinations of objective functions and realize 100 bootstrap chains, each based on a different combination of target weights and different realizations of noise-perturbed data. We use the same random seeds in both optimization to create the same random weights and noise-perturbations. The highscore list of models, on which the statistics for new model samples are generated during the direct search, keeps a fixed number of  $4 \cdot n_{\text{par}} + 1$  low-misfit models.

For the exploratory optimization we choose parameter bounds as could be chosen by an informed and cautious, conservative investigator, who has had access to the BP results and the displacement maps. For the source locations this results in 20 km wide ranges for north and east source locations around the approximate center of the signals. For the onset time of each source the parameter range is set from 0s to 20s for both sources, with 20s roughly being the rupture duration as given by the SCARDEC catalog (Vallée and Douet, 2016) for the 2016 Muji earthquake. To pre-constrain the source mechanism parameters (strike, dip, rake), we set 80 degrees wide parameter bounds, centered around the expected focal mechanisms from the World Strain Map (Kreemer et al., 2014). For each source the model parameter slip can range from 0 m to 4.5 m, the parameter width from 0 m to 15000 m and the depth (top edge) from 0 m to 7500 m. The prior probability is uniform for all these parameters.

For the optimization starting with the guided phase we base the model parameter prior distributions on the available estimates of the BP results and/or the displacement map segmentation, or the same priors as in the exploratory optimization. The aim is to well constrain the 2016 Muji



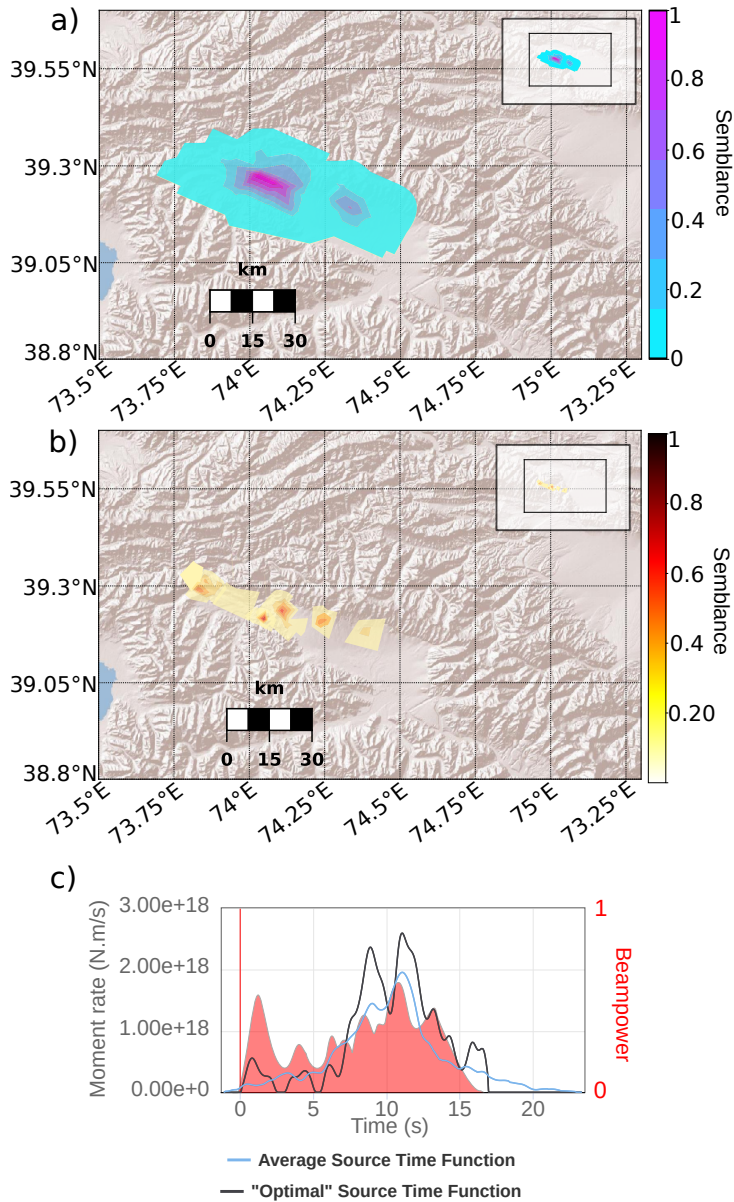


Figure 3.5: Cumulative spatial semblance map for the (a) low- and (b) high-frequency BPs. Contour lines are colored after the cumulative semblance. The figures are a zoom in upon the area of interest from the main grid. The inset window in the top right shows the extent of the grid. C) Beampower of the high-frequency BP as a function over time as a red and filled function of time together with the optimal (black line) and average (blue line) source time functions from the SCARDEC catalog (Vallée and Douet, 2016).



### 3 Data-driven constraints on earthquake modeling and rupture segmentation

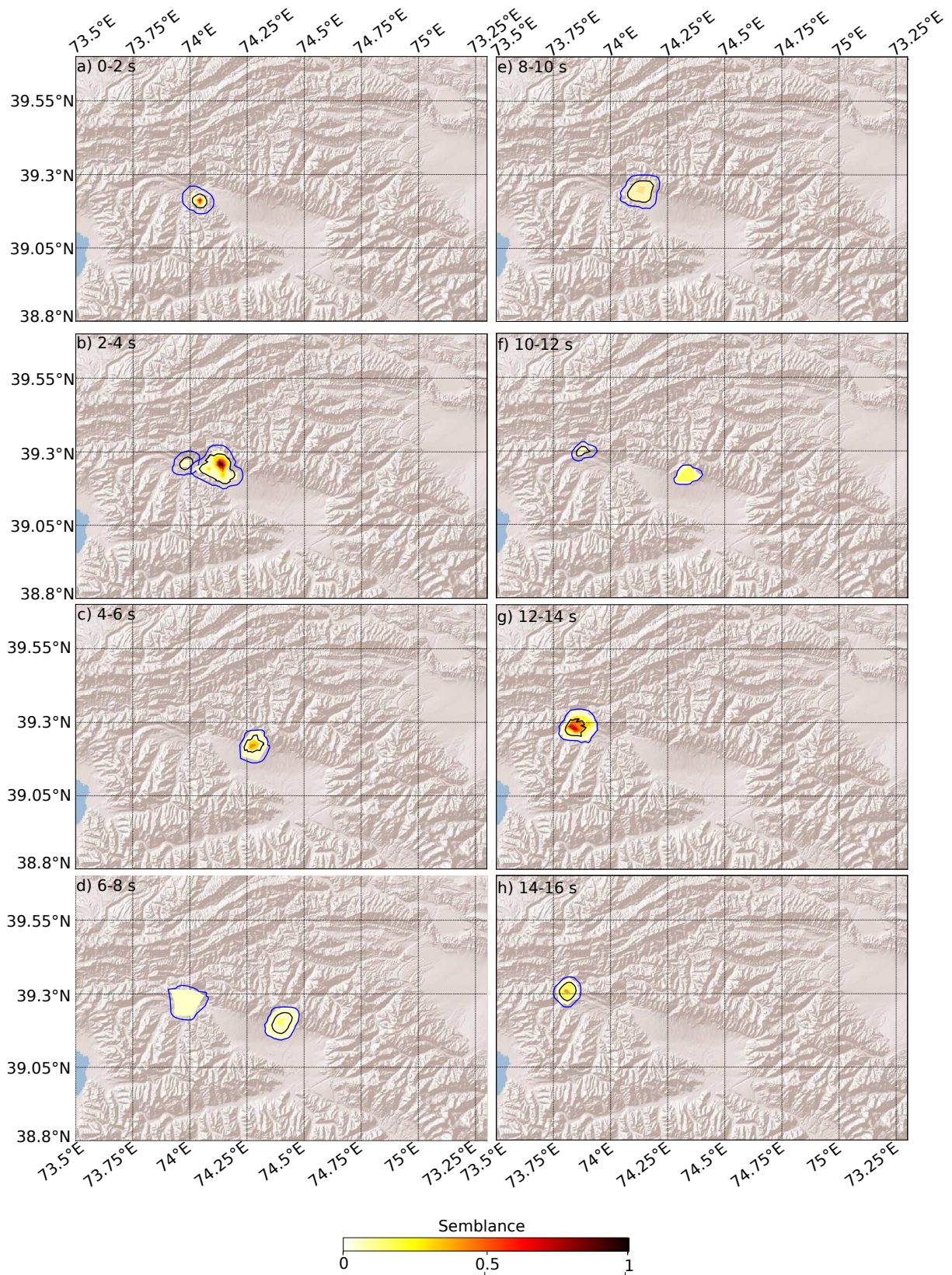


Figure 3.6: HF BP incremental spatial semblance map for 10 s time windows moving with 2 s time steps. Solid outlines mark 95% (black) and 68% (blue) of all maximum semblance locations from bootstrapping.

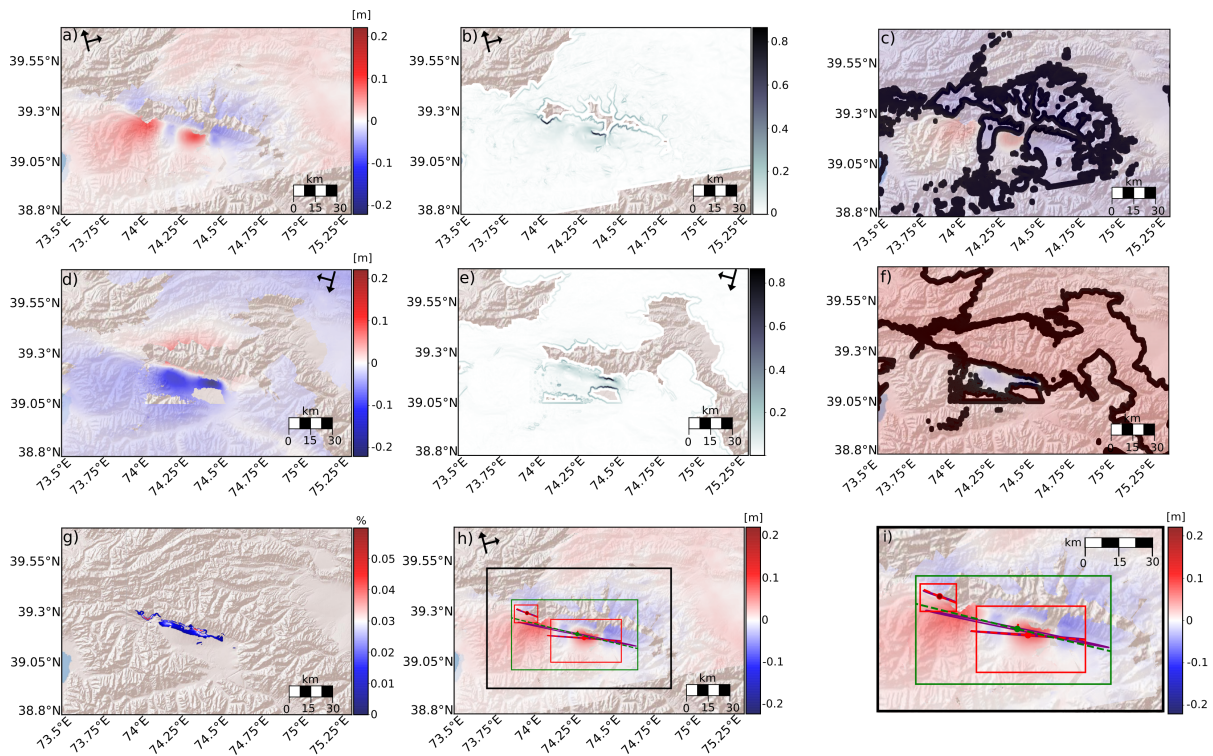


Figure 3.7: Displacement map segmentation results for the 2016 Muji earthquake. a) shows the ascending line-of-sight displacement data, (b) the corresponding gradient map and c) the gradient of the sign change mask, superimposed on the displacement data. d) shows the descending line-of-sight displacement data, e) the corresponding gradient and f) the gradient of the sign change, superimposed on the displacement data. g) Combined pseudo-probability map of fault location adding ascending and descending pseudo-probabilities. h) Minimum bounding boxes and ellipses on the pseudo-probability maps in i), enclosing the automatically determined area of interest (black box), enclosing all high pseudo-probability values (green boxes, long purple ellipse), and the separated areas of high pseudo-probability (red boxes, small purple ellipses). Major axis of the ellipses and centroids are shown as dashed lines and dots the corresponding colors for single and two segments estimations. The background shows the ascending displacement map for visual reference. i) Zoom in on the area of interest (black box in h).

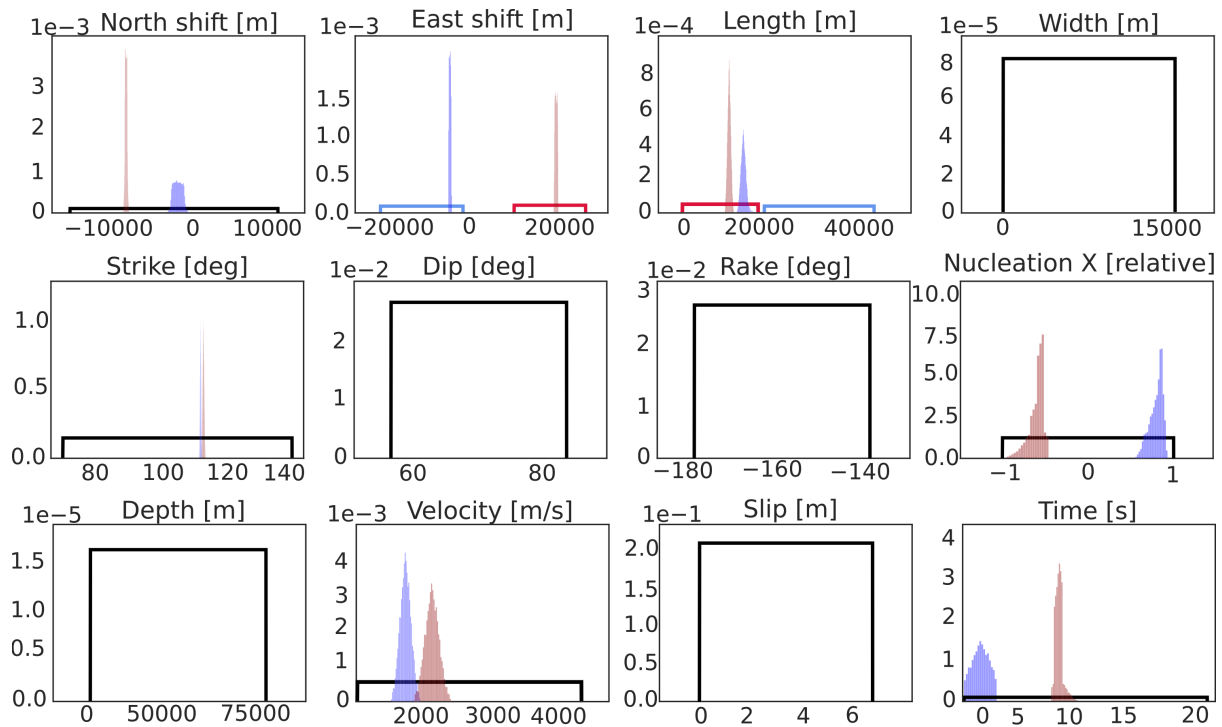


Figure 3.8: Model parameter space for the guided optimization of the Muji 2016 earthquake as specified through BP and displacement map segmentation or otherwise assumed. Black box outlines mark assumed uniform prior probabilities without any data analyses, while colored boxes and histograms show uniform or non-uniform inferred prior pseudo-probability functions for the parameters. Colored pseudo-probability functions mark priors for the two distinguished source segments in the western (light blue) and eastern (light red) part of the fault.

faulting and to compare the results of the two different optimization runs in terms of source results and performance.

In general, both optimizations converge to very close locations within the high-dimensional model space such that parameter marginals mostly cover the same parameter ranges (Fig. 3.9). The spatio-temporal evolution of the best model of the guided optimization more closely resembles the inferred spatio-temporal evolution of the BP result, in contrast to the best model of the exploratory optimization (Fig. 3.10). The inferred result from the guided optimization and the inferred BP result is however part of the ensemble of the exploratory optimization. The exploratory optimization needs more sampling to converge compared to the optimization that starts with the guided sampling (Fig. S35). The corresponding posterior probabilities have not always the same shape and also, the best-performing source models from both these optimizations are not very similar (Fig. 3.9 and Figs. S36 and S37). The best model of the guided optimization is a subset of the exploratory optimization source parameter estimates, but is not the best performing model in that ensemble. The misfit of the best fitting model from the exploratory optimization is lower than from the best fit model of the guided optimization (Fig. S35). We note that for the guided optimization several source parameters estimates converge, e.g. nucleation  $x$  and time, which do not converge in the exploratory optimization. The source parameter estimates and especially the best model of the guided optimization also represent the results of the backprojection much better (Fig. 3.10). Fits for the static displacement data can be found in Figure S1.31 and for the waveforms in Figure S1.32 with trace weights at stations shown in the Figures S1.34 and S1.33. The best fit model of the exploratory optimization produces better fits for some waveforms but performs worse for the static displacement fits in comparison to the best fit model of the guided optimization.



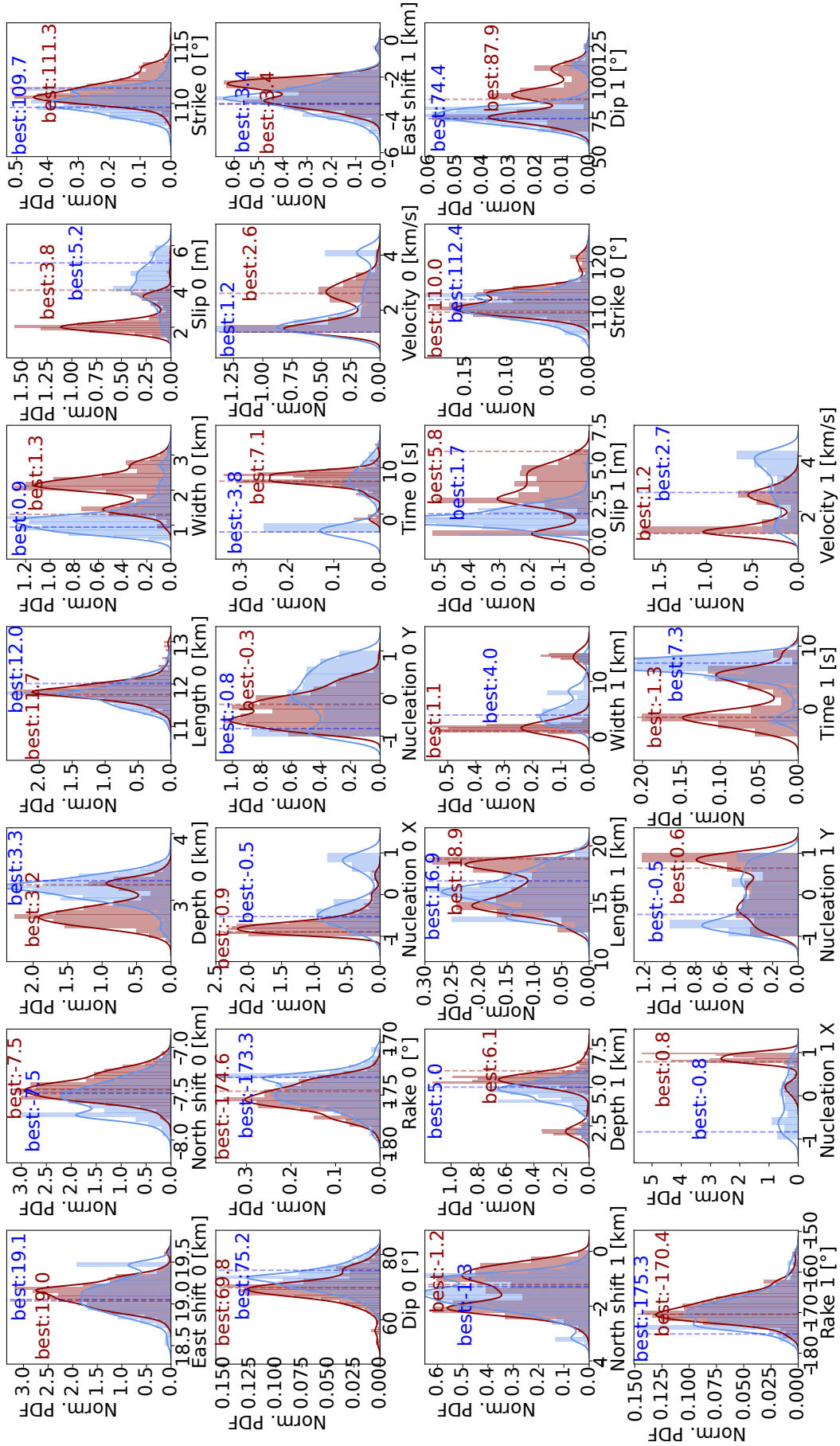


Figure 3.9: Histograms of the source parameter estimates for the exploratory (blue) and guided (red) optimizations. The best models are indicated by a dashed line. Source parameter names are indexed with 0 for the eastern segment (e.g. "Depth 0") and with 1 are for the western segment.

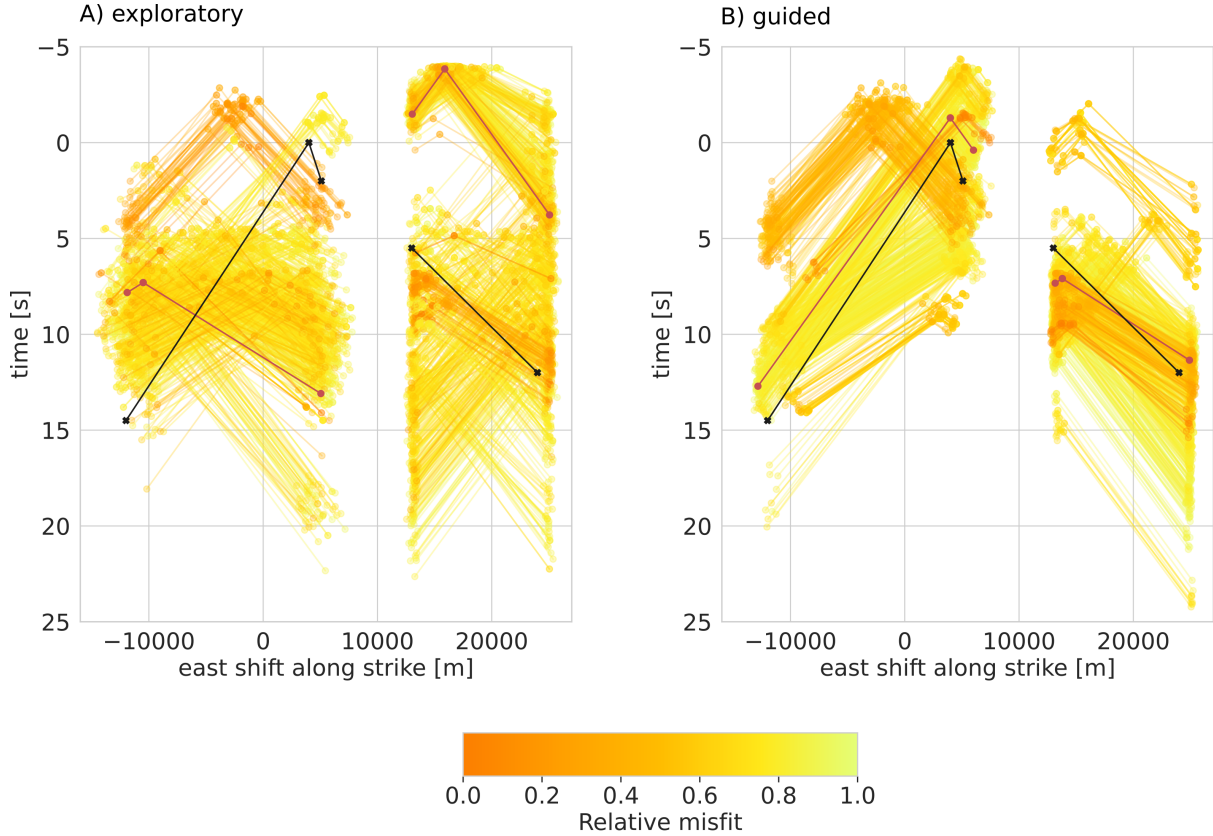


Figure 3.10: Rupture nucleation and termination times plotted as a function of distance along strike for each source segment for both exploratory (a) and guided (b) optimization ensembles (b). Single models are colored by misfit with the best model drawn in black. The corresponding unweighted HF BP result is shown with a red line.

### 3.4.5.2 Backprojection of synthetic waveforms from the 2016 Muji minimum-misfit kinematic source model

We test if the waveforms of our best-fit two-segment source model of the 2016 Muji earthquake lead to similar spatio-temporal semblance results in a multi-array BP as the observed waveforms. To synthesize waveforms we use the same assumptions for the medium model as in all other analyses and calculate synthetic waveforms up to frequencies of 8 Hz for the same stations that we used in the real-data BP and we apply the same BP settings (Section 3.5). We add no noise to the synthetic waveforms.

We obtain LF and HF BP results for synthetic P- and SH-phases shown as cumulative semblance maps in Figure 3.11 and as time-incremental semblance maps in Figure S1.30). The semblance maps strongly resemble the real-data semblance maps (Fig. S1.24 and Fig. 3.6). They show very similar locations and numbers of high-semblance peaks. The synthetic semblance is spatially somewhat more focused, particularly for the LF BP. We also carry out a synthetic BP for a best-fit single-segment source model of the Muji 2016 earthquake (Fig. S1.29). Overall the synthetic BP results of the two-segment source model match the real-data semblance pattern more closely than the BP results of the single-segment source model. The synthetic LF semblance map for the single-segment source model shows a single high-semblance peak only, which is further east compared to the real-data LF semblance map. The HF synthetic semblance is missing the particularly strong central semblance peak apparent in the real-data HF semblance map. Both these features and the timing of semblance peaks are well reproduced using the

two-segment source model.

## 3.5 Discussion

### 3.5.1 Discussion of multi-array backprojection

The presented multi-array BP shows in synthetic tests a pleasingly high performance in recovering the horizontal location, the time, and rupture history with high accuracy. In comparison to BP using data from a large array, our multi-array BP with many small-aperture arrays clearly achieves stronger spatial focusing of seismic energy (Fig. 3.2b and Fig. S1.4). The presented multi-array BP has been applied successfully to other earthquakes already, e.g. the 2016 Mw 7.1 Romanche transform-fault earthquake (Hicks et al., 2020b) and the 2008-2009 Qaidam earthquake sequence (Daout et al., 2020b).

The focusing ability of our multi-array BP in depth direction is less precise compared to the horizontal resolution. The reason is that the depth direction is subparallel to the dominant path of wave propagation from shallow earthquake sources to far-field stations of a global network. Therefore, multi-array BP shares the generally relatively poor depth resolution for Mw 6-7 earthquake studies based on the global network of seismic station (Engdahl et al., 1998; Maggi et al., 2002), which may only be improved using more sophisticated methods (Craig, 2019). To account for poor depth resolution, our multi-array BP uses a purely horizontal grid of source points at a fixed depth. Seismic energy that is emitted at depths below or above to the chosen grid depth may appear horizontally shifted to the real horizontal location in the corresponding semblance maps. The accuracy of the location of the semblance therefore depends on an appropriate grid depth compared to the seismic source and may generally vary across the semblance maps for ruptures with a large depth extent.

Potentially an inclined source grid representing a known fault could be implemented in our multi-array BP to circumvent such a bias. However, the fault geometry should be well known, since wrong assumptions on the plane location and orientation will again lead to shifts in the backprojected seismic energy. For many applications, in particular those similar to the here presented earthquake case studies, fault location and fault geometry are unknowns to be constrained in the problem. Using a volume of grid points for the BP is possible as well and could be implemented in the presented framework. However, this requires a source-station configuration with many near-enough stations providing sufficient resolution in depth to enable focusing in this direction. In the general case, using a horizontal grid is in our eyes the least strict assumption.

From the LF and HF BP results of the 2016 Muji earthquake (Figs. 3.5, S1.24 and 3.6) we infer the spatio-temporal evolution of the rupture. The 2016 Muji rupture starts at the eastern end of the western segment and from there propagates simultaneously eastwards and westwards. The time-incremental high-frequency semblance maps show five peaks within the duration of 15s. We interpret the first semblance peak as a representation of the rupture nucleation or start phase. We then observe slow rupture propagation from the nucleation point to both the east and west from that potential nucleation point. A second mapped semblance peak occurs east of that location, which we interpret as a rupture stop phase at the eastern end of the western segment. A third semblance peak occurs seconds later some five kilometers to the east, which likely represents the start phase on the eastern segment. No coherent seismic energy emission is mapped between the locality of these two mapped semblance peaks in either the low-frequency or the high-frequency semblance maps. Another high-frequency semblance peak occurs several seconds later to the east of the third peak, possibly representing the stop

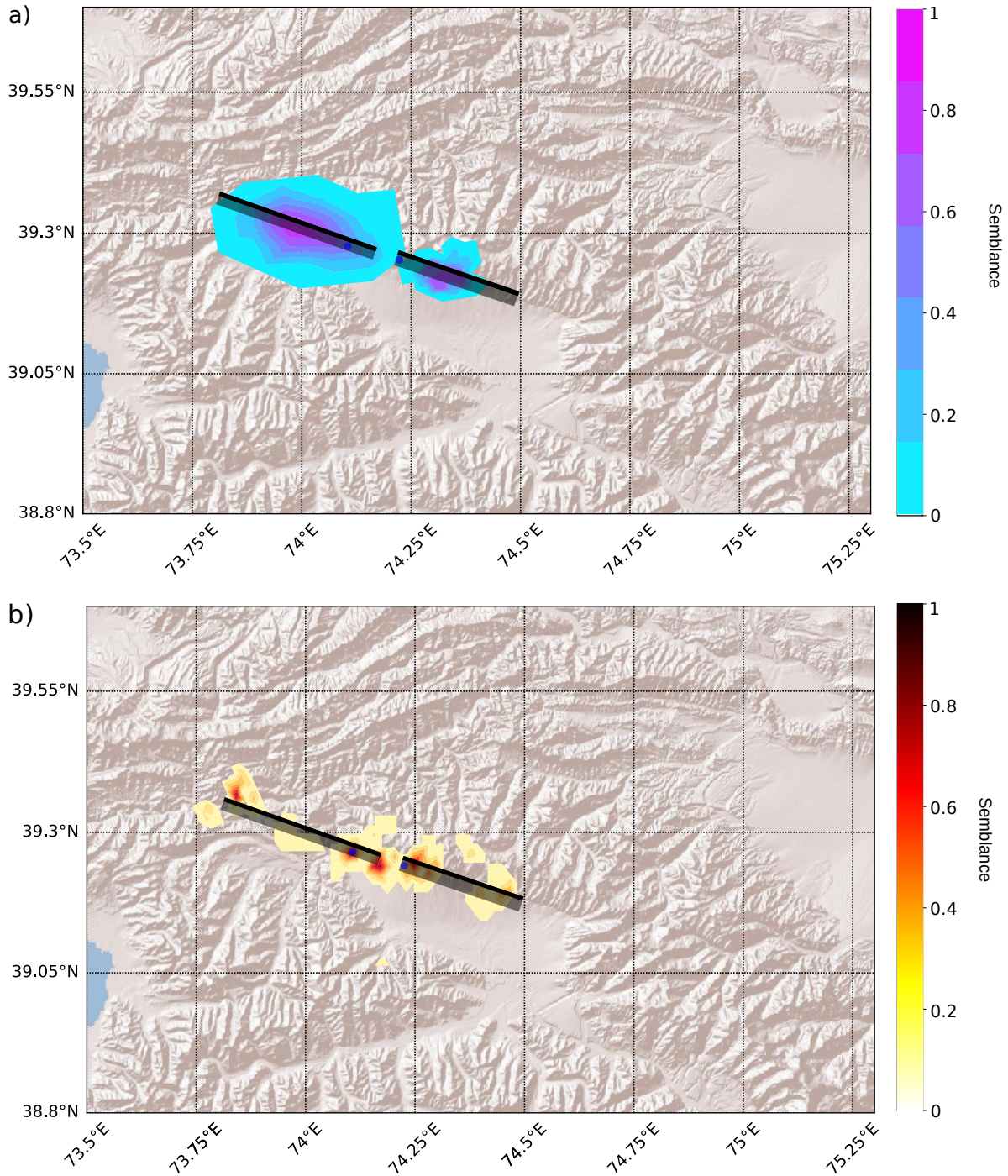


Figure 3.11: Contour plots of the LF (a) and HF (b) cumulative semblance from BP of synthetic waveforms of the minimum-misfit, two-segments kinematic source model. The source segment outlines are shown as gray-shaded rectangles, with the thick lines indicating the upper edges. Blue circles give the positions of the rupture nucleation points on each segment.



phase on the eastern segment. The last high-frequency semblance peaks is mapped 30 km west of the first semblance occurrence and potentially indicates the western-end stop phase of the western segment. We observe two distinct and separated patches of significant semblance in the low-frequency semblance map, which indicate a rupture segmentation. We interpret the time-incremental LF and HF semblance map as a bilateral rupture and the rupture jumping from the western segment to the eastern segment without emitting coherent seismic energy in between. This agrees with a previously postulated slip gap between the two segments (Feng et al., 2017). The area where the rupture segmentation and slip gap occurs coincides with mapped fluvial terraces that show a right-lateral offset across the Muji fault (Chevalier et al., 2011) and lies at the outlet of the longest glacial valley in the Muji range. The termination of the rupture on the western segment is located at a previously mapped discontinuity in the surface fault traces (Chevalier et al., 2011). We find a co-location of significant static surface displacement and the cumulative LF semblance map in the near field of the 2016 Muji earthquake. Such an agreement is to be expected and it has been observed before (Okuwaki et al., 2018; Yin and Denolle, 2019). Since static surface displacement correlates strongly with moment and therefore with fault slip, it is in close neighborhood to the excitation of seismic waves. A similarly good agreement between static InSAR surface displacements and the semblance from multi-array LF BP has been found for the 2008 and 2009 Qaidam earthquakes (Daout et al., 2020b).

We estimate the rupture velocity of the 2016 Muji earthquake based on the HF spatio-temporal semblance to be within the range from 1.8 km/s to 2.1 km/s for the larger western segment and from 2.1 km/s to 2.6 km/s for the eastern segment (Fig. S1.25). These velocities are much slower than the rupture velocity of 3.7 km/s found in the Muji source analysis by Bie et al., 2018 for their most plausible scenario, based on the inferred source time functions and the rupture geometry. Bie et al., 2018 see a significant overlap of the two modelled subevent source-time functions that seems to indicate a near simultaneous rupture of both rupture segments. HF semblance peaks in the BP results appear co-located with boundaries of high gradients in static InSAR surface displacements. This is similar to results found for the 2008 and 2009 Qaidam earthquakes (Daout et al., 2020b). Furthermore, no HF semblance is mapped in the area of an apparent slip gap between two regions of high static surface displacement. The first HF high-semblance peak that is close to the eastern edge of the western segment and the rupture seems to propagate through or jump the area which has been identified in previous studies as a slip gap (Bie et al., 2018; Feng et al., 2017), without emitting significant coherent seismic energy within the frequency bands considered in this study. The rupture on the western segment appears to start slow (Fig. 3.6b). The estimate of the rupture velocity on the western segment is likely representing an average between the initial and late stage rupture velocities (Fig S1.25). The total duration of the rupture as inferred from the beampower of our multi-array BP agrees well with the duration of the optimal SCARDEC source-time functions (Vallée and Douet, 2016), see Fig. 3.5), but is shorter by 1 s or 2 s in comparison to the average SCARDEC STF. Further comparisons between STFs and beampower, e.g. in shape, are not meaningful, since they represent different measures of the rupture process.

Intriguing is the strong resemblance of the real-data multi-array BP semblance with the semblance based on synthetic waveforms of the best-fit two-segment source model (Fig. 3.11), despite the fact that the kinematic source model is rather simple. It consists of only two rectangular source models with uniform slip and constant rupture velocity. Already such first-order source characteristics appear to describe the source well enough to well predict the waveforms up to a frequency of at least 1.5 Hz. It proves that our multi-array BP can reveal source geometry properties as well as other first-order rupture parameters for  $M < 7$  earthquakes. Multi-array BP shows a high potential to add value in future inverse source modeling problems.

### 3.5.2 Surface displacement map segmentation method

The image segmentation methods that we apply on surface displacement maps to extract probable fault traces prove to work well in synthetic tests (Figs. 3.3, S1.15 and S1.18). They enable recovering of the true source position with an accuracy of 100 m and the true length with an accuracy of 500 m. The inferred fault traces are closely located to the well studied fault traces for the 2016 Muji and the 2009 L’Aquila earthquakes. However, we caution against the direct use of the inferred fault trace location in fault mapping or as a fixed position in source optimizations, for a number of reasons. First, it is debated how well observed surface ruptures and surface deformation represent the slip and fault geometry at depth (Dolan and Haravitch, 2014; Soliva et al., 2008). Second, we observe biases in the fault trace location estimates for deeper earthquake sources and due to the line-of-sight projection of the three-dimensional surface displacement in InSAR data. Using more than one dataset that have different line-of-sight vectors will reduce this bias to some degree. We also note that the method might be susceptible to a very heterogeneous slip distribution. We underline again that the aim of the method is not to find the true fault line but rather derive pseudo-probabilities of the fault location for prior model parameter distributions. The assumption of the here used very simple source geometries, e.g. a planar fault, is suitable for low-parametric source modeling.

Our application of surface displacement map segmentation was very successful in synthetic tests (Figs. 3.2, S1.29, S1.5, S1.2 and Figures in Supplement 7) and on the InSAR data of the 2016 Muji earthquake. The co-seismic fault trace identified in previous studies (Li et al., 2019a) agrees well with the result of our obtained fault pseudo-probability map (Fig. 3.7) and we note an agreement of the inferred fault traces (Fig. 3.7) with the field mapping of the Muji fault trace (Chevalier et al., 2016; Chevalier et al., 2011) and the reported co-seismic surface ruptures (Li et al., 2019b; Chen et al., 2016).

The presented set of methods is straightforward. We believe that with few modifications only they can be applied to pixel-offset maps from optical images and to wrapped-phase interferograms. The image segmentation can be profitable also as a stand-alone signal detection method that in an automated way is used to detect significant deformation signals at specific sites and in big-data catalogues. As we show, the method is suited to produce fast estimates of source parameters. The method can be applied to big-data catalogues of InSAR surface displacements to automatically identify and characterize first-order source parameters.

### 3.5.3 Guided optimization

In our guided optimization we use the source parameter pseudo-probabilities which we estimated beforehand based on the multi-array backprojection and the image segmentation of surface displacement maps. With these source parameter prior distributions we succeed in automatically tailoring the model space for an efficient start of the direct parameter search. The guided optimization, in comparison with a more exploratory optimization, needs significantly less sampling to converge. It is not possible to give a simple indicator on performance gain here, because the gain strongly depends on the model parameter space that is chosen for the exploratory optimization, which in itself strongly depends on the problem. Usually, the model space of exploratory optimizations is either based on parameter bounds chosen by the researcher based on earthquake information, data visuals, experience and else, or on very wide parameter ranges that allow for almost all possible solutions. In the first case the benefit of the here proposed methods stems less from the potentially reduced optimization cost, but rather from the reduced need of supervision by a human researcher. In the latter case the gain will definitely be largely reduced computational cost, while the implementation of multi-array backprojection and image segmentation comes at its own cost. From our point of view, the main advantage of including

prior information from multi-array backprojection method into kinematic modeling is that it gives physics-based evidence to model rupture segmentation with distinct sources.

Tailoring of the model space potentially excludes the global minimum model, which is a serious risk. While the chosen priors include extra margins from bootstrapping, we further reduce this risk by enlarging the model space after the initial tailored phase in the optimization. From this point of only the parameter distributions of low-misfit models drive the selection of new models in the widened model space.

We used some soft model space tailoring in the exploratory optimization as well, which also form the enlarged model space of the guided optimization after its initial phase. For the source parameters strike, dip and rake we based this soft tailoring on the expected focal mechanisms from the World Strain Map (Kreemer et al., 2014). Similarly we employed information from source time functions in the SCARDEC catalog (Vallée and Douet, 2016) for the onset time of 2016 Muji earthquake in the exploratory optimization. Both these data sources could also inform future operational source parameter optimizations in an automated fashion.

We demonstrate the practicality of the guided optimization in its application to the 2016 Muji earthquake. Here, it decreased the parameter ranges of the model space to be searched significantly. As a consequence, the guided optimization arrived comparatively early at low-misfit models (Fig. S36). The final source parameters for length, strike and position are close to the prior distributions (Fig. 3.8) determined by the surface displacement map segmentation method. The estimated prior distributions of source parameters compare well to the kinematic source model parameter estimates. This is also true for the source parameters nucleation position and time as inferred from the multi-array backprojection. Including prior parameter distributions in this way not only speeds up the convergence, it also helps resolving common parameter trade-offs in kinematic source modeling, e.g. between the onset times and positions of the nucleation points in case of two sub-sources. We note that the best-performing models of the guided and exploratory optimizations differ for the onset time, nucleation position and rupture velocity. Here, the source model ensembles of the guided optimization form a subset of the ensembles of the exploratory optimization.

## 3.6 Conclusions

We present a multi-array backprojection (BP) method and image segmentation applied to InSAR surface displacement measurements to improve the imaging of the spatio-temporal evolution of the rupture process of an earthquake. The information that we assemble based on these methods not only boosts follow-up non-linear kinematic source optimizations. They also enable an beforehand objectively informed setting of the number of source segments for a rupture. The multi-array BP method uses many small virtual arrays instead of a single large array to form a combined semblance maps from many single-array responses. We realize a large number of arrays with good coverage across azimuth and distance by clustering the globally available broadband stations into virtual arrays. In the combined semblance unwanted side lobes are suppressed that may result from e.g. depth phases. Additionally, we combine P- and SH-wave semblances to further increase the resolution of the semblance. Furthermore, our multi-array BP allows for an estimation of the semblance precision by using Bayesian bootstrapping of the single array contribution. In this bootstrapping we account for modeling errors due to uncertainties in the earth velocity structure by randomly perturbing traveltimes. Our synthetic tests with realistic station distributions and real noise proved the method to be robust. We show that it is capable of resolving the location of synthetic sources with a location error of less than 5 km in low-frequency semblance maps and with less than 2 km in high-frequency semblance maps.

### 3 *Data-driven constraints on earthquake modeling and rupture segmentation*

Included in our presentation of the multi-array BP is a novel approach for obtaining empirical travel time corrections. It is based on a semi-automatic search of a set of traveltimes maximizing the semblance of an fore- or aftershock.

We apply the multi-array BP method successfully to the real data of the 2016 Mw 6.6 Muji earthquake. For the semblance maps from the 2016 Mw 6.6 Muji earthquake we find a spatial precision of maximum 30 km and 7 km for the low-frequency and high-frequency semblance maps, respectively. We note that significant cumulative semblance, especially in the low-frequency results, corresponds well with significant surface displacement measured with InSAR. This in turn strongly supports the high accuracy that we estimated in the synthetic tests. From the BP results we infer a bilateral and segmented rupture starting close to the eastern end of the western segment, jumping a seismic gap to the eastern segment and propagating on both segments simultaneously. The rupture terminates first on the smaller eastern segment. We find a higher average rupture velocity of 2.1 km/s to 2.6 km/s for the eastern segment in comparison to the average 1.8 km/s to 2.1 km/s for the larger western segment.

The second presented method, an image segmentation approach applied to surface displacement maps as measured with InSAR that, performs well in estimating the location, orientation and the number of segments of a rupture. We show how this information can be cast into prior model parameter distributions for a multi-segment finite kinematic source model. In synthetic tests we demonstrate that with image segmentation we successfully recover fault strike, length, horizontal position and number of input sources. In the application of this method to the InSAR data of the 2016 Muji earthquake we find very good agreements of the results with the results of the multi-array BP, field mappings of the fault trace and also estimated fault characteristics in other source studies of this earthquake.

Both developed methods can be used separately and as stand-alone methods, to provide useful information about the rupture process. They could become regular parts in future operative frameworks. All developed algorithms are available as open-source software. In our work here we implemented them to ultimately infer prior model parameter distributions to be used in a guided joint-data two-sources non-linear optimization of the 2016 Muji earthquake. The resulting two-segment kinematic rupture model is not only consistent with the seismic waveforms and surface displacement data used in the inverse modeling, but also with the rupture evolution as inferred through the multi-array backprojection. Additionally the this guided optimization converged faster compared to the exploratory optimization without such prior source information.

Our results supports previous reports that 2016 Muji earthquake has been a bilateral rupture, with the rupture starting on the western segment to propagate eastward and westward on this segment. After an initiation phase the rupture appears to jump to the eastern segment.

The presented methods ease the detection of significant rupture segmentation, in particular for shallow crustal earthquakes with  $M_w < 7$ , and are suitable to be applied in an automated fashion. A better and more frequent imaging of rupture complexity can be crucial for a better mapping of crustal faults and understanding of crustal faulting.

## **Data availability statement**

Data from regional seismometers are available via FDSN services from GEOFON and IRIS. SAR images used are openly available from the Copernicus Open Access Hub at <https://scihub.copernicus.eu>. The dynamic Green's function store is uploaded on the Pyrocko project Green's mill repository <https://greens-mill.pyrocko.org/> as "*global\_4hz*" for reproduction. The static Green's function store is uploaded for reproduction as "*pamir\_static*". The software and algorithms for the displacement map segmentation have been released on github under <https://github.com/braunfuss/weathertop> and for the multi-array backprojection have been released on github under <https://github.com/braunfuss/palantiri>.

## **Author contribution statement**

A.S. wrote the original draft, developed and conceptualized the method and software, visualized and processed the data. H.S. reviewed and edited the draft, provided supervision, project administration and conceptualized the methods. F.K. reviewed and edited the draft, provided supervision and conceptualized the backprojection method.

All authors have read, agreed, and participated to the published version of the manuscript.

## **Acknowledgments**

This research was funded by the German Research Foundation DFG through an Emmy-Noether Young-Researcher-Grant (Number 276464525, "Bridging Geodesy and Seismology for improved and automated estimation of faulting events").

Contains modified Copernicus Sentinel data (2016) for Sentinel data.

The facilities of IRIS Data Services, and specifically the IRIS Data Management Center, were used for access to waveforms, related metadata, and/or derived products used in this study. IRIS Data Services are funded through the Seismological Facilities for the Advancement of Geoscience and EarthScope (SAGE) Proposal of the National Science Foundation under Cooperative Agreement EAR-1261681.

We thank Dr. Simon Daout and Dr. Hannes Vasyura-Bathke for helpful discussions on the method and results.

# 4 Paper III - Illuminating the spatio-temporal evolution of the 2008-2009 Qaidam earthquake sequence with the joint use of InSAR time series and teleseismic data

Simon Daout<sup>1,2,\*</sup>, Andreas Steinberg<sup>2,3,\*</sup>, Marius Paul Isken<sup>2,4</sup>, Sebastian Heimann<sup>4</sup>, Henriette Sudhaus<sup>2</sup>

<sup>1</sup> COMET, Department of Earth Sciences, University of Oxford

<sup>2</sup> Department of Geosciences, Kiel University

<sup>3</sup> Federal Institute for Geosciences and Natural Resources (BGR)

<sup>4</sup> Helmholtz Centre Potsdam, GFZ German Research Centre for Geosciences

\* These authors contributed equally to this work.

Published in *Remote Sensing*, Vol. 12, Issue 17, Pages 2850

## 4.1 Abstract

Inferring the geometry and evolution of an earthquake sequence is crucial to understand how fault systems are segmented and interact. However, structural geological models are often poorly constrained in remote areas and fault inference is an ill-posed problem with a reliability that depends on many factors. Here, we investigate the geometry of the Mw6.3 2008 and 2009 Qaidam earthquakes, in northeast Tibet, by combining InSAR time series and teleseismic data. We conduct a multi-array back-projection analysis from broadband teleseismic data and process three overlapping Envisat tracks covering the two earthquakes to extract the spatio-temporal evolution of seismic ruptures. We then integrate both geodetic and seismological data into a self-consistent kinematic model of the earthquake sequence. Our results constrain the depth and along-strike segmentation of the thrust-faulting sequence. The 2008 earthquake ruptured a  $\sim 32^\circ$  north-dipping fault that roots under the Olongbulak pop-up structure at  $\sim 12$  km depth and fault slip evolved post-seismically in a downdip direction. The 2009 earthquake ruptured three south-dipping high-angle thrusts and propagated from  $\sim 9$  km depth to the surface and bilaterally along the south-dipping segmented  $55 - 75^\circ$  high-angle faults of the Olonbulak pop-up structure that displace basin deformed sedimentary sequences above Paleozoic bedrock. Our analysis reveals that the inclusion of the post-seismic afterslip into modelling is beneficial in the determination of fault geometry, while teleseismic back-projection appears to be a robust tool to identify rupture segmentation for moderate-sized earthquakes. These findings support the hypothesis that the Qilian Shan is expanding southward along a low-angle décollement that partitions the oblique convergence along multiple flower and pop-up structures.

## 4.2 Introduction

Inferring earthquake slip distributions is useful to understand the spatial and temporal evolution of crustal strain, to investigate how faults are segmented and interact, and to study the relationship of an earthquake with the structural tectonics of an area. However, earthquake fault inversion is an ill-posed problem. Its solution is limited by data resolution, model simplifications and biases, the non-linearity between the data and the unknown parameters, the impact of the topography and lateral variations of lithology, and/or significant dependence between inverted parameters (e.g., Duputel et al., 2014; Ragon et al., 2018b; Langer et al., 2020; Steinberg et al., 2020b). The reliability of any earthquake fault inversion depends on many factors including the segmentation and size of the rupture, the quality of the data, the uncertainties in the subsurface model, the chosen optimisation method to infer earthquake fault parameters, and the *a priori* inferences of the earthquake geometry or mechanisms. For these reasons, different research groups often find different solutions for the same earthquake (Mai et al., 2016).

One way to reduce the non-uniqueness of an inversion and the impact of data errors is to combine several data sets with different characteristics (e.g., space-based imaging, seismic data, pixel offsets, tsunami records) (e.g., Bletery et al., 2014; Marchandon et al., 2018; Akoğlu et al., 2018; Gombert et al., 2018). In particular, several studies (e.g., Weston et al., 2014a; Huang et al., 2016b; Frietsch et al., 2019b; Vasyura-Bathke et al., 2020; Steinberg et al., 2020b) have shown the benefit of complementing the high spatial resolution of near-field geodetic observations with the high temporal resolution of far-field seismic waveforms. Seismic waveforms carry information about the rupture onset time, its spatio-temporal evolution and duration, as well as the fault mechanism and seismic moment. Near-field surface data provide constraints on the fault location and mechanism, the amount of slip, and the extension of the rupture. Another way to limit biases in the inversion is to account for data and model parameter uncertainties due to the data noise and the imperfect knowledge of the medium through data weighting (e.g., Lohman and Simons, 2005b; Sudhaus and Sigurjón, 2009; Duputel et al., 2014; Cesca et al., 2020), and to rigorously propagate errors through optimisation algorithms, such as with un-regularised Bayesian optimisation frameworks (e.g., Minson et al., 2013b; Minson et al., 2014; Daout et al., 2016a; Gombert et al., 2018; Ragon et al., 2018b; Hong et al., 2018; Vasyura-Bathke et al., 2020)

Differential Interferometric Synthetic Aperture Radar (DInSAR) detects surface displacements in the line-of-sight (LOS) direction between satellite acquisitions before and after an earthquake, and is commonly used to infer earthquake fault parameters due to its high spatial resolution (e.g., Wright et al., 2004b; Lasserre et al., 2005; Sudhaus and Jónsson, 2011; Elliott et al., 2016a; Mackenzie et al., 2016; Ganas et al., 2018). Despite the large benefits brought by the measurement of the surface displacements across wide swaths, DInSAR is also polluted by changes of atmospheric conditions between the two acquisitions, associated with the turbulent and stratified components of the atmosphere and the electron content in the ionosphere (Hanssen, 2001b; Doin et al., 2009; Gomba et al., 2015). In addition, due to the revisit time of the satellites of more than a few days, most inferred earthquake fault models based solely on DInSAR observations are biased by early post-seismic displacement signals. Apart from few studies that account for early post-seismic signals (e.g., Floyd et al., 2016; Ragon et al., 2019), most fault inferences neglect the contribution of early post-seismic deformation in the inverse problems with the consequences that it is attributed to the co-seismic rupture. However, since the first surface displacement image of an earthquake following the 1992 Landers earthquake (Massonnet et al., 1993b), numerous advances in the DInSAR technique have been made to derive multi-temporal time series (TS) of ground displacements by processing multiple SAR acquisitions. This increases the number of locations where displacement can be measured and reduces associated errors (e.g., Berardino et al., 2002; Hooper, 2008; Doin et al., 2015). Advances have also been made in reducing atmospheric contributions by the use of atmospheric models (e.g., Doin et al., 2009;

#### 4 Spatio-temporal evolution of the 2008-2009 Qaidam earthquake sequence

Jolivet et al., 2011; Daout et al., 2020a), empirical methods (e.g., Cavalié et al., 2007; Doin et al., 2015; Lin et al., 2010; Isken et al., 2017c; Yu et al., 2018; Dini et al., 2019) or by data stacking and TS analysis (e.g., Floyd et al., 2016; Wimpenny et al., 2017; Barnhart et al., 2018; Daout et al., 2019). The latter is beneficial to derive the cumulative surface displacements (contrary to single interferograms) and separates the various inter-, co- and post-seismic phases of the seismic cycle. In addition, TS analysis allows researchers to check the consistency of each interferogram within the network, increases the signal-to-noise ratio via data redundancy and attenuates the effects of turbulent atmospheric noise by smoothing of the TS. Recent developments in InSAR methodologies as well as the new generation of SAR satellites (Sentinel-1, ALOS-2) with shorter revisit times and systematic acquisitions in both ascending and descending geometries, therefore, raise queries about the prospects of multi-temporal InSAR TS for subsurface fault slip inferences.

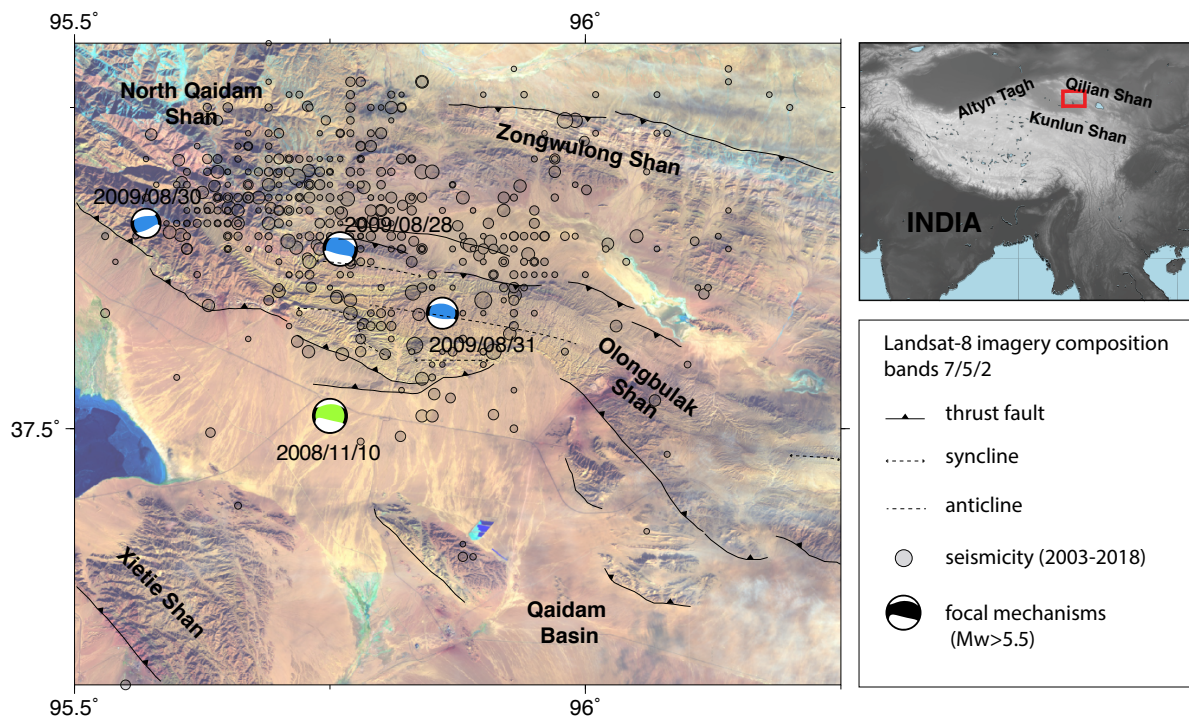


Figure 4.1: Seismotectonic setting of the Olongbulak ranges in the northeastern part of the Tibetan Plateau superimposed on a false colour Landsat 8 satellite image (U.S. Geological Survey, <https://earthexplorer.usgs.gov/>). The uplifted Paleogene, Cretaceous and Jurassic deposits form a distinctive yellow band within the Olongbulak pop-up, between dark Jurassic to Cambrian bedrock. Mapped faults from our own analysis are shown as black lines. Locations and focal mechanisms of the three  $M_w > 5.2$  earthquakes of the 2008-2009 Qaidam sequence are shown with their mechanisms as lower-hemisphere stereo-projections (Ekström et al., 2012) (2008 and 2009 in green and blue, respectively). Grey transparent circles show the historical seismicity from 2003 to 2018 from the U.S. Geological Survey catalogue ( $M > 4.0$ ) and a regional Chinese catalogue ( $M > 2.0$ , <http://data.earthquake.cn>)

The North Qaidam thrust (NQT) system is located at the southernmost part of the Qilian Shan-Nan Shan and is marked by recent active seismicity within the Olongbulak ranges (Fig. 4.1). The  $\sim 16$  km deep 10<sup>th</sup> November 2008 and the  $\sim 5$  km deep 28<sup>th</sup> August 2009 Haixi  $M_w$  6.3 earthquakes occurred in close proximity ( $\sim 15$  km) to each other within the Olongbulak Shan and were followed by a period of increased rate of seismicity in the region (Elliott et al., 2011b; Guihua et al., 2013). The 2009 earthquake was followed by a  $M_w$  5.4 and a  $M_w$  5.6 aftershock one and two days, respectively, after the main-shock, as many as 34  $M_w > 4$  aftershocks within a month



(USGS), and time-dependent after-slip of similar pattern to the co-seismic slip (Feng, 2015; Liu et al., 2016b; Liu et al., 2016a; Daout et al., 2017). The two earthquakes represent particular examples of two  $\sim M_w$  6 earthquakes that occurred nearby in space and time, highlighting the need to constrain both along-depth and along-strike segmentation of thrusting events to better quantify seismic hazards (Elliott et al., 2011b). Their segmentations and geometries also need to be placed in the context of the regional tectonic as the deformation style of the northeastern part of the Tibetan plateau is at the heart of the debates about its dynamic evolution. In a first class of deformation models, Burchfiel et al., 1989 (Burchfiel et al., 1989) first postulated a basement décollement fault in the middle crust of the Qaidam basin that connect to the Qilian Shan-Nan Shan thrust belts in the north, absorbing progressively the left-lateral slip on the Altyn-Tagh Fault (Fig. 4.1). Then, Metivier et al, 1998 (Métivier et al., 1998); Meyer et al., 1998 (Meyer et al., 1998) and Tapponnier et al., 2001 (Tapponnier et al., 2001) suggested that the Qaidam basin may have been trapped of the surrounding reliefs in the middle-late Miocene as a result of the northward stepwise jumping of the intra-continental deformation. This first class of model proposes that the oblique convergence between the India-Eurasia collision is absorbed by crustal thickening along the major Kunlun or Qilian Shan suture zones, where strike-slip and thrust faults root at depth to extrude laterally and partition vertically the deformation causing mountain uplift on localised ranges (Fig. S1a). Conversely, Dupont et al., 2004 (Dupont-Nivet et al., 2004), Yin et al., 2008a (Yin et al., 2008a) and Bush et al., 2016 (Bush et al., 2016) suggested a plausible and simultaneous early Eocene onset of the Kunlun and Qilian ranges. This second class of model suggests that the strain from the India-Asia collision was transmitted rapidly to the northern edge of the modern Tibetan Plateau via preexisting and complex zones of weaknesses created during pre-Cenozoic (Yin and Harrison, 2000; Yin et al., 2008a; Yin et al., 2008b) or via homogeneous deformation driven by mantle or crustal flow (England and Houseman, 1988; Royden et al., 1997; Clark and Royden, 2000) (Fig. S1b). Those model contradictions leave thus open the debate on the geometry of the NQT at depth and its possible relations with the Qilian ranges, to the north (Yin and Harrison, 2000; Tapponnier et al., 2001).

The study of these earthquakes is also challenging from a methodological point of view. First, because of the deeper source of the 2008 earthquake, the data can be explained by conjugate south-dipping or north-dipping planes, as illustrated by the various solutions found by different authors (Elliott et al., 2011b; Guihua et al., 2013; Feng, 2015). Secondly, the larger gradients and the more complex surface displacement patterns of the 2009 earthquake, in comparison to the 2008 earthquake, suggest a segmented and shallow rupture. These surface displacement features have been explained by varying numbers of fault segments in the literature (Elliott et al., 2011b; Liu et al., 2015; Feng, 2015), and this earthquake sequence, therefore, also represents a good case study to evaluate the level of complexity required in a fault model to explain the data.

In this study, we investigate the spatio-temporal evolution of the 2008 and 2009 earthquakes using seismological back-projection analysis and three overlapping InSAR time series (TS) data of the Envisat satellite covering the two earthquakes. We then integrate both geodetic and seismological data into a self-consistent fault model. The goals of this study are multi-folds. We first investigate the fitness of back-projection to describe rupture characteristics of moderate-size earthquakes. We then inspect the benefits of an InSAR TS analysis approach for earthquake fault modelling and discuss the improved signal to noise ratio of such data sets in comparison to traditional co-seismic interferograms, as well as the additional constraints offered by the extracted post-seismic surface displacements from InSAR time-series data. We finally integrate our fault characteristic estimations to the local tectonic context to propose a structural model of the Olongbulak ranges.

## 4.3 Materials and Methods

### 4.3.1 Seismic back-projection source imaging

Time-domain seismic back-projection images the spatio-temporal evolution of earthquakes by mapping the location of coherent seismic wave emissions recorded at a seismic network (e.g., Krüger and Ohrnberger, 2005; Kiser and Ishii, 2017; Ruppert et al., 2018; Hicks et al., 2020a). It relies on constructive and destructive stacking of seismic waveforms. In comparison to kinematic fault inversion, it has the advantage of requiring no assumption of the fault geometry, and is, therefore, a useful complement to inverse modelling. The only model assumptions required are the travel times derived from a 1-D Earth velocity model.

#### 4.3.1.1 Data and Station Clustering

We first download all available broadband records from the international web service (FDSNWS) Geofon and IRIS (Hanka and Kind, 1994b; Trabant et al., 2012), for the 2008 and 2009 Qaidam earthquakes. We consider waveforms from broadband stations between  $20^\circ$  and  $93^\circ$  distance from the source and only use stations that recorded both earthquakes (Fig. S2). We cluster the available stations using the  $k$ -means algorithm into many small virtual arrays (minimum number of 5 stations). Virtual arrays are formed assuming a minimum number of stations and a maximum aperture up to  $3.5^\circ$ . The use of many small virtual arrays has the advantage of minimising the effect of velocity differences between stations in an array as well as the effect of radiation patterns and source directivity (Rössler et al., 2010).

#### 4.3.1.2 Multi-array back-projection method

We carry out the back-projection for point locations on a horizontal grid. We perform the back-projection separately for high-frequencies (HF) and low-frequencies (LF), to explore areas with changes of frequency content over time, which can indicate changes in slip velocity/acceleration (Madariaga, 1977) or rupture initiation points (Ide, 2002). We perform the back-projection on moving time windows of 2 s steps and 10 s length for HF and of 8 s steps and 26 s length for LF. We bandpass-filter for the HF back-projection between the earthquake corner frequency ( $2/T_r$ , with  $T_r$  being the reported gCMT rupture duration (Ekström et al., 2012)) and 1.5 Hz. For the LF back-projection we bandpass-filter between 0.01 Hz and the earthquakes' estimated corner frequency  $f_c = 0.25$  Hz.

We use a phase-weighted stacking method (Schimmel and Paulssen, 1997) and stack in separate time windows for P- and SH-phases. Waveforms are back-projected for each time step and each point on a given spatial grid. Un-modeled path effects cause systematic travel-time shifts, which lead to a regularly biased source location. To reduce the impact of this effect, we calibrate travel-time shifts for each station using empirical corrections (Palo et al., 2014; Ishii et al., 2007; Meng et al., 2016; Fan and Shearer, 2017) based on nearby 2008-11-10 03:47:23 Mw 5 aftershock to calibrate the empirical travel-time and correct the travel time shifts of the P and SH waves of the two earthquakes (Fig. S3). As a result of the back-projection, we obtain the phase semblance (a measure of phase coherence) of the waveform records at each array for the specific time window and grid point considered. Semblance is a strictly positive function of waveform coherence and can be interpreted as a likelihood of seismic energy released (Rössler et al., 2010). We also calculate the beampower, which is an absolute measure of the stacked amplitudes (Efron, 1982). Beampower is calculated by integrating the energy of all arrays.

To access the uncertainty of the obtained back-projection results, we make use of bootstrapping and travel-time perturbations derived from the 1-D velocity model. For 100 bootstraps, we calculate the back-projection with different array weights and perturb the waveform records randomly by  $\pm 2$  s for the P-phase window and by  $\pm 4$  s for the SH-phase, extracted from the standard deviation of the normal distribution. To avoid azimuthal biases, we subdivide the azimuth into 12 sectors of  $30^\circ$ , based on the azimuth of the earthquake epicenter to the array center, and each array is assigned to its corresponding azimuth sector. The semblance from each azimuth sector is normalised, such that each azimuthal sector has the same influence on the combined semblance.

### 4.3.2 Kinematic fault inversion

We seek to explore the range of possible fault geometries for the two  $M_w > 6$  2008 and 2009 earthquakes that explain the surface displacements and the seismological observations with minimum prior constraints on fault geometry and fully accounting for data uncertainties. We optimise both near-field and far-field data with a Bayesian bootstrapping algorithm implemented in the open source Grond earthquake inversion framework (Heimann et al., 2018b; D. et al., 2020; Steinberg et al., 2020b) and part of the Pyrocko software (<https://pyrocko.org/grond/docs/current/method/index.html>).

#### 4.3.2.1 Teleseismic data

We select stations at epicentral distances between  $20^\circ$  and a maximum of  $93^\circ$ . Those distances are large enough such that near-field wave terms are attenuated and small enough such that phase triplications do not occur and the direct P and S waves are recorded first. We visually check and select the data quality after the automated pre-selection. As a result, we retrieve for the 2008 and 2009 earthquakes good-quality recordings at 72 and 45 stations, respectively. The waveforms are trimmed and filtered between the corner frequency ( $f_c = 0.25$  Hz) and 1.5 Hz, and are then cut and filtered with a frequency taper falling with a cosine flank.

For the 2009 earthquake, we observe several waveform records contaminated by a signal from a  $M_w 6.9$  earthquake that occurred in the Banda Sea  $\sim 1$  min prior. We thus select stations within an azimuth of  $-105^\circ$  and  $105^\circ$  and between distances of  $0^\circ$  to  $40^\circ$ , where the 2009 earthquake signals arrived before the Banda Sea earthquake signals. Additionally, we only use P-phases, because the SH-phases are potentially contaminated.

#### 4.3.2.2 InSAR time series (TS) data

We construct InSAR TS of surface displacements from the complete Envisat archive along two  $\sim 300$  km long overlapping descending tracks (T319, T047) and one ascending track (T455) (Fig. S4). Extensive details about the filtering and unwrapping procedure can be found in Daout et al., 2019 (Daout et al., 2019). In contrast to the processing of only few co-seismic interferograms, we here take advantage of the regional extent of the data and the large number of interferograms to perform empirical corrections after unwrapping, which we validate with a time-series analysis approach. First, we correct the 215 interferograms for orbital and atmospheric errors. To do so, within non-deforming regions, we jointly estimate the LOS-elevation relationship with the azimuth and the LOS-range relationship as follows:

$$LOS(x, y) = az + bzy + cx^2 + dx + ey + f, \quad (4.1)$$

where  $LOS(x, y)$  is the LOS displacements for each interferogram,  $x, y, z$  are respectively the range direction, the azimuth direction, and the elevation and  $a, b, c, d, e,$  and  $f$  the inverted coefficients. Inconsistencies of parameters  $a, b, c, d, e,$  and  $f$  are afterwards detected within the interferometric network by a least-squares inversion of all independent coefficients for each acquisition date and then re-estimated for all interferograms before applying the correction. After empirical corrections, the phase TS is constructed with the method of Doin et al., 2015 (Doin et al., 2015) and inconsistencies in the interferometric network, mainly due to phase unwrapping errors, are further detected and corrected with iterative and automatic approaches (López-Quiroz et al., 2009). We finally extract the co-seismic and post-seismic surface displacements of the 10<sup>th</sup> November 2008 and the 28<sup>th</sup> August 2009 Haixi earthquake by decomposing pixel-by-pixel the TS data into a linear trend, two steps and two logarithmic post-seismic functions (Fig. 4.2a), such as:

$$\begin{aligned}
 LOS(t) = & v \cdot t + A_{2008} \cdot H(t - t_{2008}) + B_{2008} \cdot \log\left(1 + \frac{t - t_{2008}}{\tau_{2008}}\right) + \\
 & A_{2009} \cdot H(t - t_{2009}) + B_{2009} \cdot \log\left(1 + \frac{t - t_{2009}}{\tau_{2009}}\right).
 \end{aligned}
 \tag{4.2}$$

where  $t$  is the SAR acquisition time,  $v$ , the long-term velocity between 2003 to 2011,  $A, B,$  and  $\tau$ , the amplitude of the Heaviside step functions (H), the amplitude of logarithmic functions, and the characteristic time of the logarithmic relaxation, respectively (Fig. 4.2a). Given the moderate size of the shallow earthquakes, the short-time period observation following them, the short-wavelength of the post-seismic signal, and the similar signs and patterns of the post-seismic and co-seismic surface displacements, we discard any viscoelastic relaxation or poro-elastic rebound in the shallow crust (e.g., Peltzer et al., 1998; Rollins et al., 2015; Zhao et al., 2018) and associate the deformation to afterslip (Marone, 1998; Perfettini and Avouac, 2004). We explore several post-seismic relaxation times,  $\tau_{2008}$  and  $\tau_{2009}$  but notice no significant differences in the misfit due to the temporal sampling of few months of the data and the moderate magnitude of the earthquakes and associated after-slip (Fig. S5). However, as we only interpret and invert later the modeled cumulative after-slip displacements, the choice of the relaxation time does not influence the interpretation of the results, and choose a characteristic time of half a month that minimises the misfit of the decomposition. We impose that displacements from the logarithmic functions must have the same sense of direction as their associated coseismic steps, and solve the constrained inverse problem with a sequential least-squares algorithm. The resulting co- and post-seismic ground motion maps (Fig. 4.2b) show a very smooth signal, which validates the robustness of the pixel-by-pixel approach.

In addition to this TS decomposition approach, we find, for each of the three tracks, the image pair with the shortest temporal baseline spanning the 10<sup>th</sup> November 2008 earthquake, and produce filtered, unwrapped and empirically corrected interferograms for each pair. These are interferograms 20081105-20081210, 20081017-20081226, and 20080905-20081114, from tracks 319, 047 and 455, respectively (Fig. 4.3a). We use for the 28<sup>th</sup> August 2009 earthquake, interferograms 20090708-20091021, 20090130-20091211, and 20090708-20091021 from tracks T319, T047 and T455, respectively (Fig. 4.3b). We also compute for each track, stacks of filtered, unwrapped and corrected interferograms encompassing the two earthquakes (Fig. 4.3c,d). InSAR displacement maps obtained from the parametric decomposition of the TS data (Fig. 4.2), interferograms and stacks (Fig. 4.3) constitute data sets with various characteristics that we use as input for the kinematic inversion.

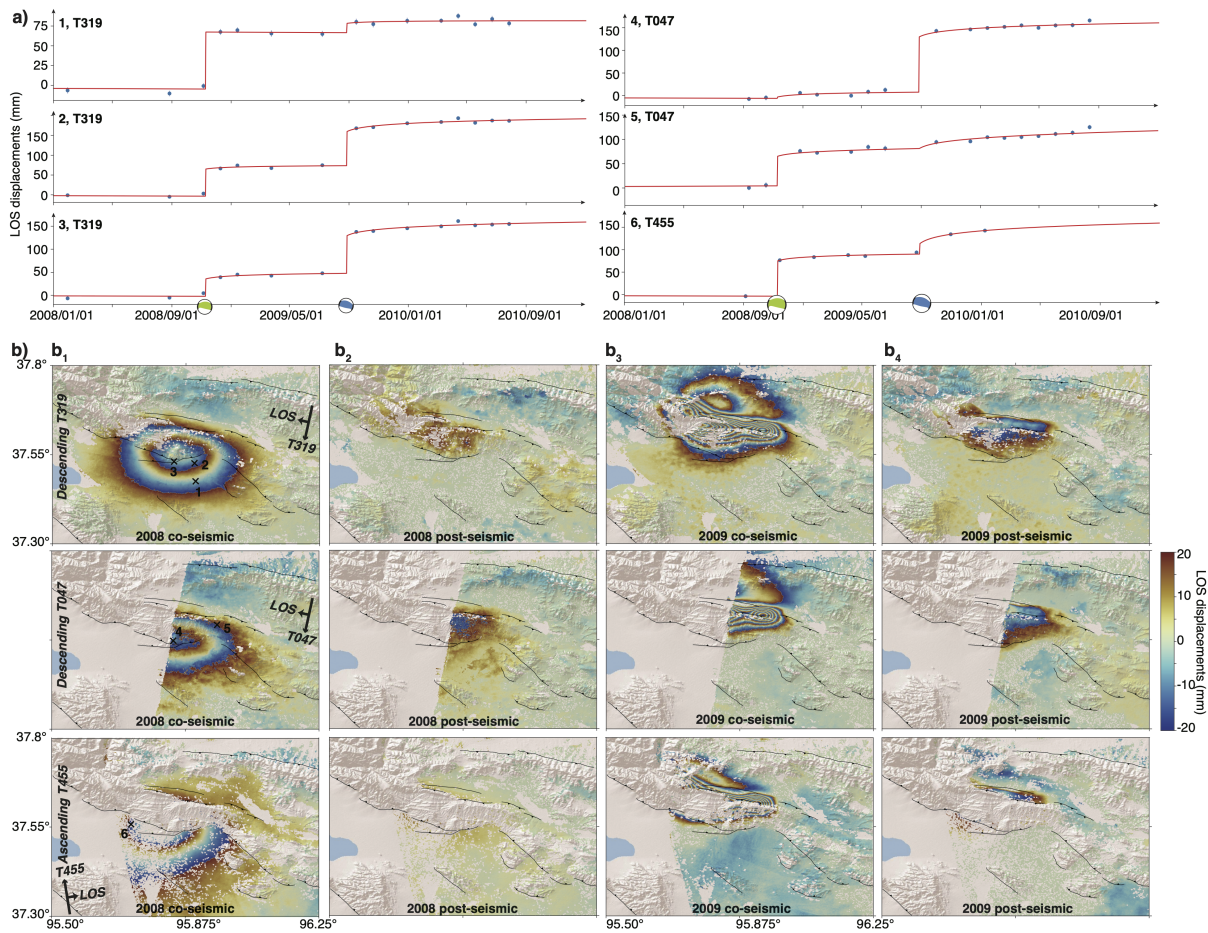


Figure 4.2: a) Parametric TS decomposition for four pixels of the tracks T319, T047, and T455 marked by crosses in (b). b) LOS surface displacement maps wrapped between -20 mm and 20 mm associated with the 2008 (b<sub>1</sub>) and 2009 (b<sub>3</sub>) co-seismic surface displacements, and the corresponding afterslip surface displacements over a 4 month interval (b<sub>2,4</sub>) extracted from the parametric decomposition of tracks T319 (top), T047 (middle) and T455 (bottom). Black lines show mapped fault traces of the NQT and Xietie-Shan thrust (XT).



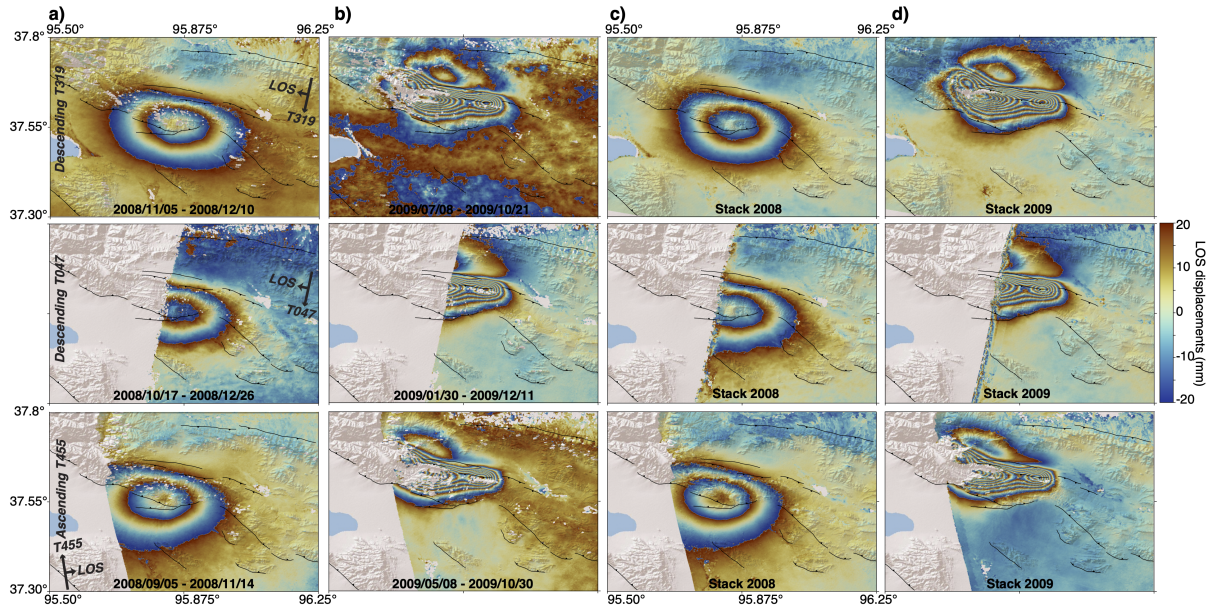


Figure 4.3: Co-seismic Differential interferograms and stacks from track 319 (top), 047 (middle), 455 (bottom). a) 2008 coseismic Differential interferograms. b) 2009 coseismic Differential interferograms. c) Stack of 2008 coseismic Differential interferograms. d) Stack of 2009 coseismic Differential interferograms.

#### 4.3.2.3 Fault inference method

Synthetic seismic waveforms and static surface displacements in a layered medium are computed with the Green's Functions (GFs) calculated using QSEIS and PSGRN/PSCMP, respectively (Wang et al., 2006b; Wang, 1999). For seismological data, layering of the Earth is defined by the AK135 1D velocity model (Kennett and Engdahl, 1991b), while for InSAR data, we use the elastic moduli from the local Global Crustal Database based on empirical 1D velocity models derived from seismic reflection and refraction profiles (Mooney et al., 1998) (Fig. S6).

Fault optimisations are performed with a bootstrapping approach running in parallel 200 evaluations of the model misfit based on different realisations of random Bayesian weights (far-field) and random synthetic noise (InSAR) (Heimann et al., 2018b; D. et al., 2020; Steinberg et al., 2020b) (<https://pyrocko.org/grond/docs/current/method/index.html>). In a first exploration phase of the optimisation, the model space is randomly sampled. Afterwards, the exploration domain within the model space is defined by the model parameter covariances computed from a list of low misfit model realisations. Only one model in the best-fitting model list is allowed to be changed per iteration. Additionally, the center points for the sampling distributions are randomly offset from the mean value of the list to avoid becoming stuck in local minima. By doing so, a multi-modal misfit surface can be efficiently explored.

#### 4.3.2.4 Fault inference of the 2008 earthquake

We optimize one rectangular fault for the coseismic slip in the 2008 earthquake and a second fault for the postseismic deformation that followed. We explore the time offset of the earthquake in comparison to gCMT solution (Time), the position in comparison to the Global Centroid Moment Tensor (Global CMT) solution (northing, easting, depth), the fault dimension (length, width), the fault orientation (strike, dip, rake), the amount of slip (slip), the nucleation starting point (nucleation X, nucleation Y), and the rupture velocity (velocity) (Tables S2 and S3). We

define the fault position (northing, easting, depth) as the center of the top edge of the rectangular fault, while the nucleation starting point is set relative to the plane center (0,0 is the center). In addition, to these earthquake fault model parameters, we also invert for a bilinear ramp in the InSAR data in east and north directions to tie the data to the model.

We perform a series of tests to explore the likelihoods of north-dipping and south-dipping planes. As a first test, we explore separately both north-dipping ( $\mathcal{U}(250, 310)^\circ$  and  $\mathcal{U}(0, 80)^\circ$  prior distributions for strike and dip angles, respectively) and south-dipping solutions ( $\mathcal{U}(80, 140)^\circ$  and  $\mathcal{U}(0, 80)^\circ$  prior distributions for strike and dip angles, respectively) in agreement with the co-seismic and post-seismic displacement maps and look for independent solutions that show coplanarity between the co-seismic and the post-seismic slip. In a second test, we invert for the stack of 2008 co-seismic displacement interferograms, that include both co-seismic and post-seismic deformation, leaving as free parameters the dip angle of the fault plane ( $\mathcal{U}(80, 310)^\circ$  and  $\mathcal{U}(0, 180)^\circ$  prior distributions for strike and dip angles, respectively).

#### 4.3.2.5 Fault inference of the 2009 earthquake

Because of the asymmetric displacement patterns that illuminate three distinct strike angles and based on the following back-projection analysis, we model the 2009 earthquake with three rectangular faults with only few and loose *a priori* constraints on the fault locations based on InSAR surface displacements.

We model three distinct and independent fault segments at the same time, with a full set of fault parameters as described for the 2008 earthquake. We impose that no overlap between fault segments can occur (Table S4). Prior distributions of the individual fault positions are chosen such that they roughly describe a central segment and one segment to the east and west.

In order to also assess the fault geometry and slip responsible for both 2009 co- and post-seismic displacements, we additionally explored both stacks of 2009 co-seismic and post-seismic interferograms together with the seismic waveforms within the same inversion framework as the co-seismic fault optimisation based on TS data. We here chose to not invert for post-seismic surface displacements extracted from the TS analysis as the model is too complex (three independent fault parameters) for the available data set (InSAR post-seismic data only).

## 4.4 Results

### 4.4.1 Back-projection imaging of the 2008-2009 sequence

Beam-power functions indicate that the 2008 rupture begins and terminates slowly with a maximum peak of energy after 5 s (Fig. 4.4a). The beam power function of the 2009 earthquake reflects its rupture segmentations with three peaks at 2.5, 5.5 and 8.5 s (Fig. 4.4a). The rupture durations estimated from the beam-power (8.3 s for the 2008 earthquake and 9.4 s for the 2009 earthquake) are consistent with initial seismological observations from the gCMT catalog.

In space, we observe for the 2008 earthquake a smooth southeast-northwest elongation of high semblance in both HF and LF coherent energy emissions (Fig. 4.4b, Fig. S7). The highest average HF semblance is achieved using a 16 km deep grid of points for the 2008 earthquake back-projection. In contrast, the 2009 rupture process appears to be more shallow ( $\sim 9$  km) and spatially more focused (Fig. 4.4b, Fig. S8). It is reflected by three distinct peaks of HF energy, which suggest rupture of three separate steeply dipping ramps. The rupture of the 2009 earthquake starts in the center area and propagates bilaterally. In the eastern part, HF

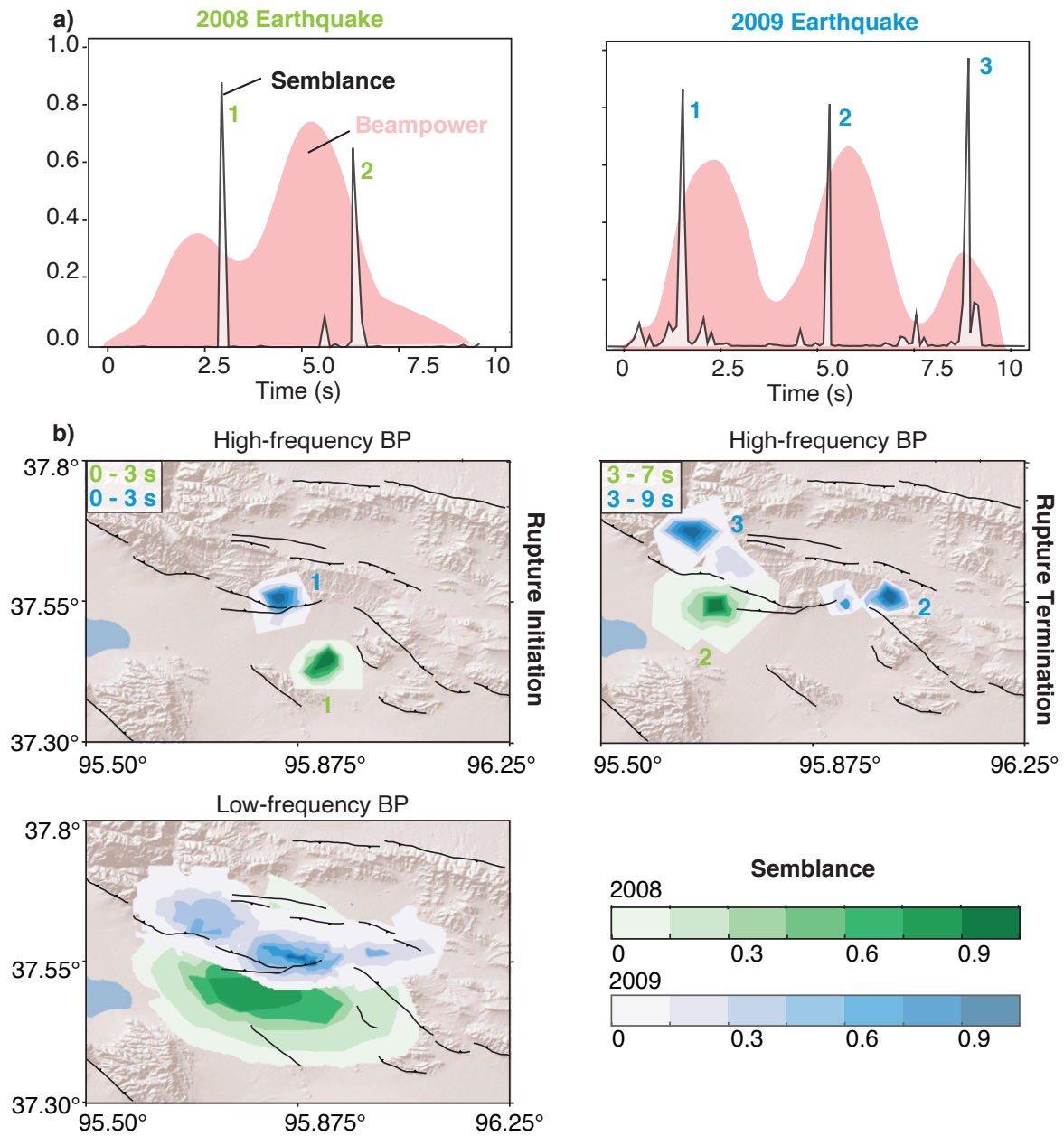


Figure 4.4: Seismic back-projection for the 10<sup>th</sup> November 2008 and the 28<sup>th</sup> August 2009 Haixi earthquakes. a) P wave beampower (filled red curve) and maximum semblance from both LF and HF emissions (white filled curve) as a function of time for the 2008 (left) and 2009 (right) earthquakes. b) Back-projected stack amplitudes shown for given time intervals and grid depths for the two earthquakes (green: 2008, blue: 2009) with warm colours associated with higher semblance. Semblance peaks are numbered 1, 2, and, 3.



is emitted during an intermediate time step (3-6 s), in an area that roughly matches a gap in the geodetic displacement data (Fig. 4.2b) and may be associated with the jump of the rupture across fault-segments and the activation of a third fault segment. The central area shows some back-projected energy during the intermediate time step (3-6 s). The western area shows back-projection energy in the last stage of the rupture, associated to the activation with a third fault segment.

#### 4.4.2 2008 fault characteristics estimations

Among north-dipping solutions for the 2008 earthquake (Figs. 4.5, 4.6a), the models that best fit jointly the InSAR TS and teleseismic data feature a  $16 \pm 2.5$  km long and  $3.6 \pm 1.4$  km wide segment with a top edge center located at  $11.9 \pm 0.5$  km depth. The best-fitting solution converges toward a  $264 \pm 8^\circ$ -striking plane dipping at a low-angle of  $32 \pm 2^\circ$  towards the north. Waveform fits for the 2008 earthquake north-dipping solution for 5 randomly selected stations are shown in Fig. S9.

The north-dipping fault model that best explains the first 4 months of post-seismic deformation following the 2008 event (imaged using TS data) is a narrow segment,  $18.5 \pm 1.4$  km long and  $0.6 \pm 0.3$  km wide, with a top edge center located at  $12.5 \pm 0.8$  km depth. Slip is  $1.2 \pm 0.4$  m for the co-seismic rupture and also of  $1.2 \pm 0.3$  m for the 4-month post-seismic period on the narrow fault patch. While the strike of the co-seismic solution is oriented parallel to the southernmost branch of the Olongbulak Shan, the post-seismic solution has a strike of  $287 \pm 2^\circ$ , perpendicular to the overall  $\sim N20^\circ E$  regional shortening (Liang et al., 2013; Wang et al., 2017b). The dip angle is also slightly lower than the co-seismic solution, dipping at  $20 \pm 1.3^\circ$  towards the north.

In comparison, south-dipping solutions (Figs. 4.5, 4.6b) converge towards a  $96 \pm 4^\circ$ -striking co-seismic plane and a  $102 \pm 2^\circ$ -striking post-seismic plane with high-angle dips of  $60 \pm 2.5^\circ$  and  $70 \pm 1.5^\circ$ , respectively. Slip is of  $1.7 \pm 0.5$  m for the co-seismic rupture and of  $0.05 \pm 0.003$  m for the 4-month post-seismic period on the  $29.7 \pm 0.5$  km wide and  $16.5 \pm 1.4$  km long fault patch. As for the north-dipping solution, the south-dipping solution presents a very low misfit as shown in the comparison between the geodetic data and the best-fitting model (Fig. S10). While the north-dipping co- and post-seismic solutions are almost co-planar, south-dipping solutions indicate two distinct planes located almost  $\sim 5$  km apart.

Additionally, from the joint probabilistic inversion of the near-field stack of co-seismic interferograms and the far-field waveforms data emitted by the 2008 earthquake (Fig. 4.7), we converge towards a  $14 \pm 1.8$  km long and  $5.8 \pm 2$  km wide rupture plane with a top edge centre located at  $9.8 \pm 1$  km depth. Although both north and south-dipping solutions, which are sampled during the whole optimisation (Fig. 4.7b), show low misfit values due to the ambiguity if the displacement patterns of the buried fault plane, the best-fitting solution is a north-dipping plane striking at an angle of  $286 \pm 80^\circ$  and dipping at an angle of  $32 \pm 10^\circ$ . There is a good agreement between both geodetic and seismological observations and predictions for the three independent tracks (Fig. 4.7a).

#### 4.4.3 2009 fault characteristics estimations

For the joint probabilistic three-fault inversion of the 28<sup>th</sup> August 2009  $M_w$  6.3 earthquake based on InSAR and far-field teleseismic data (Figs. 4.5), the optimisation converges towards a central segment of  $10.0 \pm 0.5$  km long and of  $1.6 \pm 0.5$  km wide with a top edge centre located at  $2.7 \pm 1.2$  km depth. The eastern segment is constrained with a length of  $4.7 \pm 0.5$  km, a width of  $1.8 \pm 0.5$  km, and a depth of  $3.1 \pm 1.5$  km, while the third western segment is of  $9.0 \pm 1$  km length,

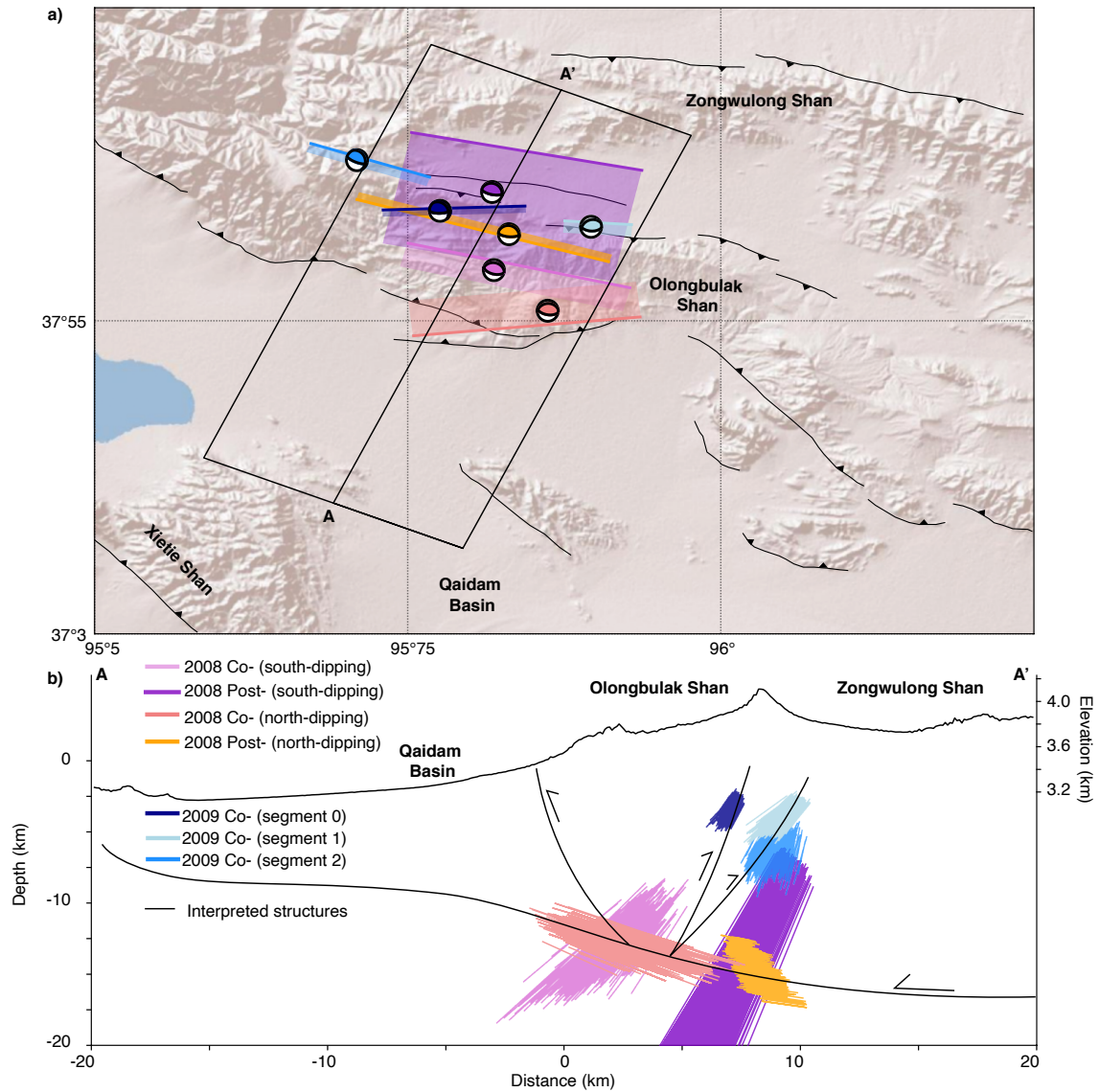


Figure 4.5: Posterior models for the 10<sup>th</sup> November 2008 and 28<sup>th</sup> August 2009 earthquakes and their post-seismic deformation from optimisations obtained with fixed dip directions. a) Best-fitting posterior geometries in map view for the 2008 north-dipping co-seismic (coral red), the 2008 north-dipping post-seismic (orange), the 2008 south-dipping co-seismic (pink), the 2008 south-dipping post-seismic (magenta), and for the three segments of the 2009 co-seismic (dark blue, cyan, blue) fault inferences. b) As for top figure but along the N22°E profile perpendicular to the Olongbulak Shan marked A-A' in (a) and with interpreted fault geometry in the middle/upper crust. Based on the coplanarity of the 2008 co- and post-seismic slip, we interpret that the 2008 earthquake ruptured a 32° north-dipping plane at 12 km depth rooting below the Olongbulak Shan and that the after-slip was mainly down-dip of the rupture plane. The 2009 earthquake broke three distinct 55-75° high-angle south-dipping back-thrust segments of the Olongbulak pop-up structure.

#### 4 Spatio-temporal evolution of the 2008-2009 Qaidam earthquake sequence

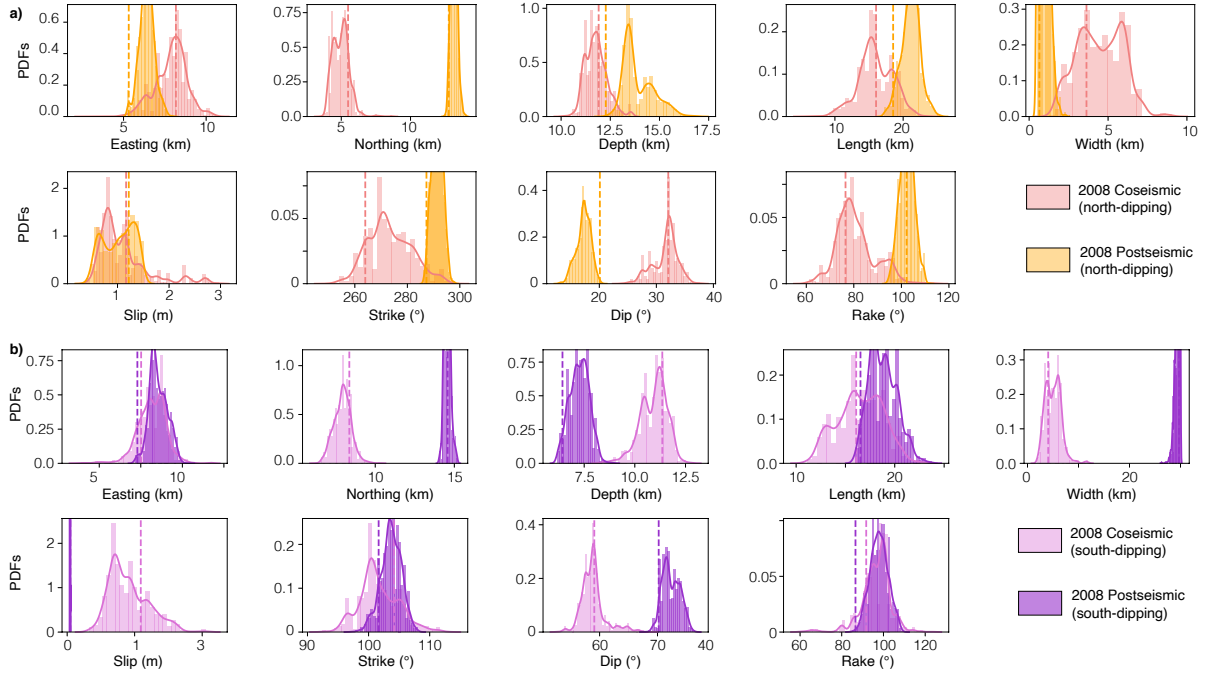


Figure 4.6: a) Summary of the posterior PDFs for the optimisation of one north-dipping rectangular fault in agreement with the co-seismic (coral red) and post-seismic (orange) surface displacements of the 2008 earthquake. Dashed vertical lines are best-fitting models. b) Same as (a) but for the optimisation of one south-dipping rectangular fault in agreement with the co-seismic (coral red) and post-seismic (orange) surface displacements of the 2008 earthquake.

$2.5 \pm 1$  km width, and at  $4.5 \pm 0.5$  km depth. All three segments have narrow widths and are respectively dipping with  $71 \pm 2^\circ$ ,  $57 \pm 3^\circ$ , and  $73 \pm 3^\circ$  high-angles to the south. Slip on the fault segments amounts to  $2.0 \pm 0.4$  m,  $2.2 \pm 0.3$  m and  $1.9 \pm 0.5$  m. A summary of all posterior PDFs is available in the Fig. 4.8 while waveform fits for the 2009 earthquake north-dipping solution for 5 random stations are shown in Fig. S9b.

Additionally, from the joint probabilistic inversion of the near-field stack of co-seismic interferograms and the far-field waveforms data emitted by the 2009 earthquake (Figs. 4.8, S11), we converge towards a middle-segment of  $9.4 \pm 0.5$  km long and  $4.1 \pm 1.2$  km wide with a top centre edge located at  $2.5 \pm 0.3$  km depth. The eastern segment is constrained with a length of  $6.1 \pm 1.0$  km, a width of  $2.8 \pm 0.9$  km, and a depth of  $2.5 \pm 0.2$  km, while the third western segment is of  $6.8 \pm 0.6$  km-length,  $2.8 \pm 0.4$  km-width, and  $4.0 \pm 0.5$  km-depth. The three segments all dip steeply to the south, at  $73 \pm 3^\circ$ ,  $61 \pm 4^\circ$ , and  $59 \pm 7^\circ$ , respectively. Fault geometries are therefore very similar to the three fault segments obtained from the inversion of the co-seismic surface displacements only, and we can therefore, reasonably conclude that post-seismic slip occurred on the same fault geometries as the coseismic rupture. Slip on the fault segments is  $1.5 \pm 0.6$  m,  $1.3 \pm 0.2$  m and  $1.9 \pm 0.4$  m, respectively.

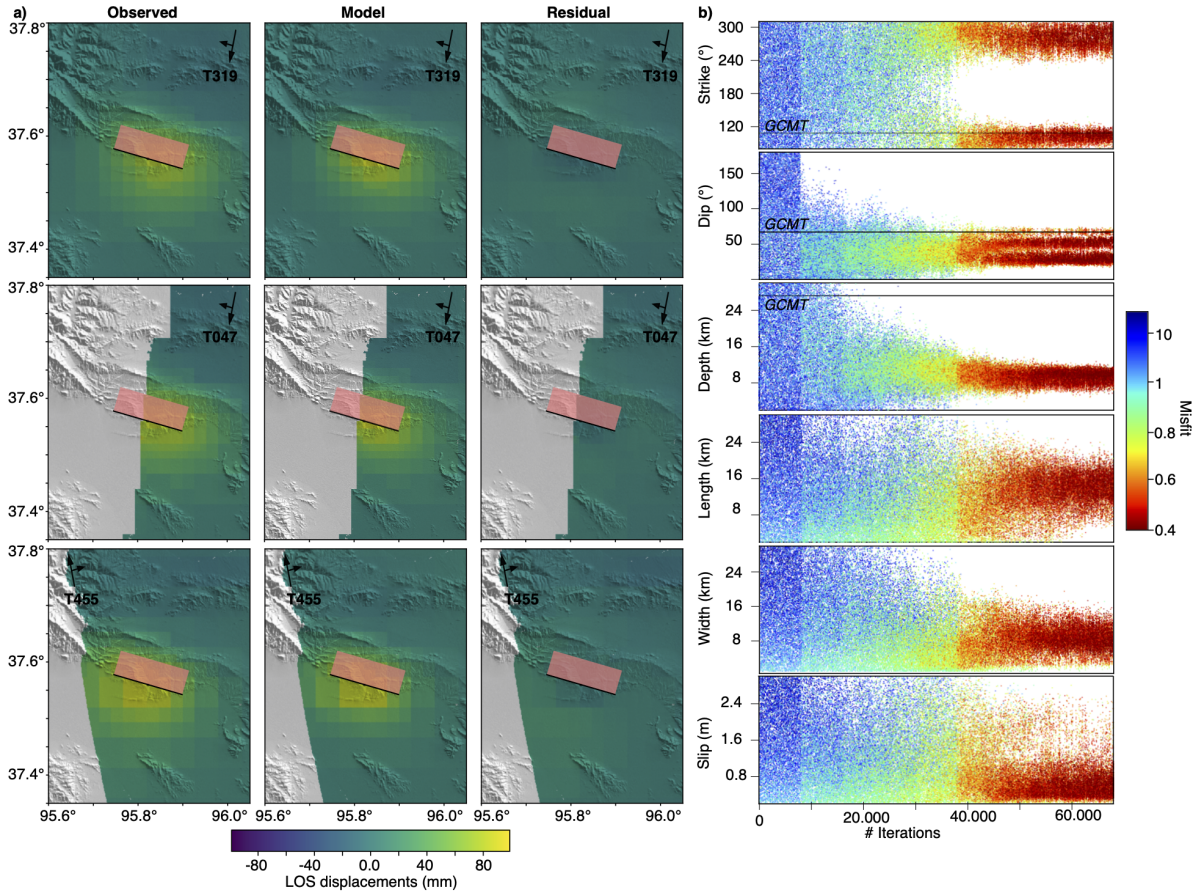


Figure 4.7: Posterior models for the 10<sup>th</sup> November 2008 earthquake obtained from the optimisation with a free dip-angle orientation based on both stack of long-baselines interferograms and teleseismic data. a) Comparison between data and model from the optimisation. Left: Sub-sampled surface displacements for tracks 319 (top), 047 (middle) and 455 (bottom). Middle: Modeled displacements associated with the maximum likelihood of the posterior probability distribution. Right: Residuals between the forward model and the observations. b) Sequence plots for selected parameters of the optimisation with a color-scale that varies depending on the misfit from high (blue) to low (red). As sampling in all regions is encouraged by random offsets, north-dipping and south-dipping bimodal solutions are explored simultaneously. The Bayesian bootstrap inversion converges towards an  $9.8 \pm 1$  km deep plane dipping towards the north with an angle of  $32 \pm 10^\circ$ .



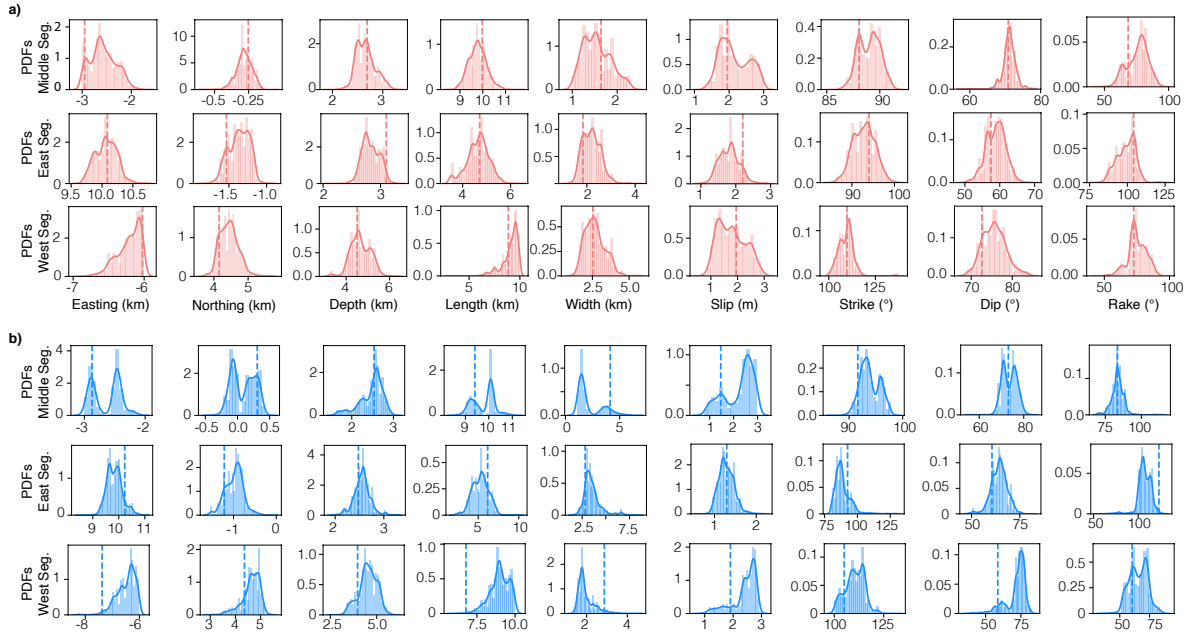


Figure 4.8: Summary of the posterior PDFs for the optimisation of the three rectangular faults (middle, east, west) in agreement with the co-seismic surface displacements of 2009 earthquake (a) and with a stack of co-seismic interferograms of 2009 earthquake (b). Dashed vertical lines are best-fitting models.

## 4.5 Discussions

### 4.5.1 Benefits of InSAR time series (TS) for fault inference

Traditionally, an earthquake is imaged with an interferogram, which contains the phase delay between two acquisitions. However, the travel time difference between the two acquisitions does not only contain the surface displacements associated with the earthquake but also multiple undesired signals such as ionospheric and atmospheric delays, orbital ramps, and topographic phase errors. Depending on the time span between the acquisitions prior to and after an earthquake, the interferometric phase may also include some transient post-seismic surface displacements. Therefore, in comparison to single interferograms, modeled TS maps present lower variances and covariances (Table S5). The final data variances from the TS data range from 0.2 to  $3 \times 10^{-6} \text{ m}^2$  while the correlation lengths are about 0.5-2 km.

The stack of co-seismic interferograms also helps improve the unwrapping coverage and the signal-to-noise ratio. Stacking is a simple way of removing turbulent atmospheric phase patterns that are random in time and space, and improves the spatial coverage, as interferograms used for the stack have varying unwrapping coverage depending on their temporal and geometrical baselines and their respective noises. Conversely, TS data have only information for pixels where the TS analysis and the time decomposition is possible, ie. when there is enough unwrapped interferogram for a given pixel for the inversion to be reliable. However, and contrary to a TS approach, a stack may also constructively add tropospheric signal if it is of the same sign in all stacked interferograms and, therefore, may also contain more correlated noise than differential interferograms, as illustrated by the higher correlation length values of the stacked data in Table S5. In addition, by using long-temporal baseline interferograms that cover the post-seismic period within the stack, the stacking operation also increases the amount of post-seismic deformation within the data. This effect is illustrated in the 2008 fault inference constrained with stacked

interferograms as posterior solutions are spatially located between co-seismic and post-seismic solutions inferred with the TS data (Fig. 4.7a).

To further evaluate the benefits of the TS approach, we perform another north-dipping 2008 co-seismic fault inference jointly constrained with the DInSAR interferograms shown in Fig. 4.3 and with teleseismic data. We then compare the posterior PDFs with those derived from the joint inversion of co-seismic TS maps and teleseismic data (Fig. 4.9). The analysis shows that, as for the solution constrained with the stack of co-seismic interferograms (Fig. 4.7), the fault parameters inference constrained with DInSAR are biased towards a solution that averages the co-seismic and the post-seismic solutions derived from TS data (Fig. 4.6). The solution is pushed further north, where post-seismic slip occurred, at  $10 \pm 0.2$  km of the gCMT solution, and towards a  $18.2 \pm 2.2$  km long and narrow  $1.7 \pm 0.4$  km wide rupture plane with a top located at  $12.1 \pm 0.5$  km depth. Posterior PDFs of the depth indicate higher values for the DInSAR optimisations than the TS optimisations, which is also in agreement with the fact that post-seismic slip occurred at a greater depth than the co-seismic slip (Fig. 4.6). The best-fitting values for slip, strike, and rake are  $2.0 \pm 0.4$  m,  $284 \pm 14^\circ$ , and  $87 \pm 15^\circ$ , and their PDFs are wider than those obtained from the inversion of TS and teleseismic data. Slip for DInSAR is also expected to be higher due to the presence of early afterslip in the data. The DInSAR best-fitting  $22 \pm 4^\circ$  northward dip angle is  $\sim 10^\circ$  lower than the dip angle reported in the gCMT catalog and the one of the northward-dip constrained by TS solutions, but again closer to the dip solution obtained from the post-seismic fault (Fig. 4.6). Posterior PDFs of the easting, depth, slip, strike, dip, and rake parameters have higher standard deviations when constrained from DInSAR than the TS maps, but, inversely, posterior PDFs for the northing and width fault parameters are narrower with DInSAR. This comparison shows that the inclusion of afterslip in the co-seismic modeling may introduce some large biases in the results towards the post-seismic solution. Those biases are proportional to the magnitude of the aseismic slip and the period between the two acquisitions of the co-seismic interferogram. Also, higher posterior uncertainties in the fault characteristics estimation are expected for the DInSAR optimisation in comparison to TS due to the higher noise in the co-seismic interferograms. However, wider PDFs for DInSAR is not, in this case, clearly highlighted for all parameters, which may be due to efficient empirical corrections performed on the DInSAR interferograms.

A pixel-by-pixel decomposition of the cumulative InSAR displacement TS has the limitation of providing a solution that may not have a spatial physical meaning and with reliability that depends on the number of acquisition dates and/or on the residual noise in the TS data. A multi-pixel TS decomposition approach (Jolivet and Simons, 2018) may tackle part of these limitations by accounting for the spatially correlated noise in the surface displacement data. However, the spatial consistency obtained in the decomposition (Fig. 4.2), validates the pixel-by-pixel method and the reliability of the results. In addition, the simplicity of the inverse problem (contrary to a multi-pixel approach that demands the inversion of a large matrix function of the number of InSAR points) allows us to perform optimisation with some additional constraints, such as imposing post-seismic surface displacements of the same sign than co-seismic surface displacements. An alternative approach would be a decomposition of the InSAR time-series data by joint and direct inversion of slip on the co-seismic and post-seismic fault planes. Such approach would impose a physical meaning of the decomposition contrary to a pixel-by-pixel or multi-pixel decomposition in time. However, it also requires a fixed fault geometry (e.g., Feng, 2015; Floyd et al., 2016; Liu et al., 2016a; Wimpenny et al., 2017) as the joint optimisation of both fault source parameters and temporal basis functions for each InSAR point is computationally expensive and such a modelling tool is currently not available to our knowledge.

#### 4 Spatio-temporal evolution of the 2008-2009 Qaidam earthquake sequence

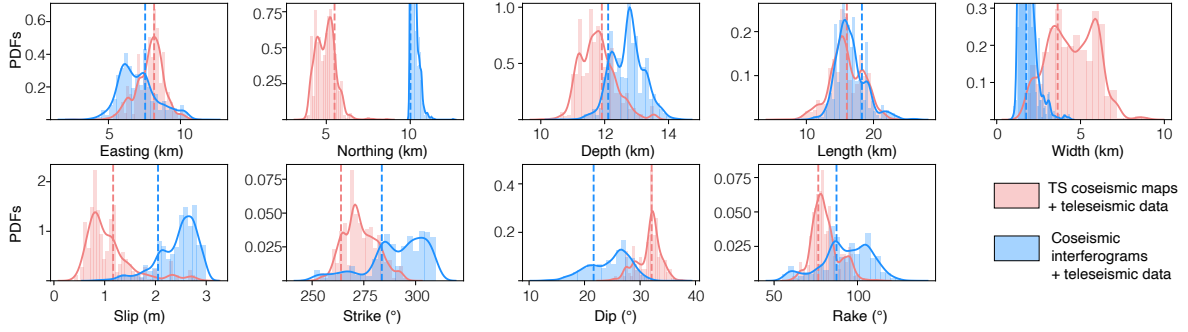


Figure 4.9: Comparison between posterior Probability Density Functions (PDFs) of the 2008 earthquake parameters obtained from the optimisation of InSAR co-seismic TS data + teleseismic data (blue) and DInSAR interferograms + teleseismic data (coral red). Dashed vertical lines are best-fitting models.

#### 4.5.2 Back-projection imaging for moderate-size earthquakes

The derived 2008 earthquake’s beam-power time function (Fig. 4.4a) is very similar to the source time function from the SCARDEC database (Vallée and Douet, 2016) (<http://scardec.projects.sismo.ipgp.fr/>). Of particular note, the method retrieves information about the source of the 2009 earthquake even if some waveforms might be contaminated by the 2009 Banda Sea Earthquake. The method therefore, shows its efficiency in comparison to other approaches to suppress unwanted signals arriving from other azimuths through destructive inferences (Kiser and Ishii, 2017). It is robust against signals from outside the defined source grid due to the stacking procedure.

The back-projection tool has also located the coherent emissions of both earthquakes with a remarkable agreement with geodetic data. It also shows, with the 2009 earthquake, promise as a method to infer the level of segmentation of a rupture without formal kinematic modeling, even for moderately sized earthquakes.

#### 4.5.3 The 2008-2009 Qaidam earthquake sequence

By reconciling co- and post-seismic geodetic observations, back-projection imaging, kinematic fault inferences, and previous structural interpretations, we develop a model for the fault geometry of the Qaidam thrust system shown in Fig. 4.10, with overall fault and fold geometry typical of foreland fold-and-thrust belts

Daout et al., 2019 (Daout et al., 2019) modeled, from Envisat measurements across the Zolobulak Shan, the short-term after-slip following the 17<sup>th</sup> April 2003 Delingha earthquake with a shallow segmented ramp-flat-ramp north-dipping structure that steepens as it approaches the surface under the Delingha anticline, and inferred a low-angle north-dipping fault for the 2003 earthquake (orange line in Fig. 4.10). The north-dipping gCMT solution of the 2003 earthquake is very similar to the 2008 gCMT solution with a  $\sim 30^\circ$  dip angle rupture plane at about 16 km depth (Table S1, red focal mechanism in Fig. 4.10). In addition, the two  $\sim 18$  km and  $\sim 21$  km deep April 2004 right-lateral  $\sim M_w$  5.3 earthquakes and the  $\sim 12$  km deep October 2004 thrust  $\sim M_w$  5.5 earthquake (according to gCMT, Table S1) may belong to the same flower structure that ruptured in 2003 (Fig. 4.10). Static stress transfer within this flower structure may have triggered the 2004 sequence of earthquakes one year after the 2003 earthquake.

This study show that kinematic inversion alone cannot resolve rigorously the ambiguity between

the north-dipping and south-dipping geometries due to the low misfits of both solutions. Biases may also arise from assumptions on the 1D crustal structure or the absence of topography in the model, although bootstrapping technique can efficiently estimate model parameter uncertainties by propagating data errors and by assessing modelling errors. In addition, the stations have individual time shifts to compensate for crustal structures, such as each station can shift its waveforms up to 4 s with respect to the earthquakes' onset time to achieve maximum fit. This compensates for unmodeled 3d-path effects.

We, here, infer a shallow north-dipping low-angle structure responsible for the 2008 earthquake (green line in Fig. 4.10), mainly constrained from the coplanarity between the co- and post-seismic north-dipping solutions (Fig. 4.5). The depth of the rupture ( $\sim 12$  km deep) is in agreement with the width of the Olongbukak range ( $\sim 10$ - $15$  km), as north-dipping and south-dipping faults bounding the Olongbulak range are expected to merge at those depths (Fig. 4.5). The presence in the morphology of a major north-dipping structure in the southern front of the Olongbulak range also challenges a hypothetical south-dipping and high-angle 2008 rupture plane, coplanar to the 2009 rupture (Fig. S1b, Fig. S12). Such coplanar fault geometries would not create a differential vertical movement between the deeper part of the south-dipping fault (where the 2008 earthquake occurred) and the shallow part of the fault, within the Olongbulak Shan (where the 2009 earthquake occurred) (Daout et al., 2016a) (Fig. S12b). The absence of differential vertical movements would, therefore, require no triple junction and shallow high-angle north-dipping plane, while this structure is identified in the southern front of the Olongbulak Shan. As a triple junction is not stable over long time scale and as the current morphology involves multiples deformation stages, it is difficult to conclude from this observation. However, the main north-dipping vergence of the NQT and the current activity of its southernmost branches, as within the Olongbulak pop-up, support our view of a low-angle north-dipping plane, responsible for the 2003 and 2008 earthquakes, branching at the roots of the shallow high-angle thrusts of the NQ ranges and of the Qaidam basin.

Our results also indicate that the 2008 earthquake did not break the southern and north-dipping high-angle branch of the Olongbulak pop-up structure. Post-seismic slip is constrained down-dip of the co-seismic rupture on a very narrow plane with slip of the same order of magnitude than the co-seismic slip. Surface displacements might not be very sensitive to the amount of down-dip afterslip, and the amount of slip might therefore be over-estimated for the north-dipping solution. In this regards, we performed several tests forcing a higher fault width or lower fault slip. We observed that with such prior values, posterior PDFs tend to be asymmetric towards the boundary values, indicating that the data require such high slip and fault width. The modelling, therefore, shows that the observed short-term post-seismic displacements can not be explained by fault movement on the north-dipping shallow and high-angle branch of the Olongbulak pop-up structure, leaving thus an open question on the seismic potential of this branch of the Olongbulak range.

The 2009 rupture is the result of the vertical partitioning of the shortening along the high-angle and shallow south-dipping back-thrust of the Olongbulak Shan (blue line in Fig. 4.10). The rupture started at  $\sim 9$  km depth along the middle segment and then propagated bilaterally along two shallower and higher-angle segments (Figs. 4.4, 4.5) that displace basin-deformed sediments of the Olongbulak range above the Paleozoic bedrock of the Zonlongbulak range (Yin et al., 2008a; Guihua et al., 2013; Pang et al., 2019). Afterslip likely occurred on a similar fault patch surrounding the coseismic slip, in agreement with similar post-seismic and co-seismic surface displacement patterns measured with InSAR (Fig. 4.2, Fig. 4.3), the optimisation of the stack of long- and short-temporal baselines interferograms (Fig. S11), and previous studies (Feng, 2015; Liu et al., 2016b; Liu et al., 2016a). The observed rupture complexity in both geodetic displacements and back-projected seismic emissions likely reflect the along strike and along depth lithological segmentation of the Olongbulak fault system.



The 2008-2009 Qaidam earthquake sequence illuminates a short-timescale and spatially confined example of regional tectonic and geodynamic processes at play. However, the inferred flower structure, in which high-angle thrusts and back-thrusts root into a low-angle décollement, may be typical of structures and deformation styles in the South Qilian Shan at greater scale. The low-angle north-dipping structure may connect to the roots of the Olongbulak pop-up structure, the Zongbulak Shan, and the Xietie Shan thrusts and may transfer the shortening rate from the north, along the Qilian Shan, to south, in Qaidam Basin, along the high-angle folds and thrust belts (Fig. 4.10, inset, Fig. S1a). It supports regional tectonic models involving a regional décollement that connects to the Qilian Shan suture or pre-existing Cenozoic lithospheric weaknesses further north (Burchfiel et al., 1989; Meyer et al., 1998; Yin and Harrison, 2000; Yin et al., 2008a) and the southward expansion of the South Qilian Shan (Yin et al., 2008b; Pang et al., 2019).

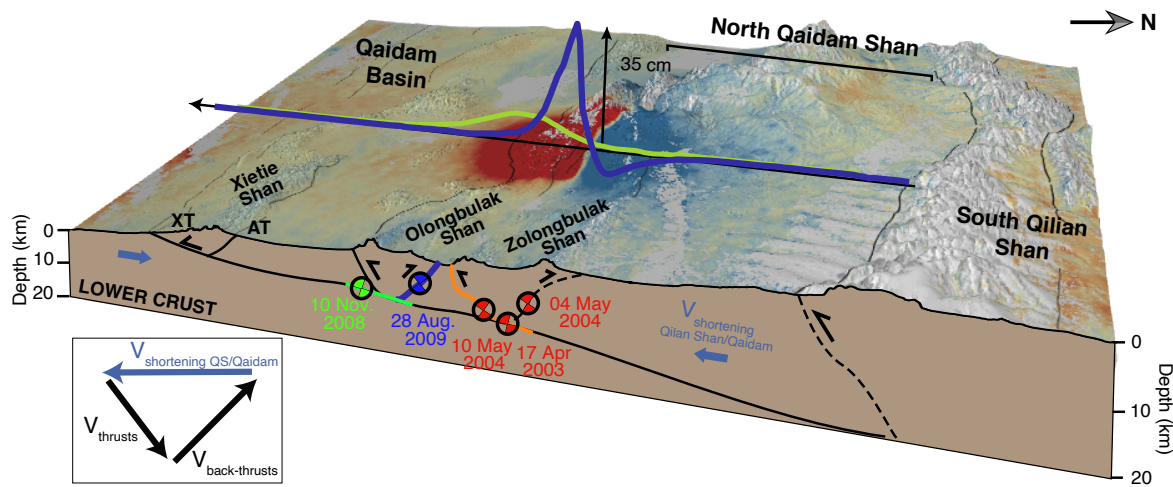


Figure 4.10: Three-dimensional block diagram of the proposed geometry for the North Qaidam thrust system superimposed on a digital elevation model (3x vertically exaggerated), along with the cumulative LOS displacement map from descending track 319 and the 10<sup>th</sup> November 2008 and 28<sup>th</sup> August 2009 co-seismic LOS displacements profiles from Fig. 4.2. Insert at the bottom left shows interpreted conservation of motion vectors across the fault-system, where high-angle thrusts and folds vertically partition the horizontal shortening transferred from the South Qilian Shan to the Qaidam basin.

## 4.6 Conclusion

In this study, we explore the benefits of an InSAR TS approach for earthquake fault inference and demonstrate the improved signal-to-noise ratio of such data sets in comparison to DInSAR, and the additional constraints offered by the post-seismic surface displacements extracted from the InSAR TS data. The 2008-2009 Qaidam earthquake sequence exemplifies typical earthquakes in remote areas, where field work is difficult and structural seismic profile or geological models are rarely available or poorly constrained, yet satellite-based geodetic and teleseismic data are easily available. We use the open source Grond toolbox (Heimann et al., 2018b), the Pyrocko framework (Heimann et al., 2017c) and the Kite toolbox (Isken et al., 2017c) for pre-processing and analysing surface displacements to infer the earthquake fault parameters from both geodetic and teleseismic data. Pyrocko provides a uniform framework for both near-field and far-field data and Green's function databases to speed up forward calculations. Our analysis reveals

that the optimisation scheme successfully explores bimodal north-dipping and south-dipping solutions for the deep 2008 earthquake, which was further validated based on the co-planarity between the inferred co-seismic and post-seismic fault planes. It also shows that the tool allows the exploration of the rupture segmentations with three independent faults, where no fault geometrical parameters are fixed *a priori*. Besides, the back-projection tool, also based on the Pyrocko framework, has located the coherent emissions of both earthquakes with a remarkable agreement with geodetic data. It also constrains the segmentation of 2009 ruptures in accordance with the InSAR-based fault models, and therefore shows promise as a useful tool even for moderate earthquakes.

## 4.7 Contributions

S.D. designed the study, processed the radar data and wrote the first version of the manuscript. A.S. performed the seismological analysis. S.D., A.S. and H.S. conducted the inversions. A.S., M.I., S.H. and H.S. developed the inversion tools. All authors have read, agreed, and participated to the published version of the manuscript.

## 4.8 Funding

This research was funded by the German Research Foundation DFG (Number 276464525: Bridging Geodesy and Seismology for improved and automated estimation of faulting events) through an Emmy-Noether Young-Researcher-Grant. S.D. is funded by the Natural Environment Research Council through the Looking into the Continents from Space (LiCS) large grant (NE/K011006/1) and the Centre for the Observation and modelling of Earthquakes, Volcanoes and Tectonics (COMET).

## 4.9 Acknowledgements

The SAR data set was provided by the European Space Agency (ESA, <https://scihub.copernicus.eu>). Landsat-8 image courtesy of the U.S. Geological Survey. The facilities of IRIS Data Services, and specifically the IRIS Data Management Center, were used for access the waveforms, related metadata, and/or derived products used in this study. IRIS Data Services are funded through the Seismological Facilities for the Advancement of Geoscience and EarthScope (SAGE) Proposal of the National Science Foundation under Cooperative Agreement EAR-1261681. We are grateful to Chris Rollins and one anonymous reviewer for their constructive comments and editing of the English language.

# 5 Summary and Discussion

## 5.1 Summary

The primary outcomes of each chapter are:

- The main investigative goal of this chapter was to determine if rupture segmentation can be detected and if it is significant meaningfully modelled in an earthquake source parameter inversion. Inversion of four different earthquakes from telseismic and InSAR datasets with rigours uncertainty estimation and variable source model complexities showed that consideration of rupture segmentation is important in earthquake source modeling studies. I present a strategy based on the Akaike informational Criterion (AIC) to detect significant rupture segmentation. To parsimoniously choose an appropriately complex model, the data and modeling uncertainties are taken into account: A model with given complexity (i.e. number of adjustable parameters) is considered an appropriate solution if increasing its complexity does not improve the AIC values and the rotational distances of angles between mechanisms of simpler and complex models are not significantly larger than difference of the rotational mechanism due to data and modeling errors. A significant difference in the estimated source mechanisms based on different source model complexities shows that rupture segmentation, or absence thereof, can be resolved from far-field data and especially from near-field data for earthquakes in the magnitude range  $M_w$  6 to  $M_w$  7. Using a model that is too simple limited the amount of information that can be learned from earthquake source modeling. Thus, an appropriate choice of model segmentation allows a more robust estimation of source mechanisms and reduces systematic biases and trade-offs.
- Modeling of rupture segmentation with multiple sources results in an increased parameter space. Two methods are developed to provide data-driven model-independent constraints to inform parameter prior pseudo-probability estimates in a kinematic earthquake source optimisation. This are a time-domain multi-array backprojection of teleseismic data and image analysis methods applied to InSAR surface displacements. The multi-array backprojection aims to infer the spatio-temporal evolution of the rupture, including detection of potential rupture segmentation based on the number of coherent high-frequency sources. The developed improved multi-array backprojection method has significantly increased resolution compared to the traditional use of large array backprojection and uses P- and S-phase body waves. I calibrate the backprojection using empirical traveltimes corrections from maximizing semblance for a fore- or after-shock. The multi-array backprojection method also provides robust and precise estimates based on bootstrapping of the travel-time models and array weights. Compared to single-array methods the new multi-array backprojection method provides a significant resolution improvement. The second method uses image analysis methods on InSAR surface displacement maps to infer modeling constraints on rupture characteristics (e.g. strike and length) and the number of potential segments. Both methods provide model-independent constraints on fault location, dimension, orientation and rupture timing, applicable to form prior probabilities of model parameters. The methods are applied to data from the 25.11.2016 Muji  $M_w$  6.6 earthquake and inform a joint-data source parameter inversion. The results indicate rupture segmentation and bilateral rupturing for the 2016 Muji earthquake. A good agreement between backprojected

coherent energy and the static displacement measured by InSAR is found. The results of the backprojection using high-frequency filtered teleseismic waveforms in particular shows the capability to illuminate the spatio-temporal rupture evolution with the potential to resolve the start and stop phases of individual fault segments. The agreement between backprojection results of synthetic waveforms from the best fitting source model and the observed waveforms indicates the possibility of creating synthetic forward calculated backprojection images and comparing them to the data to find a plausible model.

- This chapter looked at a depth-segmented earthquake sequence to determine the fault system geometry and as a case study for the application of the developed methods to smaller moment magnitude earthquakes. The developed backprojection and inversion methods are applied successfully to determine the fault geometry of the Qaidam 2008-2009 earthquake sequence, which consists of two  $M_w$  6.3 earthquakes, using seismological and geodetic data. The high-frequency teleseismic multi-array back-projection was able to identify rupture segmentation for moderate-sized earthquakes. The 2008 Qaidam earthquake is a deep shallow dipping earthquake with no indication of rupture segmentation from the backprojection results. Post-seismic afterslip of the 2008 earthquake is modelled to occur on a down-dip segment. The 2009 Qaidam earthquake ruptured three distinct south-dipping high-angle thrusts, rupture propagated to the surface, jumping from the fault segment in the middle, on which rupture initiated, to both other segments in a bilateral rupture. The backprojection results agree remarkably well with the InSAR time series displacement data, indicating a relationship between slip magnitude and coherent seismic energy radiation.

## 5.2 Further application of the developed methods and tools

The in this thesis developed methods and tools have been developed as open-source community-software for further use. They are not limited to investigation of rupture and fault segmentation but can also be used to study earthquake sources in general. For example I applied the developed multi-array method and code to observe and aid in the first description of a backpropagating rupture during the  $M_w$  7.1 Romanche transform fault earthquake (Hicks et al., 2020b). The earthquake took place in the Romanche trench on a single ocean transform fault in the Atlantic Ocean. The super-shear speed rupture propagated first around 40 km eastwards (Fig. 5.1,a-c) from the nucleation point. The rupture then propagates back westwards. The rupture front crosses the nucleation point again (Fig. 5.1,e-f), a few kilometers above, as inferred from slip inversions (Hicks et al., 2020a). The rupture terminates finally around 20 km west of the nucleation point (Fig. 5.1,h). The backpropagating rupture process is possibly the effect of depth segmentation (Hicks et al., 2020a). Backpropagating ruptures had not been observed before. After this discovery more studies were encouraged to report similar behaviour (Tadapansawut et al., 2020) and theoretical background of the phenomenon (Idini and Ampuero, 2020). Ocean transform faults are considered one of the simplest manifestations of faults on Earth (Hensen et al., 2019; Hicks et al., 2020b). That still such a dynamic behaviour was observed along a 'simple' fault highlights the need for data-driven analysis of earthquakes, which consider the source complexity. The developed multi-array backprojection method is further employed to investigate the 1995 Aqaba earthquake (Vasyura-Bathke et al., 2021; Bathke et al., 2016). The available broadband data have been much sparser in 1995, especially dedicated arrays. The multi-array clustering method maximises the information that can be gained under these circumstances. The spatio-temporal evolution of this rupture is resolved and rupture segmentation on three distinct faults is detected (Vasyura-Bathke et al., 2021). The multi-array backprojection method can be improved upon in the future to work with near-field waveform data and to not only backproject body waves but also surface waves.

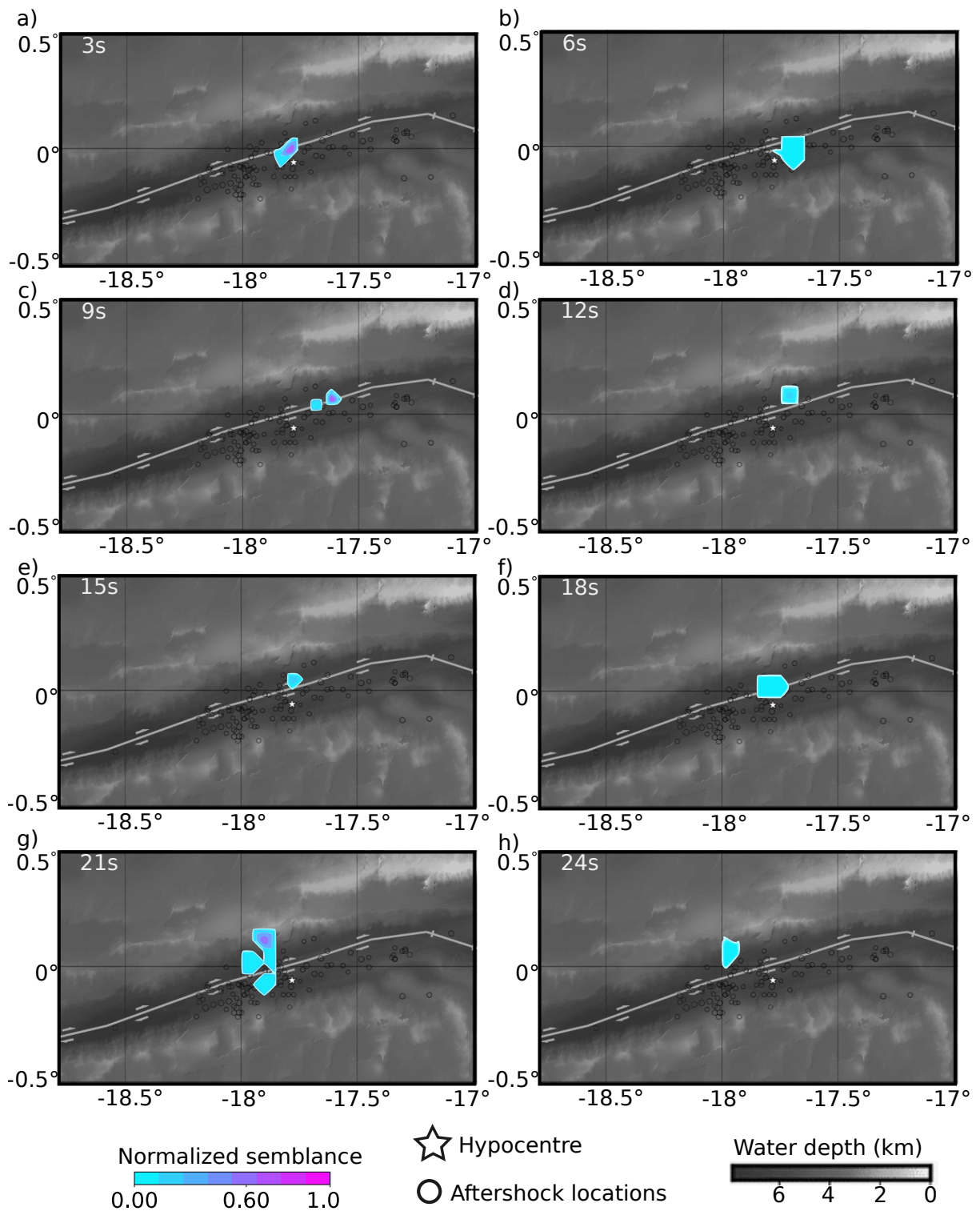


Figure 5.1: Step-wise semblance maps of the  $M_w$  7.1 2016 Romanche earthquake from multi-array backprojection of high-frequency filtered teleseismic data in 3s steps. The hypocenter is indicated by a white star and the recorded aftershocks with black circles. The gray scale background map is based on bathymetry (Hicks et al., 2020a). Location of the 2016 Romanche earthquake can be seen in Fig 5.2. Processing details can be found in Hicks et al., 2020a.

The presented multi-array backprojection and surface displacement map image segmentation could be applied independently in the future in an automated fashion. Both methods are computationally relatively cheap and can deliver reliable statistical information on their own. Both methods can deliver, if run routinely, labels for future machine learning approaches. Routine application of the multi-array backprojection can provide fast evaluation of the spatio-temporal rupture evolution with rigorous uncertainty estimates from the bootstrapping of array weights and perturbation of the travel times. Statistics on the occurrence of coherent high-frequency emitters during the rupture process could be compared to other observables, e.g. shaking intensity at strong motion stations and geologically studied rock damage zones. The good agreement between the coherent energy emissions mapped by this improved backprojection method with the static displacement for both the 2016 Muji and as well for the 2008-2009 Qaidam earthquakes warrants further investigation. The image segmentation of InSAR displacement maps can not only be deployed to infer data-driven priors for finite fault modeling but also to detect and describe deformation signals in general. This can be applied to derive statistics from big data InSAR data catalogs such as the LiCSAR InSAR data archive (Lazecky et al., 2020). The presented method can also be applied to other surface displacement datasets, such as pixel offset measurements from optical and radar images or differential LiDAR measurements.

### 5.3 Earthquake rupture segmentation modeling impact and outlook

The source parameter inferences for source models with different model complexity vary significantly (Chapter 2) indicating the relevance of studying earthquake source segmentation at the fault scale level thoroughly for further down-stream analysis. The level of rupture segmentation studied in this thesis, on the fault segment scale, is observable with globally available data and can have direct impact on hazard estimations like probabilistic seismic hazard analysis. As faults and rupture processes are governed by fractal distributions and fractal behaviour at all scales (Okubo and Aki, 1987; Savage and Brodsky, 2011), it should be possible to resolve also rupture segmentation or similar processes occurring on smaller scales. As described in Chapter 2 the low frequency filtered teleseismic waveform data are a limiting factor for the resolution of the detailed spatio-temporal evolution of the earthquake process. It is not possible to resolve rupture features smaller than half a wavelength. This is somewhat relegated by the high frequency waveforms used in the multi-array backprojection, but due to noise at higher frequencies the available frequency bands are limited as well. The developed methods in this thesis maximise the information that can be gained from globally available data for intermediate sized earthquake. Therefore to study smaller earthquakes or provide more detailed studies of the rupture segmentation would require the inclusion of more near-field data. These datasets could be pixel offsets from optical data, differential LiDAR measurements and near-field seismic waveforms, e.g. from strong motion sensors or distributed acoustic sensing.

In frameworks like the Uniform California Earthquake Rupture Forecast calculated hazard differs between more or less segmented faults (Field et al., 2014; Field et al., 2015). The exact implications of rupture segmentation to near-field shaking intensities and shaking duration and therefore the direct hazard of rupture segmentation are few (Mai and Meyers, 2009), because of the lack of observational statistics and lack of modeling efforts (Mai and Meyers, 2009). Rupture segmentation can be expected to increase the duration of the shaking in some cases. Future research could focus on possible connections between recorded shaking intensities and the coherent high-frequency radiators mapped in the backprojection results.

The consideration of model complexity can help geological field work in remote areas, as shown for the investigation of the 2008-2009 Qaidam earthquake sequence. A standardized earthquake source model database with statistics on rupture segmentation, including intermediate sized

earthquakes in the magnitude range  $M_w$  5.5 to 7, also allows for follow up statistically analysis to investigate the phenomena of rupture segmentation further. A database of rupture segmentation and mechanisms is needed alongside geologically determined fault lines in earthquake cycle simulators (Richards-Dinger and Dieterich, 2012; Luo et al., 2017).

More robust statistics on rupture fault segments can help in one of, in my opinion, the most interesting and hotly debated topics in earthquake physics. This is how an earthquakes nucleates and what role the initial nucleation phase plays in determining the final earthquake size and moment. A certain amount of stress change is necessary to overcome the initial nucleation phase and develop a full rupture of a fault segment (Ohnaka, 2000). A characteristic necessary size of the nucleation area in relation to the full fault area is therefore assumed to be necessary to facilitate co-seismic ruptures (Ohnaka, 2000) supported by rate-and-state friction laws and lab observations (Dieterich, 1992; Lapusta and Rice, 2003). It is an open question if the initial moment rate during nucleation, or early phase, is in relation to the total moment release over time. This would either imply that earthquakes are (weakly) deterministic (Melgar and Hayes, 2017) or, if this not the case, that earthquakes are not deterministic at all (Meier et al., 2017; Meier et al., 2020). The current studies (Meier et al., 2017; Melgar and Hayes, 2017) are based on the total source-time function of earthquakes, without consideration of rupture segmentation, which could potentially have had an impact on such observations.

## 5.4 Inferences on rupture segmentation characteristics from studied earthquakes

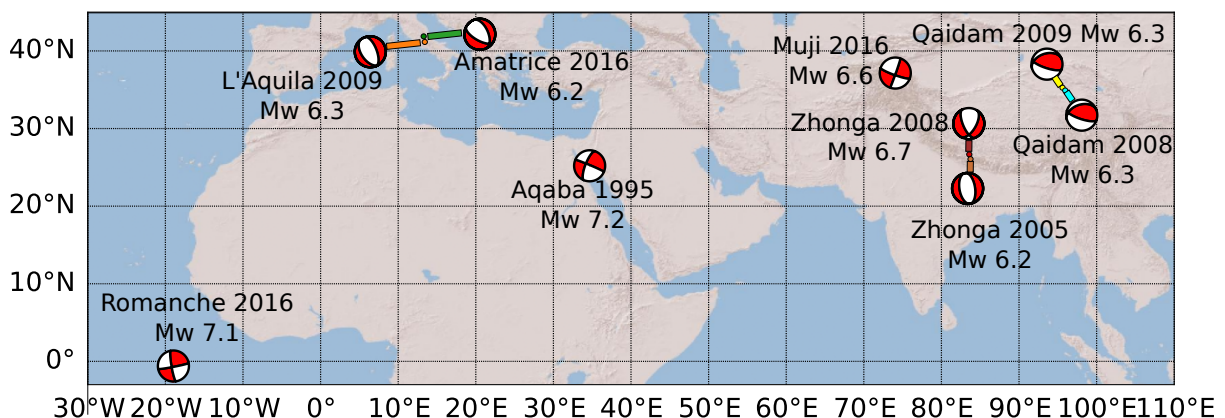


Figure 5.2: Location of all earthquakes studied in this thesis or with the methods developed in this thesis, with source mechanism estimates plotted as a single beachball.

From all earthquakes investigated as case studies in this thesis (Fig. 5.2) no correlation between the number of inferred rupture segments and moment magnitude can be found (Tab. 5.1). The two smallest studied earthquakes with  $M_w$  6.2 differ in the degree of the preferred source complexity with the 2005 Zhongba earthquake not showing signs of rupture segmentation but the 2016 Amatrice earthquake showing clear indications for two distinct rupture segments. The studied earthquakes of  $M_w$  6.3 earthquakes range from showing no indication of rupture segmentation, for the 2009 L'Aquila earthquake, to three distinct segments for the 2009 Qaidam earthquake. The deepest crustal earthquake studied, the 2008 Qaidam earthquake (Chapter 4) with a top edge depth of around 12km shows no sign of rupture segmentation. Based on InSAR data alone the observation of no apparent rupture segmentation can be biased, as the surface deformation signal of deeper deformation sources tends to smooth out. However the multi-array backprojection results also show only two coherent high-frequency semblance peaks,



## 5 Summary and Discussion

Table 5.1: Summary of earthquakes studied in this thesis or with the methods developed in this thesis, with best fit source parameter estimates and inferred source complexity. Depth is given as top depth of the finite rectangular source or as the mean top depth in case of multiple finite sources. The abbreviation bsl indicates a source depth below sea level. The 2016 Romanche earthquake is a depth segmented rupture, the star for the length source parameter in this case indicates the width. Length is given for all rupture segments, ordered by time of rupture initiation.

Parameter	Magnitude	Depth (km)	Duration (s)	Number of segments	Length (km)
2005 Zhongba	6.2	2.7	6	None	15.6
2016 Amatrice	6.2	2	12	2	9.7 8.6
2008 Qaidam	6.3	11.9	8.3	None	16
2009 Qaidam	6.3	2.7	9.4	3	10 4.7 6.1
2009 L'Aquila	6.3	2.2	10	None	13
2016 Muji	6.6	1.9	22	2	19 12
2008 Zhongba	6.7	2	15	2	18.8 17.4
1995 Aqaba	7.3	3 (bsl)	22	(3)	16 33 6
2016 Romanche	7.1	10 (bsl)	30	(2)	20* 10*

indicating the start and stop phases, with no other high-frequency peaks as indication of rupture segmentation. This supports that the relatively deep 2008 Qaidam earthquake occurred as a simple rupture process. If however deeper crustal earthquake sources are less segmented than shallower crustal earthquakes needs to be investigated from a broader sample as present in this thesis.

The theory that a rupture is unlikely to jump between segments for more than 5 km (Wesnousky, 2006; Wesnousky and Biasi, 2011) can be rejected by the observations in this thesis, especially by observations of the rupture processes of the 2016 Muji earthquake and also the 1995 Aqaba earthquake (Bathke et al., 2016; Vasyura-Bathke et al., 2021), supporting recent findings (Hamling et al., 2017). The length of the observed fault segments is worthy of note. They are smaller than what could be assumed from scaling laws (Blaser et al., 2010) and much smaller (see summary Tab. 5.1) than the one-half of the seismogenic thickness minimum length of a fault segment assumed in the UCERF model (Milner et al., 2013). The hypothesis of "typical" reasonable minimum length of 10 km for a fault segment can be challenged by the source geometry inferences in this thesis. Based on the smallest fault segments in thesis it is valid to claim that it is possible to resolve at least around 4 km long fault segments with globally available data. A common modeling assumption is that a rupture segment is identical to a fault segment (Milner et al., 2013) which is not the case for the observed segments in the case studies.

In all case studies the rupture starts on the larger segment (see summary Tab. 5.1). The only exception is the 1995 Aqaba earthquake. However for this case the assumption of rectangular source model geometries might bias the source geometry inferences, as the surface fault trace of the 1995 Aqaba earthquake has been shown to be curved from high-resolution bathymetry (Ribot et al., 2020). Around the inflection in a curved fault it could be that multiple coherent high-frequency signals are emitted, due to the rupture slowing down around the inflection and accelerating afterwards. Fault segmentation between two completely distinct rupture segments



might therefore only be apparent. Consideration of curved fault geometry (Dutta et al., 2020) could be necessary and would lead to a single large fault on which the rupture initiated. The Qaidam 2009 earthquake could also involve a curved segment. Robust modeling of a curved fault geometry does require high-resolution near-field data (Dutta et al., 2020) and therefore limits the global applicability, making the assumption of rectangular source geometries still necessary.

For all segmented earthquakes studied in this thesis a common property is that the nucleation starts close to the center of the initial rupture segment and that a bilateral rupture evolves. This could relate to the hypothesis that a characteristic necessary size of the nucleation area in relation to the full fault area is needed (Ohnaka, 2000). Based on the limited observation in this thesis it could be hypothesised that rupture, which initiates at the border of a rupture segment, does not evolve to an earthquake with rupture segmentation. This also seems to be true for rupture that already jumped to another segment. For the 2009 Qaidam earthquake and the 1995 Aqaba earthquake rupture that already jumped from one rupture segment to another does not propagate to further rupture segments, if the nucleation of the jumped to rupture segment was close to the edge of the respective modeled source.

## 5.5 Data-driven optimisation schemes to determine appropriate source model complexity

### 5.5.1 Transdimensional earthquake source modeling

The next step forward, based on this thesis, could be a finite source modeling framework which directly takes into account the potential earthquake rupture segmentation. An outline for combining all methods developed in this thesis is presented here to achieve this. To automatically evaluate the performance of different source model complexities I first tried to make use of a transdimensional optimisation scheme. Transdimensional methods, or reversible jump algorithms, are statistical methods for Bayesian inference with a variable number of unknowns (Sambridge et al., 2013), so that the number of models tested does not have to be fixed but is decided on during testing, parsimoniously navigating the curse of dimensionality (Bodin and Sambridge, 2009). Several models can contribute to the data fit and the associated uncertainties be considered simultaneously (Sambridge, 2013; Sambridge et al., 2013). Transdimensional methods have been applied to geoscientific problems in general (Sambridge et al., 2013; Sambridge, 2013; Bodin et al., 2012) and to slip in finite fault modeling in particular (Dettmer et al., 2014; Amey et al., 2019), where it is employed to circumvent regularization a priori. Transdimensional models adapt according to Bayesian parsimony locally to the data (Bodin et al., 2012), reducing the need for any subjective choices on the model complexity or regularizations (Dettmer et al., 2014). Parsimonious behaviour is inherent in this approach (Bodin and Sambridge, 2009). This makes the transdimensional approach interesting for the issue of the data-driven choice of the degree of source model complexity. At every step the reversible jump Monte Carlo Markov Chain allows for so called *births* or *deaths* (Sambridge et al., 2013), the addition or reduction of the dimensionality by one degree (or multiples) from the currently evaluated dimensionality of the model. As a third alternative, the current dimensionality can be kept. The choice is based upon a draw from a proposal density. The choice of the proposal distribution however is one of the greatest problem when applying this method to large-scale problems (Dettmer et al., 2014; Brooks et al., 2011).

Applying the transdimensional method to optimize the source of the 2016 Muji  $M_w$  6.7 earthquake however proved to be unstable. My implementation of the algorithm tried to evaluate the proposal density at every step for a possible change of source complexity, using the AIC as fitness criterion. A condition of non-overlapping areas of the drawn source models is applied. The results either

indicated an unreasonable high number of fault segments (40+) or never exceeded one, depending on the choice of the proposal density. I attribute this failure mainly to the abrupt jumps in the likelihood function due to doubling or halving of the source parameters, when a new model is added or an existing one is removed from consideration. The source parameters of a finite earthquake source model are also highly dependent. Adding a new source does not directly lead to a reduction of the misfit. This is because of the high number of source parameters of an added source and the trade-offs between the source parameters. This means that any added source model parameters have to converge first to achieve a comparable fit to already evaluated source models, which had more iterations to converge. This problem is exemplified considering a simple single source model when applied for a dataset like the 2016 Muji  $M_w$  6.7 earthquake. The InSAR surface displacement strongly points to segmented deformation, showing a slip gap between two segments. The strong signal that needs to be modeled coincides with the two distinct segments, while the displacement low does not show any signal. The source parameter controlling the area and moment will therefore tend to grow very large to encompass both main signal lobes, because this directly this brings an immediate and drastic reduction of misfit. This also holds for the seismic waveforms, in which the misfit, caused by the high amplitudes of the seismic waveform data, is reduced at first order with a large signal. If in such a situation a new source is added by choice of the proposal draw, it is furthermore unclear where this new source should be positioned in relation to already drawn sources. Simply reducing the existing source by a factor would lead to falsification of posterior statistics. If these sources are placed at random, they will tend to fit very localized signals, often noise, as the main signal is already covered by a single large source model. I caution usage of this approach due to these complications. Transdimensional modeling can however potentially be useful for slip inversions at a second step, after the fault geometry has been determined, and potentially also in determining the degree of curved faults with fixed surface traces (Dutta et al., 2020).

### **5.5.2 Simultaneous parallel modeling of multiple earthquake sources model geometries with different number of sources**

As an alternative to the transdimensional approach I have developed a simultaneous parallel modeling of multiple earthquake sources model geometries with different number of sources. This approach utilizes the methods developed in the thesis to produce a distribution of likely choice of an appropriate source model complexity and data-driven choice of the appropriate number of source models. The approach is based on the evaluation of the model performance in terms of the Akaike Informational Criterion (AIC) as described in Chapter 2, Eq. 2.7. This approach uses the likelihood of each model considering the resolution of the model parameter and also the trade-offs between them by using the assumption of a multivariate normal distribution. I use the maximum log-likelihood value from each models bootstrap ensemble to calculate the AIC. The inversion scheme is based on the guided optimisation presented in Chapter 3. Additionally to the misfit based high-score list of each bootstrap chain an additional complexity high-score list is considered. For the complexity high-score list the criterion for model evaluation and sorting the complexity high-score list is the AIC. The complexity high-score list holds the model, the number of sources in the model and the respective AIC. At the beginning an equal number of slots in the complexity high-score list are reserved for each a prior assumed number of source models in the complexity high-score list. This means that at the start (during the guided optimisation phase) the best performing 50 models from all bootstrap chains, for each considered source model complexity, are included in the complexity high-score list. All random weights and noise perturbations are kept the same for each of the assumed model complexities. A model with a lower AIC score can push the model with the highest AIC score from the complexity high-score list. However as convergence of earthquake source models with more sources takes longer than convergence of models with less model parameters, a comparison between a model from 1000

iteration for a one-source model with a two-sources model from the same number of iterations would be unfair, I add an inertia factor dependent on the number of source model parameters,  $n_{par}$ , chosen to be a  $100 * n_{par}$  iterations delay. This inertia factor controls after which number of iterations an earthquake source model with a certain number of sources is allowed to be pushed out of the high-score list. Up until that number of iterations the fixed number of source models remains in the complexity high-score list to allow for a set of models to be compared fairly. Other previously 'unlocked' earthquake source models with a lower number of sources can however compete. This results in an ensemble of models evaluated in the same framework, e.g the same data weights as given by the Bayesian bootstrapping and the Randomize-then-Optimize procedure are applied, with a different number of source models, compared and ranked according to the performance of the models according to the AIC. The different earthquake source models with different number of sources can be directly compared, as all source model complexities are assessed at each step with the same weights.

I applied the presented framework to the 2016 Muji  $M_w$  6.7 earthquake data, as described in Chapter 3, and kept 50 models in the complexity high-score at the beginning for 1, 2 and 3 sources. Each of the earthquake source models with a different number of sources is optimized for in parallel with 100 individual bootstrap chains. The resulting evolution of complexity high-score can be seen in Fig 5.3, showing that in the beginning one-source models are favored but are kicked out in favour of a two-sources model at the end. This is expected as the fit can initially be strongly improved with one large area source with high slip without fine sampling of other source parameters controlling the geometry but are outclassed once convergence of those geometric parameters begins in the two-sources model. Also the three-sources model is not considered after an initial phase, potentially indicating that the lag parameter for evaluation of the model fitness further needs to be tuned. This parallel inversion framework also provides the best fit source models of the non-preferred source model complexities, an information source for further investigations.

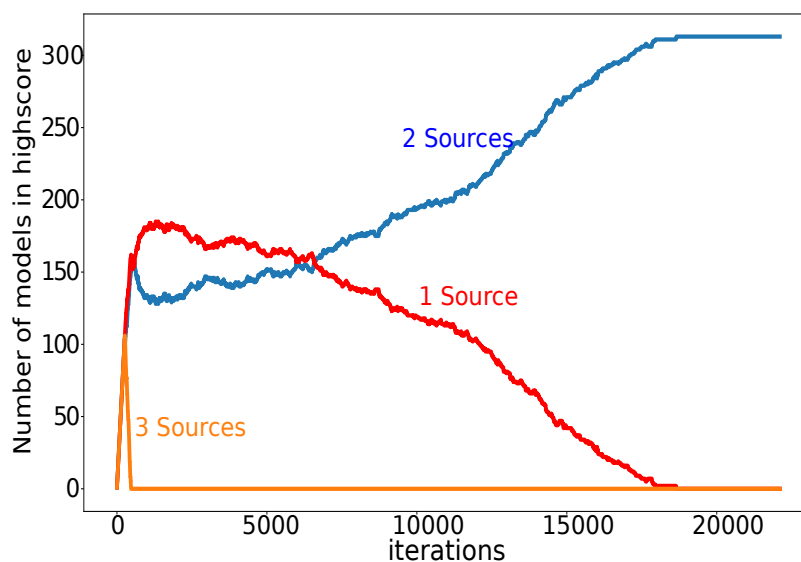


Figure 5.3: The models kept in the complexity high-score list in the simultaneous parallel modeling of multiple earthquake sources model complexities optimisation of the 2016 Muji  $M_w$  6.7 earthquake. Plotted is iterations against the number of models in the complexity high-score from the parallel optimisation. The red line indicates the models in the complexity high-score from an optimisation with a one-source model, the blue line from an optimisation with a two-sources model and the orange line from a three-sources model optimisation.

## 5.6 Outlook on improved operational earthquake source modeling under consideration of potential rupture segmentation

The methods developed in this thesis present an important step towards a deep-rooted joint use of teleseismic and geodetic data to robustly characterize shallow crustal earthquakes as finite rupture processes with data-driven decision on source model complexity to represent rupture segmentation. The combination of currently available teleseismic and geodetic data constrains the earthquake source model parameters well enough to allow for the detection of significant rupture segmentation in smaller moment magnitude earthquakes than previously considered. Rupture segmentation could potentially remain undetected in the current state of operational source analyses and therefore can remain unmodeled without expert intervention, especially for moderate magnitude earthquakes. If methods like the presented multi-array backprojection and surface displacement map segmentation are applied on a regular basis in combination with joint data modeling a catalogue of earthquake sources, considering their source complexity might be feasible. Especially the backprojection of seismic waves is an essential tool to judge on the occurrence of rupture segmentation. I argue that rupture segmentation inferred from backprojection results gives the modeling of multiple faults credibility to not only being a model requirement but to actually represent a physical process. Combined with the independent inference based on the InSAR displacement map image segmentation results, availability of statistics on rupture segmentation occurrence could be greatly increased.

The outlined simultaneous parallel modeling of multiple earthquake source models with different number of sources employs all methods developed in this thesis. I can envision that a similar optimisation framework could run alongside other routine modeling in an earthquake source model service at a data-center. This also necessitates that the methods developed in Chapter 3, the multi-array backprojection and the surface displacement image segmentation analysis, are carried out regularly. Some improvements to the simultaneous parallel modeling of multiple earthquake sources model complexities optimisation scheme will be necessary but overall the performance for the 2016 Muji  $M_w$  6.7 earthquake dataset is highly promising. Further developments into the framework should e.g. include other finite source types. A second stage after the determination of the fault geometry could be the inversion for a slip distribution and a inversion for the spatio-temporal slip evolution ( e.g. based on Vasyura-Bathke et al., 2020) under consideration of the model error stemming from the choice of source model complexity. A single-source finite fault model should always be published for fast response. The simultaneous parallel modeling of multiple earthquake source model complexities is in its current form not a fast procedure. This is because of the relatively long forward modeling times for a single model, of up to seconds for the high-frequency (near-field) seismic waveforms and the large-scale static deformation calculations. In the future this could be speeded up using the fast developing machine learning methods. Machine learning would however be still dependent on labels to be learned from, which can be provided by the methods presented in this thesis.

## 6 Bibliography

- Akaike, H. (1998). “Information theory and an extension of the maximum likelihood principle”. In: *Selected Papers of Hirotugu Akaike*. Springer, pp. 199–213.
- Akaike, H. (1985). “Prediction and entropy”. In: *Selected Papers of Hirotugu Akaike*. Springer, pp. 387–410.
- Aki, K. (1966). “Generation and Propagation of G Waves from the Niigata Earthquake of June 16, 1964: Part 1. A statistical analysis”. In: *Bulletin of the Earthquake Research Institute, University of Tokyo* 44.1, pp. 23–72.
- (1989). “Geometric features of a fault zone related to the nucleation and termination of an earthquake rupture”. In: *Proceedings of Conference XLV. Fault Segmentation Controls of Rupture Initiation and Termination*, pp. 1–9.
- Aki, K. and P. G. Richards (2002). *Quantitative seismology*.
- Akoğlu, A. M., S. Jónsson, T. Wang, Z. Çakır, U. Dogan, S. Ergintav, B. Osmanoğlu, G. Feng, C. Zabcı, A. Özdemir, et al. (2018). “Evidence for tear faulting from new constraints of the 23 October 2011 Mw 7.1 van, Turkey, earthquake based on InSAR, GPS, coastal uplift, and field observationevidence for tear faulting from new constraints of the 2011 van, Turkey, earthquake”. In: *Bulletin of the Seismological Society of America* 108.4, pp. 1929–1946.
- Amey, R., A. Hooper, and Y. Morishita (2019). “Going to Any Lengths: Solving for Fault Size and Fractal Slip for the 2016, M w 6.2 Central Tottori Earthquake, Japan, Using a Transdimensional Inversion Scheme”. In: *Journal of Geophysical Research: Solid Earth* 124.4, pp. 4001–4016.
- Anantrasirichai, N., J. Biggs, F. Albino, and D. Bull (2019). “The Application of Convolutional Neural Networks to Detect Slow, Sustained Deformation in InSAR Time Series”. In: *Geophysical Research Letters* 46.21, pp. 11850–11858.
- Anantrasirichai, N., J. Biggs, F. Albino, P. Hill, and D. Bull (2018). “Application of machine learning to classification of volcanic deformation in routinely generated InSAR data”. In: *Journal of Geophysical Research: Solid Earth* 123.8, pp. 6592–6606.
- Aochi, H., E. Fukuyama, and M. Matsu’ura (2000). “Spontaneous rupture propagation on a non-planar fault in 3-D elastic medium”. In: *Pure and Applied Geophysics* 157.11-12, pp. 2003–2027.
- Archuleta, R. J., E. Cranswick, C. Mueller, and P. Spudich (1982). “Source parameters of the 1980 Mammoth Lakes, California, earthquake sequence”. In: *Journal of Geophysical Research: Solid Earth* 87.B6, pp. 4595–4607.
- Atzori, S. and A. Antonioli (2011). “Optimal fault resolution in geodetic inversion of coseismic data”. In: *Geophysical Journal International* 185.1, pp. 529–538.
- Atzori, S., I. Hunstad, M. Chini, S. Salvi, C. Tolomei, C. Bignami, S. Stramondo, E. Trasatti, A. Antonioli, and E. Boschi (2009). “Finite fault inversion of DInSAR coseismic displacement of the 2009 L’Aquila earthquake (central Italy)”. In: *Geophysical Research Letters* 36.15, pp. 1–6. ISSN: 00948276. DOI: 10.1029/2009GL039293.
- Backus, G. and M. Mulcahy (1976). “Moment tensors and other phenomenological descriptions of seismic sources—I. Continuous displacements”. In: *Geophysical Journal International* 46.2, pp. 341–361.
- Bai, K. and J.-P. Ampuero (2017). “Effect of seismogenic depth and background stress on physical limits of earthquake rupture across fault step overs”. In: *Journal of Geophysical Research: Solid Earth* 122.12, pp. 10–280.
- Bao, H., J.-P. Ampuero, L. Meng, E. J. Fielding, C. Liang, C. Milliner, T. Feng, and H. Huang (2019). “Early and persistent supershear rupture of the 2018 magnitude 7.5 Palu earthquake”. In: *Nature Geoscience* 12.3, pp. 200–205.
- Bardsley, J. M., A. Solonen, H. Haario, and M. Laine (2014). “Randomize-then-optimize: A method for sampling from posterior distributions in nonlinear inverse problems”. In: *SIAM Journal on Scientific Computing* 36.4, A1895–A1910.
- Barka, A. and K. Kadinsky-Cade (1988). “Strike-slip fault geometry in Turkey and its influence on earthquake activity”. In: *Tectonics* 7.3, pp. 663–684.
- Barker, J. S. and C. A. Langston (1982). “Moment tensor inversion of complex earthquakes”. In: *Geophysical Journal International* 68.3, pp. 777–803.

## 6 Bibliography

- Barnhart, W. D., C. M. Brengman, S. Li, and K. E. Peterson (2018). “Ramp-flat basement structures of the Zagros Mountains inferred from co-seismic slip and afterslip of the 2017 Mw 7.3 Darbandikhan, Iran/Iraq earthquake”. In: *Earth and Planetary Science Letters* 496, pp. 96–107.
- Bathke, H., G. Feng, S. Heimann, M. Nikkhoo, O. Zielke, S. Jónsson, and M. Mai (2016). “Kinematic source parameter estimation for the 1995 Mw 7.2 Gulf of Aqaba Earthquake by using InSAR and teleseismic data in a Bayesian framework”. In: *EGUGA*, EPSC2016–16000.
- Bekaert, D. P., M. Karim, J. P. Linick, H. Hua, S. Sangha, M. Lucas, N. Malarout, P. S. Agram, L. Pan, S. E. Owen, et al. (2019). “Development of open-access Standardized InSAR Displacement Products by the Advanced Rapid Imaging and Analysis (ARIA) Project for Natural Hazards”. In: *AGUFM 2019*, G23A–04.
- Berardino, P., G. Fornaro, R. Lanari, and E. Sansosti (2002). “A new algorithm for surface deformation monitoring based on small baseline differential SAR interferograms”. In: *Geoscience and Remote Sensing, IEEE Transactions on* 40.11, pp. 2375–2383.
- Berberian, M. (1979). “Earthquake faulting and bedding thrust associated with the Tabas-e-Golshan (Iran) earthquake of September 16, 1978”. In: *Bulletin of the Seismological Society of America* 69.6, pp. 1861–1887.
- Beresnev, I. A. (2003). “Uncertainties in finite-fault slip inversions: to what extent to believe?(a critical review)”. In: *Bulletin of the Seismological Society of America* 93.6, pp. 2445–2458.
- Beroza, G. C. and P. Spudich (1988). “Linearized inversion for fault rupture behavior: Application to the 1984 Morgan Hill, California, earthquake”. In: *Journal of Geophysical Research: Solid Earth* 93.B6, pp. 6275–6296.
- Bhat, H. S., M. Olives, R. Dmowska, and J. R. Rice (2007). “Role of fault branches in earthquake rupture dynamics”. In: *Journal of Geophysical Research: Solid Earth* 112.B11.
- Biasi, G. P. and R. J. Weldon (Oct. 2006). “Estimating Surface Rupture Length and Magnitude of Paleoearthquakes from Point Measurements of Rupture Displacement”. In: *Bulletin of the Seismological Society of America* 96.5, pp. 1612–1623. ISSN: 0037-1106. DOI: 10.1785/0120040172. URL: <http://www.bssaonline.org/cgi/doi/10.1785/0120040172>.
- Biasi, G. P. and S. G. Wesnousky (2016). “Steps and gaps in ground ruptures: Empirical bounds on rupture propagation”. In: *Bulletin of the Seismological Society of America* 106.3, pp. 1110–1124.
- Bie, L., S. Hicks, T. Garth, P. Gonzalez, and A. Rietbrock (2018). “‘Two go together’: Near-simultaneous moment release of two asperities during the 2016 Mw 6.6 Muji, China earthquake”. In: *Earth and Planetary Science Letters* 491, pp. 34–42.
- Biggs, J., E. Bergman, B. Emmerson, G. J. Funning, J. Jackson, B. Parsons, and T. J. Wright (2006). “Fault identification for buried strike-slip earthquakes using InSAR: The 1994 and 2004 Al Hoceima, Morocco earthquakes”. In: *Geophysical Journal International* 166.3, pp. 1347–1362.
- Biggs, J. and T. J. Wright (2020). “How satellite InSAR has grown from opportunistic science to routine monitoring over the last decade”. In: *Nature Communications* 11.1, pp. 1–4.
- Blaser, L., F. Krüger, M. Ohrnberger, and F. Scherbaum (2010). “Scaling relations of earthquake source parameter estimates with special focus on subduction environment”. In: *Bulletin of the Seismological Society of America* 100.6, pp. 2914–2926.
- Bletery, Q., A. Sladen, B. Delouis, M. Vallée, J.-M. Nocquet, L. Rolland, and J. Jiang (2014). “A detailed source model for the Mw9.0 Tohoku-Oki earthquake reconciling geodesy, seismology, and tsunami records”. In: *Journal of Geophysical Research: Solid Earth* 119.10, pp. 7636–7653.
- Bodin, T., M. Sambridge, H. Tkalčić, P. Arroucau, K. Gallagher, and N. Rawlinson (Feb. 2012). “Trans-dimensional inversion of receiver functions and surface wave dispersion”. In: *Journal of Geophysical Research: Solid Earth* 117.B2, n/a–n/a. ISSN: 01480227. DOI: 10.1029/2011JB008560. URL: <http://doi.wiley.com/10.1029/2011JB008560>.
- Bodin, T. and M. Sambridge (2009). “Seismic tomography with the reversible jump algorithm”. In: *Geophysical Journal International* 178.3, pp. 1411–1436.
- Bondár, I., E. R. Engdahl, X. Yang, H. A. Ghalib, A. Hofstetter, V. Kirichenko, R. Wagner, I. Gupta, G. Ekström, E. Bergman, et al. (2004). “Collection of a reference event set for regional and teleseismic location calibration”. In: *Bulletin of the Seismological Society of America* 94.4, pp. 1528–1545.
- Bonini, L., R. Basili, P. Burrato, V. Cannelli, U. Fracassi, F. E. Maesano, D. Melini, G. Tarabusi, M. M. Tiberti, P. Vannoli, et al. (2019). “Testing different tectonic models for the source of the Mw 6.5, 30 October 2016, Norcia earthquake (central Italy): a youthful normal fault, or negative inversion of an old thrust?” In: *Tectonics* 38.3, pp. 990–1017.
- Bracewell, R. N. and R. N. Bracewell (1986). *The Fourier transform and its applications*. Vol. 31999. McGraw-Hill New York.

## 6 Bibliography

- Brooks, S., A. Gelman, G. Jones, and X.-L. Meng (2011). *Handbook of markov chain monte carlo*. CRC press.
- Brune, J. N. (1970). “Tectonic stress and the spectra of seismic shear waves from earthquakes”. In: *Journal of geophysical research* 75.26, pp. 4997–5009.
- Burchfiel, B., D. Quidong, P. Molnar, L. Royden, W. Yipeng, Z. Peizhen, and Z. Weiqi (1989). “Intracrustal detachment within zones of continental deformation”. In: *Geology* 17.8, pp. 748–752.
- Burnham, K. P. and D. R. Anderson (2004). “Multimodel inference: understanding AIC and BIC in model selection”. In: *Sociological methods & research* 33.2, pp. 261–304.
- Bush, M. A., J. E. Saylor, B. K. Horton, and J. Nie (2016). “Growth of the Qaidam Basin during Cenozoic exhumation in the northern Tibetan Plateau: Inferences from depositional patterns and multiproxy detrital provenance signatures”. In: *Lithosphere* 8.1, pp. 58–82.
- Cakir, Z., S. Ergintav, A. M. Akoğlu, R. Çakmak, O. Tatar, and M. Meghraoui (2014). “InSAR velocity field across the North Anatolian Fault (eastern Turkey): Implications for the loading and release of interseismic strain accumulation”. In: *Journal of Geophysical Research: Solid Earth* 119.10, pp. 7934–7943.
- Cavalié, O., M.-P. Doin, C. Lasserre, and P. Briole (2007). “Ground motion measurement in the Lake Mead area, Nevada, by differential synthetic aperture radar interferometry time series analysis: Probing the lithosphere rheological structure”. In: *J. Geophys. Res. (1978–2012)* 112.B3.
- Cesca, S., S. Heimann, K. Stammler, and T. Dahm (June 2010). “Automated procedure for point and kinematic source inversion at regional distances”. In: *Journal of Geophysical Research* 115.B6, B06304. ISSN: 0148-0227. DOI: 10.1029/2009JB006450. URL: <http://doi.wiley.com/10.1029/2009JB006450>.
- Cesca, S., J. Letort, H. N. Razafindrakoto, S. Heimann, E. Rivalta, M. P. Isken, M. Nikkhoo, L. Passarelli, G. M. Petersen, F. Cotton, et al. (2020). “Drainage of a deep magma reservoir near Mayotte inferred from seismicity and deformation”. In: *Nature Geoscience* 13.1, pp. 87–93.
- Chan, T. F. and L. A. Vese (2001). “Active contours without edges”. In: *IEEE Transactions on image processing* 10.2, pp. 266–277.
- Cheloni, D., R. Giuliani, E. D’Anastasio, S. Atzori, R. Walters, L. Bonci, N. D’Agostino, M. Mattone, S. Calcaterra, P. Gambino, et al. (2014). “Coseismic and post-seismic slip of the 2009 L’Aquila (central Italy) Mw 6.3 earthquake and implications for seismic potential along the Campotosto fault from joint inversion of high-precision levelling, InSAR and GPS data”. In: *Tectonophysics* 622, pp. 168–185.
- Chen, J., T. Li, J. Sun, L. Fang, Y. Yao, Y. Li, H. Wang, and B. Fu (2016). “Coseismic surface rupture and seismogenic Muji fault of the 25 November 2016 Aketao Mw 6.6 earthquake in northern Pamir”. In: *Seismol. Geol* 38, pp. 1160–1174.
- Chen, P., T. H. Jordan, and L. Zhao (2005). “Finite-moment tensor of the 3 September 2002 Yorba Linda earthquake”. In: *Bulletin of the Seismological Society of America* 95.3, pp. 1170–1180.
- Chevalier, M.-L., P. H. Leloup, and H. Li (2016). “Comment on “No late Quaternary strike-slip motion along the northern Karakoram fault” published by Robinson et al. in EPSL, 2015”. In: *Earth and Planetary Science Letters* 443, pp. 216–219.
- Chevalier, M.-L., H. Li, J. Pan, J. Pei, F. Wu, W. Xu, Z. Sun, and D. Liu (2011). “Fast slip-rate along the northern end of the Karakorum fault system, western Tibet”. In: *Geophysical Research Letters* 38.22.
- Chevalier, M.-L., J. Pan, H. Li, D. Liu, and M. Wang (2015). “Quantification of both normal and right-lateral late Quaternary activity along the Kongur Shan extensional system, Chinese Pamir”. In: *Terra Nova* 27.5, pp. 379–391.
- Cirella, A., A. Piatanesi, E. Tinti, M. Chini, and M. Cocco (2012). “Complexity of the rupture process during the 2009 L’Aquila, Italy, earthquake”. In: *Geophysical Journal International* 190.1, pp. 607–621.
- Clark, M. K. and L. H. Royden (2000). “Topographic ooze: Building the eastern margin of Tibet by lower crustal flow”. In: *Geology* 28.8, pp. 703–706.
- Craig, T. (2019). “Accurate Depth Determination for Moderate-Magnitude Earthquakes Using Global Teleseismic Data”. In: *Journal of Geophysical Research: Solid Earth* 124.2, pp. 1759–1780.
- Custódio, S., M. T. Page, and R. J. Archuleta (2009). “Constraining earthquake source inversions with GPS data: 2. A two-step approach to combine seismic and geodetic data sets”. In: *Journal of Geophysical Research: Solid Earth* 114.B1.
- D., K., H. S., I. M. P., R. E., and D. B. (2020). “Probabilistic Moment Tensor Inversion for Hydrocarbon-Induced Seismicity in the Groningen Gas Field, The Netherlands”. In: *Bull. Seismol. Soc. Am.* DOI: 10.1785/0120200099.
- Dahlen, F. and J. Tromp (1998). *Theoretical global seismology*. Princeton university press.

## 6 Bibliography

- Dahm, T. and F. Krüger (2014). “Moment tensor inversion and moment tensor interpretation”. In: *New Manual of Seismological Observatory Practice 2 (NMSOP-2)*. Deutsches GeoForschungsZentrum GFZ, pp. 1–37.
- Daout, S., S. Barbot, G. Peltzer, M.-P. Doin, Z. Liu, and R. Jolivet (2016a). “Constraining the Kinematics of Metropolitan Los Angeles Faults with a Slip-Partitioning Model”. In: *Geophys. Res. Lett.*
- Daout, S., R. Jolivet, C. Lasserre, M.-P. Doin, S. Barbot, P. Tapponnier, G. Peltzer, A. Socquet, and J. Sun (2016b). “Along-strike variations of the partitioning of convergence across the Haiyuan fault system detected by InSAR”. In: *GJI* 205.1, pp. 536–547.
- Daout, S., B. Dini, W. Haeberli, M.-P. Doin, and B. Parsons (2020a). “Ice loss in the Northeastern Tibetan Plateau permafrost as seen by 16 yr of ESA SAR missions”. In: *Earth and Planetary Science Letters* 545, p. 116404.
- Daout, S., M.-P. Doin, G. Peltzer, C. Lasserre, A. Socquet, M. Volat, and H. Sudhaus (2018). “Strain partitioning and present-day fault kinematics in NW Tibet from Envisat SAR interferometry”. In: *Journal of Geophysical Research: Solid Earth* 123.3, pp. 2462–2483.
- Daout, S., M.-P. Doin, G. Peltzer, A. Socquet, and C. Lasserre (2017). “Large scale InSAR monitoring of permafrost freeze-thaw cycles on the Tibetan Plateau”. In: *Geophys. Res. Lett.*
- Daout, S., A. Steinberg, M. P. Isken, S. Heimann, and H. Sudhaus (2020b). “Illuminating the Spatio-Temporal Evolution of the 2008–2009 Qaidam Earthquake Sequence with the Joint Use of InSAR Time Series and Teleseismic Data”. In: *Remote Sensing* 12.17, p. 2850.
- Daout, S., H. Sudhaus, T. Kausch, A. Steinberg, and B. Dini (2019). “Interseismic and postseismic shallow creep of the North Qaidam Thrust faults detected with a multitemporal InSAR analysis”. In: *Journal of Geophysical Research: Solid Earth* 124.7, pp. 7259–7279.
- Das, S. and B. Kostrov (1990). “Inversion for seismic slip rate history and distribution with stabilizing constraints: Application to the 1986 Andreanof Islands earthquake”. In: *Journal of Geophysical Research: Solid Earth* 95.B5, pp. 6899–6913.
- Delouis, B., D. Giardini, P. Lundgren, and J. Salichon (2002). “Joint inversion of InSAR, GPS, teleseismic, and strong-motion data for the spatial and temporal distribution of earthquake slip: Application to the 1999 Izmit mainshock”. In: *Bulletin of the Seismological Society of America* 92.1, pp. 278–299.
- DePolo, C. (1989). “Historical Basin and Range Province surface faulting and fault segmentation segmentation”. In: *Fault segmentation and controls of rupture initiation and termination*, pp. 131–162.
- Dettmer, J., R. Benavente, P. R. Cummins, and M. Sambridge (2014). “Trans-dimensional finite-fault inversion”. In: *Geophysical Journal International* 199.2, pp. 735–751.
- Dieterich, J. H. (1992). “Earthquake nucleation on faults with rate-and state-dependent strength”. In: *Tectonophysics* 211.1-4, pp. 115–134.
- Dieterich, J. H. and K. B. Richards-Dinger (2010). “Earthquake recurrence in simulated fault systems”. In: *Seismogenesis and Earthquake Forecasting: The Frank Evison Volume II*. Springer, pp. 233–250.
- Dini, B., S. Daout, A. Manconi, and S. Loew (2019). “Classification of slope processes based on multitemporal DInSAR analyses in the Himalaya of NW Bhutan”. In: *Remote Sensing of Environment* 233, p. 111408.
- Doin, M.-P., C. Lasserre, G. Peltzer, O. Cavalié, and C. Doubre (2009). “Corrections of stratified tropospheric delays in SAR interferometry: Validation with global atmospheric models”. In: *J. Applied Geophysics* 69, pp. 35–50.
- Doin, M.-P., C. Twardzik, G. Ducret, C. Lasserre, S. Guillaso, and S. Jianbao (2015). “InSAR measurement of the deformation around Siling Co Lake: Inferences on the lower crust viscosity in central Tibet”. In: *J. Geophys. Res.: Solid Earth* 120.7, pp. 5290–5310.
- Dolan, J. F. and B. D. Haravitch (2014). “How well do surface slip measurements track slip at depth in large strike-slip earthquakes? The importance of fault structural maturity in controlling on-fault slip versus off-fault surface deformation”.
- Donner, S., A. Ghods, F. Krüger, D. Rößler, A. Landgraf, and P. Ballato (2015). “The Ahar-Varzeghan Earthquake Doublet (M w 6.4 and 6.2) of 11 August 2012: Regional Seismic Moment Tensors and a Seismotectonic Interpretation”. In: *Bulletin of the Seismological Society of America* 105.2A, pp. 791–807.
- Donner, S., D. Rößler, F. Krüger, A. Ghods, and M. R. Strecker (2013). “Segmented seismicity of the M w 6.2 Baladeh earthquake sequence (Alborz Mountains, Iran) revealed from regional moment tensors”. In: *Journal of seismology* 17.3, pp. 925–959.
- Douze, E. and S. Laster (1979). “Statistics of semblance”. In: *Geophysics* 44.12, pp. 1999–2003.



## 6 Bibliography

- Duan, B. and D. D. Oglesby (2006). “Heterogeneous fault stresses from previous earthquakes and the effect on dynamics of parallel strike-slip faults”. In: *Journal of Geophysical Research: Solid Earth* 111.B5.
- Duman, T. Y., O. Emre, A. Dogan, and S. Ozalp (2005). “Step-over and bend structures along the 1999 Duzce earthquake surface rupture, North Anatolian fault, Turkey”. In: *Bulletin of the Seismological Society of America* 95.4, pp. 1250–1262.
- Dupont-Nivet, G., B. Horton, R. F. Butler, J. Wang, J. Zhou, and G. Waanders (2004). “Paleogene clockwise tectonic rotation of the Xining-Lanzhou region, northeastern Tibetan Plateau”. In: *Journal of Geophysical Research: Solid Earth* 109.B4.
- Duputel, Z., P. S. Agram, M. Simons, S. E. Minson, and J. L. Beck (2014). “Accounting for prediction uncertainty when inferring subsurface fault slip”. In: *Geophysical Journal International* 197.1, pp. 464–482.
- Duputel, Z., H. Kanamori, V. C. Tsai, L. Rivera, L. Meng, J.-P. Ampuero, and J. M. Stock (2012a). “The 2012 Sumatra great earthquake sequence”. In: *Earth and Planetary Science Letters* 351, pp. 247–257.
- Duputel, Z., L. Rivera, Y. Fukahata, and H. Kanamori (2012b). “Uncertainty estimations for seismic source inversions”. In: *Geophysical Journal International* 190.2, pp. 1243–1256.
- (2012c). “Uncertainty estimations for seismic source inversions”. In: *Geophysical Journal International* 190.2, pp. 1243–1256. ISSN: 0956540X. DOI: 10.1111/j.1365-246X.2012.05554.x.
- Dutta, R., S. Jonsson, and H. Vasyura-Bathke (2020). “Simultaneous Bayesian Estimation of Non-Planar Fault Geometry and Spatially-Variable Slip”. In:
- Dziewonski, A., T.-A. Chou, and J. Woodhouse (1981). “Determination of earthquake source parameters from waveform data for studies of global and regional seismicity”. In: *Journal of Geophysical Research: Solid Earth* 86.B4, pp. 2825–2852.
- Efron, B. (1982). *The jackknife, the bootstrap and other resampling plans*. SIAM.
- Ekström, G., M. Nettles, and A. Dziewoński (2012). “The global CMT project 2004–2010: Centroid-moment tensors for 13,017 earthquakes”. In: *Physics of the Earth and Planetary Interiors* 200, pp. 1–9.
- Elliott, J. R., B. Parsons, J. A. Jackson, X. Shan, R. A. Sloan, and R. T. Walker (2011a). “Depth segmentation of the seismogenic continental crust: The 2008 and 2009 Qaidam earthquakes”. In: *Geophysical Research Letters* 38.6, pp. 1–6. ISSN: 00948276. DOI: 10.1029/2011GL046897.
- Elliott, J. R., R. J. Walters, P. C. England, J. A. Jackson, Z. Li, and B. Parsons (2010). “Extension on the Tibetan plateau: Recent normal faulting measured by InSAR and body wave seismology”. In: *Geophysical Journal International* 183.2, pp. 503–535. ISSN: 0956540X. DOI: 10.1111/j.1365-246X.2010.04754.x.
- Elliott, J., R. Jolivet, P. González, J.-P. Avouac, J. Hollingsworth, M. Searle, and V. Stevens (2016a). “Himalayan megathrust geometry and relation to topography revealed by the Gorkha earthquake”. In: *Nature Geoscience* 9.2, pp. 174–180.
- Elliott, J., B. Parsons, J. Jackson, X. Shan, R. Sloan, and R. Walker (2011b). “Depth segmentation of the seismogenic continental crust: The 2008 and 2009 Qaidam earthquakes”. In: *Geophysical research letters* 38.6.
- Elliott, J., R. Walters, and T. Wright (2016b). “The role of space-based observation in understanding and responding to active tectonics and earthquakes”. In: *Nature communications* 7.1, pp. 1–16.
- Ellsworth, W. and G. Beroza (1995). “Seismic evidence for an earthquake nucleation phase”. In: *Science* 268.5212, pp. 851–855.
- Engdahl, E. R., R. van der Hilst, and R. Buland (1998). “Global teleseismic earthquake relocation with improved travel times and procedures for depth determination”. In: *Bulletin of the Seismological Society of America* 88.3, pp. 722–743.
- England, P. C. and G. Houseman (1988). “The mechanics of the Tibetan Plateau”. In: *Phil. Trans. R. Soc. Lond. A* 326.1589, pp. 301–320.
- Fan, W. and P. M. Shearer (2017). “Investigation of backprojection uncertainties with M6 earthquakes”. In: *Journal of Geophysical Research: Solid Earth* 122.10, pp. 7966–7986.
- Fang, X., W. Zhang, Q. Meng, J. Gao, X. Wang, J. King, C. Song, S. Dai, and Y. Miao (2007). “High-resolution magnetostratigraphy of the Neogene Huaitoutala section in the eastern Qaidam Basin on the NE Tibetan Plateau, Qinghai Province, China and its implication on tectonic uplift of the NE Tibetan Plateau”. In: *Earth and Planetary Science Letters* 258.1-2, pp. 293–306.
- Farr, T. G. and M. Kobrick (2000). “Shuttle Radar Topography Mission produces a wealth of data”. In: *Eos, Transactions American Geophysical Union* 81.48, pp. 583–585.
- Feng, W. (2015). “Modelling co-and post-seismic displacements revealed by InSAR, and their implications for fault behaviour”. PhD thesis. University of Glasgow.

## 6 Bibliography

- Feng, W., Z. Li, J. R. Elliott, Y. Fukushima, T. Hoey, A. Singleton, R. Cook, and Z. Xu (2013). “The 2011MW 6.8 Burma earthquake: Fault constraints provided by multiple SAR techniques”. In: *Geophysical Journal International* 195.1. ISSN: 0956540X. DOI: 10.1093/gji/ggt254.
- Feng, W., Y. Tian, Y. Zhang, S. Samsonov, R. Almeida, and P. Liu (2017). “A slip gap of the 2016 M w 6.6 Muji, Xinjiang, China, earthquake inferred from Sentinel-1 TOPS interferometry”. In: *Seismological Research Letters* 88.4, pp. 1054–1064.
- Ferreira, A., J. Weston, and G. Funning (2011). “Global compilation of interferometric synthetic aperture radar earthquake source models: 2. Effects of 3-D Earth structure”. In: *Journal of Geophysical Research: Solid Earth* 116.B8.
- Field, E. H., R. J. Arrowsmith, G. P. Biasi, P. Bird, T. E. Dawson, K. R. Felzer, D. D. Jackson, K. M. Johnson, T. H. Jordan, C. Madden, et al. (2014). “Uniform California earthquake rupture forecast, version 3 (UCERF3)—The time-independent model”. In: *Bulletin of the Seismological Society of America* 104.3, pp. 1122–1180.
- Field, E. H., G. P. Biasi, P. Bird, T. E. Dawson, K. R. Felzer, D. D. Jackson, K. M. Johnson, T. H. Jordan, C. Madden, A. J. Michael, et al. (2015). “Long-term time-dependent probabilities for the third Uniform California Earthquake Rupture Forecast (UCERF3)”. In: *Bulletin of the Seismological Society of America* 105.2A, pp. 511–543.
- Floyd, M. A., R. J. Walters, J. R. Elliott, G. J. Funning, J. L. Svarc, J. R. Murray, A. J. Hooper, Y. Larsen, P. Marinkovic, R. Bürgmann, et al. (2016). “Spatial variations in fault friction related to lithology from rupture and afterslip of the 2014 South Napa, California, earthquake”. In: *Geophysical Research Letters* 43.13, pp. 6808–6816.
- Frietsch, M., A. Ferreira, G. Funning, and J. Weston (2019a). “Multiple fault modelling combining seismic and geodetic data: the importance of simultaneous subevent inversions”. In: *Geophysical Journal International* 218.2, pp. 958–976.
- (2019b). “Multiple fault modelling combining seismic and geodetic data: the importance of simultaneous subevent inversions”. In: *Geophysical Journal International* 218.2, pp. 958–976.
- Frohlich, C. et al. (1994). “Earthquakes with non-double-couple mechanisms”. In: *Science-AAAS-Weekly Paper Edition-including Guide to Scientific Information* 264.5160, pp. 804–809.
- Fukahata, Y., Y. Yagi, and L. Rivera (2013). “Theoretical relationship between back-projection imaging and classical linear inverse solutions”. In: *Geophysical Journal International* 196.1, pp. 552–559.
- Funning, G. J., Y. Fukahata, Y. Yagi, and B. Parsons (2014). “A method for the joint inversion of geodetic and seismic waveform data using ABIC: application to the 1997 Manyi, Tibet, earthquake”. In: *Geophysical Journal International* 196.3, pp. 1564–1579.
- Funning, G. J. (2005). “Source parameters of large shallow earthquakes in the Alpine-Himalayan belt from InSAR and waveform modelling”. PhD thesis. University of Oxford.
- Gallovič, F., W. Imperatori, and P. M. Mai (2015). “Effects of three-dimensional crustal structure and smoothing constraint on earthquake slip inversions: Case study of the Mw6.3 2009 L’Aquila earthquake”. In: *Journal of Geophysical Research: Solid Earth* 120.1, pp. 428–449.
- Ganas, A., P. Kourkoulis, P. Briole, A. Moshou, P. Elias, and I. Parcharidis (2018). “Coseismic displacements from moderate-size earthquakes mapped by Sentinel-1 differential interferometry: the case of February 2017 Gulpinar earthquake sequence (Biga Peninsula, Turkey)”. In: *Remote Sensing* 10.7, p. 1089.
- Geersen, J., J. M. Bull, L. C. McNeill, T. J. Henstock, C. Gaedicke, N. Chamot-Rooke, and M. Delescluse (2015). “Pervasive deformation of an oceanic plate and relationship to large > Mw 8 intraplate earthquakes: The northern Wharton Basin, Indian Ocean”. In: *Geology* 43.4, pp. 359–362.
- Getreuer, P. (2012). “Chan-ve segmentation”. In: *Image Processing On Line* 2, pp. 214–224.
- Goldstein, R. M. and C. L. Werner (1998). “Radar interferogram filtering for geophysical applications”. In: *Geophysical research letters* 25.21, pp. 4035–4038.
- Goldstein, R. M., H. A. Zebker, and C. L. Werner (1988). “Satellite radar interferometry: Two-dimensional phase unwrapping”. In: *Radio science* 23.4, pp. 713–720.
- Gomba, G., A. Parizzi, F. De Zan, M. Eineder, and R. Bamler (2015). “Toward operational compensation of ionospheric effects in SAR interferograms: The split-spectrum method”. In: *IEEE Transactions on Geoscience and Remote Sensing* 54.3, pp. 1446–1461.
- Gombert, B., Z. Duputel, R. Jolivet, C. Doubre, L. Rivera, and M. Simons (2018). “Revisiting the 1992 Landers earthquake: a Bayesian exploration of co-seismic slip and off-fault damage”. In: *Geophysical Journal International* 212.2, pp. 839–852.
- Graymer, R. W., V. Langenheim, R. W. Simpson, R. C. Jachens, and D. A. Ponce (2007). “Relatively simple through-going fault planes at large-earthquake depth may be concealed by the surface complexity of strike-slip faults”. In: *Geological Society, London, Special Publications* 290.1, pp. 189–201.

## 6 Bibliography

- Guihua, C., X. Xiwei, Z. Ailan, Z. Xiaoqing, Y. Renmao, Y. Klinger, and J.-M. Nocquet (2013). “Seismotectonics of the 2008 and 2009 Qaidam earthquakes and its implication for regional tectonics”. In: *Acta Geologica Sinica-English Edition* 87.2, pp. 618–628.
- Guo, Y., S. Hu, W. Wu, Y. Wang, and J. Senthilnath (2020). “Multitemporal time series analysis using machine learning models for ground deformation in the Erhai region, China”. In: *Environmental monitoring and assessment* 192.7, pp. 1–16.
- Gurov, E. and A. Y. Yamnichenko (1995). “Morphology of rim of complex terrestrial craters”. In: *Lunar and Planetary Science Conference*. Vol. 26.
- Hamling, I. J., S. Hreinsdóttir, K. Clark, J. Elliott, C. Liang, E. Fielding, N. Litchfield, P. Villamor, L. Wallace, T. J. Wright, et al. (2017). “Complex multifault rupture during the 2016 Mw 7.8 Kaikōura earthquake, New Zealand”. In: *Science* 356.6334.
- Hanka, W. and R. Kind (1994a). “The GEOFON program”. In: *Annals of Geophysics* 37.5.
- (1994b). “The GEOFON program”. In: *Annals of Geophysics* 37.5.
- Hanssen, R. F. (2001a). *Radar interferometry: data interpretation and error analysis*. Vol. 2. Springer Science & Business Media.
- (2001b). *Radar interferometry: data interpretation and error analysis*. Vol. 2. Springer Science & Business Media.
- Harris, R. A. and S. M. Day (1993). “Dynamics of fault interaction: Parallel strike-slip faults”. In: *Journal of Geophysical Research: Solid Earth* 98.B3, pp. 4461–4472.
- Hartzell, S. and C. Langer (1993). “Importance of model parameterization in finite fault inversions: Application to the 1974 Mw 8.0 Peru earthquake”. In: *Journal of Geophysical Research: Solid Earth* 98.B12, pp. 22123–22134.
- Hartzell, S., P. Liu, C. Mendoza, C. Ji, and K. M. Larson (2007). “Stability and uncertainty of finite-fault slip inversions: Application to the 2004 Parkfield, California, earthquake”. In: *Bulletin of the Seismological Society of America* 97.6, pp. 1911–1934.
- Hartzell, S. H. and T. H. Heaton (1983). “Inversion of strong ground motion and teleseismic waveform data for the fault rupture history of the 1979 Imperial Valley, California, earthquake”. In: *Bulletin of the Seismological Society of America* 73.6A, pp. 1553–1583.
- Hauksson, E., L. M. Jones, and K. Hutton (2002). “The 1999 M w 7.1 Hector Mine, California, earthquake sequence: complex conjugate strike-slip faulting”. In: *Bulletin of the Seismological Society of America* 92.4, pp. 1154–1170.
- Hayes, G. P. (2017). “The finite, kinematic rupture properties of great-sized earthquakes since 1990”. In: *Earth and Planetary Science Letters* 468, pp. 94–100.
- He, P., K. Ding, and C. Xu (2018). “The 2016 Mw 6.7 Aketao earthquake in Muji range, northern Pamir: Rupture on a strike-slip fault constrained by Sentinel-1 radar interferometry and GPS”. In: *International journal of applied earth observation and geoinformation* 73, pp. 99–106.
- Heidbach, O., M. Rajabi, X. Cui, K. Fuchs, B. Müller, J. Reinecker, K. Reiter, M. Tingay, F. Wenzel, F. Xie, et al. (2018). “The World Stress Map database release 2016: Crustal stress pattern across scales”. In: *Tectonophysics* 744, pp. 484–498.
- Heimann, S., M. Isken, D. Kühn, H. Sudhaus, A. Steinberg, H. Vasyura-Bathke, S. Daout, S. Cesca, and T. Dahm (2018a). “Grond-A probabilistic earthquake source inversion framework”. In: *GFZ data services*.
- Heimann, S., M. Kriegerowski, M. Isken, S. Cesca, S. Daout, F. Grigoli, C. Juretzek, T. Megies, N. Nooshiri, A. Steinberg, et al. (2017a). “Pyrocko-An open-source seismology toolbox and library”. In: *GFZ Data Services*.
- Heimann, S., H. Vasyura-Bathke, H. Sudhaus, M. P. Isken, M. Kriegerowski, A. Steinberg, and T. Dahm (2019a). “A Python framework for efficient use of pre-computed Green’s functions in seismological and other physical forward and inverse source problems”. In: *Solid Earth* 10.6, pp. 1921–1935. DOI: 10.5194/se-10-1921-2019. URL: <https://se.copernicus.org/articles/10/1921/2019/>.
- Heimann, S. (2011). “A Robust Method To Estimate Kinematic Earthquake Source Parameters”. In: URL: <http://ediss.sub.uni-hamburg.de/volltexte/2011/5357/>.
- Heimann, S., M. Isken, D. Kühn, H. Sudhaus, A. Steinberg, H. Vasyura-Bathke, S. Daout, S. Cesca, and T. Dahm (2018b). *Grond - A probabilistic earthquake source inversion framework*. Version 1.0. DOI: 10.5880/GFZ.2.1.2018.003. URL: <http://pyrocko.org/grond/docs/current/> (visited on 08/27/2018).
- Heimann, S., M. Kriegerowski, M. Isken, S. Cesca, S. Daout, F. Grigoli, C. Juretzek, T. Megies, N. Nooshiri, A. Steinberg, H. Sudhaus, H. Vasyura-Bathke, T. Willey, and T. Dahm (2017b). *Pyrocko - An open-source seismology toolbox and library*. DOI: 10.5880/gfz.2.1.2017.001.

## 6 Bibliography

- Heimann, S., M. Kriegerowski, M. Isken, S. Cesca, S. Daout, F. Grigoli, C. Juretzek, T. Megies, N. Nooshiri, A. Steinberg, H. Sudhaus, T. Vasyura-Bathke Hannes; Willey, and T. Dahm (2017c). “Pyrocko - An open-source seismology toolbox and library.” In: *GFZ Data Services*. DOI: <http://doi.org/10.5880/GFZ.2.1.2017.001>.
- Heimann, S., H. Vasyura-Bathke, H. Sudhaus, M. P. Isken, M. Kriegerowski, A. Steinberg, and T. Dahm (2019b). “A Python framework for efficient use of pre-computed Green’s functions in seismological and other physical forward and inverse source problems”. In:
- Heinecke, A., A. Breuer, S. Rettenberger, M. Bader, A.-A. Gabriel, C. Pelties, A. Bode, W. Barth, X.-K. Liao, K. Vaidyanathan, et al. (2014). “Petascale high order dynamic rupture earthquake simulations on heterogeneous supercomputers”. In: *SC’14: Proceedings of the International Conference for High Performance Computing, Networking, Storage and Analysis*. IEEE, pp. 3–14.
- Hensen, C., J. C. Duarte, P. Vannucchi, A. Mazzini, M. A. Lever, P. Terrinha, L. Géli, P. Henry, H. Villinger, J. Morgan, et al. (2019). “Marine transform faults and fracture zones: a joint perspective integrating seismicity, fluid flow and life”. In: *Frontiers in Earth Science* 7, p. 39.
- Hernandez, B., F. Cotton, and M. Campillo (1999). “Contribution of radar interferometry to a two-step inversion of the kinematic process of the 1992 Landers earthquake”. In: *Journal of Geophysical Research: Solid Earth* 104.B6, pp. 13083–13099.
- Hicks, S. P., R. Okuwaki, A. Steinberg, C. A. Rychert, N. Harmon, R. E. Abercrombie, P. Bogiatzis, D. Schlaphorst, J. Zahradnik, J.-M. Kendall, et al. (2020a). “Back-propagating supershear rupture in the 2016 M w 7.1 Romanche transform fault earthquake”. In: *Nature Geoscience*, pp. 1–7.
- (2020b). “Back-propagating supershear rupture in the 2016 M w 7.1 Romanche transform fault earthquake”. In: *Nature Geoscience* 13.9, pp. 647–653.
- Hong, S., X. Zhou, K. Zhang, G. Meng, Y. Dong, X. Su, L. Zhang, S. Li, and K. Ding (2018). “Source model and stress disturbance of the 2017 Jiuzhaigou Mw 6.5 earthquake constrained by InSAR and GPS measurements”. In: *Remote Sensing* 10.9, p. 1400.
- Hong, T.-L. and K. Fujita (1981). “Modelling of depth phases and source processes of some central Aleutian earthquakes”. In: *Earth and Planetary Science Letters* 53.3, pp. 333–342.
- Hooper, A. (2008). “A multi-temporal InSAR method incorporating both persistent scatterer and small baseline approaches”. In: *Geophys. Res. Lett.* 35.16.
- Huang, M.-H., E. J. Fielding, C. Liang, P. Milillo, D. Bekaert, D. Dreger, and J. Salzer (2017). “Coseismic deformation and triggered landslides of the 2016 Mw 6.2 Amatrice earthquake in Italy”. In: *Geophysical Research Letters*. ISSN: 00948276. DOI: 10.1002/2016GL071687. URL: <http://doi.wiley.com/10.1002/2016GL071687>.
- Huang, M.-H., H. Tung, E. J. Fielding, H.-H. Huang, C. Liang, C. Huang, and J.-C. Hu (2016a). “Multiple fault slip triggered above the 2016 Mw 6.4 MeiNong earthquake in Taiwan”. In: *Geophysical Research Letters* 43.14, pp. 7459–7467.
- (2016b). “Multiple fault slip triggered above the 2016 Mw 6.4 MeiNong earthquake in Taiwan”. In: *Geophysical Research Letters* 43.14, pp. 7459–7467.
- Ide, S. (2002). “Estimation of radiated energy of finite-source earthquake models”. In: *Bulletin of the Seismological Society of America* 92.8, pp. 2994–3005.
- Ide, S., G. C. Beroza, and J. J. McGuire (2005). “Imaging earthquake source complexity”. In: *Seismic Earth: Array Analysis of Broadband Seismograms*, pp. 117–135.
- Idini, B. and J.-P. Ampuero (2020). “Fault-zone damage promotes pulse-like rupture and back-propagating fronts via quasi-static effects”. In: *Geophysical Research Letters* 47.23, e2020GL090736.
- Ingleby, T., T. Wright, A. Hooper, T. Craig, and J. Elliott (2020). “Constraints on the Geometry and Frictional Properties of the Main Himalayan Thrust Using Coseismic, Postseismic, and Interseismic Deformation in Nepal”. In: *Journal of Geophysical Research: Solid Earth* 125.2, e2019JB019201.
- Ishii, M., P. M. Shearer, H. Houston, and J. E. Vidale (2007). “Teleseismic P wave imaging of the 26 December 2004 Sumatra-Andaman and 28 March 2005 Sumatra earthquake ruptures using the Hi-net array”. In: *Journal of Geophysical Research: Solid Earth* 112.B11.
- (2005). “Extent, duration and speed of the 2004 Sumatra-Andaman earthquake imaged by the Hi-Net array.” In: *Nature* 435.7044, pp. 933–936. ISSN: 0028-0836. DOI: 10.1038/nature03675.
- Isken, M., H. Sudhaus, S. Heimann, A. Steinberg, S. Daout, and H. Vasyura-Bathke (2017a). “Kite—Software for rapid earthquake source optimisation from InSAR surface displacement”. In: *GFZ Data Services*.
- Isken, M., H. Sudhaus, S. Heimann, A. Steinberg, S. Daout, and H. Vasyura-Bathke (2017b). *Kite - Software for Rapid Earthquake Source Optimisation from InSAR Surface Displacement*. DOI: 10.5880/gfz.2.1.2017.001.

## 6 Bibliography

- Isken, M., H. Sudhaus, S. Heimann, A. Steinberg, S. Daout, and H. Vasyura-Bathke (2017c). “Kite - Software for Rapid Earthquake Source Optimisation from InSAR Surface Displacement”. In: *GFZ Data Services*. DOI: <http://doi.org/10.5880/GFZ.2.1.2017.002>.
- Jarvis, A., H. I. Reuter, A. Nelson, E. Guevara, et al. (2008). “Hole-filled SRTM for the globe Version 4”. In: *available from the CGIAR-CSI SRTM 90m Database (<http://srtm.csi.cgiar.org>)*.
- Ji, C., D. V. Helmberger, D. J. Wald, and K.-F. Ma (2003). “Slip history and dynamic implications of the 1999 Chi-Chi, Taiwan, earthquake”. In: *Journal of Geophysical Research: Solid Earth* 108.B9.
- Ji, C., D. J. Wald, and D. V. Helmberger (2002). “Source description of the 1999 Hector Mine, California, earthquake, part I: Wavelet domain inversion theory and resolution analysis”. In: *Bulletin of the Seismological Society of America* 92.4, pp. 1192–1207.
- Johnson, D. H. and D. E. Dudgeon (1993). *Array signal processing: concepts and techniques*. PTR Prentice Hall Englewood Cliffs.
- Jolivet, R., R. Grandin, C. Lasserre, M.-P. Doin, and G. Peltzer (2011). “Systematic InSAR tropospheric phase delay corrections from global meteorological reanalysis data”. In: *Geophys. Res. Lett.* 38.17.
- Jolivet, R. and M. Simons (2018). “A multipixel time series analysis method accounting for ground motion, atmospheric noise, and orbital errors”. In: *Geophysical Research Letters* 45.4, pp. 1814–1824.
- Jonsson, S., S. Metzger, H. Sudhaus, R. Dutta, and W. Xu (2014). “Bayesian Estimation and Deterministic Optimization of Earthquake and Interseismic Model Parameters from InSAR and GPS Data”. In: *AGU Fall Meeting Abstracts*.
- Jónsson, S., H. Zebker, P. Segall, and F. Amelung (2002). “Fault slip distribution of the 1999 Mw 7.1 Hector Mine, California, earthquake, estimated from satellite radar and GPS measurements”. In: *Bulletin of the Seismological Society of America* 92.4, pp. 1377–1389.
- Jordan, T. H. and A. Juarez (2019). “Representation of complex seismic sources by orthogonal moment-tensor fields”. In: *Geophysical Journal International* 216.3, pp. 1867–1889.
- Jost, M. u. and R. Herrmann (1989). “A student’s guide to and review of moment tensors”. In: *Seismological Research Letters* 60.2, pp. 37–57.
- Julian, B. R., A. D. Miller, and G. Foulger (1998). “Non-double-couple earthquakes 1. Theory”. In: *Reviews of Geophysics* 36.4, pp. 525–549.
- Kagan, Y. (1991). “3-D rotation of double-couple earthquake sources”. In: *Geophysical Journal International* 106.3, pp. 709–716.
- Kagan, Y. and L. Knopoff (1987). “Random stress and earthquake statistics: time dependence”. In: *Geophysical Journal International* 88.3, pp. 723–731.
- Kawasaki, I. (1982). “A method for the near-source anisotropy by the pair-event inversion of Rayleigh-wave radiation patterns”. In: *Geophysical Journal International* 71.2, pp. 395–424.
- Kennett, B. and E. Engdahl (1991a). “Traveltimes for global earthquake location and phase identification”. In: *Geophysical Journal International* 105.2, pp. 429–465.
- (1991b). “Traveltimes for global earthquake location and phase identification”. In: *Geophysical Journal International* 105.2, pp. 429–465.
- Kikuchi, M. and H. Kanamori (1982). “Inversion of complex body waves”. In: *Bulletin of the Seismological Society of America* 72.2, pp. 491–506.
- King, G. (1983). “The accommodation of large strains in the upper lithosphere of the earth and other solids by self-similar fault systems: the geometrical origin of b-value”. In: *Pure and Applied Geophysics* 121.5-6, pp. 761–815.
- King, G. and J. Nábělek (1985). “Role of fault bends in the initiation and termination of earthquake rupture”. In: *Science* 228.4702, pp. 984–987.
- King, G. C., R. S. Stein, and J. Lin (1994). “Static stress changes and the triggering of earthquakes”. In: *Bulletin of the Seismological Society of America* 84.3, pp. 935–953.
- Kiser, E. and M. Ishii (2013). “Hidden aftershocks of the 2011 Mw 9.0 Tohoku, Japan earthquake imaged with the backprojection method”. In: *Journal of Geophysical Research: Solid Earth* 118.10, pp. 5564–5576.
- (2017). “Back-Projection Imaging of Earthquakes”. In: *Annual Review of Earth and Planetary Sciences* 45, pp. 271–299.
- Kletting, P. and G. Glatting (2009). “Model selection for time-activity curves: the corrected Akaike information criterion and the F-test”. In: *Zeitschrift für medizinische Physik* 19.3, pp. 200–206.
- Klinger, Y. (2010). “Relation between continental strike-slip earthquake segmentation and thickness of the crust”. In: *Journal of Geophysical Research: Solid Earth* 115.B7.
- Kreemer, C., G. Blewitt, and E. C. Klein (2014). “A geodetic plate motion and Global Strain Rate Model”. In: *Geochemistry, Geophysics, Geosystems* 15.10, pp. 3849–3889.

## 6 Bibliography

- Kreemer, C., W. E. Holt, and A. J. Haines (2003). “An integrated global model of present-day plate motions and plate boundary deformation”. In: *Geophysical Journal International* 154.1, pp. 8–34.
- Krüger, F. and M. Ohrnberger (2005). “Tracking the rupture of the M w= 9.3 Sumatra earthquake over 1,150 km at teleseismic distance”. In: *Nature* 435.7044, p. 937.
- Langer, L., T. Ragon, A. Sladen, and J. Tromp (2020). “Impact of topography on earthquake static slip inversions”. In:
- Lapusta, N. and J. R. Rice (2003). “Nucleation and early seismic propagation of small and large events in a crustal earthquake model”. In: *Journal of Geophysical Research: Solid Earth* 108.B4.
- Lasserre, C., G. Peltzer, F. Crampé, Y. Klinger, J. Van der Woerd, and P. Tapponnier (2005). “Coseismic deformation of the 2001 Mw= 7.8 Kokoxili earthquake in Tibet, measured by synthetic aperture radar interferometry”. In: *J. Geophys. Res. (1978–2012)* 110.B12.
- Lavecchia, G., R. Castaldo, R. de Nardis, V. De Novellis, F. Ferrarini, S. Pepe, F. Brozzetti, G. Solaro, D. Cirillo, M. Bonano, P. Boncio, F. Casu, C. De Luca, R. Lanari, M. Manunta, M. Manzo, A. Pepe, I. Zinno, and P. Tizzani (2016). “Ground deformation and source geometry of the August 24, 2016 Amatrice earthquake (Central Italy) investigated through analytical and numerical modeling of DInSAR measurements and structural-geological data”. In: *Geophysical Research Letters* 1. ISSN: 00948276. DOI: 10.1002/2016GL071723. URL: <http://doi.wiley.com/10.1002/2016GL071723>.
- Lazecky, M., K. Spaans, P. J. González, Y. Maghsoudi, Y. Morishita, F. Albino, J. Elliott, N. Greenall, E. Hatton, A. Hooper, et al. (2020). “LiCSAR: An automatic InSAR tool for measuring and monitoring tectonic and volcanic activity”. In: *Remote Sensing* 12.15, p. 2430.
- Li, J., G. Liu, X. Qiao, W. Xiong, D. Liu, J. Sun, A. Yushan, S. Yusan, W. Fang, Q. Wang, et al. (2019a). “Rupture Characteristics of the 25 November 2016 Aketao earthquake (M w 6.6) in Eastern Pamir revealed by GPS and teleseismic data”. In: *Earthquakes and Multi-hazards Around the Pacific Rim, Vol. II*. Springer, pp. 49–61.
- Li, T., L. M. Schoenbohm, J. Chen, Z. Yuan, W. Feng, W. Li, J. Xu, L. A. Owen, E. R. Sobel, B. Zhang, et al. (2019b). “Cumulative and Coseismic (During the 2016 Mw 6.6 Aketao Earthquake) Deformation of the Dextral-Slip Muji Fault, Northeastern Pamir Orogen”. In: *Tectonics* 38.11, pp. 3975–3989.
- Li, W., Y. Chen, X. Yuan, B. Schurr, J. Mechie, I. Oimahmadov, and B. Fu (2018). “Continental lithospheric subduction and intermediate-depth seismicity: Constraints from S-wave velocity structures in the Pamir and Hindu Kush”. In: *Earth and Planetary Science Letters* 482, pp. 478–489.
- Liang, S., W. Gan, C. Shen, G. Xiao, J. Liu, W. Chen, X. Ding, and D. Zhou (Oct. 2013). “Three-dimensional velocity field of present-day crustal motion of the Tibetan Plateau derived from GPS measurements”. In: *J. Geophys. Res.* 118.10, pp. 5722–5732.
- Lin, Y.-n. N., M. Simons, E. A. Hetland, P. Muse, and C. DiCaprio (2010). “A multiscale approach to estimating topographically correlated propagation delays in radar interferograms”. In: *Geochemistry, Geophysics, Geosystems* 11.9.
- Liu, P. and R. J. Archuleta (2004). “A new nonlinear finite fault inversion with three-dimensional Green’s functions: Application to the 1989 Loma Prieta, California, earthquake”. In: *Journal of Geophysical Research: Solid Earth* 109.B2.
- Liu, Y., C. Xu, Z. Li, Y. Wen, J. Chen, and Z. Li (2016a). “Time-dependent afterslip of the 2009 mw 6.3 dachaidan earthquake (China) and viscosity beneath the qaidam basin inferred from postseismic deformation observations”. In: *Remote Sensing* 8.8, p. 649.
- Liu, Y., C. Xu, Y. Wen, and H. S. Fok (2015). “A new perspective on fault geometry and slip distribution of the 2009 Dachaidan Mw 6.3 earthquake from InSAR observations”. In: *Sensors* 15.7, pp. 16786–16803.
- Liu, Y., C. Xu, Y. Wen, and Z. Li (2016b). “Post-seismic deformation from the 2009 Mw 6.3 Dachaidan earthquake in the northern Qaidam Basin detected by small baseline subset InSAR technique”. In: *Sensors* 16.2, p. 206.
- Lo, Y.-C., H. Yue, J. Sun, L. Zhao, and M. Li (2019). “The 2018 Mw6. 4 Hualien earthquake: Dynamic slip partitioning reveals the spatial transition from mountain building to subduction”. In: *Earth and Planetary Science Letters* 524, p. 115729.
- Lohman, R. B. and M. Simons (2005a). “Some thoughts on the use of InSAR data to constrain models of surface deformation: Noise structure and data downsampling”. In: *Geochemistry, Geophysics, Geosystems* 6.1.
- (2005b). “Some thoughts on the use of InSAR data to constrain models of surface deformation: Noise structure and data downsampling”. In: *Geochemistry, Geophysics, Geosystems* 6.1.
- López-Quiroz, P., M.-P. Doin, F. Tupin, P. Briole, and J.-M. Nicolas (2009). “Time series analysis of Mexico City subsidence constrained by radar interferometry”. In: *J. Applied Geophysics* 69.1, pp. 1–15.

## 6 Bibliography

- Luo, Y., J. Ampuero, P. Galvez, M. Van den Ende, and B. Idini (2017). “QDYN: a Quasi-DYNAMIC earthquake simulator (v1. 1)”. In: *Zenodo*.(doi: 10.5281/zenodo.322459).
- Ma, Y., X. Qiao, W. Chen, and Y. Zhou (2018). “Source model of 2016 Mw6. 6 Aketao earthquake, Xinjiang derived from Sentinel-1 InSAR observation”. In: *Geodesy and Geodynamics* 9.5, pp. 372–377.
- Mackenzie, D., J. Elliott, E. Altunel, R. Walker, Y. Kurban, J.-L. Schwenninger, and B. Parsons (2016). “Seismotectonics and rupture process of the Mw 7.1 2011 Van reverse-faulting earthquake, eastern Turkey, and implications for hazard in regions of distributed shortening”. In: *Geophysical Journal International* 206.1, pp. 501–524.
- Madariaga, R. (1977). “High-frequency radiation from crack (stress drop) models of earthquake faulting”. In: *Geophysical Journal International* 51.3, pp. 625–651.
- Magen, Y., A. Ziv, A. Inbal, G. Baer, and J. Hollingsworth (2020). “Fault rerupture during the July 2019 Ridgecrest earthquake pair from joint slip inversion of InSAR, optical imagery, and GPS”. In: *Bulletin of the Seismological Society of America* 110.4, pp. 1627–1643.
- Maggi, A., K. Priestley, and J. Jackson (2002). “Focal depths of moderate and large size earthquakes in Iran”. In:
- Mai, P., J. Burjanek, B. Delouis, G. Festa, C. Francois-Holden, D. Monelli, T. Uchide, and J. Zahradnik (2007). “Earthquake source inversion blindtest: Initial results and further developments”. In: *AGUFM 2007*, S53C–08.
- Mai, P. M. and R. Meyers (2009). *Ground Motion: Complexity and Scaling in the Near Field of Earthquake Ruptures*.
- Mai, P. M., D. Schorlemmer, M. Page, J.-P. Ampuero, K. Asano, M. Causse, S. Custodio, W. Fan, G. Festa, M. Galis, et al. (2016). “The earthquake-source inversion validation (SIV) project”. In: *Seismological Research Letters* 87.3, pp. 690–708.
- Manighetti, I., M. Campillo, S. Bouley, and F. Cotton (2007a). “Earthquake scaling, fault segmentation, and structural maturity”. In: *Earth and Planetary Science Letters* 253.3-4, pp. 429–438.
- (2007b). “Earthquake scaling, fault segmentation, and structural maturity”. URL: <http://www.sciencedirect.com/science/article/pii/S0012821X06007916>.
- Manighetti, I., D. Zigone, M. Campillo, and F. Cotton (2009). “Self-similarity of the largest-scale segmentation of the faults: Implications for earthquake behavior”. In: *Earth and Planetary Science Letters* 288.3-4, pp. 370–381.
- Marchandon, M., M. Vergnolle, H. Sudhaus, and O. Cavalié (2018). “Fault Geometry and Slip Distribution at Depth of the 1997 Mw 7.2 Zirkuh Earthquake: Contribution of Near-Field Displacement Data”. In: *Journal of Geophysical Research: Solid Earth* 123.2, pp. 1904–1924.
- Marone, C. (1998). “Laboratory-derived friction laws and their application to seismic faulting”. In: *Annual Review of Earth and Planetary Sciences* 26.1, pp. 643–696.
- Martinez-Garzón, P., Y. Ben-Zion, N. Abolfathian, G. Kwiątek, and M. Bohnhoff (2016). “A refined methodology for stress inversions of earthquake focal mechanisms”. In: *Journal of Geophysical Research: Solid Earth* 121.12, pp. 8666–8687.
- Massonnet, D., M. Rossi, C. Carmona, F. Adragna, G. Peltzer, K. Feigl, and T. Rabaute (1993a). “The displacement field of the Landers earthquake mapped by radar interferometry”. In: *Nature* 364.6433, pp. 138–142.
- Massonnet, D., M. Rossi, C. Carmona, F. Adragna, G. Peltzer, K. Feigl, and T. Rabaute (1993b). “The displacement field of the Landers earthquake mapped by radar interferometry”. In: *nature* 364.6433, pp. 138–142.
- McCloskey, J. and S. S. Nalbant (2009). “Near-real-time aftershock hazard maps”. In: *Nature Geoscience* 2.3, pp. 154–155.
- Meier, M.-A., J. Ampuero, and T. H. Heaton (2017). “The hidden simplicity of subduction megathrust earthquakes”. In: *Science* 357.6357, pp. 1277–1281.
- Meier, M.-A., J.-P. Ampuero, E. Cochran, and M. Page (2020). “Apparent earthquake rupture predictability”. In: *Geophysical Journal International*.
- Melgar, D. and G. P. Hayes (2017). “Systematic observations of the slip pulse properties of large earthquake ruptures”. In: *Geophysical Research Letters* 44.19, pp. 9691–9698.
- Mendoza, C. (1995). “Finite-fault analysis of the 1979 March 14 Petatlan, Mexico, earthquake using teleseismic P waveforms”. In: *Geophysical Journal International* 121.3, pp. 675–683.
- Meng, L., J.-P. Ampuero, J. Stock, Z. Duputel, Y. Luo, and V. Tsai (2012a). “Earthquake in a maze: Compressional rupture branching during the 2012 Mw 8.6 Sumatra earthquake”. In: *Science* 337.6095, pp. 724–726.

## 6 Bibliography

- Meng, L., J.-P. Ampuero, A. Sladen, and H. Rendon (Apr. 2012b). “High-resolution backprojection at regional distance: Application to the Haiti M 7.0 earthquake and comparisons with finite source studies”. In: *Journal of Geophysical Research: Solid Earth* 117.B4, n/a–n/a. ISSN: 01480227. DOI: 10.1029/2011JB008702. URL: <http://doi.wiley.com/10.1029/2011JB008702>.
- Meng, L., A. Zhang, and Y. Yagi (2016). “Improving back projection imaging with a novel physics-based aftershock calibration approach: A case study of the 2015 Gorkha earthquake”. In: *Geophysical Research Letters* 43.2, pp. 628–636.
- Métivier, F., Y. Gaudemer, P. Tapponnier, and B. Meyer (1998). “Northeastward growth of the Tibet Plateau deduced from balanced reconstruction of two depositional areas: The Qaidam and Hexi Corridor Basins, China”. In: *Tectonics* 17.6, pp. 823–842.
- Meyer, B., P. Tapponnier, L. Bourjot, F. Metivier, Y. Gaudemer, G. Peltzer, G. Shunmin, and C. Zhitai (1998). “Crustal thickening in Gausu-Qinghai, lithospheric mantle subduction, and oblique, strike-slip controlled growth of the Tibet Plateau”. In: *Geophys. J. Int.* 135.
- Mildon, Z., G. P. Roberts, J. F. Walker, and S. Toda (2019). “Coulomb pre-stress and fault bends are ignored yet vital factors for earthquake triggering and hazard”. In: *Nature communications* 10.1, pp. 1–9.
- Milner, K. R., M. T. Page, E. H. Field, T. Parsons, G. P. Biasi, and B. E. Shaw (2013). “Appendix T—Defining the inversion rupture set using plausibility filters”. In: *US Geol. Surv. Open-File Rept. 2013-1165*.
- Minson, S. E., A. S. Baltay, E. S. Cochran, S. K. McBride, and K. R. Milner (2021). “Shaking is Almost Always a Surprise: The Earthquakes That Produce Significant Ground Motion”. In: *Seismological Society of America* 92.1, pp. 460–468.
- Minson, S., M. Simons, and J. Beck (2013a). “Bayesian inversion for finite fault earthquake source models I—Theory and algorithm”. In: *Geophysical Journal International* 194.3, pp. 1701–1726.
- (2013b). “Bayesian inversion for finite fault earthquake source models I. Theory and algorithm”. In: *Geophysical Journal International* 194.3, pp. 1701–1726.
- Minson, S., M. Simons, J. Beck, F. Ortega, J. Jiang, S. Owen, A. Moore, A. Inbal, and A. Sladen (2014). “Bayesian inversion for finite fault earthquake source models—II: the 2011 great Tohoku-oki, Japan earthquake”. In: *Geophysical Journal International* 198.2, pp. 922–940.
- Mooney, W. D., G. Laske, and T. G. Masters (1998). “CRUST 5.1: A global crustal model at  $5 \times 5$ ”. In: *Journal of Geophysical Research: Solid Earth* 103.B1, pp. 727–747.
- Morishita, Y., M. Lazecky, T. J. Wright, J. R. Weiss, J. R. Elliott, and A. Hooper (2020). “LiCSBAS: An Open-Source InSAR Time Series Analysis Package Integrated with the LiCSAR Automated Sentinel-1 InSAR Processor”. In: *Remote Sensing* 12.3, p. 424.
- Nishikawa, T., T. Matsuzawa, K. Ohta, N. Uchida, T. Nishimura, and S. Ide (2019). “The slow earthquake spectrum in the Japan Trench illuminated by the S-net seafloor observatories”. In: *Science* 365.6455, pp. 808–813.
- Ohnaka, M. (2000). “A physical scaling relation between the size of an earthquake and its nucleation zone size”. In: *Pure and Applied Geophysics* 157.11-12, pp. 2259–2282.
- Okada (1992). “Internal deformation due to shear and tensile faults in a half space”. In: *Bulletin of the Seismological Society of America* 82.2, pp. 1018–1040. URL: <http://bssa.geoscienceworld.org/content/82/2/1018.short>.
- Okada, Y. (1985). “Surface deformation due to shear and tensile faults in a half-space”. In: *International Journal of Rock Mechanics and Mining Sciences Geomechanics Abstracts* 75.4, pp. 1135–1154. ISSN: 00371106. DOI: 10.1016/0148-9062(86)90674-1. URL: <http://linkinghub.elsevier.com/retrieve/pii/0148906286906741>.
- Okubo, P. G. and K. Aki (1987). “Fractal geometry in the San Andreas fault system”. In: *Journal of Geophysical Research: Solid Earth* 92.B1, pp. 345–355.
- Okuwaki, R. and Y. Yagi (2017). “Role of geometric barriers in irregular-rupture evolution during the 2008 Wenchuan earthquake”. In: *Geophysical Journal International*.
- Okuwaki, R., A. Kasahara, Y. Yagi, S. Hirano, and Y. Fukahata (2018). “Backprojection to image slip”. In: *Geophysical Journal International* 216.3, pp. 1529–1537.
- Olson, A. H. and R. J. Apsel (1982). “Finite faults and inverse theory with applications to the 1979 Imperial Valley earthquake”. In: *Bulletin of the Seismological Society of America* 72.6A, pp. 1969–2001.
- Otsu, N. (1979). “A threshold selection method from gray-level histograms”. In: *IEEE transactions on systems, man, and cybernetics* 9.1, pp. 62–66.
- Ozawa, S., M. Murakami, S. Fujiwara, and M. Tobita (Sept. 1997). “Synthetic aperture radar interferogram of the 1995 Kobe Earthquake and its geodetic inversion”. In: *Geophysical Research Letters* 24.18,



## 6 Bibliography

- pp. 2327–2330. ISSN: 00948276. DOI: 10.1029/97GL02318. URL: <http://doi.wiley.com/10.1029/97GL02318>.
- Palo, M., F. Tilmann, F. Krueger, L. Ehlert, and D. Lange (2014). “High-frequency seismic radiation from Maule earthquake (M w 8.8, 2010 February 27) inferred from high-resolution backprojection analysis”. In: *Geophysical Journal International* 199.2, pp. 1058–1077.
- Pang, J., J. Yu, D. Zheng, W. Wang, Y. Ma, Y. Wang, C. Li, Y. Li, and Y. Wang (2019). “Neogene expansion of the Qilian Shan, north Tibet: Implications for the dynamic evolution of the Tibetan Plateau”. In: *Tectonics* 38.3, pp. 1018–1032.
- Peltzer, G., P. Rosen, F. Rogez, and K. Hudnut (1998). “Poroelastic rebound along the Landers 1992 earthquake surface rupture”. In: *Journal of Geophysical Research: Solid Earth* 103.B12, pp. 30131–30145.
- Perfettini, H. and J.-P. Avouac (2004). “Postseismic relaxation driven by brittle creep: A possible mechanism to reconcile geodetic measurements and the decay rate of aftershocks, application to the Chi-Chi earthquake, Taiwan”. In: *Journal of Geophysical Research: Solid Earth* 109.B2.
- Philibosian, B. and A. J. Meltzner (2020). “Segmentation and supercycles: A catalog of earthquake rupture patterns from the Sumatran Sunda Megathrust and other well-studied faults worldwide”. In: *Quaternary Science Reviews* 241, p. 106390.
- Pino, N. A. and F. Di Luccio (Dec. 2009). “Source complexity of the 6 April 2009 L’Aquila (central Italy) earthquake and its strongest aftershock revealed by elementary seismological analysis”. In: *Geophysical Research Letters* 36.23, pp. 1–6. ISSN: 00948276. DOI: 10.1029/2009GL041331. URL: <http://doi.wiley.com/10.1029/2009GL041331>.
- Pizzi, A., A. Di Domenica, F. Gallovič, L. Luzi, and R. Puglia (2017). “Fault segmentation as constraint to the occurrence of the main shocks of the 2016 Central Italy seismic sequence”. In: *Tectonics* 36.11, pp. 2370–2387.
- Preuss, S., J. P. Ampuero, T. Gerya, and Y. v. Dinther (2020). “Characteristics of earthquake ruptures and dynamic off-fault deformation on propagating faults”. In: *Solid Earth* 11.4, pp. 1333–1360.
- Ragon, T., A. Sladen, Q. Bletery, M. Vergnolle, O. Cavalié, A. Avallone, J. Balestra, and B. Delouis (2019). “Joint Inversion of Coseismic and Early Postseismic Slip to Optimize the Information Content in Geodetic Data: Application to the 2009 M w 6.3 L’Aquila Earthquake, Central Italy”. In: *Journal of Geophysical Research: Solid Earth* 124.10, pp. 10522–10543.
- Ragon, T., A. Sladen, and M. Simons (2018a). “Accounting for uncertain fault geometry in earthquake source inversions–I: theory and simplified application”. In: *Geophysical Journal International* 214.2, pp. 1174–1190.
- (2018b). “Accounting for uncertain fault geometry in earthquake source inversions–I: theory and simplified application”. In: *Geophysical Journal International* 214.2, pp. 1174–1190.
- Razafindrakoto, H. N. T. and M. P. Mai (2014). “Uncertainty in earthquake source imaging due to variations in source time function and earth structure”. In: *Bulletin of the Seismological Society of America* 104.2, pp. 855–874. ISSN: 19433573. DOI: 10.1785/0120130195.
- Razafindrakoto, H. N., P. M. Mai, M. G. Genton, L. Zhang, and K. K. Thingbaijam (2015). “Quantifying variability in earthquake rupture models using multidimensional scaling: Application to the 2011 Tohoku earthquake”. In: *Geophysical Journal International* 202.1, pp. 17–40.
- Ribot, M., Y. Klinger, S. Jónsson, U. Avsar, E. Pons-Branchu, R. Matrau, and F. L. Mallon (2020). “Active faults’ geometry in the Gulf of Aqaba, southern Dead Sea fault, illuminated by multi beam bathymetric data”. In:
- Richards-Dinger, K. and J. H. Dieterich (2012). “RSQSim earthquake simulator”. In: *Seismological Research Letters* 83.6, pp. 983–990.
- Rollins, C., S. Barbot, and J.-P. Avouac (2015). “Postseismic Deformation Following the 2010

$$M = 7.2$$

- El Mayor-Cucapah Earthquake: Observations, Kinematic Inversions, and Dynamic Models”. In: *Pure and Applied Geophysics* 172.5, pp. 1305–1358.
- Rongier, G., C. Rude, T. Herring, and V. Pankratius (2019). “Generative modeling of InSAR interferograms”. In: *Earth and Space Science* 6.12, pp. 2671–2683.
- Rosen, P. A., S. Hensley, S. Shaffer, L. Veilleux, M. Chakraborty, T. Misra, R. Bhan, V. R. Sagi, and R. Satish (2015). “The NASA-ISRO SAR mission-An international space partnership for science and societal benefit”. In: *2015 IEEE Radar Conference (RadarCon)*. IEEE, pp. 1610–1613.

## 6 Bibliography

- Ross, Z. E., B. Idini, Z. Jia, O. L. Stephenson, M. Zhong, X. Wang, Z. Zhan, M. Simons, E. J. Fielding, S.-H. Yun, et al. (2019). “Hierarchical interlocked orthogonal faulting in the 2019 Ridgecrest earthquake sequence”. In: *Science* 366.6463, pp. 346–351.
- Rössler, D., F. Krueger, M. Ohrnberger, and L. Ehlert (2010). “Rapid characterisation of large earthquakes by multiple seismic broadband arrays”. In: *Natural Hazards and Earth System Sciences* 10.4, pp. 923–932.
- Rost, S. and C. Thomas (2002). “Array seismology: Methods and applications”. In: *Reviews of geophysics* 40.3, pp. 2–1.
- (2009). “Improving seismic resolution through array processing techniques”. In: *Surveys in Geophysics* 30.4-5, pp. 271–299.
- Royden, L. H., B. C. Burchfiel, R. W. King, E. Wang, Z. Chen, F. Shen, and Y. Liu (1997). “Surface deformation and lower crustal flow in eastern Tibet”. In: *science* 276.5313, pp. 788–790.
- Rubin, D. B. (1981). “The bayesian bootstrap”. In: *The annals of statistics*, pp. 130–134.
- Ruppert, N. A., C. Rollins, A. Zhang, L. Meng, S. G. Holtkamp, M. E. West, and J. T. Freymueller (2018). “Complex faulting and triggered rupture during the 2018 MW 7.9 offshore Kodiak, Alaska, earthquake”. In: *Geophysical Research Letters* 45.15, pp. 7533–7541.
- Ryder, I., R. Bürgmann, and E. Fielding (2012). “Static stress interactions in extensional earthquake sequences: An example from the South Lunggar Rift, Tibet”. In: *Journal of Geophysical Research: Solid Earth* 117.B9.
- Sambridge, M. (2013). “A parallel tempering algorithm for probabilistic sampling and multimodal optimization”. In: *Geophysical Journal International* 196.1, pp. 357–374.
- Sambridge, M., T. Bodin, K. Gallagher, and H. Tkalčić (2013). “Transdimensional inference in the geosciences”. In: *Philosophical Transactions of the Royal Society A: Mathematical, Physical and Engineering Sciences* 371.1984, p. 20110547.
- Savage, H. M. and E. E. Brodsky (2011). “Collateral damage: Evolution with displacement of fracture distribution and secondary fault strands in fault damage zones”. In: *Journal of Geophysical Research: Solid Earth* 116.B3.
- Schimmel, M. and J. Gallart (2007). “Frequency-dependent phase coherence for noise suppression in seismic array data”. In: *Journal of Geophysical Research: Solid Earth* 112.B4.
- Schimmel, M. and H. Paulssen (1997). “Noise reduction and detection of weak, coherent signals through phase-weighted stacks”. In: *Geophysical Journal International* 130.2, pp. 497–505.
- Scholz, C. and A. Gupta (2000). “Fault interactions and seismic hazard”. In: *Journal of Geodynamics* 29.3-5, pp. 459–467.
- Scholz, C. H. and C. Aviles (1986). “The fractal geometry of faults and faulting”. In: *Earthquake source mechanics* 37, pp. 147–155.
- Schwartz, D. P. (1989). “Paleoseismicity, persistence of segments, and temporal clustering of large earthquakes—examples from the San Andreas, Wasatch, and Lost River Fault Zones”. In: *Proceedings of Conference XLV ‘Fault Segmentation and Controls of Rupture Initiation and Termination,’ US Geol. Surv. Open File Rep., 890*. Vol. 315. Citeseer, pp. 361–375.
- Schwartz, D. P. and K. J. Coppersmith (1984). “Fault behavior and characteristic earthquakes: Examples from the Wasatch and San Andreas fault zones”. In: *Journal of Geophysical Research: Solid Earth* 89.B7, pp. 5681–5698.
- Segall, P. and D. Pollard (1980). “Mechanics of discontinuous faults”. In: *Journal of Geophysical Research: Solid Earth* 85.B8, pp. 4337–4350.
- Shaus, A. and E. Turkel (2016). “Chan-Vese revisited: relation to Otsu’s method and a parameter-free non-PDE solution via morphological framework”. In: *International Symposium on Visual Computing*. Springer, pp. 203–212.
- Shearer, P. M. (1997). “Improving local earthquake locations using the L1 norm and waveform cross correlation: Application to the Whittier Narrows, California, aftershock sequence”. In: *Journal of Geophysical Research: Solid Earth* 102.B4, pp. 8269–8283.
- Shi, Q., S. Wei, and M. Chen (2018). “An MCMC multiple point sources inversion scheme and its application to the 2016 Kumamoto M w 6.2 earthquake”. In: *Geophysical Journal International* 215.2, pp. 737–752.
- Shimizu, K., Y. Yagi, R. Okuwaki, and Y. Fukahata (2019). “Development of an inversion method to extract information on fault geometry from teleseismic data”. In:
- Sibson, R. H. (2003). “Thickness of the seismic slip zone”. In: *Bulletin of the Seismological Society of America* 93.3, pp. 1169–1178.

## 6 Bibliography

- Simons, M., Y. Fialko, and L. Rivera (2002). “Coseismic Deformation from the 1999 Mw 7.1 Hector Mine, California, Earthquake as Inferred from InSAR and GPS Observations”. In: *Bulletin of the Seismological Society of America* 92.4, pp. 1390–1402.
- Sipkin, S. A. (1986). “Interpretation of non-double-couple earthquake mechanisms derived from moment tensor inversion”. In: *Journal of Geophysical Research: Solid Earth* 91.B1, pp. 531–547.
- Sokos, E. N. and J. Zahradnik (2008). “ISOLA a Fortran code and a Matlab GUI to perform multiple-point source inversion of seismic data”. In: *Computers & Geosciences* 34.8, pp. 967–977.
- Soliva, R., A. Benedicto, R. Schultz, L. Maerten, and L. Micarelli (2008). “Displacement and interaction of normal fault segments branched at depth: Implications for fault growth and potential earthquake rupture size”. In: *Journal of Structural Geology* 30.10, pp. 1288–1299.
- Stähler, S. C. and K. Sigloch (2016). “Fully probabilistic seismic source inversion—Part 2: Modelling errors and station covariances”. In:
- Stein, R. S. (1999). “The role of stress transfer in earthquake occurrence”. In: *Nature* 402.6762, pp. 605–609.
- Stein, R. S. and G. C. King (1984). “Seismic potential revealed by surface folding: 1983 Coalinga, California, earthquake”. In: *Science* 224.4651, pp. 869–872.
- Steinberg, A., H. Sudhaus, S. Heimann, and F. Krüger (2020a). “Sensitivity of InSAR and teleseismic observations to earthquake rupture segmentation”. In: *Geophysical Journal International*.
- (2020b). “Sensitivity of InSAR and teleseismic observations to earthquake rupture segmentation”. In: *Geophysical Journal International*.
- Steinhaus, H. (1956). “Sur la division des corp materiels en parties”. In: *Bull. Acad. Polon. Sci* 1.804, p. 801.
- Stirling, M. W., S. G. Wesnousky, and K. Shimazaki (1996). “Fault trace complexity, cumulative slip, and the shape of the magnitude-frequency distribution for strike-slip faults: A global survey”. In: *Geophysical Journal International* 124.3, pp. 833–868.
- Storn, R. and K. Price (1997). “Differential evolution—a simple and efficient heuristic for global optimization over continuous spaces”. In: *Journal of global optimization* 11.4, pp. 341–359.
- Styron, R. (Aug. 2019). *GEMScienceTools/gem-global-active-faults: First release of 2019*. Version 2019.0. DOI: 10.5281/zenodo.3376300. URL: <https://doi.org/10.5281/zenodo.3376300>.
- Sudhaus, H. (2010). “Improving earthquake source studies using InSAR: data error estimation and propagation to model parameter uncertainties”. PhD thesis. ETH Zurich.
- Sudhaus, H. and S. Jónsson (Feb. 2009). “Improved source modelling through combined use of InSAR and GPS under consideration of correlated data errors: application to the June 2000 Kleifarvatn earthquake, Iceland”. In: *Geophysical Journal International* 176.2, pp. 389–404. ISSN: 0956540X. DOI: 10.1111/j.1365-246X.2008.03989.x. URL: <https://academic.oup.com/gji/article-lookup/doi/10.1111/j.1365-246X.2008.03989.x>.
- (2011). “Source model for the 1997 Zirkuh earthquake (MW= 7.2) in Iran derived from JERS and ERS InSAR observations”. In: *Geophysical Journal International* 185.2, pp. 676–692.
- Sudhaus, H. and J. Sigurjón (2009). “Improved source modelling through combined use of InSAR and GPS under consideration of correlated data errors: application to the June 2000 Kleifarvatn earthquake, Iceland”. In: *Geophysical Journal International* 176.2, pp. 389–404.
- Sweeney, J. (1998). “Criteria for selecting accurate event locations from NEIC and ISC bulletins”. In: *Lawrence Livermore National Laboratory*.
- Tadapansawut, T., R. Okuwaki, Y. Yagi, and S. Yamashita (2020). “Rupture Process of the 2020 Caribbean Earthquake along the Oriente Transform Fault, Involving Supershear Rupture and Geometric Complexity of Fault”. In: *Geophysical Research Letters*, e2020GL090899.
- Tape, W. and C. Tape (2012). “Angle between principal axis triples”. In: *Geophysical Journal International* 191.2, pp. 813–831.
- Tapponnier, P., X. Zhiqin, F. Roger, B. Meyer, N. Arnaud, G. Wittlinger, and Y. Jingsui (Nov. 2001). “Oblique Stepwise Rise and Growth of the Tibet Plateau”. In: *Science* 294.5547, pp. 1671–1677.
- Teshebaeva, K., H. Sudhaus, H. Ehtler, B. Schurr, and S. Roessner (2014). “Strain partitioning at the eastern Pamir-Alai revealed through SAR data analysis of the 2008 Nura earthquake”. In: *Geophysical Journal International* 198.2, pp. 760–774. ISSN: 1365246X. DOI: 10.1093/gji/ggu158.
- Tinti, E., L. Scognamiglio, A. Michelini, and M. Cocco (2016). “Slip heterogeneity and directivity of the ML 6.0, 2016, Amatrice earthquake estimated with rapid finite-fault inversion”. In: *Geophysical Research Letters* 43.20, pp. 10, 745–10, 752. ISSN: 19448007. DOI: 10.1002/2016GL071263.

## 6 Bibliography

- Torres, R., S. Lokas, G. Di Cosimo, D. Geudtner, and D. Bibby (2017). “Sentinel 1 evolution: Sentinel-1C and-1D models”. In: *2017 IEEE International Geoscience and Remote Sensing Symposium (IGARSS)*. IEEE, pp. 5549–5550.
- Tothong, P., C. A. Cornell, and J. Baker (2007). “Explicit directivity-pulse inclusion in probabilistic seismic hazard analysis”. In: *Earthquake Spectra* 23.4, pp. 867–891.
- Trabant, C., A. R. Hutko, M. Bahavar, R. Karstens, T. Ahern, and R. Aster (2012). “Data products at the IRIS DMC: Stepping stones for research and other applications”. In: *Seismological Research Letters* 83.5, pp. 846–854.
- Ulrich, T., A.-A. Gabriel, J.-P. Ampuero, and W. Xu (2019). “Dynamic viability of the 2016 Mw 7.8 Kaikōura earthquake cascade on weak crustal faults”. In: *Nature communications* 10.1, pp. 1–16.
- Vallée, M. and M. Bouchon (2004). “Imaging coseismic rupture in far field by slip patches”. In: *Geophysical Journal International* 156.3, pp. 615–630.
- Vallée, M. and V. Douet (2016). “A new database of source time functions (STFs) extracted from the SCARDEC method”. In: *Physics of the Earth and Planetary Interiors* 257, pp. 149–157.
- Vallée, M., M. Landès, N. M. Shapiro, and Y. Klinger (2008). “The 14 November 2001 Kokoxili (Tibet) earthquake: High-frequency seismic radiation originating from the transitions between sub-Rayleigh and supershear rupture velocity regimes”. In: *Journal of Geophysical Research: Solid Earth* 113.B7.
- Van der Walt, S., J. L. Schönberger, J. Nunez-Iglesias, F. Boulogne, J. D. Warner, N. Yager, E. Gouillart, and T. Yu (2014). “scikit-image: image processing in Python”. In: *PeerJ* 2, e453.
- Vasyura-Bathke, H., J. Dettmer, A. Steinberg, S. Heimann, M. P. Isken, O. Zielke, P. M. Mai, H. Sudhaus, and S. Jónsson (2020). “The Bayesian Earthquake Analysis Tool”. In: *Seismological Research Letters* 91.2A, pp. 1003–1018.
- Vasyura-Bathke, H., A. Steinberg, F. Krüger, P. Mai, S. Jónsson, and F. G (2021). “Dynamic P-wave triggering of the 1995 Aqaba earthquake”. In: *JGR* tba.tba, tba.
- Victor, P., M. Sobiesiak, J. Glodny, S. Nielsen, and O. Oncken (2011). “Long-term persistence of subduction earthquake segment boundaries: Evidence from Mejillones Peninsula, northern Chile”. In: *Journal of Geophysical Research: Solid Earth* 116.B2.
- Visini, F., A. Valentini, T. Chartier, O. Scotti, and B. Pace (2020). “Computational tools for relaxing the fault segmentation in probabilistic seismic hazard modelling in complex fault systems”. In: *Pure and Applied Geophysics* 177.5, pp. 1855–1877.
- Walsh, J., W. Bailey, C. Childs, A. Nicol, and C. Bonson (2003). “Formation of segmented normal faults: a 3-D perspective”. In: *Journal of Structural Geology* 25.8, pp. 1251–1262.
- Walters, R. J., J. R. Elliott, N. D’Agostino, P. C. England, I. Hunstad, J. A. Jackson, B. Parsons, R. J. Phillips, and G. Roberts Edinburgh (2009). “The 2009 L’Aquila earthquake (central Italy): A source mechanism and implications for seismic hazard”. In: *Geophysical Research Letters* 36.17, pp. 1–6. ISSN: 00948276. DOI: 10.1029/2009GL039337.
- Wang, D., H. Kawakatsu, J. Mori, B. Ali, Z. Ren, and X. Shen (2016). “Backprojection analyses from four regional arrays for rupture over a curved dipping fault: The Mw 7.7 24 September 2013 Pakistan earthquake”. In: *Journal of Geophysical Research: Solid Earth* 121.3, pp. 1948–1961.
- Wang, R. (1999). “A Simple Orthonormalization Method for Stable and Efficient Computation of Green’s Functions”. In: *Bulletin of the Seismological Society of America* 89.3, pp. 733–741.
- Wang, R., S. Heimann, Y. Zhang, H. Wang, and T. Dahm (2017a). “Complete synthetic seismograms based on a spherical self-gravitating Earth model with an atmosphere–ocean–mantle–core structure”. In: *Geophysical Journal International* 210.3, pp. 1739–1764.
- Wang, R., F. Lorenzo-Martin, and F. Roth (2006a). “PSGRN/PSCMP—a new code for calculating co-and post-seismic deformation, geoid and gravity changes based on the viscoelastic-gravitational dislocation theory”. In: *Computers & Geosciences* 32.4, pp. 527–541.
- (2006b). “PSGRN/PSCMP: a new code for calculating co-and post-seismic deformation, geoid and gravity changes based on the viscoelastic-gravitational dislocation theory”. In: *Computers & Geosciences* 32.4, pp. 527–541.
- Wang, W., X. Qiao, S. Yang, and D. Wang (2017b). “Present-day velocity field and block kinematics of Tibetan Plateau from GPS measurements”. In: *Geophys.J. Int.* 208.2, pp. 1088–1102.
- Werner, C., U. Wegmüller, T. Strozzi, and A. Wiesmann (2000). “Gamma SAR and interferometric processing software”. In: *Proceedings of the ers-envisat symposium, gothenburg, sweden*. Vol. 1620, p. 1620.
- Wesnousky, S. G. (1988). “Seismological and structural evolution of strike-slip faults”. In: *Nature* 335.6188, p. 340.
- (2006). “Predicting the endpoints of earthquake ruptures”. In: *Nature* 444.7117, p. 358.

## 6 Bibliography

- Wesnousky, S. G. and G. P. Biasi (2011). “The length to which an earthquake will go to rupture”. In: *Bulletin of the Seismological Society of America* 101.4, pp. 1948–1950.
- Weston, J., A. Ferreira, and G. Funning (2014a). “Joint earthquake source inversions using seismo-geodesy and 3-D earth models”. In: *Geophysical Journal International* 198.2, pp. 671–696.
- (June 2014b). “Joint earthquake source inversions using seismo-geodesy and 3-D earth models”. In: *Geophysical Journal International* 198.2, pp. 671–696. ISSN: 0956-540X. DOI: 10.1093/gji/ggu110. URL: <https://academic.oup.com/gji/article-lookup/doi/10.1093/gji/ggu110>.
- Weston, J., A. M. Ferreira, and G. J. Funning (2012). “Systematic comparisons of earthquake source models determined using InSAR and seismic data”. In: *Tectonophysics* 532, pp. 61–81. ISSN: 00401951. DOI: 10.1016/j.tecto.2012.02.001.
- Wimpenny, S., A. Copley, and T. Ingleby (2017). “Fault mechanics and post-seismic deformation at Bam, SE Iran”. In: *Geophysical Journal International* 209.2, pp. 1018–1035.
- Woessner, J., D. Laurentiu, D. Giardini, H. Crowley, F. Cotton, G. Grünthal, G. Valensise, R. Arvidsson, R. Basili, M. B. Demircioglu, et al. (2015). “The 2013 European seismic hazard model: key components and results”. In: *Bulletin of Earthquake Engineering* 13.12, pp. 3553–3596.
- Wollherr, S., A.-A. Gabriel, and C. Uphoff (2018). “Off-fault plasticity in three-dimensional dynamic rupture simulations using a modal Discontinuous Galerkin method on unstructured meshes: implementation, verification and application”. In: *Geophysical Journal International* 214.3, pp. 1556–1584.
- Wright, T. J. (2002). “Remote monitoring of the earthquake cycle using satellite radar interferometry”. In: *Philosophical Transactions of the Royal Society of London. Series A: Mathematical, Physical and Engineering Sciences* 360.1801, pp. 2873–2888.
- Wright, T. J., B. Parsons, P. C. England, and E. J. Fielding (2004a). “InSAR observations of low slip rates on the major faults of western Tibet”. In: *Science* 305.5681, pp. 236–239.
- Wright, T. J., B. E. Parsons, and Z. Lu (2004b). “Toward mapping surface deformation in three dimensions using InSAR”. In: *Geophysical Research Letters* 31.1.
- Wright, T., B. Parsons, J. Jackson, M. Haynes, E. Fielding, P. England, and P. Clarke (1999). “Source parameters of the 1 October 1995 Dinar (Turkey) earthquake from SAR interferometry and seismic bodywave modelling”. In: *Earth and Planetary Science Letters* 172.1-2, pp. 23–37.
- Xu, C., Y. Liu, Y. Wen, and R. Wang (2010). “Coseismic slip distribution of the 2008 mw 7.9 Wenchuan earthquake from joint inversion of GPS and InSAR data”. In: *Bulletin of the Seismological Society of America* 100.5 B, pp. 2736–2749. ISSN: 00371106. DOI: 10.1785/0120090253.
- Xu, Y., K. D. Koper, O. Sufri, L. Zhu, and A. R. Hutko (2009). “Rupture imaging of the Mw 7.9 12 May 2008 Wenchuan earthquake from back projection of teleseismic P waves”. In: *Geochemistry, Geophysics, Geosystems* 10.4.
- Xu, Y., J.-H. LIU, F.-T. LIU, L.-R. ZHU, H.-Y. LONG, and B. Wei (2006). “Crustal velocity structure and seismic activity in the Tianshan-Pamir conjunctive zone”. In: *Chinese Journal of Geophysics* 49.2, pp. 417–425.
- Yagi, Y., A. Nakao, and A. Kasahara (2012). “Smooth and rapid slip near the Japan Trench during the 2011 Tohoku-oki earthquake revealed by a hybrid back-projection method”. In: *Earth and Planetary Science Letters* 355, pp. 94–101.
- Yao, H., P. M. Shearer, and P. Gerstoft (2012). “Subevent location and rupture imaging using iterative backprojection for the 2011 Tohoku M w 9.0 earthquake”. In: *Geophysical Journal International* 190.2, pp. 1152–1168.
- Yin, A., Y.-Q. Dang, L.-C. Wang, W.-M. Jiang, S.-P. Zhou, X.-H. Chen, G. E. Gehrels, and M. W. McRivette (2008a). “Cenozoic tectonic evolution of Qaidam Basin and its surrounding regions (Part 1): The southern Qilian Shan-Nan Shan thrust belt and northern Qaidam Basin”. In: *Geological Society of America Bulletin* 120.7-8, pp. 813–846.
- Yin, A., Y.-Q. Dang, M. Zhang, X.-H. Chen, and M. W. McRivette (2008b). “Cenozoic tectonic evolution of the Qaidam Basin and its surrounding regions (Part 3): Structural geology, sedimentation, and regional tectonic reconstruction”. In: *Geological Society of America Bulletin* 120.7-8, pp. 847–876.
- Yin, A. and T. M. Harrison (2000). “Geologic evolution of the Himalayan-Tibetan orogen”. In: *Annual Review of Earth and Planetary Sciences* 28.1, pp. 211–280.
- Yin, J. and M. A. Denolle (2019). “Relating teleseismic backprojection images to earthquake kinematics”. In: *Geophysical Journal International* 217.2, pp. 729–747.
- Yu, C., Z. Li, N. T. Penna, and P. Crippa (2018). “Generic atmospheric correction model for Interferometric Synthetic Aperture Radar observations”. In: *Journal of Geophysical Research: Solid Earth* 123.10, pp. 9202–9222.

## 6 Bibliography

- Zahradník, J. and E. Sökes (2014). “The M<sub>w</sub> 7.1 Van, Eastern Turkey, earthquake 2011: two-point source modelling by iterative deconvolution and non-negative least squares”. In: *Geophysical Journal International* 196.1, pp. 522–538.
- Zhao, D., C. Qu, X. Shan, R. Bürgmann, W. Gong, and G. Zhang (2018). “Spatiotemporal Evolution of Postseismic Deformation Following the 2001 Mw7.8 Kokoxili, China, Earthquake from 7 Years of InSAR Observations”. In: *Remote Sensing* 10.12, p. 1988.
- Zielke, O., M. Galis, and P. M. Mai (2017). “Fault roughness and strength heterogeneity control earthquake size and stress drop”. In: *Geophysical Research Letters* 44.2, pp. 777–783.

# 7 Acknowledgments and Declaration

## Acknowledgments

This work would not have been possible without the support of many people. Especially, I thank:

- Dr. Henriette Sudhaus, my supervisor and mentor. I am deeply grateful for allowing me to work in her project, teaching me how to do proper science and for all of her patience and guidance. One can simply not wish for a more engaged and motivational supervisor.
- apl. Prof. Dr. Frank Krüger for putting me on the path of seismology, his brilliant advice and all his efforts of support.
- Prof. Dr. Jörg Ebbing for generously hosting me at his working group, critical questions to put my work in perspective and for fostering a very healthy and good climate to work in.
- Dr. Sebastian Heimann for his fantastic Pyrocko framework and for being the giant on which shoulders my work stands.
- Dr. Simon Daout for showing me that earthquake research goes beyond source modelling and generally for critical and helpful discussions. I am sure that if earthquakes could speak, they would have a french accent.
- Dr. Hannes Vasyura-Bathke for all the great, motivational and productive co-operations. His advise and tutelage was greatly appreciated.
- Marius Isken for code, beer and science.
- past and current members of the AG "Satellite and Airborne Geophysics" at Kiel University for discussions, fun gatherings and camaraderie. I thoroughly enjoyed my stay at the "AG Ebbing".
- Prof. Dr. Thorsten Dahm for hosting me as a guest scientist in his working group.
- Dr. Peter Gabler and Dr. Lars Ceranna for their kind support and patience.
- The German Research Foundation DFG for founding the Emmy-Noether Young-Researcher-Grant (Number 276464525, "Bridging Geodesy and Seismology for improved and automated estimation of faulting events" which allowed to conduct this research.
- the fantastic Pyrocko team for all the fantastic work in the project and the nerdy hackweeks.
- the open-source community (like ubuntu, NumPy, opencv, GMTSAR, ISCE, SciPy, Matplotlib, Jupyter, scikit-learn)
- for comments and suggestions: Julia, Sandra, Peter, Vanessa, Martin, Wolfgang, Florian, Diana and Manuel.
- my family!

## Erklärung

Diese Arbeit ist, abgesehen von der Beratung durch meinen Betreuer und die Zuhilfenahme der angegebenen Mittel, nach Inhalt und Form meine eigene. Die Arbeit hat weder ganz noch zum Teil bereits an anderer Stelle im Rahmen eines Prüfungsverfahrens vorgelegen. Die Arbeit wurde nicht veröffentlicht noch zur Veröffentlichung eingereicht. Die Arbeit ist unter Einhaltung der Regeln guter wissenschaftlicher Praxis der Deutschen Forschungsgemeinschaft entstanden. Mir wurde kein akademischer Grad entzogen.

Unterschrift: \_\_\_\_\_

(Ort) (Datum) (Andreas Steinberg)



# Supplement

## Supplement of "Data-driven constraints on earthquake modeling and segmentation from teleseismic multi-array backprojection and InSAR"

### Exploratory Optimization with Bayesian Bootstrapping


We estimate model parameter uncertainties alongside an optimization by Bayesian bootstrapping. Here bootstrapping is realized through Bayesian random weighting Rubin, 1981 of the seismic waveforms and through residual bootstrapping with synthetic correlated noise on the InSAR data to form multiple objective functions for a single forward-model realization. The misfit weighting of the waveforms respects the uncorrelated data error between stations caused by e. g. site effects. The synthetic noise  $\epsilon_{\text{syn},i}$  used in the residual bootstrapping is generated based on the estimated variance-covariance functions of the data error Sudhaus and Jónsson, 2009 and reflects the apparent data error. We use a large number of different sets with random weights and synthetic noise for these multiple misfit calculations, usually above 100, and achieve as many different bootstrap optimization chains. Once the optimizations converge, the best-fit models of each bootstrap chain may start to diverge, when the data error becomes significant with respect to the difference in model fit, and form model ensembles. In this way, which is very similar to the so called "Randomize-then-Optimize" procedure Bardsley et al., 2014, we retrieve source parameter distributions similar to a Markov Chain Monte Carlo sampling of the model space Jonsson et al., 2014.

The optimization that involves a large number of bootstrap chains works in the following way. Each bootstrap chain shares the same sampled models, but because of the different weighting, the misfit of a model is different in each bootstrap chain. A source model may perform well in one bootstrap chain, but poorly in another. Throughout the optimization we monitor a given number of best-fit models of each chain, to which we refer to as the highscore list of the chain. The number of models in the highscore lists is defined dependent on the number of model parameters  $N_{\text{par}}$ . The highscore list acts as a memory of past visited models, which allows the sampler to retain several good models and explore multiple minima, which is especially important for optimizing models with several earthquake sources. The highscore list of each bootstrap chain will therefore differ and converge differently. The differences between the performance of the models in each bootstrap chain represent the uncertainty of the models with respect to the data error.

The optimization is a direct-search optimization and has two distinct phases. The first phase is a random sampling (uniform distribution) of the model parameter space, constrained by given upper and lower parameter bounds. Here this first phase samples 20.000 models. The uniform distribution as prior probability of the earthquake source parameters for the initial sampling is well justified if the parameter space is large and the solution unknown. This creates a unbiased set of sampled initial starting solutions. At the end of the first phase, the best-performing models are determined for each bootstrap chain with its specific objective function and collected in the corresponding highscore lists for each bootstrap chain.

## 7 Acknowledgments and Declaration

The bootstrap chain highscore lists are playing a vital role in the second optimization phase, the "directed sampling". The bootstrap chain that shares the least number of models in its highscore list with other highscore lists determines the sampling of the next model. This ensures that also the directed phase is still exploring the model space. The new model is drawn from a multivariate normal distribution based on the variance-covariance matrix  $\mathbf{R}$  of the source model parameters from all models currently in the respective highscore list. We use the excentricity compensated method to give models with less neighbors a higher probability to be drawn and considered as the center of the search space. The search space is scaled by a factor  $a$ . This scale factor is logarithmically decreasing from the first sampling  $a_{\text{start}} = 2$  to the last sampling  $a_{\text{end}} = 1$  of this second optimization phase. In other words, the search space is an ellipsis in the model space, around a highscore list model, which is shrinking with increasing number of models sampled. Each newly drawn model is ranked in all bootstrap chains. They enter a highscore list if they outperform any of the current highscore list models. The formerly largest-misfit model in the highscore list is removed from it. With each new model in the highscore lists their statistics change and with it a search radius for a new model. At the start of the optimization the different highscore lists likely contain the same models. Only when the misfit starts to differ subtly between models, the data errors reflected in the different objective functions start to play a role in the ranking of the well-performing models.



chapter\_4/pics/scheme\_softx.pdf

Figure S1.1: a) Scheme of how the proposed methods, the multi-array backprojection and the displacement map segmentation feed prior information into a non-linear optimization. b) Sketch of finite source model used as for forward model and its source parameters modeling.

## Additional synthetic tests of the multi array backprojection



Figure S1.2: Cumulative semblance from the backprojection of a synthetic DC source backprojection (Test 1) using the Muji 2016 earthquake array setup for a) LF and P-wave only, b) LF and S-wave only, c) HF and P-wave only and d) HF and S-wave only. Semblance is plotted as contour color plot. The black outlines represent the 68% precision estimate from bootstrapping on the semblance maxima location. They are drawn as a minimum bounding outlines for the locations of the maxima from 100 bootstraps. The image is a zoom in and the extent of the whole search grid is given in the top right. The travel-time grid points are indicated as gray dots in the background. The black dot indicates the true position of the synthetic source. Coordinates are given in Latitude/Longitude (black) and UTM (blue).

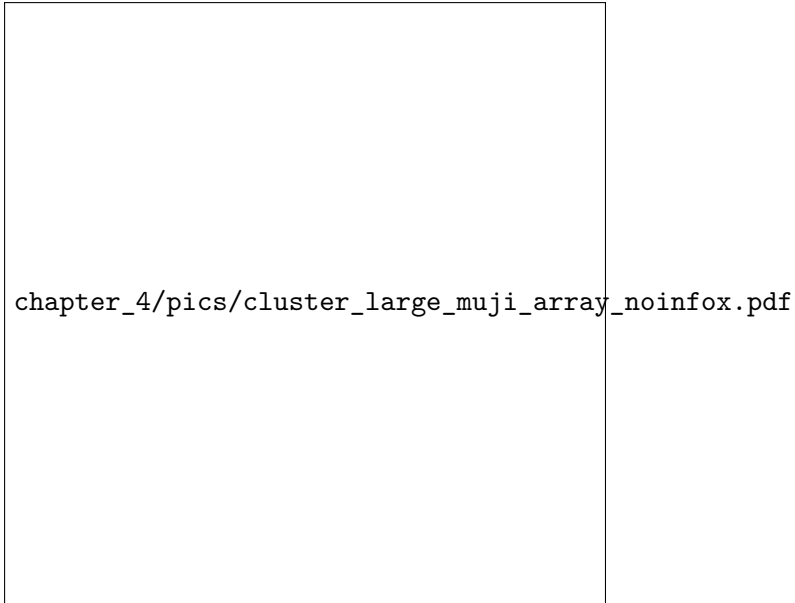


Figure S1.3: Stations combined to large arrays used for the synthetic backprojection Test 2 , (Sec. 2.1.6) for the 2016 Muji earthquake plotted on a world map. The stations belonging to the same array share the same color.

chapter\_4/pics/muij\_large\_synx.pdf

Figure S1.4: Cumulative semblance from the backprojection of a synthetic DC source (Test 2, Sec. 2.1.6) for P- and SH-waves using the large array setup for the 2016 Muji earthquake (Fig. S1.3) for a) LF and b) HF. Shown is the cumulative semblance from all timesteps from the non-bootstrapped LF synthetic single DC source backprojection using large arrays. The outlines in black for the LF and in red for the HF indicates the uncertainty from the bootstrapped semblance. Other details as in Fig. S1.2.

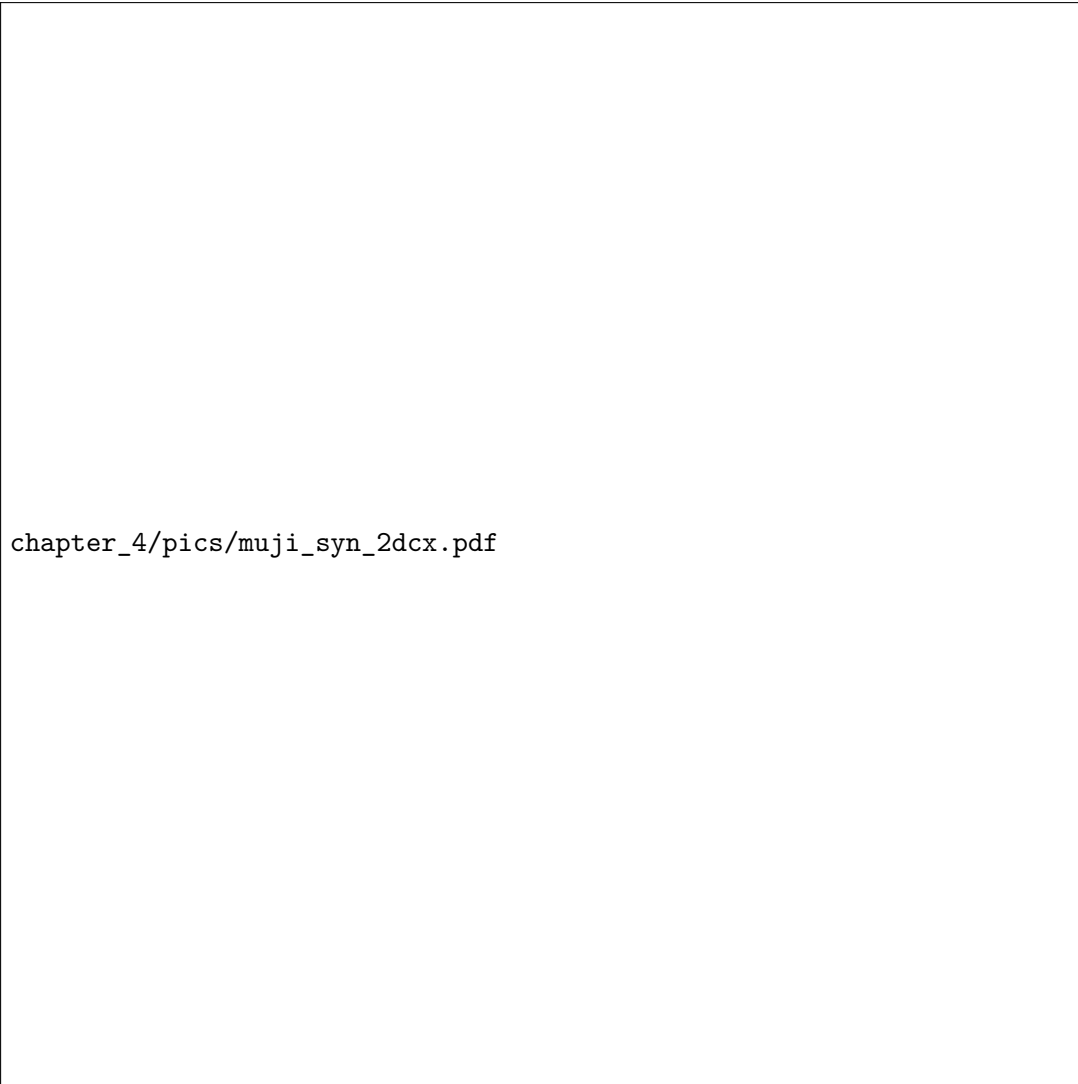


Figure S1.5: Cumulative semblance from the backprojection of two synthetic DC sources (Test 4, Sec. 2.1.6) from P- and SH-waves using the Muji 2016 earthquake array setup for a) LF and b) HF. The blue and orange dots indicate the true position of the two input sources used for forward calculation. The outlines in black for the LF and in red for the HF indicates the uncertainty from the bootstrapped semblance. Other details as in Fig. S1.2.

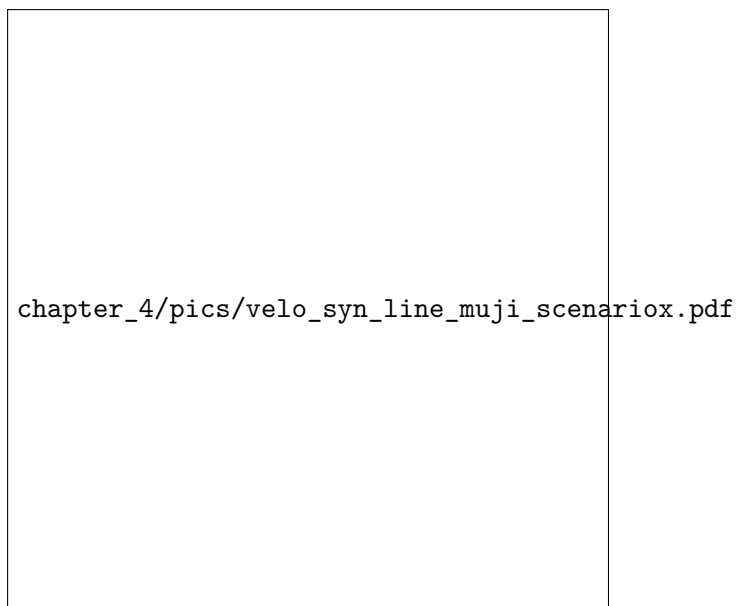


Figure S1.6: Time-Distance plot for the line source. Time is relative to the first window with semblance. Blue dots indicate the first and last maxima of the high-frequency BP, the orange line the estimated velocity ( 4000 m/s) and the red line the true velocity.

### **Additional backprojection synthetic tests based on Ahar**

We carry out additional synthetic backprojection tests based on a another set of stations, mimicking the situation for the Mw 6.3 2012 Ahar earthquake, resulting in a different azimuthal coverage and distance distribution. Again, we backproject two differently filtered datasets, one at high frequencies, 0.25-1.5 Hz and one at low frequencies, 0.01-0.24 Hz. In all cases the source is set to be equivalent of a Mw 6.3 earthquake. The waveforms have been randomly shifted by up to +/- 2s to simulate model errors. The array weights have been bootstrapped 100 times and the semblance is weighted by azimuth. For each synthetic waveform real pre-event noise from the corresponding waveform real record from before the 2012 Ahar earthquakes is added. We use a 4 Hz Green's function store to calculate the synthetics based on the QSSP code by Wang, 1999 and use the AK-135 traveltimes model.

We test for the recovery of the position of a single point-source using the clustering of stations into small virtual arrays. The station and array map can be found in Fig. S1.7. The source is defined with a triangular source-time function of 3 s duration. Backprojection results are shown for low frequencies in Fig. S1.8a and for high frequencies, 0.25-1.5 Hz, in Fig. S1.8b. At both frequencies the source position can be recovered. The source is set at 8.7 km depth and the traveltimes grid is calculated the same depth.

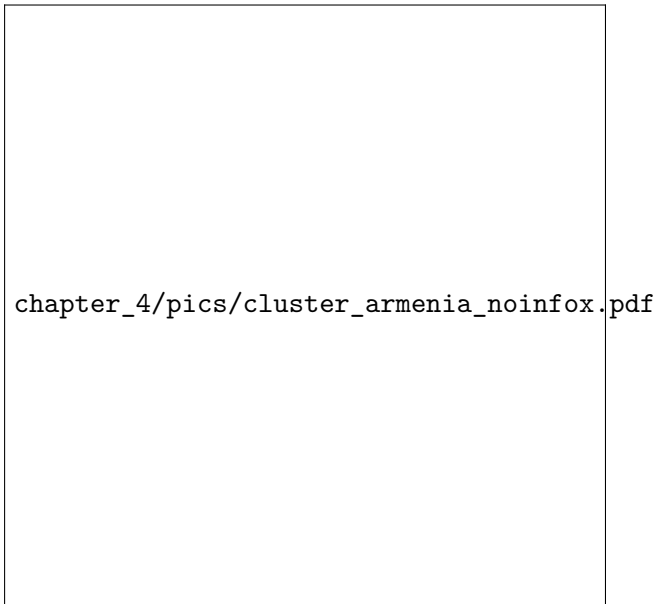


Figure S1.7: The stations used for the synthetic backprojections based on the 2012 Ahar earthquake with multi-array clusters. The stations belonging to the same array share the same color.





Figure S1.8: Cumulative semblance from the backprojection of a synthetic DC source (comparable to Test 1, Sec. 2.1.6) for P- and SH-waves using the more sparse array setup of the 2012 Ahar earthquake (Fig. S1.7) of a) LF and b) HF. The source is located approximately at the location of the 2012 Ahar earthquake. Shown is the cumulative semblance from all timesteps from the non-bootstrapped LF synthetic single DC source backprojection using large arrays. Other details as in Fig. S1.2. The outlines in black indicate the uncertainty from the bootstrapped semblance.

## 7 Acknowledgments and Declaration

Similar to the synthetic test of the Muji 2016 earthquake we repeat the same synthetic test (we keep all parameters the same as before) but use large arrays S1.9 instead of the smaller virtual arrays used before. The results (Lf and HF, Figs. S1.10a and S1.10b) shows broader distributed semblance mappings in comparison to the smaller virtual arrays.

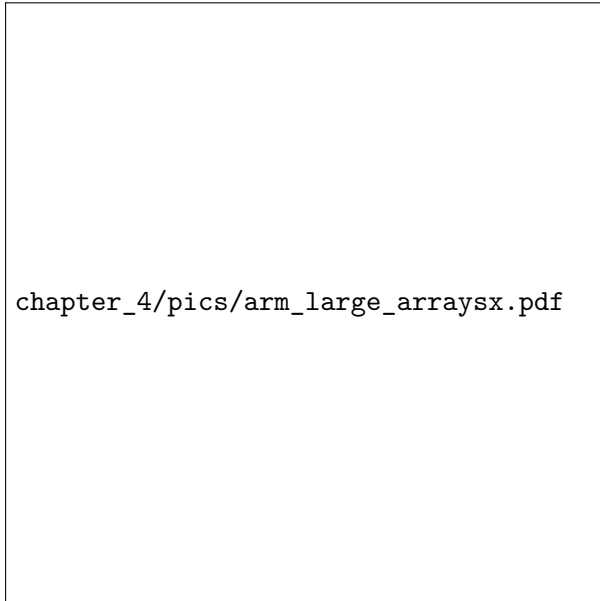


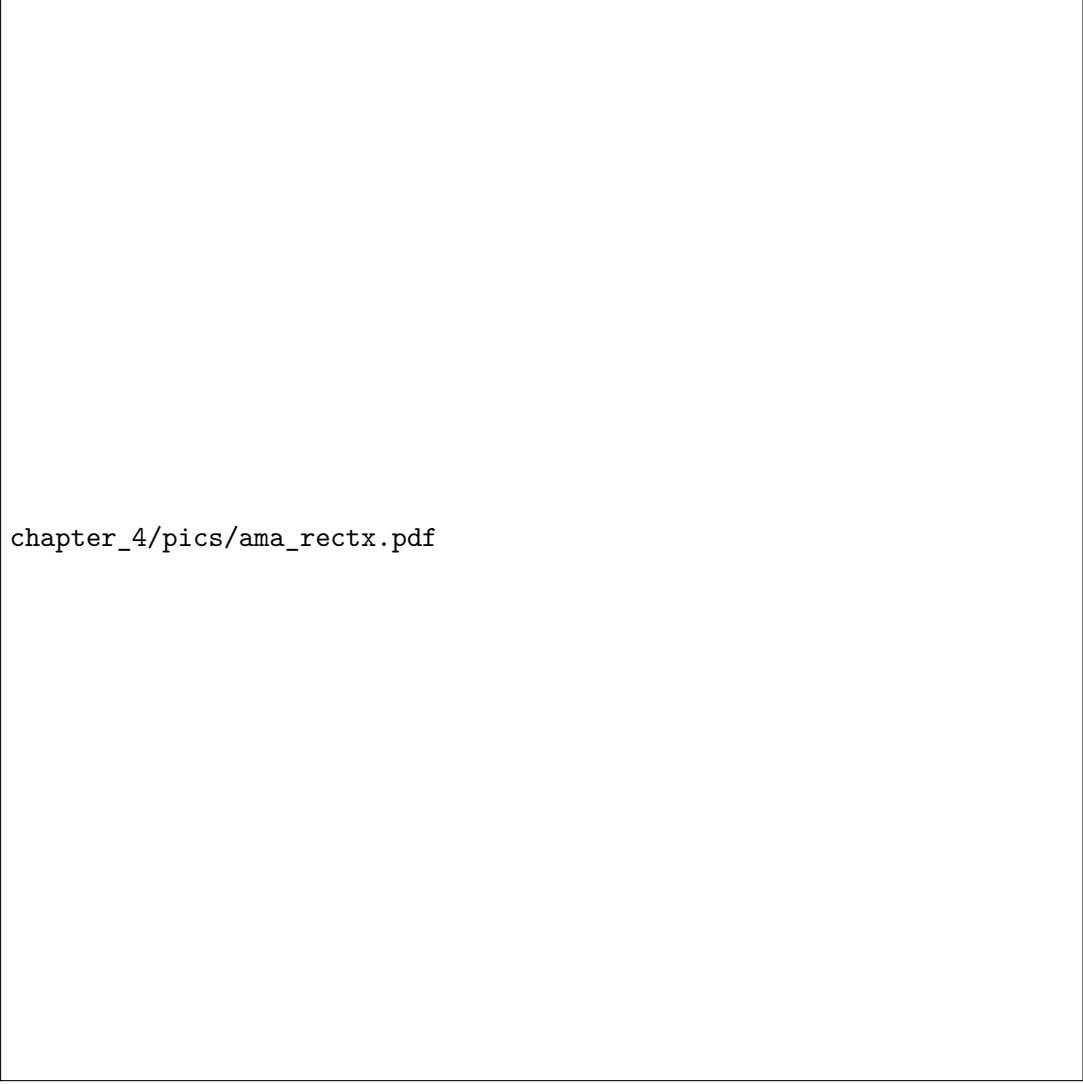
Figure S1.9: The stations used for the synthetic backprojections based on the 2012 Ahar earthquake with large arrays. The stations belonging to the same array share the same color.

chapter\_4/pics/arm\_large\_array\_dcx.pdf

Figure S1.10: Cumulative semblance from the backprojection of a synthetic DC source (comparable to Test 2, Sec. 2.1.6) for P- and SH-waves using the large-array setup of the 2012 Ahar earthquake (Fig. S1.9) and for a) LF and b) HF. The source is located approximately at the location of the 2012 Ahar earthquake. Other details as in Fig. S1.2.

## 7 Acknowledgments and Declaration

We also tested the recovery of signals from a backprojection of a synthetic forward modelled line source of 80 km length (a finite rectangular source with very small width of 0.1 m and a dip of  $90^\circ$ ) with nucleation at the eastern edge. The low-frequency backprojection shows a broader distribution of significant semblance (Fig. S1.11a). For the high-frequency backprojection (Fig. S1.11b) the start and stop phases can be recovered. The rupture speed on the fault was set to 4000 m/s and approximately recovered by taking the distance and time between the first and last semblance maxima (Fig. S1.12).



chapter\_4/pics/ama\_rectx.pdf

Figure S1.11: Cumulative semblance from the backprojection of a synthetic horizontal line source (comparable to Test 3, Sec. 2.1.6) for P- and SH-waves using the array setup of the 2012 Ahar earthquake (Fig. S1.7) for a) LF and b) HF. The source is located approximately at the location of the 2012 Ahar earthquake. Shown is the cumulative semblance from all timesteps from the non-bootstrapped LF synthetic backprojection. Other details as in Fig. S1.2.



Figure S1.12: Time-Distance plot for the synthetic line source HF backprojection of the 2012 Ahar earthquake as seen in Fig. Time is relative to the first window with semblance. S1.11b. Blue dots indicate the first and last maxima of the high-frequency backprojection, the orange line the estimated velocity ( 4000 m/s). The red line indicates the true velocity.

## 7 Acknowledgments and Declaration

Another synthetic test is conducted for a vertical line source with top depth 1 km and bottom depth 21 km (20 km length), dip  $90^\circ$  and very small width of 0.1 m. The nucleation starts at the bottom. Again we carry out the tests for low-frequency backprojections (Fig. S1.13a) and for high-frequency backprojection (Fig. S1.13b). The rupture speed on the fault was set to 4000 m/s. The start and stop phase spatially overlay each other.

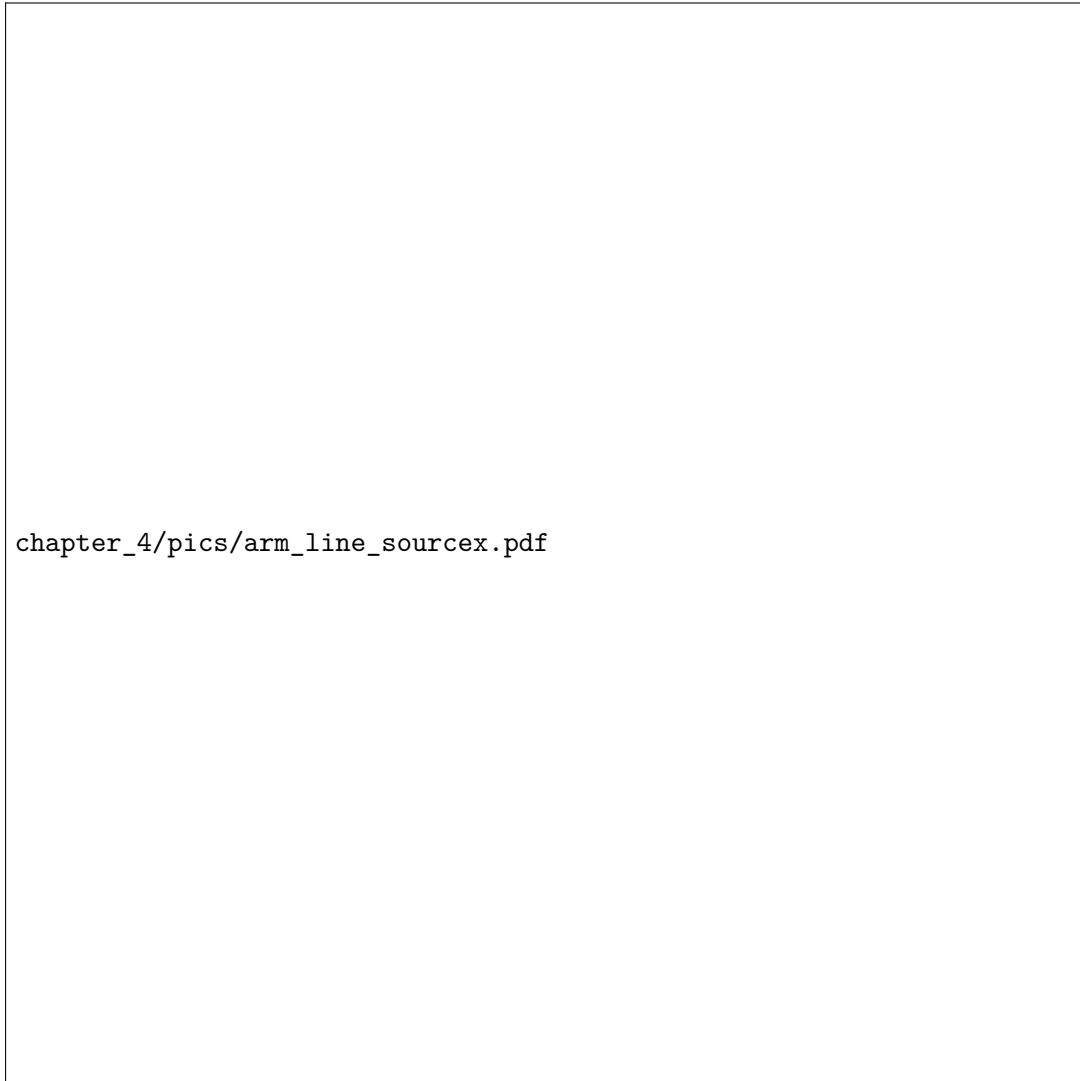


Figure S1.13: Cumulative semblance from the backprojection of a synthetic vertical line source for P- and SH-waves using the array setup of the 2012 Ahar earthquake (Fig. S1.7) of a) LF and b) HF. The source is located approximately at the location of the 2012 Ahar earthquake. Shown is the cumulative semblance from all timesteps from the non-bootstrapped LF synthetic backprojection. The gray dot indicates the true position of the synthetic line source (vertical). Other details as in Fig. S1.2.

## 7 Acknowledgments and Declaration

We also carry out a synthetic test for two point-sources of same moment, duration and timing, but which are spatially separated by 50 km (Fig. S1.14a, Fig. S1.14b).

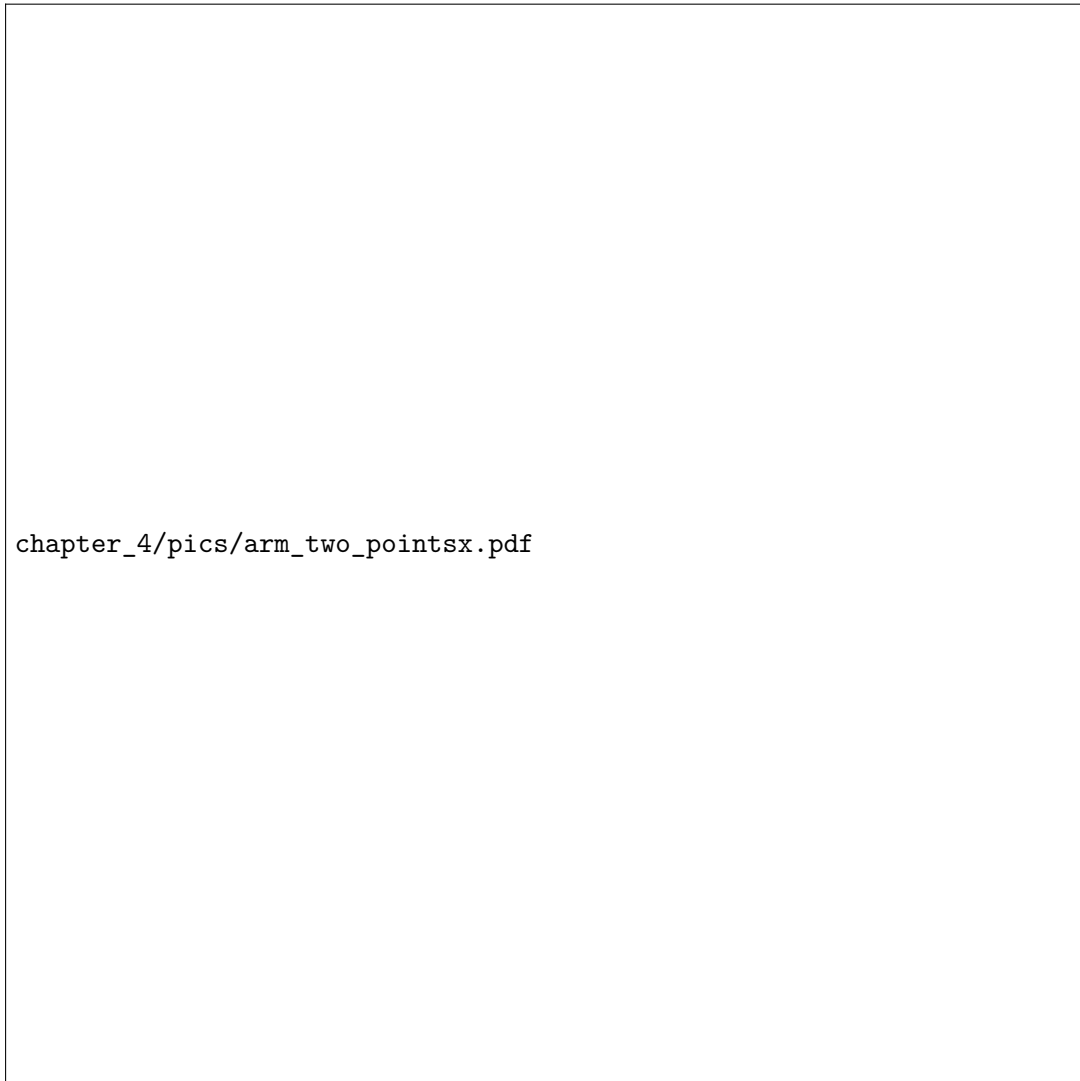


Figure S1.14: Synthetic backprojection of P- and SH-waves for two DC sources (comparable to Test 4, Sec. 2.1.6), using the array setup of the 2012 Ahar earthquake (Fig. S1.7) for a) LF and b) HF. The source is located approximately at the location of the 2012 Ahar earthquake. Shown is the cumulative semblance from all timesteps from the non-bootstrapped LF synthetic of the two DC sources backprojection. The blue circles indicate the true position of the synthetic sources. Other details as in Fig. S1.2.

**Additional synthetic tests of displacement map segmentation**





Figure S1.15: Synthetic test of the displacement map segmentation method for two strike-slip sources trending north-south at 0.5 km top edge depth. a), b) and c) contain the displacement data, the gradient and the gradient of the sign change mask (superimposed on the displacement data), respectively, for the ascending dataset and d), e) and f) accordingly for the descending data. g) shows the normalized combined product of the gradient sign change mask with the gradient from ascending and descending InSAR data. Values below 1% of the maximum value are masked out. This map is used as a probability estimate for the position of the fault(s) location centroid. h) shows the bounding boxes and ellipses applied on the product shown in g). The green box is the area of interest, zoomed into in i). The red dashed line indicates the major axis of the ellipses containing the highest values for each region found as described above. The outline of the synthetic source(s) is indicated in the figures with black lines that are thicker for the top edge. The ellipses (indicated by the purple outline) is centered at the centroid of each region.

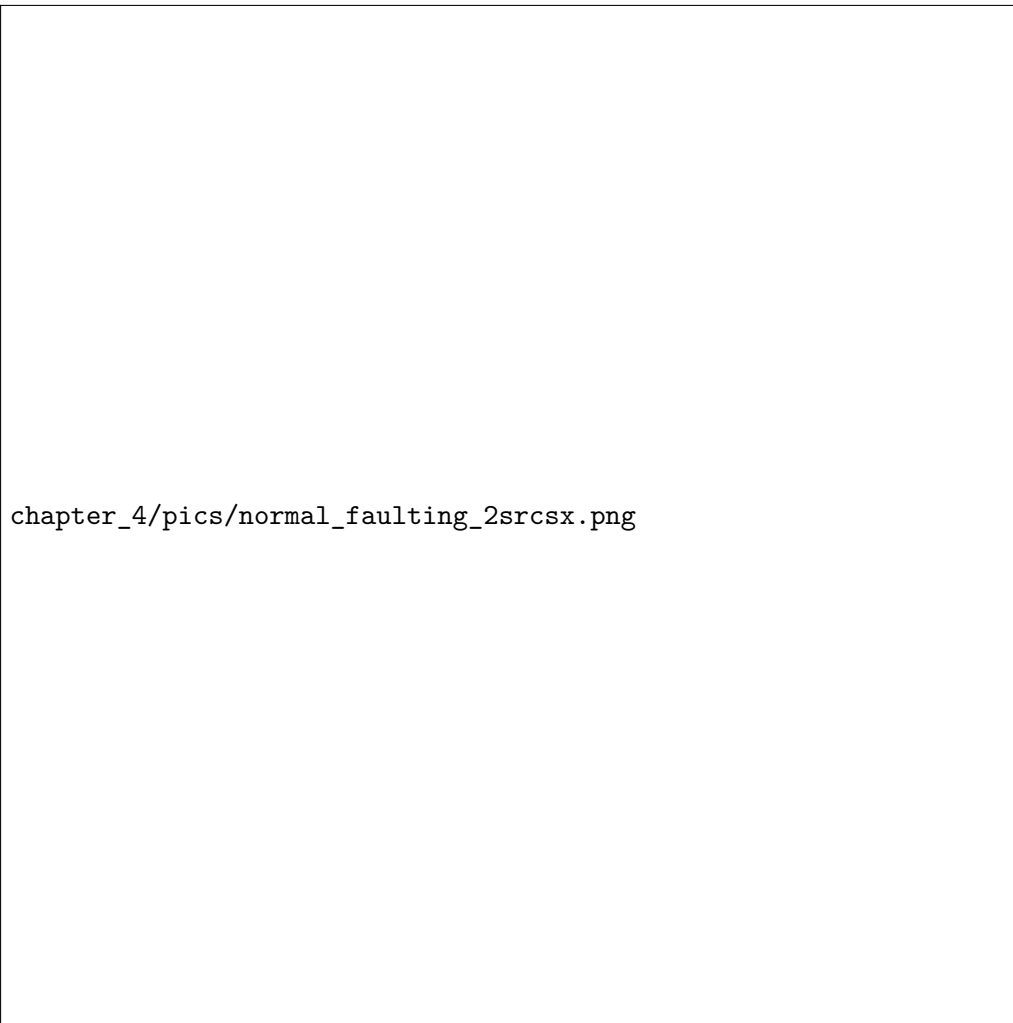


Figure S1.16: Synthetic test of the displacement map segmentation method for a two normal dip-slip earthquakes at a depth of 0.5 km. a), b) and c) contain the displacement data, the gradient and the gradient of the sign change mask (superimposed on the displacement data), respectively, for the ascending dataset and d), e) and f) accordingly for the descending data. g) shows the normalized combined product of the gradient sign change mask with the gradient from ascending and descending InSAR data. Values below 1% of the maximum value are masked out. This map is used as a probability estimate for the position of the fault(s) location centroid. h) shows the bounding boxes and ellipses applied on the product shown in g). The green box is the area of interest, zoomed into in i). The red dashed line indicates the major axis of the ellipses containing the highest values for each region found as described above. The outline of the synthetic source(s) is indicated in the figures with black lines that are thicker for the top edge. The ellipses (indicated by the purple outline) is centered at the centroid of each region.

chapter\_4/pics/normal\_faulting\_DEEPx.png

Figure S1.17: Synthetic test of the displacement map segmentation method for a single normal fault at a depth of 6 km. a), b) and c) contain the displacement data, the gradient and the gradient of the sign change mask (superimposed on the displacement data), respectively, for the ascending dataset and d), e) and f) accordingly for the descending data. g) shows the normalized combined product of the gradient sign change mask with the gradient from ascending and descending InSAR data. Values below 1% of the maximum value are masked out. This map is used as a probability estimate for the position of the fault(s) location centroid. h) shows the bounding boxes and ellipses applied on the product shown in g). The green box is the area of interest, zoomed into in i). The red dashed line indicates the major axis of the ellipses containing the highest values for each region found as described above. The outline of the synthetic source(s) is indicated in the figures with black lines that are thicker for the top edge. The ellipses (indicated by the purple outline) is centered at the centroid of each region.



Figure S1.18: Source characteristics estimation from segmentation of InSAR displacement maps applied to the real InSAR Envisat data of the 2009 L'Aquila earthquake Steinberg et al., 2020a. a), b) and c) contain the displacement data, the gradient and the gradient of the sign change mask (superimposed on the displacement data), respectively, for the ascending dataset and d), e) and f) accordingly for the descending data. g) shows the normalized combined product of the gradient sign change mask with the gradient from ascending and descending InSAR data. Values below 1% of the maximum value are masked out. This map is used as a probability estimate for the position of the fault(s) location centroid. h) shows the bounding boxes and ellipses applied on the product shown in g). The green box is the area of interest, zoomed into in i). The red dashed line indicates the major axis of the ellipses containing the highest values for each region found as described above. The outline of the synthetic source(s) is indicated in the figures with black lines that are thicker for the top edge. The ellipses (indicated by the purple outline) is centered at the centroid of each region.

## 7 Acknowledgments and Declaration

Table S1.1: Details of the Sentinel-1 SAR Data used in the study. Data are acquired in interferometric wide swath mode by Terrain Observation with Progressive Scans (TOPS) in VV polarization. The single look complex SAR images were downloaded from the Copernicus Open Access Hub.

rel. orbit (track)	primary date	secondary date	L baseline [m]
107 (dsc)	2016/11/25	2016/12/19	78.2
27 (asc)	2016/10/20	2016/12/07	98.6

Table S1.2: Earthquake source model parameters for the 2016 Muji earthquake from published point and finite source models. Models from Bie et al., 2018 for InSAR and seismology, and for seismology only from USGS and GCMT Dziewonski et al., 1981 catalogs.

	Time	Lat	Lon	Depth	Strike	Dip	Rake	$M_o$	Length	Width	Slip
		ř	ř	km	ř	ř	ř	$10^{18} N \cdot m$	km	km	m
Bie 1. source seis.	+7.88s	39.2313	74.1428	14	108/198	78/88	178/12	5.07			
Bie 2. source seis.	+10.52s	39.1681	74.4208	10.1	108/198	78/88	178/12	1.905			
Bie 1. source InSAR		39.2261	74.11165	8.5	106.4	70	-176	5.420			0.9
Bie 2. source InSAR		39.1754	74.3869	4.7	106.4	70	-176	2.847			1.31
USGS (body-wave)		39.273	73.978	17	19/288	86/86	4/176	7.5			
USGS (W-phase)		39.273	73.978	11.5	107/199	76/84	174/14	8.746			
USGS (Centroid)		39.273	73.978	16.7	113/18	63/81	-170/-28	10.5			
GCMT		39.27	74.14	19.1	110/19	78/87	-177/-12	11.3			
Feng InSAR	39.226	74.219	<15	105.5	80 (+/-4)	-161 (+/-12)	9.87	55	20		
He InSAR/GNSS		39.21	74.254	-	110.7 ± 0.5	83.7 ± 1.0	167 ± 1.0	12.03	38.4	18.3	0.56 ± 0.3

### Additional information for the 2016 Muji earthquake



Figure S1.19: The layered 1-d velocity model for the static displacement modeling, based on Xu et al., 2006 and Li et al., 2018.

### Additional Muji 2016 earthquake backprojection results

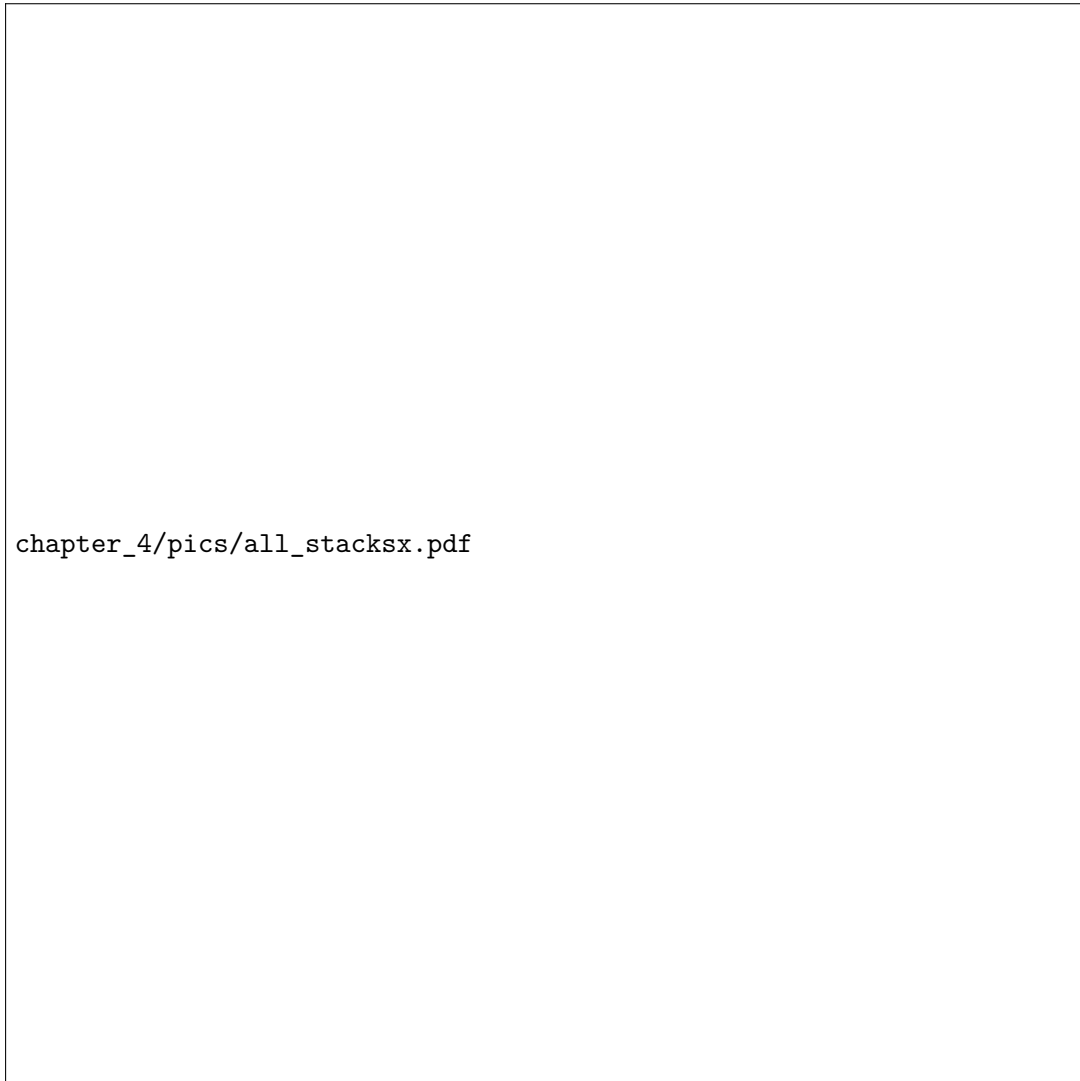


Figure S1.20: Linear stacking for both P- and SH-phases for the grid point closest to the hypocenter, compared to phase-weighted stacked waveforms. P-wave phases stacks for A) linear and B) phase-weighted methods. SH-wave phase stack for C) linear and D) phase-weighted methods. Note the difference in the scaling of the amplitude between diagrams.

chapter\_4/pics/waveforms\_p1x.pdf

Figure S1.21: Example waveform data from an exemplary array used in the backprojection of the Muji 2016 earthquake (array number 16, located in central Europe). A) shows the array's waveform spectra of the z-component, color-coded for each station. The gray shaded spectrum shows the average noise spectrum from all stations immediately before the event. Inset B) shows the array location and stations. C) and D) show normalised waveforms with the P-wave onset for C) the low-frequency filtered data (0.003-0.16 Hz) and D) the high-frequency filtered data (0.16-1.5 Hz).



chapter\_4/pics/waveforms\_p2x.pdf

Figure S1.22: SH-wave onset waveforms from the exemplary array in central Europe (see also Fig. S1.21). A) the low-frequency filtered data (0.003-0.16 Hz) and B) the high-frequency filtered data (0.16-1.5 Hz).

chapter\_4/pics/timeshifts\_mujix.pdf

Figure S1.23: Empirical time shifts for different phases at the stations used in the backprojection that maximize the semblance of the reference event and are used for the BP of the 2016 Muji earthquake. Shown timeshifts for the low-frequency backprojection are in a) of the P-phase and in b) for the SH-phase, while the high-frequency backprojections are shown in c) for the P-phase and in d) for the SH-phase. Timeshifts are given relative to the gCMT onset time.

chapter\_4/pics/muji\_lf\_all\_timex.pdf

Figure S1.24: Time-incremental low-frequency semblance maps from the backprojection of the 2016 Muji earthquake for every timestep of 8 s individually in a) to d). The time given is relative to the onset of the first occurrence of significant semblance.

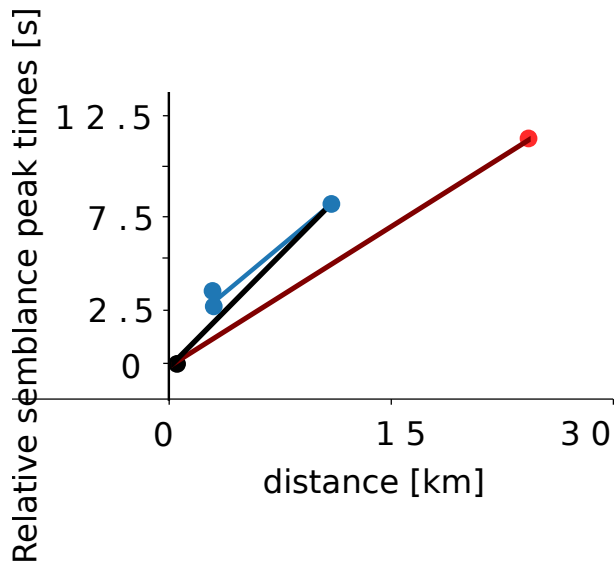
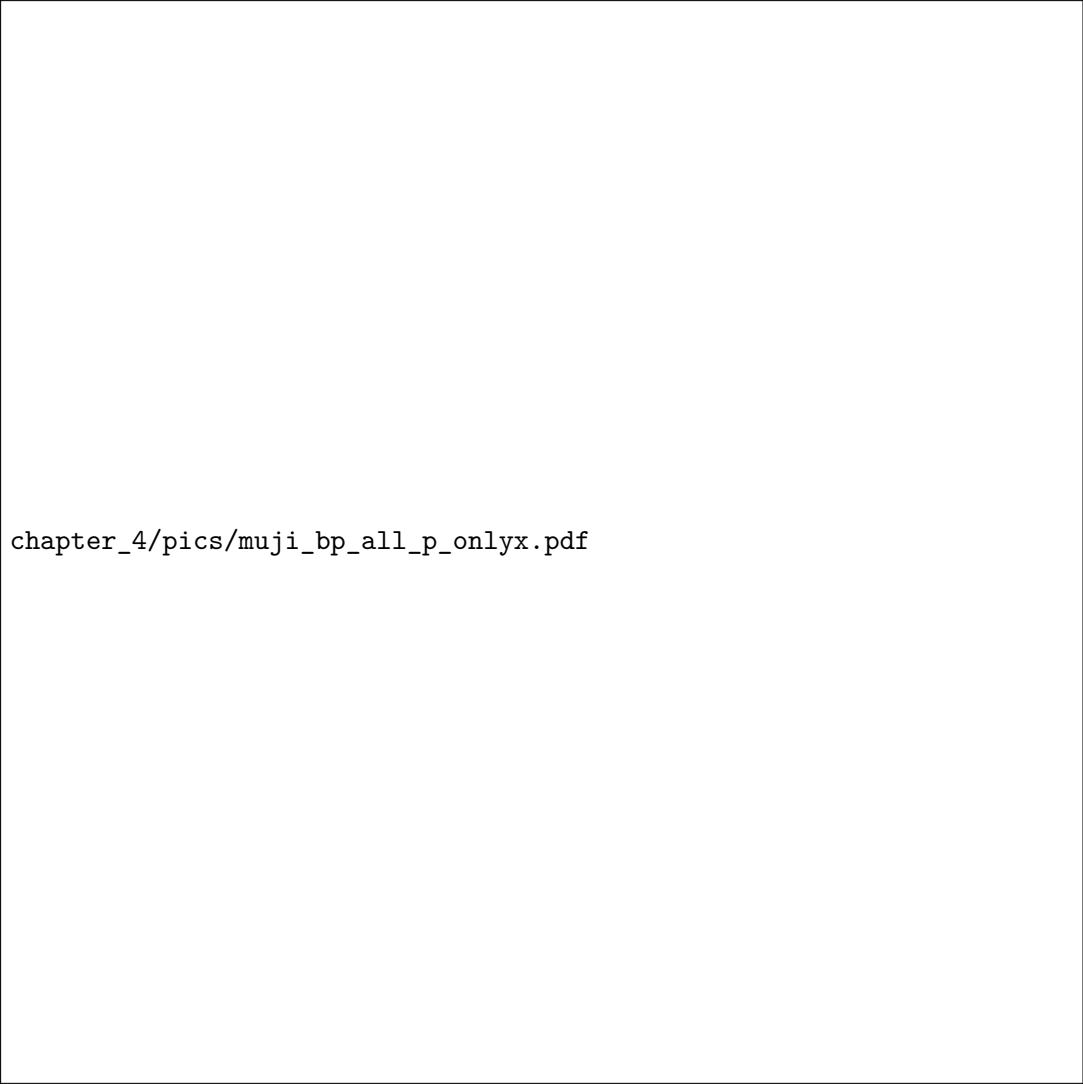


Figure S1.25: Rupture velocity estimate for the 2016 Muji earthquake from the high-frequency BP at the western segment (red line) and at the eastern segment (black line), measured from the nucleation point to the last respective semblance mapping. Time is relative to the first window with semblance. The blue line shows the rupture velocity estimate for the eastern segment, from its rupture start of the eastern segment only to the respective end of rupture on each segment, indicated by the two blue dots at the beginning.

chapter\_4/pics/muji\_1s\_all\_quer\_resamx.pdf

Figure S1.26: Time-incremental high-frequency semblance maps for the backprojection of the 2016 Muji earthquake for every timestep of 1 s from 0 s in a) to 15 s in o). The time given is relative to the onset of the first occurrence of significant semblance.



chapter\_4/pics/muji\_bp\_all\_p\_onlyx.pdf

Figure S1.27: Cumulative low-frequency P-phase semblance map, from all timesteps of the backprojection of the 2016 Muji earthquake.

chapter\_4/pics/muji\_bp\_all\_s\_onlyx.pdf

Figure S1.28: Cumulative low-frequency SH-phase semblance map, from all timesteps of the backprojection of 2016 Muji earthquake.

chapter\_4/pics/muji\_fwd\_comb\_singleex.pdf

Figure S1.29: Cumulative semblance maps from a synthetic backprojection of a single-segment kinematic source model representing the 2016 Muji earthquake for a) high-frequency and b) low-frequency waveforms. The thick black line indicates the upper edge of the fault and the gray-shaded area the fault projection to the surface. The blue dot indicates the rupture nucleation point.



chapter\_4/pics/syn\_muji\_timex.pdf

Figure S1.30: Time-incremental high-frequency semblance mappings for all timesteps in a) to d) from a synthetic backprojection of a single-segment kinematic source model representing the 2016 Muji earthquake. The thick black line indicates the upper edge of the fault and the gray-shaded area the fault projection to the surface. The blue dot indicates the nucleation point. h) Beampower of the high-frequency BP as a function over time as a red and filled function of time together with the optimal (black line) source time functions from the SCARDEC catalog Vallée and Douet, 2016. Additionally shown is the beampower from using the single large array aperture backprojection as a red line.

**Additional optimization results for the 2016 Muji**

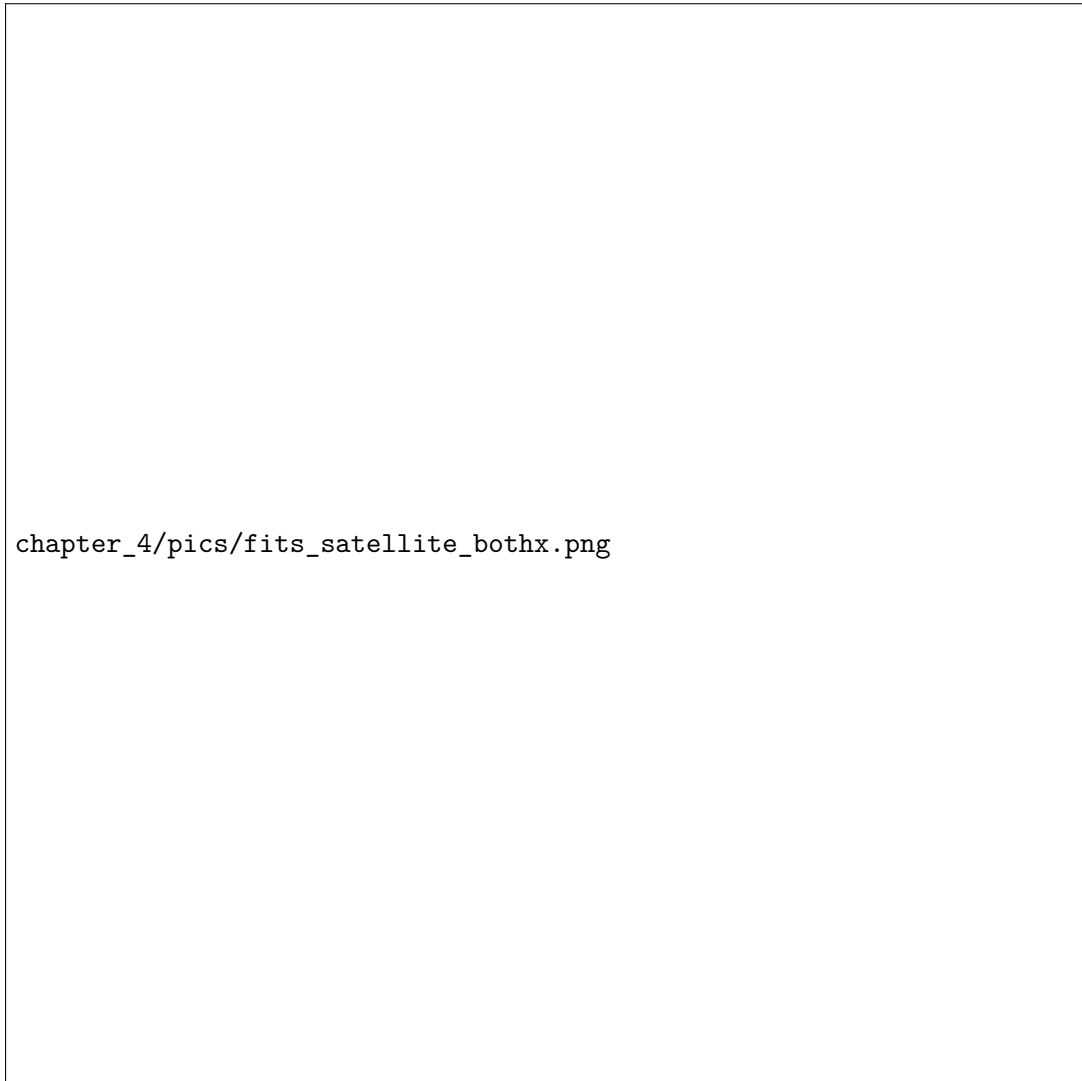


Figure S1.31: Data, model and residual for the InSAR line-of-sight displacements for the best-performing model from the exploratory optimization for a) ascending data and b) descending data as well as from the guided optimization for c) ascending data and d) descending data.



Figure S1.32: Waveform fits for the ensemble of the exploratory and guided optimizations side-by-side for selected stations. Left rows show the exploratory and right rows the guided optimization fits.  $Z$ -components and for some stations also the  $T$ -components are shown. In each subplot the black lines show the original waveforms data, and colored waveforms show the modelled synthetic waveforms with blue to red showing decreasing misfits (with blue poor and red good misfit). The light yellow shading shows the applied waveform taper. At the bottom of each panel the absolute waveform misfit with time is plotted in red.

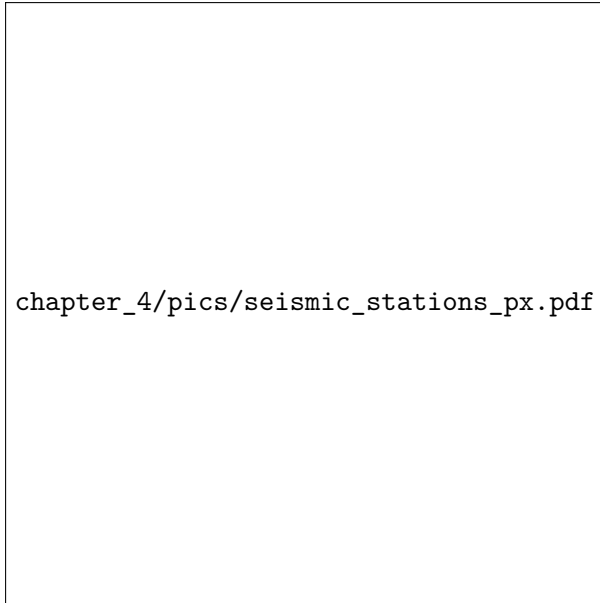


Figure S1.33: Station map indicating trace weights in the non-linear optimization for the Z-component (P-phase).

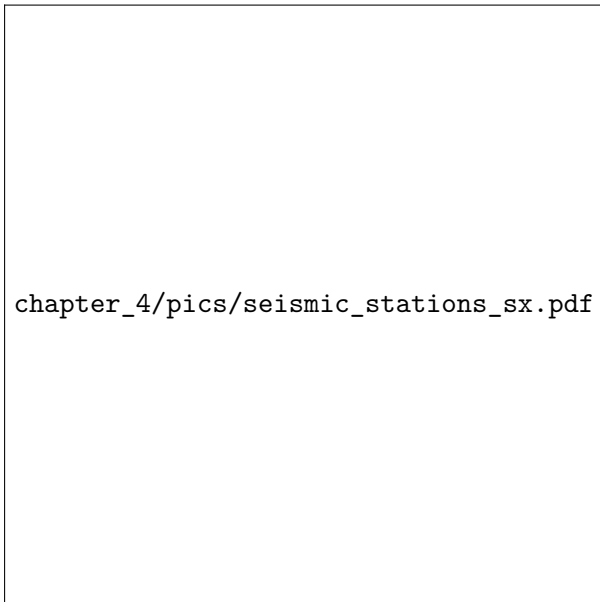
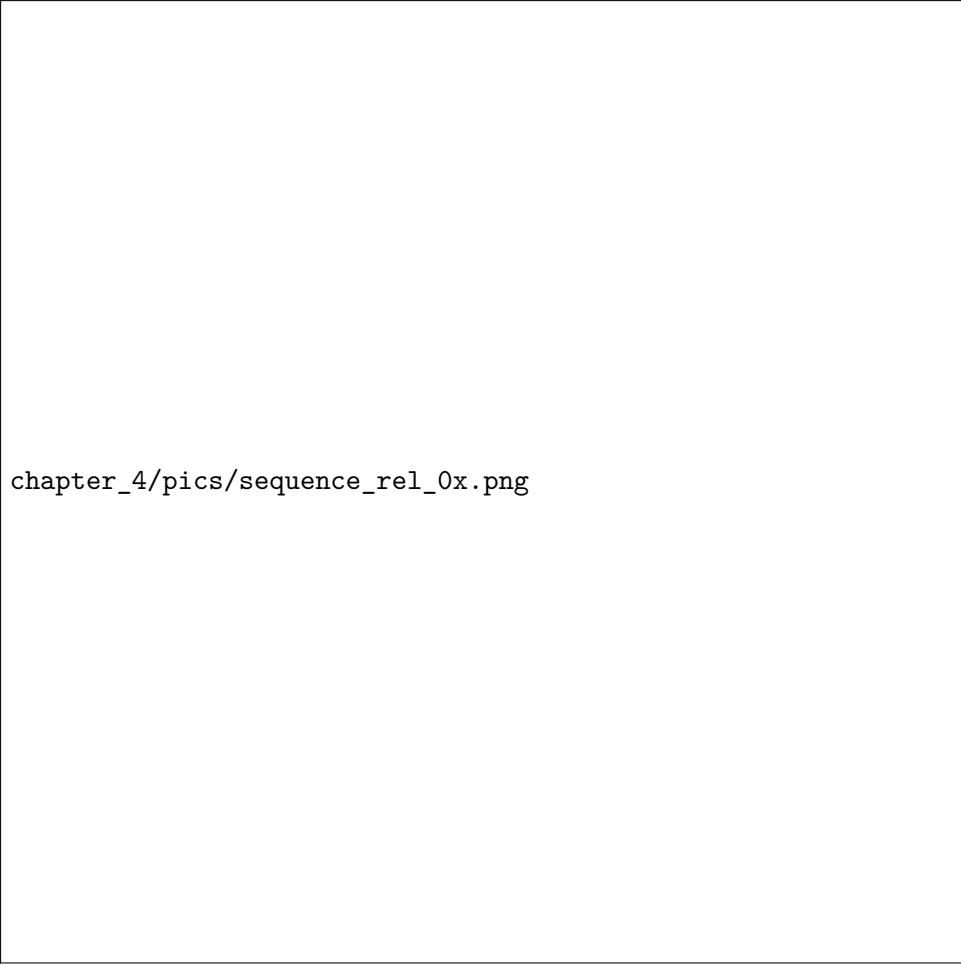


Figure S1.34: Station map indicating trace weights in the non-linear optimization for the T-component (SH-phase).

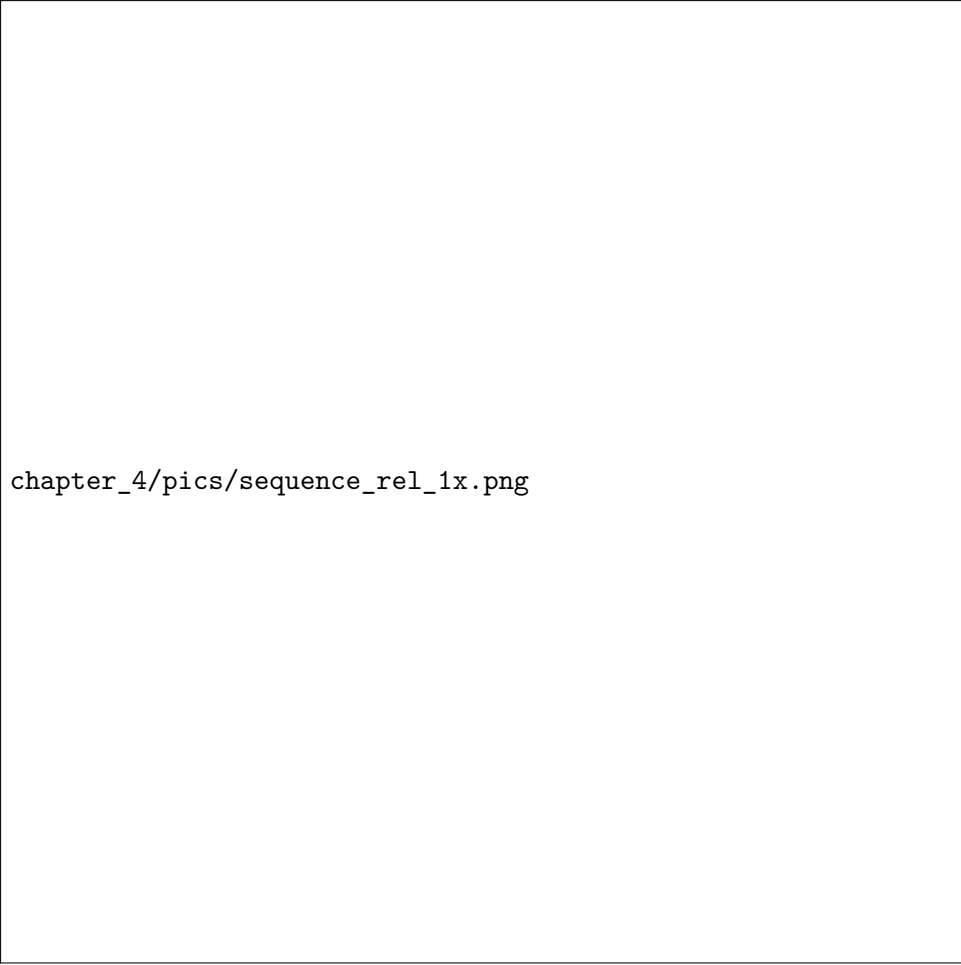
chapter\_4/pics/sequence\_guided\_vs\_non\_guidedx.pdf

Figure S1.35: Bootstrap chain misfits (ensemble) as a function of the sample number for the guided optimization (red) compared to the exploratory optimization (blue).



chapter\_4/pics/sequence\_rel\_0x.png

Figure S1.36: Sampled parameter values for the eastern source segment as a function of sample number, color-coded according to misfit, with warmer colors showing lower misfits. Shown are the source parameters sampled for the eastern source segment from the guided (right column) and exploratory optimizations (left column) in comparison. Shown are only source parameters with different priors in the two optimizations.



chapter\_4/pics/sequence\_rel\_1x.png

Figure S1.37: Sampled parameter values for the western source segment as a function of sample number, color-coded according to misfit, with warmer colors showing lower misfits. Shown are the source parameters sampled for the western source segment from the guided (right column) and exploratory optimizations (left column) in comparison. Shown are only source parameters with different priors in the two optimizations.

**Supplement of "Illuminating the spatio-temporal evolution of the 2008-2009 Qaidam earthquake sequence with the joint use of InSAR time series and teleseismic data"**



Table S2.1: Summary of the gCMT solutions Ekström et al., 2012 for the 8  $M_w > 5.2$  earthquakes that occurred in Qaidam between 2003 and 2009.

Parameters	2003/04/17	2004/05/04	2004/05/04b	2004/05/10	2008/11/10	2009/08/28	2009/08/30	2009/08/31
Magnitude	6.3	5.3	5.2	5.5	6.3	6.3	5.4	5.8
Depth (km)	16	18.6	21.6	12	27.2	12	16.8	12
Half duration (s)	3.6	1.2	1.0	1.4	3.6	3.3	1.2	3.6
strike1 (°)	294	145	140	272	252	295	272	277
dip1 (°)	29	83	87	33	28	31	45	33
rake1 (°)	88	175	-178	69	57	102	118	90
strike2 (°)	116	236	50	116	108	101	55	98
dip2 (°)	61	85	88	59	67	60	51	57
rake2 (°)	91	7	-3	103	106	83	64	90

chapter\_3/supplement/modelsx.pdf

Figure S2.1: Simplified sketches summarising the two opposite geodynamic deformation models of northeastern Tibet with their implications for the faults geometry of the North Qaidam thrust system. Numerous other interpretations might fit within those two end-member models. OLT: Olongbulak thrusts. XT: Xietieshan thrusts.

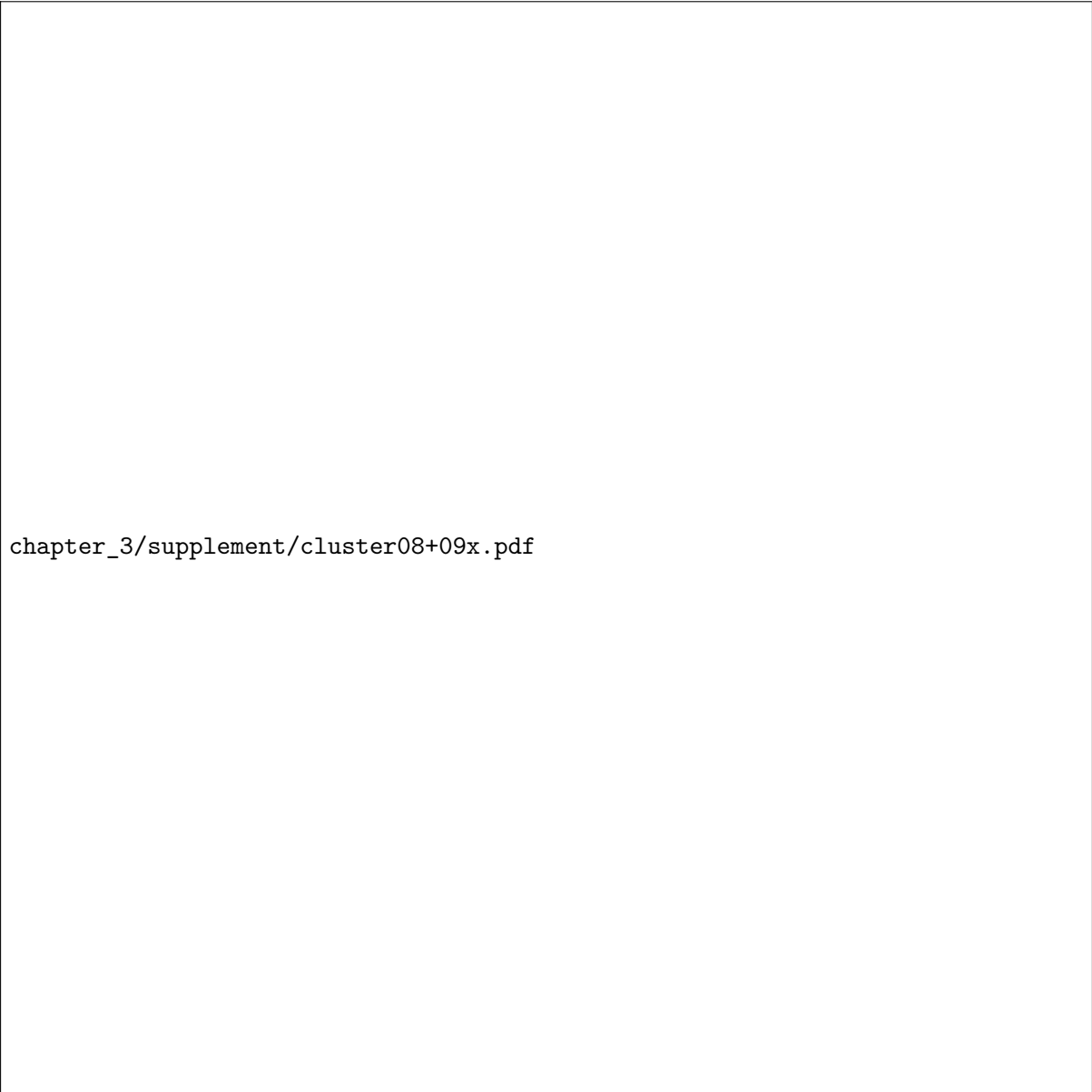


Figure S2.2: Station array locations used for the backprojection of the 2008 and 2009 earthquakes. Blue lines are distances in degree and red lines are the inner and outer circles of the station selection at  $22^\circ$  and  $94^\circ$ . Stations are colored after the virtual array they belong to.



Figure S2.3: Empirical time shifts at virtual array stations for the P-phase for a) low-frequency and b) high-frequency backprojections that maximise the semblance of the reference event and are used for the backprojection. The color at each station indicates the time shift in seconds.

Table S2.2: Summary of the prior probabilities for the 2008 co-seismic rectangular fault inference  $\mathcal{U}$  defines normal distribution. Northing and Easting positions are relative to the gCMT solution.

<b>Parameters</b>	<b>prior</b>
<b>Easting (km)</b>	$\mathcal{U}(-2, 15)$
<b>Northing (km)</b>	$\mathcal{U}(0, 20)$
<b>Depth (km)</b>	$\mathcal{U}(2, 30)$
<b>Length (km)</b>	$\mathcal{U}(2, 30)$
<b>Width (km)</b>	$\mathcal{U}(.5, 30)$
<b>Slip (m)</b>	$\mathcal{U}(0.2, 3)$
<b>Strike (<math>^{\circ}</math>)</b>	$\mathcal{U}(80, 310)$
<b>Dip (<math>^{\circ}</math>)</b>	$\mathcal{U}(0, 80)$
<b>Rake (<math>^{\circ}</math>)</b>	$\mathcal{U}(55, 135)$
<b>Nucleation X</b>	$\mathcal{U}(-1, 1)$
<b>Nucleation Y</b>	$\mathcal{U}(-1, 1)$
<b>Velocity (m/s)</b>	$\mathcal{U}(2000, 4000)$
<b>Time (s)</b>	$\mathcal{U}(-10, 10)$

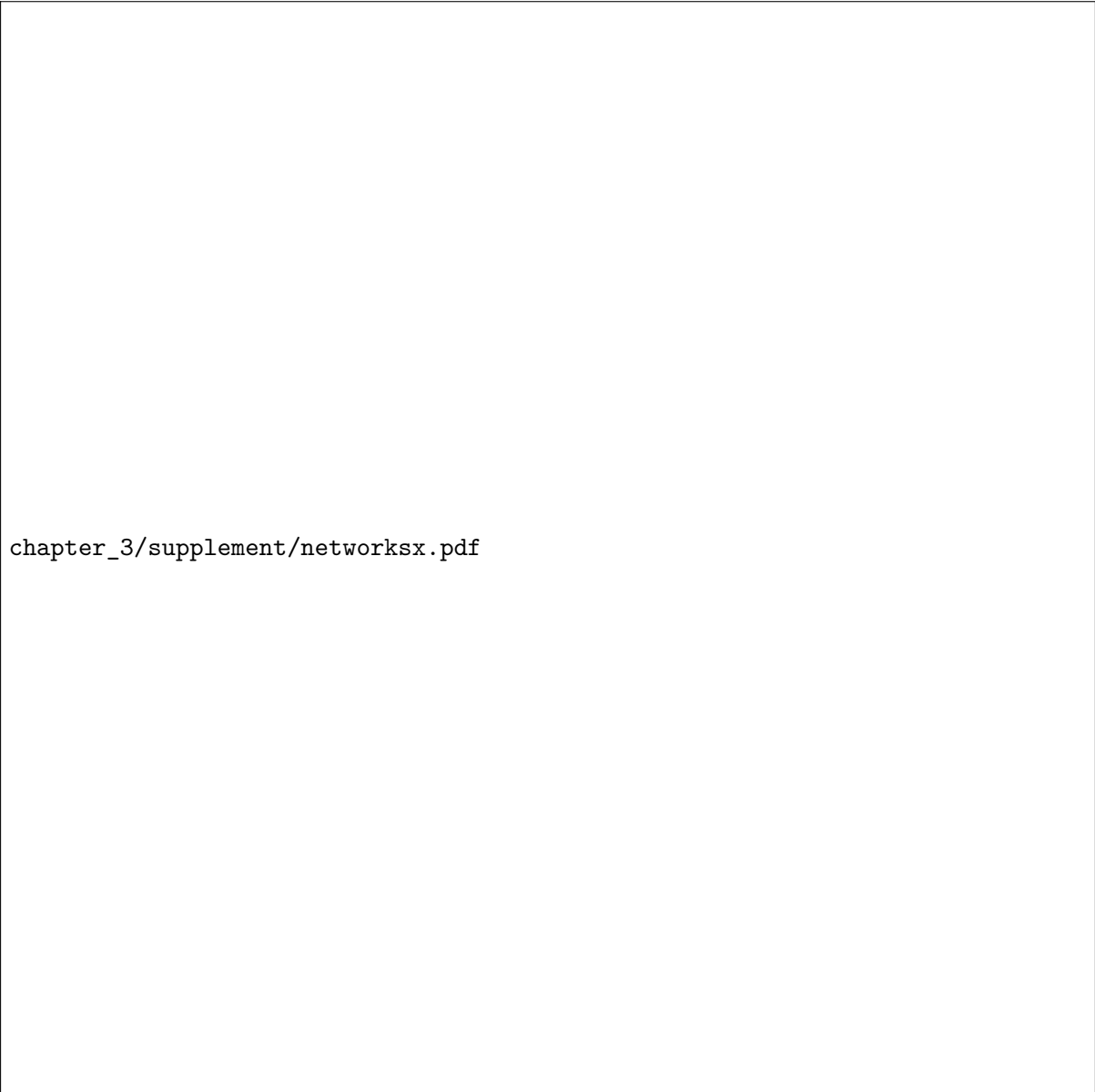


Figure S2.4: Computed interferograms for the three tracks. Triangles are SAR acquisitions with sizes according to their spatial extent. The "primary" images are shown with a blue triangle.

chapter\_3/supplement/test\_taux.pdf

Figure S2.5: Time series of surface displacements from 2008 to 2011 for the pixel 2 of track 319 of Figure 2 (blue circles) with best-fitting estimations of long-term velocities, 2008, 2009 co-seismic offsets and logarithmic afterslip functions for three relaxations times (1 day in red, 15 days in blue and 45 days in green).

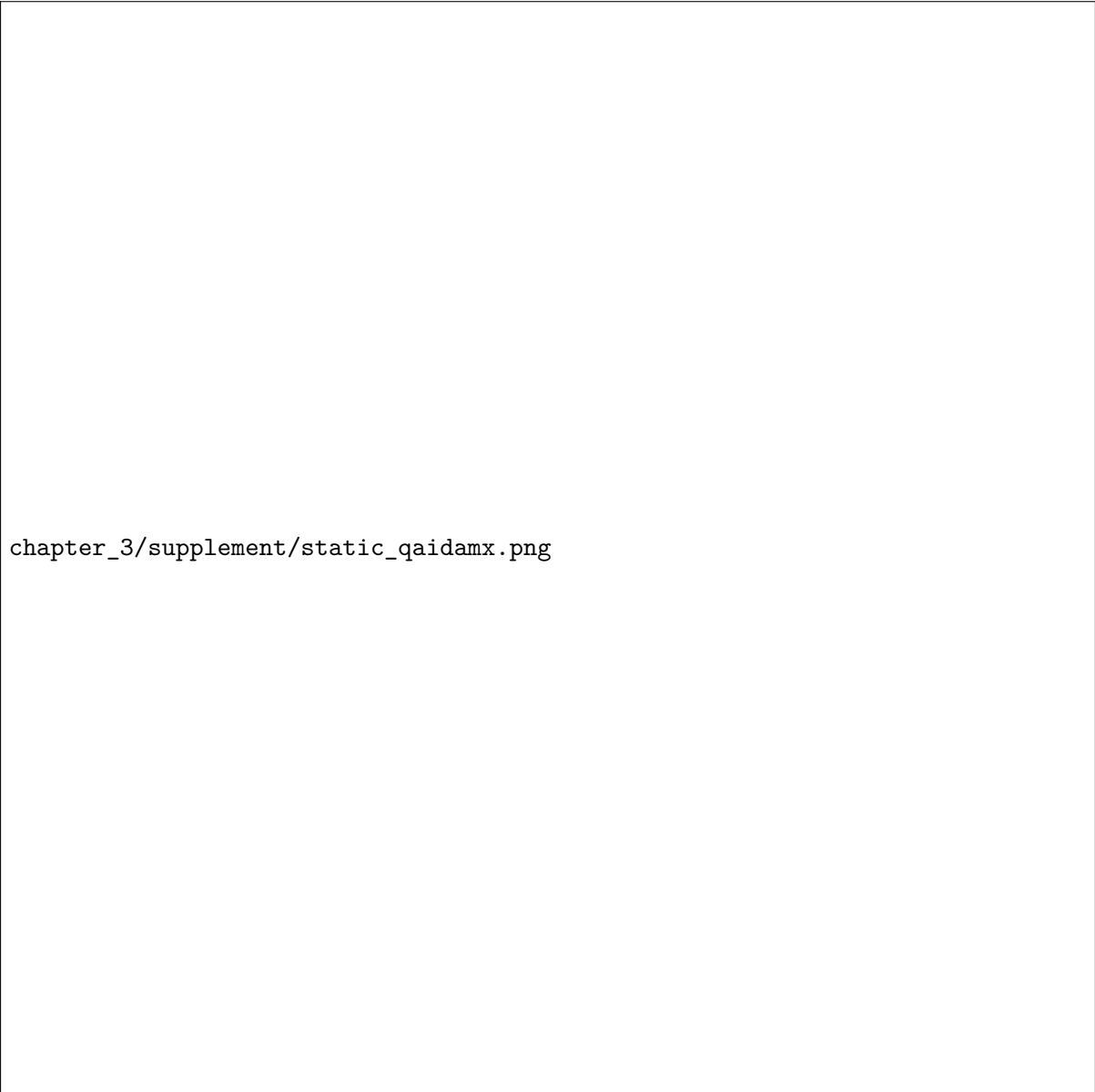


Figure S2.6: Crustal velocity model of the elastic stratified medium used to compute the near-field surface displacements.

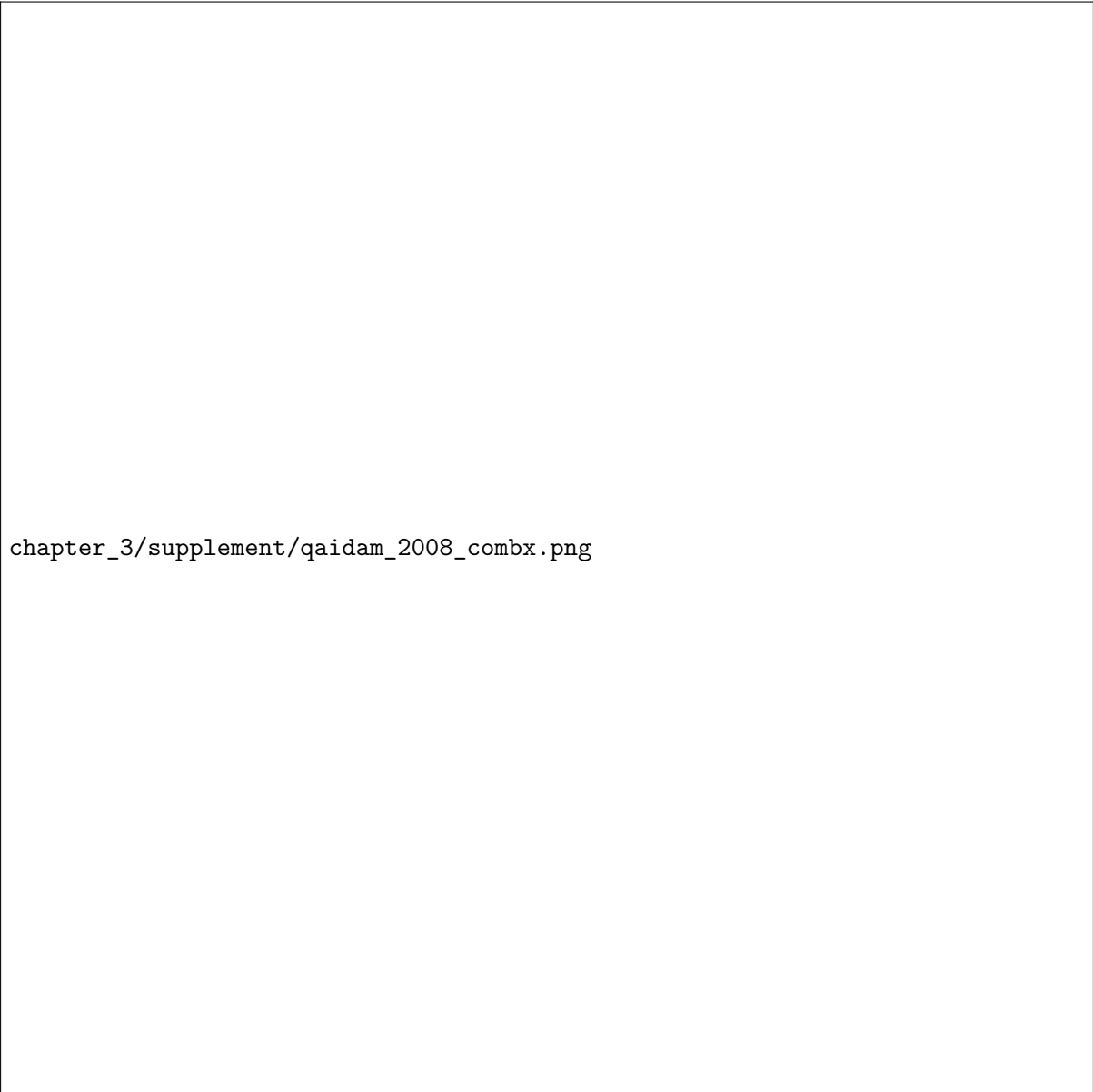
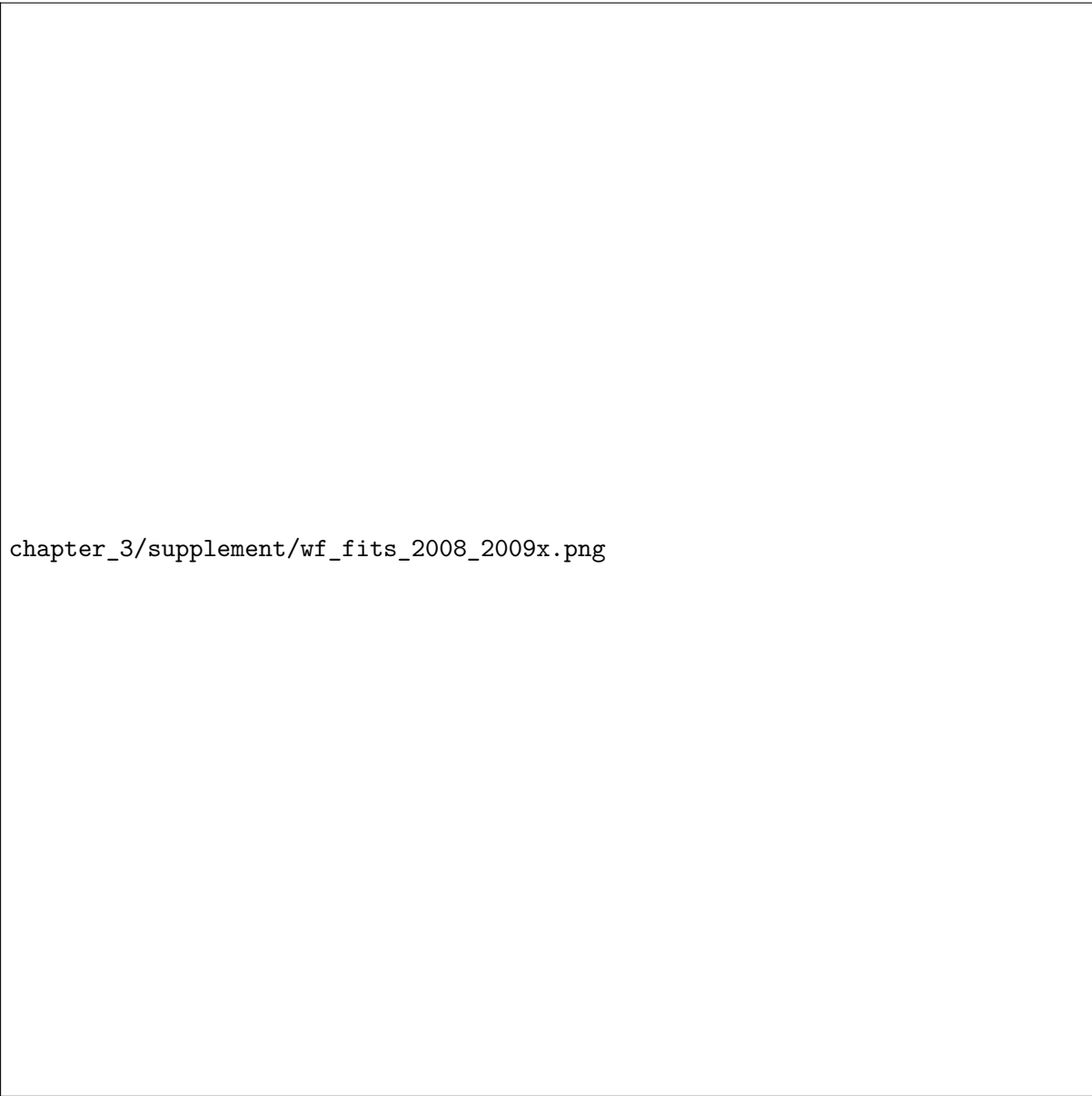


Figure S2.7: Semblance mapping for each time-steps for the 2008 Qaidam earthquake. Contour lines are colored after the cumulative semblance at any time-step. The black outlines represent the spatial uncertainty of 86% of the semblance values and the blue outlines the spatial uncertainty of 96% of the semblance values. They uncertainties are drawn as minimum bounding outlines for the locations of the semblance from 100 bootstrapped realisations of the semblance. a) Low-frequency semblance mappings for every time-step of 8 s and window length of 26 s individually. b-c) High-frequency semblance mappings for every time step of 2 s.





Figure S2.8: Semblance mapping for each time-step for the 2009 Qaidam earthquake, contour lines are colored after the cumulative semblance at any time-step. The black outlines represent the spatial uncertainty of 86% of the semblance values and the blue outlines the spatial uncertainty of 96% of the semblance values. They uncertainties are drawn as minimum bounding outlines for the locations of the semblance from 100 bootstrapped realisations of the semblance. The low-frequency semblance mappings for every time-step of 8 s and window length of 26 s individually in each of the subfigures a) and b). High-frequency semblance mappings for every time-step of 2 s individually in each of the subfigures c)-g).



chapter\_3/supplement/wf\_fits\_2008\_2009x.png


Figure S2.9: Waveform fits of the P-phase for the 2008 earthquake north-dipping solution (a) and the 2009 earthquake (b) for five random stations, which are common to both datasets. Restituted and filtered traces without tapering are in light grey while traces with tapering and processing are in dark grey. The filtered, tapered, and shifted synthetic traces for the 200 bootstraps are colored according to their misfit from red (best fit) to blue (worst fit). The amplitudes of the traces are scaled according to the weights (small weight, small amplitude) and normed relative to the maximum amplitude. The bottom panel shows residuals for all 200 bootstraps chains. Stations information (name with the component, distance to the source, azimuth of station with respect to the source) is given on the left-top. The background shaded area shows the applied taper function.

Table S2.3: Summary of the prior probabilities for the 2008 post-seismic rectangular fault inference. Northing and Easting positions are relative to the gCMT solution.

Parameters	prior
<b>Easting (km)</b>	$\mathcal{U}(-2, 15)$
<b>Northing (km)</b>	$\mathcal{U}(0, 20)$
<b>Depth (km)</b>	$\mathcal{U}(2, 30)$
<b>Length (km)</b>	$\mathcal{U}(2, 30)$
<b>Width (km)</b>	$\mathcal{U}(.5, 30)$
<b>Slip (m)</b>	$\mathcal{U}(0.02, 1.5)$
<b>Strike (<math>^{\circ}</math>)</b>	$\mathcal{U}(250, 310)$
<b>Dip (<math>^{\circ}</math>)</b>	$\mathcal{U}(0, 80)$
<b>Rake (<math>^{\circ}</math>)</b>	$\mathcal{U}(55, 135)$

Table S2.4: Summary of the prior probabilities for the 2009 co-seismic rectangular fault inference. The three sources are numerated 0 (middle), 1 (east) and 2 (west). Northing and Easting positions are relative to the gCMT solution.

Parameters	prior	Parameters	prior
<b>Depth 0 (km)</b>	$\mathcal{U}(.5, 10)$	<b>Strike 0 (<math>^{\circ}</math>)</b>	$\mathcal{U}(80, 140)$
<b>Depth 1 (km)</b>	$\mathcal{U}(.5, 10)$	<b>Strike 1 (<math>^{\circ}</math>)</b>	$\mathcal{U}(80, 140)$
<b>Depth 2 (km)</b>	$\mathcal{U}(.5, 10)$	<b>Strike 2 (<math>^{\circ}</math>)</b>	$\mathcal{U}(100, 140)$
<b>Dip 0 (<math>^{\circ}</math>)</b>	$\mathcal{U}(30, 70)$	<b>Width 0 (km)</b>	$\mathcal{U}(2, 9)$
<b>Dip 1 (<math>^{\circ}</math>)</b>	$\mathcal{U}(30, 70)$	<b>Width 1 (km)</b>	$\mathcal{U}(2, 9)$
<b>Dip 2 (<math>^{\circ}</math>)</b>	$\mathcal{U}(30, 70)$	<b>Width 2 (km)</b>	$\mathcal{U}(2, 9)$
<b>Easting 0 (km)</b>	$\mathcal{U}(-1, 2)$	<b>Nucleation X0</b>	$\mathcal{U}(-1, 1)$
<b>Easting 1 (km)</b>	$\mathcal{U}(6, 15)$	<b>Nucleation X1</b>	$\mathcal{U}(-1, 1)$
<b>Easting 2 (km)</b>	$\mathcal{U}(-15, -9)$	<b>Nucleation X2</b>	$\mathcal{U}(-1, 1)$
<b>Length 0 (km)</b>	$\mathcal{U}(6, 16)$	<b>Nucleation Y0</b>	$\mathcal{U}(-1, 1)$
<b>Length 1 (km)</b>	$\mathcal{U}(2, 10)$	<b>Nucleation Y1</b>	$\mathcal{U}(-1, 1)$
<b>Length 2 (km)</b>	$\mathcal{U}(2, 10)$	<b>Nucleation Y2</b>	$\mathcal{U}(-1, 1)$
<b>Northing 0 (km)</b>	$\mathcal{U}(-5, 9)$	<b>Velocity 0 (m/s)</b>	$\mathcal{U}(2000, 4500)$
<b>Northing 1 (km)</b>	$\mathcal{U}(-5, 9)$	<b>Velocity 1 (m/s)</b>	$\mathcal{U}(2000, 4500)$
<b>Northing 2 (km)</b>	$\mathcal{U}(2.5, 9)$	<b>Velocity 2 (m/s)</b>	$\mathcal{U}(2000, 4500)$
<b>Rake 0 (<math>^{\circ}</math>)</b>	$\mathcal{U}(-180, 180)$	<b>Time 0 (s)</b>	$\mathcal{U}(-10, 10)$
<b>Rake 1 (<math>^{\circ}</math>)</b>	$\mathcal{U}(-180, 180)$	<b>Time 1 (s)</b>	$\mathcal{U}(-10, 10)$
<b>Rake 2 (<math>^{\circ}</math>)</b>	$\mathcal{U}(-180, 180)$	<b>Time 2 (s)</b>	$\mathcal{U}(-10, 10)$
<b>Slip 0 (m)</b>	$\mathcal{U}(0.2, 3)$		
<b>Slip 1 (m)</b>	$\mathcal{U}(0.2, 3)$		
<b>Slip 2 (m)</b>	$\mathcal{U}(0.2, 3)$		



chapter\_3/supplement/maps\_sdx.png

Figure S2.10: Comparison between data and model from the optimisation of one rectangular south-dipping fault in agreement with the 10<sup>th</sup> November 2008 earthquake data. Left: Sub-sampled surface displacements for tracks 319, 047 and 455. Middle: Modeled displacements associated with the maximum likelihood of the posterior probability distribution. Right: Residuals between the forward model and the observations.

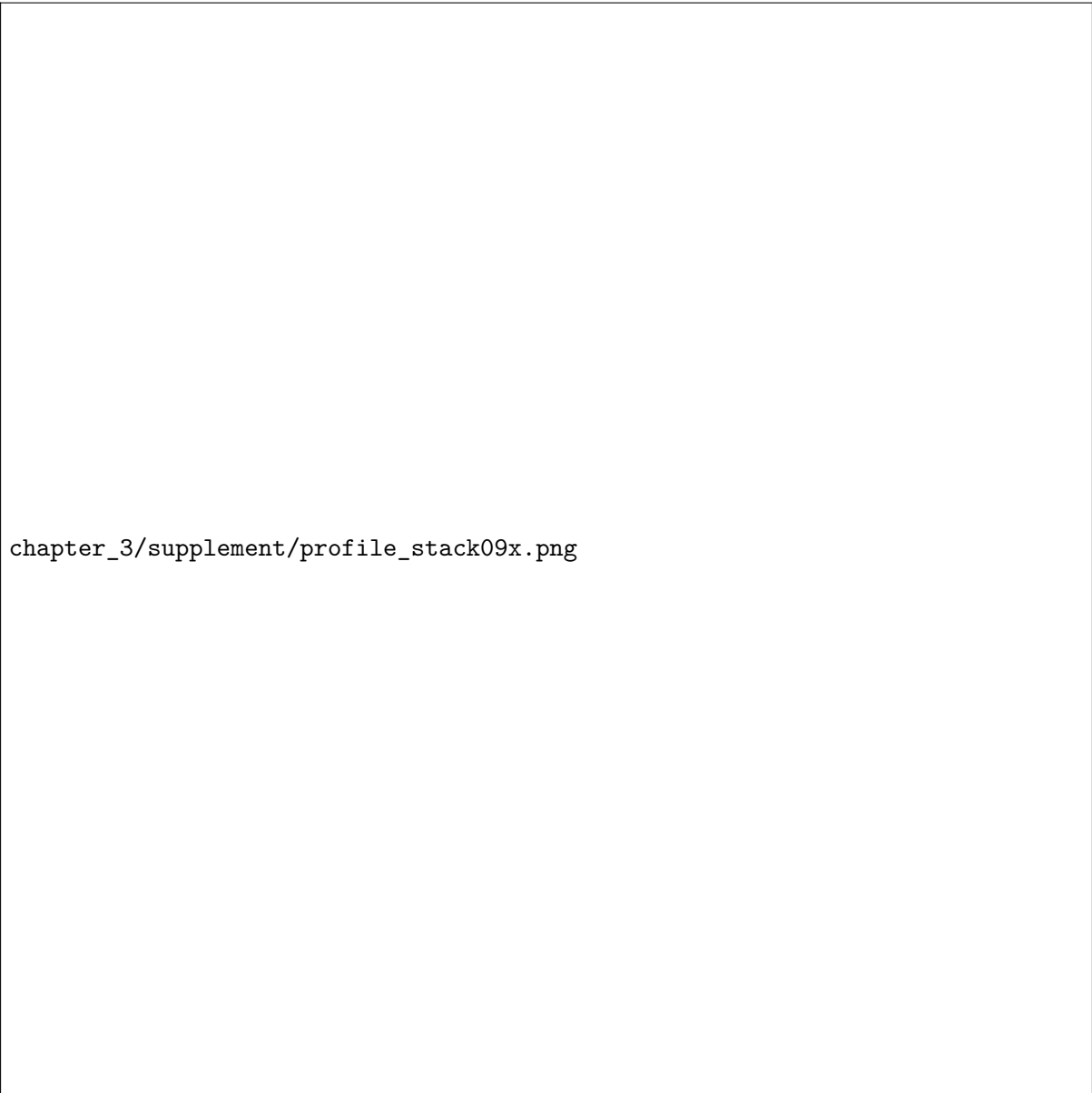


Figure S2.11: Posterior models for the 28<sup>th</sup> August 2009 earthquake obtained from the optimisation of three rectangular faults in agreement with a stack of co-seismic interferograms. a) Best-fitting posterior geometries in map view for the three segments of the 2009 co-seismic and post-seismic (dark blue, cyan, blue) source inferences. b) As for top figure, but along the N22°E profile perpendicular to the Olongbulak Shan marked AA' in (a) and with interpreted fault geometry at depth. Fault geometries are very similar to the three fault segments obtained from the optimisation of the co-seismic surface displacements from the time series data, suggesting that post-seismic slip occurred on similar fault planes than co-seismic slip.

chapter\_3/supplement/slip-partitioningx.pdf

Figure S2.12: Conservation of the kinematic motion across the Olongbulak pop-up (OLT) for the south-dipping scenario. a) If the dip angle of the deep-seated fault, where the 2008 earthquake occurred ( $\gamma - \alpha$ ), is smaller than the dip angle of the shallow high-angle fault, where the 2009 earthquake occurred ( $\gamma$ ), then the change of dip angle between the two faults creates a differential of vertical uplift between the Qaidam Basin (QB) and the Olongbulak ranges accommodated by a shallow back-thrust fault dipping to the north ( $180 - \beta$ ). Slip on each fault segment is controlled by the geometry with equations provided in Daout et al., 2016a. b) If the deep-seated segment is coplanar to the shallow segment, then no back-thrust is kinematically required.

Table S2.5: Comparison of the variance-covariance estimations of the InSAR co-seismic Time Series (TS) data maps, co-seismic interferograms (IFG), and stack of co-seismic interferograms

		Variance (m <sup>2</sup> )	Auto-covariance (m <sup>2</sup> )	Correlation distance (m <sup>2</sup> )
2008 Co- TS	T319	$1.4 \times 10^{-6}$	$1.7 \times 10^{-6}$	0.6
2008 Co- TS	T047	$2.7 \times 10^{-6}$	$3.8 \times 10^{-6}$	1.6
2008 Co- TS	T455	$3.2 \times 10^{-6}$	$3.7 \times 10^{-6}$	1.4
2008 Co- IFG	T319	$3.2 \times 10^{-6}$	$3.2 \times 10^{-6}$	1.1
2008 Co- IFG	T047	$9.6 \times 10^{-6}$	$9.0 \times 10^{-6}$	1.6
2008 Co- IFG	T455	$4.2 \times 10^{-6}$	$6.2 \times 10^{-6}$	0.7
2008 Stack	T319	$3.7 \times 10^{-6}$	$4.3 \times 10^{-6}$	1.1
2008 Stack	T047	$1.1 \times 10^{-5}$	$1.2 \times 10^{-5}$	1.2
2008 Stack	T455	$9.8 \times 10^{-6}$	$1.4 \times 10^{-5}$	1.8
2009 Co- TS	T319	$1.0 \times 10^{-6}$	$1.5 \times 10^{-6}$	1.2
2009 Co- TS	T047	$2.3 \times 10^{-7}$	$2.6 \times 10^{-7}$	1.3
2009 Co- TS	T455	$1.6 \times 10^{-6}$	$2.2 \times 10^{-6}$	2.2
2009 Co- IFG	T319	$6.2 \times 10^{-5}$	$6.8 \times 10^{-5}$	1.8
2009 Co- IFG	T047	$6.4 \times 10^{-6}$	$8.6 \times 10^{-6}$	0.9
2009 Co- IFG	T455	$8.8 \times 10^{-6}$	$8.9 \times 10^{-6}$	1.1
2009 Stack	T319	$6.3 \times 10^{-6}$	$7.2 \times 10^{-6}$	1.2
2009 Stack	T047	$1.4 \times 10^{-5}$	$1.4 \times 10^{-5}$	2.6
2009 Stack	T455	$1.7 \times 10^{-5}$	$1.8 \times 10^{-5}$	1.9